Geochemistry and organic petrology of lacustrine petroleum source rocks: Implications for paleo-depositional environment and organic matter accumulation

Von der Fakultät für Georessourcen und Materialtechnik der
Rheinisch-Westfälischen Technischen Hochschule Aachen

zur Erlangung des akademischen Grades eines

Doktors der Naturwissenschaften

genehmigte Dissertation

vorgelegt von

Zhongrui Wu, M.Sc.

Berichter: Univ. -Prof. Dr. rer. nat. Ralf Littke

Univ. -Prof. Dr. Reinhard Sachsenhofer

Tag der mündlichen Prüfung: 08.03.2024

ACKNOWLEDGEMENTS

Successfully navigating this doctoral journey gave me an impressive life experience. As I finish the last chapter of this thesis, my heart is brimming with appreciation for the invaluable support and encouragement provided by numerous individuals who have been by my side throughout this journey.

Foremost, I express my deep gratitude to Prof. Dr. Ralf Littke for allowing me to pursue my Ph.D. studies at the Institute of Geology and Geochemistry of Petroleum and Coal at the RWTH Aachen University, offering guidance, and enabling the development and realization of innovative ideas. I want to acknowledge his steadfast support throughout my academic and personal growth. Furthermore, I sincerely thank Prof. Dr. Jan Schwarzbauer for his exceptional supervision in molecular organic geochemistry, continuous support, and valuable guidance. I also want to thank Prof. Dr. Reinhard Sachsenhofer (Montanuniversität Leoben) for dedicating his valuable time to reviewing my thesis and serving as the co-examiner for my Ph.D.

I want to express my appreciation to Dr. Sebastian Grohmann for his significant contributions to my publications. Engaging in in-depth discussions with him has dramatically enhanced my critical thinking and scientific writing abilities.

I extend my sincere appreciation to my colleagues and fellow researchers, including Dr. Laura Zieger, Dr. Alireza Baniasad, Dr. Jinqi Qiao, Dr. Tianyu Zheng, Dr. Zibin Zhao, Dr. Nada Vidovic, Dr. Sebastian Amberg, Dr. Linda Burnaz, Arysthasya Arysanto, Saeed Khajooie, and Leidy Castro Vera. The dialogues, discussions, and collaborative endeavors have deepened my knowledge and fostered a friendship, making this journey both enjoyable and rewarding. I express my deep gratitude to Donka Macherey, Annette Schneiderwind, and Kerstin Windeck for their meticulous help with sample preparation and measurements. My sincere gratitude goes to Michelle Evertz for her assistance concerning administrative work.

My special thanks go to my former supervisor, Prof. Sheng He (China University of Geosciences, Wuhan), for his endless caring and encouragement over the past several years. Senior engineer Zhi Yang (Research Institute of Petroleum Exploration & Development, PetroChina) and Prof. Yuanjia Han (China University of Geosciences, Wuhan) are acknowledged for providing support and help for my thesis.

I would like to thank LEK and the China Scholarship Council (CSC) for providing the resources, facilities, and environment essential for my PhD study in Germany.

I extend profound gratitude to my family for their care and love. Their encouragement has been a constant force throughout this academic pursuit. I would not have had the opportunity to complete a Ph.D. abroad without the understanding and encouragement of my family.

Finally, I extend my appreciation to all those whose names may not be mentioned here but have made significant contributions that have left a lasting impact on my academic journey. I am profoundly thankful to all the friends, mentors, and well-wishers who have supported me. In addition, I express heartfelt gratitude to those who played a role in my doctoral research, providing valuable insights and

constructive feedback at various stages. Their collective expertise has notably enriched the quality and depth of my work.

ABSTRACT

Lacustrine organic matter (OM)-rich shale has historically served as an important source and reservoir rocks for conventional and unconventional hydrocarbon production. This thesis is dedicated to studying the characteristics of lacustrine petroleum source rocks in China and Europe, placing particular emphasis on aspects such as hydrocarbon generation potential, depositional environments, the origin of OM, paleoclimatic conditions, and mechanisms of OM accumulation. Chapter 1 contains the objectives of the thesis, geological information on the three study areas, and an overview on each of the three main chapters.

In Chapter 2, data on core samples from the CY1 well in the Yuqia Sag, northern Qaidam Basin, are presented and discussed; these samples were subjected to analysis, including organic petrography, inorganic geochemistry, as well as bulk and molecular organic geochemistry. The objective was to evaluate the thermal maturity of the rocks, assess hydrocarbon generation potential, reconstruct the paleoclimate, and understand the depositional environments during the deposition of the seventh member of the Dameigou Formation (J_2d^7). Moreover, the connection between these factors and OM accumulation was explored. The dominant source of OM is lake plankton, including halophilic algae and cyanobacteria. Three distinct source rock units were identified, exhibiting varying total organic carbon (TOC) contents. The lower unit was deposited in an oxic freshwater column under warm, humid climatic conditions and intense weathering along the lake margin. The OM in this unit is inferred to originate primarily from terrestrial higher plants. In contrast, overlying units 2 and 3 were deposited in sub-oxic to oxic freshwater and anoxic saline environments, respectively. The deposition of units 2 and 3 reflects progressive aridification in the hinterland, evidenced by the decreasing chemical index of alteration (CIA) values. Unit 2's OM was sourced from a combination of terrestrial higher plants and algal biomass. Conversely, unit 3 shows a decrease in terrigenous OM content. The primary source of OM in unit 3 was lake plankton, including halophilic algae and cyanobacteria.

In Chapter 3, bulk and molecular organic geochemistry alongside major and trace element data for the first member of the Qingshankou Formation (K_2qn^1) in the Songliao Basin are presented, utilizing 38 core samples. The primary objectives of the study are to unravel the depositional environments during the K_2qn^1 sedimentation and elucidate the key factors influencing the mechanisms of OM accumulation. All studied rocks are thermally oil-mature. Within the examined well, two distinct types of lacustrine source rocks (units 1 and 2) are identified, with unit I further featuring two OM-rich layers. Essentially, the older unit 1 is characterized by lower TOC content and the younger unit 2 is characterized by higher TOC content. Additionally, thin marine transgressive layers of approximately 1–2 meters were detected within unit 1. Unit 1 is marked by the lowest TS contents, averaging 0.56 wt%. In contrast, unit 2 samples exhibit significantly higher TS contents (average 1.24 wt%). Samples representing the presumed marine transgressive events display the highest TOC (average 2.82 wt%) and TS contents (average 2.01 wt%). Unit 1 was primarily deposited under oxic-dysoxic and freshwater-brackish water conditions, as evidenced by multiple organic and inorganic geochemical indicators. Conversely, unit 2 and the marine transgressive layers were deposited under less oxygenated and more saline bottom water. Source rocks from the K_2qn^1 generally

show minor input of terrestrial OM. However, unit 1, containing type II-III kerogen, indicates a slightly more pronounced contribution from terrigenous higher plants compared to unit 2 and the marine transgressive layers, where the kerogen is predominantly derived from planktonic/algal and microbial biota.

In Chapter 4, data on organic petrology, stable carbon isotopes, as well as bulk and molecular geochemistry, along with elemental geochemistry, are presented and discussed based on analysis of 36 outcrop samples of Early Permian lacustrine shale from the Usclas-St. Privat (USPF), Tuilières-Loiras Formation (TLF), and Viala Formation (VF) in the Lodève Basin, southern France. The study mainly unravels the alterations in the environmental conditions of the paleolake during the deposition of these formations and establishes an OM accumulation model for the lacustrine fine-grained sediments. All analyzed samples are thermally oil-mature. The lower section of the USPF exhibits TOC and TS contents of 4.28 wt% and 1.09 wt% on average, respectively. In contrast, the upper section of the USPF, TLF, and VF show considerably lower TOC and TS contents. The lower section of the USPF was deposited in an oxygen-depleted and saline lacustrine environment, likely associated with more humid climatic conditions and potential marine influence. In contrast, the upper section of the USPF, TLF, and VF were deposited in oxic-dysoxic and freshwater-brackish bottom water conditions with a significant shift towards arid conditions. Biomarker analysis suggests that the OM in most samples primarily originates from planktonic/algal biomass with additional microbial OM. Only the lower section of the USPF shows a slightly increased contribution of terrestrial OM input and a higher detrital influx. It is inferred that the basin's structural evolution from a narrow, deep setting to a wider, shallower configuration, along with postulated marine transgressive events during the early stages, played a pivotal role in shaping the deposition environments of these two distinct lacustrine shale sets, influencing OM accumulation mechanisms. Conversely, substantial climatic aridification appears to have a relatively minor impact on OM sources and water column conditions.

Chapter 5 exhibits and compares the geochemistry characteristics of the typical lacustrine shales with different depositional settings in China and Europe. In addition, the depositional models for different types of lacustrine OM-rich source rocks are summarized.

ZUSAMMENFASSUNG

Lakustrine organikreiche Sedimentgesteine spielten in der Vergangenheit eine wichtige Rolle als Mutter- und Reservoirgesteine für die konventionelle und unkonventionelle Kohlenwasserstoffproduktion. Diese Dissertation widmet sich der Untersuchung der Eigenschaften lakustriner Erdölmuttergesteine in China und Europa, wobei besonderes Augenmerk auf Aspekte wie das Kohlenwasserstoffbildungspotenzial, die Ablagerungsbedingungen, die Herkunft des organischen Materials (OM), paläoklimatische Bedingungen und Mechanismen der Akkumulation des OM gelegt wird. Das erste Kapitel enthält die Zielsetzungen der Dissertation, geologische Informationen zu den drei Untersuchungsgebieten und einen Überblick über jedes der drei Hauptkapitel.

Im zweiten Kapitel werden Kernprobendaten aus dem CY1-Bohrloch im Yuqia-Sattel im nördlichen Qaidam-Becken präsentiert und diskutiert. Diese Proben wurden verschiedenen Analysen unterzogen, einschließlich organischer Petrographie, anorganischer Geochemie sowie organischer Geochemie. Das Ziel bestand darin, die thermische Reife der analysierten Gesteine zu bewerten, das Kohlenwasserstoffbildungspotenzial zu beurteilen, sowie das Paläoklima und die Bedingung während der Ablagerung des siebten „Members“ der Dameigou-Formation zu rekonstruieren. Zudem wurde der Zusammenhang dieser Faktoren und der OM-Akkumulation erforscht. Die vorherrschende Quelle des OM ist Seeplankton, einschließlich halophiler Algen und Cyanobakterien. Es wurden drei unterschiedliche Einheiten von Muttergesteinen identifiziert, die unterschiedliche organische Kohlenstoff (TOC)-Gehalte) aufweisen. Die untere Einheit 1 wurde in einer sauerstoffhaltigen Süßwassersäule unter warmfeuchten klimatischen Bedingungen und bei intensiver Verwitterung im Hinterland abgelagert. Das OM in dieser Einheit stammt hauptsächlich von höheren Landpflanzen. Im Gegensatz dazu wurden die darüber liegende Einheit 2 unter sub-oxischen bis oxischen Süßwasserbedingungen und die Einheit 3 unter anoxischen, salinen Bedingungen abgelagert. Die Ablagerungsbedingungen der Einheiten 2 und 3 spiegeln eine fortschreitende Aridifizierung im Hinterland wider, wie durch abnehmende Werte des chemischen Verwitterungsindexes (CIA) belegt. Das OM in Einheit 2 stammt aus einer Kombination von höheren Landpflanzen und Algenbiomasse. Im Gegensatz dazu zeigt Einheit 3 einen verminderten Eintrag von terrigenem OM. Die Hauptquelle von OM in Einheit 3 war Seeplankton, einschließlich halophiler Algen und Cyanobakterien.

Im dritten Kapitel werden organische Geochemie- sowie Haupt- und Spurenelementdaten von 38 Kernproben der ersten Einheit der Qingshankou-Formation (K_2qn^1) im Songliao-Becken präsentiert. Die Hauptziele der Studie bestehen darin, die Ablagerungsumgebungen während der Sedimentation der Einheit K_2qn^1 zu verstehen und die Schlüsselfaktoren zu untersuchen, die die Mechanismen der OM-Akkumulation beeinflussten. Alle untersuchten Proben befinden sich hinsichtlich ihrer thermischen Reife im Ölfenster. Innerhalb des untersuchten Bohrprofils wurden zwei verschiedene Typen von lakustrinen Muttergesteinen (Einheiten 1 und 2) identifiziert, wobei Einheit I zwei OM-reiche Schichten aufweist. Grundsätzlich zeichnet sich die ältere Einheit 1 durch einen niedrigeren Gesamt-TOC-Gehalt aus, während die jüngere Einheit 2 durch höhere TOC-Gehalte gekennzeichnet ist. Zusätzlich wurden 1 bis 2 Meter mächtige Schichten marin-transgressiven Ursprungs in Einheit 1 nachgewiesen. Einheit 1 weist die niedrigsten Gesamtschwefelgehalte auf, im Durchschnitt 0,56

Gew.-%. Im Gegensatz dazu enthalten Proben der Einheit 2 signifikant höhere Schwefelgehalte (im Durchschnitt 1,24 Gew.-%). Proben, die vermutlich marine transgressive Ereignisse repräsentieren, zeigen die höchsten TOC- (im Durchschnitt 2,82 Gew.-%) und Schwefelgehalte (im Durchschnitt 2,01 Gew.-%). Einheit 1 wurde hauptsächlich unter oxisch-dysoxischen Frisch- bis Brackwasser-Bedingungen abgelagert, wie durch mehrere organische und anorganische geochemische Indikatoren belegt. Im Gegensatz dazu wurden Einheit 2 und die marinen transgressiven Schichten in einem sauerstoffärmeren und höher salinaren Wasserkörper abgelagert. Erdölmuttergesteine aus dem K_2qn^1 weisen im Allgemeinen einen geringen Eintrag an terrestrischem OM auf. Einheit 1 enthält Kerogen des Typs II-III und weist einen etwas höheren Beitrag höherer Landpflanzen auf als Einheit 2 und die marin-transgressiven Schichten, in denen das Kerogen hauptsächlich von Plankton/Algen und Mikroben stammt.

Im vierten Kapitel werden Daten zur organischen Petrologie, zu stabilen Kohlenstoffisotopen sowie zur organischen Geochemie sowie Elementargeochemie präsentiert und diskutiert. Die Grundlage hierfür bildet die Analyse von 36 Aufschlussproben von frühpermischen lakustrinen feinkörnigen Sedimentgesteinen aus den Formationen Usclas-St. Privat (USPF), Tuilières-Loiras (TLF) und Viala (VF) aus dem Lodève-Becken im Süden Frankreichs. Die Studie weist Veränderungen in den Umweltbedingungen des Paläosees während der Ablagerung dieser Formationen nach und umfasst die Etablierung eines Modells für die OM-Anreicherung in den feinkörnigen lakustrinen Sedimentgesteinen. Alle analysierten Proben sind thermisch im Erdölfenster. Der untere Abschnitt der USPF weist TOC- und Schwefelgehalte von durchschnittlich 4,28 Gew.-% bzw. 1,09 Gew.-% auf. Im Gegensatz dazu zeigen der obere Abschnitt der USPF, TLF und VF erheblich niedrigere TOC- und Schwefelgehalte. Der untere Abschnitt der USPF wurde unter sauerstoffarmem und salinem Seewasser abgelagert, wahrscheinlich in Verbindung mit feuchteren klimatischen Bedingungen und potenziellem marinen Einfluss. Im Gegensatz dazu wurden der obere Abschnitt der USPF, TLF und VF in oxisch-dysoxischen sowie Frisch- bis Brackwasser-Bedingungen gekoppelt mit einem Wechsel hin zu ariden Bedingungen i m Hinterlandabgelagert. Die Biomarker-Analyse legt nahe, dass das OM in den meisten Proben hauptsächlich von Plankton/Algen stammt, ergänzt durch mikrobielles OM. Lediglich der untere Abschnitt der USPF zeigt einen leicht erhöhten Beitrag an terrestrischem OM und einen erhöhten detritischen Einfluss. Es wird vermutet, dass die strukturelle Entwicklung des Beckens von einer schmalen, tiefen zu einer breiteren, flacheren Senke, zusammen mit angenommenen marinen transgressiven Ereignissen in den frühen Stadien, eine entscheidende Rolle bei der Gestaltung der Ablagerungsumgebungen dieser beiden unterschiedlichen lakustrinen Einheiten spielte. Dies beeinflusste die Mechanismen der OM-Anreicherung. Im Gegensatz dazu scheint die erhebliche klimatische Aridifizierung einen vergleichsweise geringen Einfluss auf den Ursprung des OM und die Redoxbedingungen in der Wassersäule zu haben.

Kapitel 5 präsentiert und vergleicht die geochemischen Eigenschaften der typischen lakustrinen Sedimentgesteine mit unterschiedlichen Ablagerungsumgebungen in China und Europa. Zusätzlich werden die Ablagerungsmodelle für verschiedene Arten von lakustrinen, OM-reichen Erdölmuttergesteinen zusammengefasst.

CONTENTS

LIST OF TABLES

LIST OF FIGURES

LIST OF ABBREVIATIONS

USPF	Usclas-St. Privat Formation	C_{30} H	C_{30}-17α(H),21β(H)-hopane
TLF	Tuilières-Loiras Formation	C_{30} M	C_{30}-17β(H),21α(H)-moretane
VF	Viala Formation	C_{30} DiaH	C_{30}-17α-diahopane
J_2d^7	Seventh member of the Dameigou Formation	C_{31} H S	C_{31}-17α(H),21β(H),22S-homohopane
K_2qn^1	First member of the Qingshankou Formation	C_{31} H R	C_{31}-17α(H),21β(H),22R-homohopane
OM	Organic matter	Gam	Gammacerane
VR_r	Virtinite reflectance [%]	C_{32} H S	C_{32}-17α(H),21β(H),22S-homohopane
TOC	Total organic carbon	C_{32} H R	C_{32}-17α(H),21β(H),22R-homohopane
TS	Total sulfur	C_{33} H S	C_{33}-17α(H),21β(H),22S-homohopane
TIC	Total inorganic carbon	C_{33} H R	C_{33}-17α(H),21β(H),22R-homohopane
SB	Solid bitumen	C_{34} H S	C_{34}-17α(H),21β(H),22S-homohopane
S_1	Free and absorbed hydrocarbons [mg HC /g rock]	C_{34} H R	C_{34}-17α(H),21β(H),22R-homohopane
S_2	Hydrocarbons generated from pyrolysis [mg HC /g rock]	C_{35} H S	C_{35}-17α(H),21β(H),22S-homohopane
S_3	CO_2 formed by thermal breakdown of kerogen [mg CO_2 /g rock]	C_{35} H R	C_{35}-17α(H),21β(H),22R-homohopane
HI	Hydrogen index [mg HC /g TOC]	pregnane	5α,14β,17β(H)-pregnane (diginane)
OI	Oxygen index [mg CO_2 /g TOC]	homopregnane	5α,14β,17β(H)-homopregnane (20-methyldiginane)
T_{max}	Temperature of maximum pyrolysis yield [°C]	C_{27} βα dia20S	20S-13β(H),17α(H)-diacholestane
OM*	Organic matter content before sulfate reduction	C_{27} βα dia20R	20R-13β(H),17α(H)-diacholestane
CAR	Carbonate content	C_{27} αβ dia20S	20R-13α(H),17β(H)-diacholestane
SIL	Silicate content	C_{27} αβ dia20R	20S-13α(H),17β(H)-diacholestane
CIA	Chemical index of alteration	C_{27} ααα 20S	20S-5α(H),14α(H),17α(H)-cholestane
CIW	Chemical index of weathering	C_{27} αββ 20R + C_{29}dβα20S	20R-5α(H),14β(H),17β(H)-cholestane +13β,17α,20S-diastigmastane
PIA	Plagioclase index of alteration	C_{27} αββ 20S	20S-5α(H),14β(H),17β(H)-cholestane
EF	Enrichment factor	C_{27} ααα 20R	20R-5α(H),14α(H),17α(H)-cholestane
WI	Waxiness index	C_{28} ααα 20S	20S-24-Methyl-5α(H),14α(H),17α(H)-cholestane
TAR	Terrigenous/aquatic ratio	C_{28} αββ 20R	20R-24-Methyl-5α(H),14β(H),17β(H)-cholestane
HHI	Homohopane index	C_{28} αββ 20S	20S-24-Methyl-5α(H),14β(H),17β(H)-cholestane
ETR	Extended tricyclic terpane ratio	C_{28} ααα 20R	20R-24-Methyl-5a(H),14a(H),17a(H)-cholestane
CPI	Carbon Preference Index	C_{29} ααα 20S	20S-24-Ethyl-5α(H),14α(H),17α(H)-cholestane
OEP	Odd-to-even predominance	C_{29} αββ 20R	20R-24-Ethyl-5α(H),14β(H),17β(H)-cholestane
TNR-1	Trimethylnaphthalene ratio 1	C_{29} αββ 20S	20S-24-Ethyl-5α(H),14β(H),17β(H)-cholestane
TNR-2	Trimethylnaphthalene ratio 2	C_{29} ααα 20R	20R-24-Ethyl-5α(H),14α(H),17α(H)-cholestane
VR_{TNR-2}	Calculated reflectance from TNR-2	2-MN	2-methylnaphthalene
DNR-1	dimethylnaphthalene ratio 1	1-MN	1-methylnaphthalene
VR_{DNR-1}	Calculated reflectance from DNR-1	2,6- + 2,7-DMN	2,6- + 2,7-dimethylnaphthalene
TMNr	Trimethylnaphthalene ratio	1,3- + 1,7-DMN	1,3- + 1,7-dimethylnaphthalene
MPI-1	Methylphenanthrene index 1	1,6-DMN	1,6-dimethylnaphthalene
VR_{MPI-1}	Calculated reflectance from MPI-1	DBF	Dibenzofuran
XRD	X-ray diffraction	1,3,7-TMN	1,3,7-trimethylnaphthalene
XRF	X-ray fluorescence	1,3,6-TMN	1,3,6-trimethylnaphthalene
GC-FID	Gas chromatography-flame-ionization detector	1,4,6- + 1,3,5-TMN	1,4,6- + 1,3,5-trimethylnaphthalene
FID	Flame ionization detector	2,3,6-TMN	2,3,6-trimethylnaphthalene
GC-MS	Gas chromatography-mass spectrometry	1,2,7- + 1,6,7-TMN	1,2,7- + 1,6,7-trimethylnaphthalene
ICP-MS	Inductively coupled plasma mass spectrometry	1,2,6-TMN	1,2,6-trimethylnaphthalene

GC–irmMS	Gas chromatography–isotope ratio monitoring-mass spectrometry	1,2,4-TMN	1,2,4-trimethylnaphthalene
ASE	Accelerated solvent extraction	1,2,5-TMN	1,2,5-trimethylnaphthalene
SIM	Single ion monitoring	1,4,5-TMN	1,4,5-trimethylnaphthalene
LOI	Loss on ignition	FL	Fluorene
PZE	Photic zone euxinia	1,3,5,7-TeMN	1,3,5,7-tetramethylnaphthalene
DCM	Dichloromethane	1,3,6,7-TeMN	1,3,6,7-tetramethylnaphthalene
MMAs	Monomethylalkanes	1,4,6,7- + 1,2,4,6- + 1,2,4,7-TeMN	1,4,6,7- + 1,2,4,6- + 1,2,4,7-tetramethylnaphthalene
PAHs	Polycyclic aromatic hydrocarbons	1,2,5,7- + 1,3,6,8-TeMN	1,2,5,7- + 1,3,6,8-tetramethylnaphthalene
Fla	Fluoranthene	2,3,6,7-TeMN	2,3,6,7-tetramethylnaphthalene
Py	Pyrene	1,2,6,7-TeMN	1,2,6,7-tetramethylnaphthalene
BaA	Benzo[*a*]anthracene	1,2,3,7-TeMN	1,2,3,7-tetramethylnaphthalene
Ch	Chrysene	1,2,3,6-TeMN	1,2,3,6-tetramethylnaphthalene
InPy	Indeno[1,2,3-*cd*]pyrene	1,2,5,6- + 1,2,3,5-TeMN	1,2,5,6- + 1,2,3,5-Tetramethylnaphthalene
BghiP	Benzo[*ghi*]perylene	DBT	Dibenzothiophene
Pr	Pristane	P	Phenanthrene
Ph	Phytane	Cad	Cadalene
AIs	Aryl isoprenoids	3-MP	3-methylphenanthrene
C_{19}Tri	C_{19}-tricyclic terpane	2-MP	2-methylphenanthrene
C_{20}Tri	C_{20}-tricyclic terpane	9-MP	9-methylphenanthrene
C_{21}Tri	C_{21}-tricyclic terpane	1-MP	1-methylphenanthrene
C_{22}Tri	C_{22}-tricyclic terpane	3-EP	3-ethylphenanthrene
C_{23}Tri	C_{23}-tricyclic terpane	9- + 2- + 3,6-DMP	9- + 2- + 3,6-dimethylphenanthrene
C_{24}Tri	C_{24}-tricyclic terpane	1-EP	1-ethylphenanthrene
C_{25}Tri	C_{25}-tricyclic terpane	2,6- + 3,5-DMP	2,6- + 3,5-dimethylphenanthrene
C_{24}Tet	C_{24}-tetracyclic terpane	2,7-DMP	2,7-dimethylphenanthrene
C_{26}Tri R	C_{26}-R tricyclic terpane	1,3- + 3,9- + 3,10- + 2,10-DMP	1,3- + 3,9- + 3,10- + 2,10-dimethylphenanthrene
C_{26}Tri S	C_{26}-S tricyclic terpane	1,6- + 2,9- + 2,5-DMP	1,6- + 2,9- + 2,5-dimethylphenanthrene
C_{28}Tri R	C_{28}-R tricyclic terpane	1,7-DMP	1,7-dimethylphenanthrene
C_{28}Tri S	C_{28}-S tricyclic terpane	1,9- + 4,9- + 4,10-DMP	1,9- + 4,9- + 4,10-dimethylphenanthrene
C_{29}Tri R	C_{29}-R tricyclic terpane	2,3-DMP	2,3-dimethylphenanthrene
C_{29}Tri S	C_{29}-S tricyclic terpane	1,8-DMP	1,8-dimethylphenanthrene
Ts	C_{27}-18α(H)-22,29,30-trisnorneohopane	1,2-DMP	1,2-dimethylphenanthrene
Tm	C_{27}-17α(H)-22,29,30-trisnorhopane	Tet	Tetrahydroretene
C_{27} β	C_{27}-17β(H)-22,29,30-trisnorhopane	ip-iHMN	6-isopropyl-1-isohexyl-2-methylnaphthalene
C_{29} H	C_{29}-17α(H),21β(H)-norhopane	Sim	Simonellite
C_{29} Ts	C_{29}-18α(H)-30-norneohopane	Ret	Retene
C_{29} M	C_{29}-17β(H),21α(H)-30-normoretane		

1 Introduction

1.1 Objectives of the thesis

Lacustrine organic-rich shale has traditionally been regarded as an important source rock for conventional petroleum, contributing to a proportion exceeding 20% of the global conventional oil reserve (Bohacs et al., 2000). Many of these deposits, exemplified by the Qingshankou Formation in China and the Green River Formation in America, also serve as reservoirs for unconventional hydrocarbons (Ingram et al., 1983; Wu et al., 2023). Continental basins are globally pervasive, yielding substantial lacustrine shales enriched with organic matter (OM) that emerge as prime targets for the exploration of shale oil and gas resources. In addition, lake deposits can be applied to decipher detailed information concerning paleoenvironmental conditions and paleoclimate, rendering them invaluable geological archives for basic geological and geochemical research (e.g., Qiao et al., 2021a; Zheng et al., 2022). However, despite the extensive investigation of lacustrine source rocks over many years, the formation mechanism of lacustrine OM-rich shales remains a subject of controversy. Various models have been proposed, including the large deep anoxic lake model (Demaison and Moore, 1980), the hypersaline lake model (Kirkland and Evans, 1981), the oligotrophic meromictic lake model (Powell, 1986), the large mesosaline alkaline closed lake model (Kelts, 1988), the meromictic/oligomictic tropical/humid lake model (Talbot, 1988), and the moderately deep tropical lake model (Katz, 1990).

The formation of high-quality lacustrine source rocks is intricately influenced by the complex interplay of external factors, including climate evolution and nutrient input, as well as internal elements such as water chemistry and biological productivity (Gonçalves, 2002). Together, these elements collectively regulate the balance between the generation and degradation of OM. In addition, due to the comparatively limited size of water reservoirs, lakes experience higher rates of environmental change and are more susceptible to influences from terrestrial material input than

marine systems (Gonçalves, 2002; Hao et al., 2011). These factors contribute to significant fluctuations in water chemistry, such as salinity and pH, as well as variations in the input of terrestrial OM. Moreover, unlike oceans, lake systems rely on external nutrient sources to support the proliferation of algae and bacteria (Harris et al., 2004). Variations in paleoclimate can induce changes in lacustrine depositional environments, significantly influencing redox conditions, water salinity, OM sources, productivities, and lithofacies (e.g., Xie et al., 2021). Additionally, occurrences of marine incursions may lead to fluctuations in paleo-lake levels, thereby playing a governing role in determining lake water chemistry and conditions for OM preservation (Cao et al., 2020; Zhang et al., 2022). Nevertheless, it should be noted that within extensional continental rift basins, the stratigraphic sequences manifest a highly akin progression encompassing four consecutive phases: (1) an initial domain dominated by fluvial systems during the rift's initial stages, (2) a domain characterized by deep-water lacustrine conditions within an elongated and deep basin, as subsidence surpasses infill rates, (3) a lacustrine domain gradually becoming shallower, possibly evolving into a shallow playa lake environment, as sedimentation rates eventually match and surpass subsidence, and (4) a renewed period of fluvial dominance, emerging as the rift basin experiences overfilling (Lambiase, 1990; Pochat and Van Den Driessche, 2011). This process occurs universally, irrespective of geological epochs and climatic zones (Lambiase, 1990) and significantly influences the OM type of lacustrine sediments, as exemplified in the Lower Cretaceous syn-rift lacustrine shales in the Congo Basin (Harris et al., 2004).

While multiple depositional models for lacustrine source rocks have been suggested, it appears that no singular model can comprehensively elucidate the formation of diverse lacustrine source rocks. Moreover, due to the pronounced heterogeneity of lacustrine source rocks concerning lithologies, as well as the variable quantity and type of OM resulting from changeable depositional environments, understanding the enrichment mechanisms of OM in lacustrine sediments is crucial for the exploration of both conventional and unconventional hydrocarbon resources. This thesis focuses on the lacustrine sediments collected from the Middle Jurassic Dameigou and Upper Cretaceous Qingshankou formations from the Qaidam and Songliao Basins, respectively, in China, as well as the Early Permian Usclas-St. Privat Formation (USPF), Tuilières-Loiras Formation (TLF), and Viala Formation (VF) from the Lodève Basin in Southern France. The objectives are to:

1) Provide comprehensive information on the bulk geochemistry to assess the hydrocarbon generation potential of the analyzed samples and quantify their thermal maturity based on multiple biomarker proxies.

2) Reconstruct the depositional environments prevailing during the deposition of the analyzed lacustrine OM-rich deposits and provide detailed information on the biological origin of OM, particularly for the lacustrine shales from the Lodève Basin, where almost no such data have been reported so far.

3) Evaluate the weathering conditions and reconstruct paleoclimatic evolution based on

elemental data.

4) Use integrated organic geochemistry and elemental approaches to elucidate the key factors controlling the mechanisms of OM accumulation in lacustrine sediments.

1.2 Geology of Qaidam Basin

1.2.1 Tectonic evolution

The Qaidam basin, with an area of around 120,000 km^2, is the largest high-altitude terrestrial petroliferous basin in the northeastern Tibetan Plateau and serves as a crucial oil- and coal-bearing basin in Northwest China (Jian et al., 2013; Li et al., 2014; Wu et al., 2022). Encompassing an exceptionally thick Mesozoic and Cenozoic sedimentary succession, with an average thickness reaching up to 8 km (Jian et al., 2013), the basin plays a pivotal role in geological studies. The primary structural unit of the Qaidam Basin is its northern margin (Fig. 1.1), which preserves comprehensive Mesozoic and Cenozoic sedimentary records (Zhang et al., 2020).

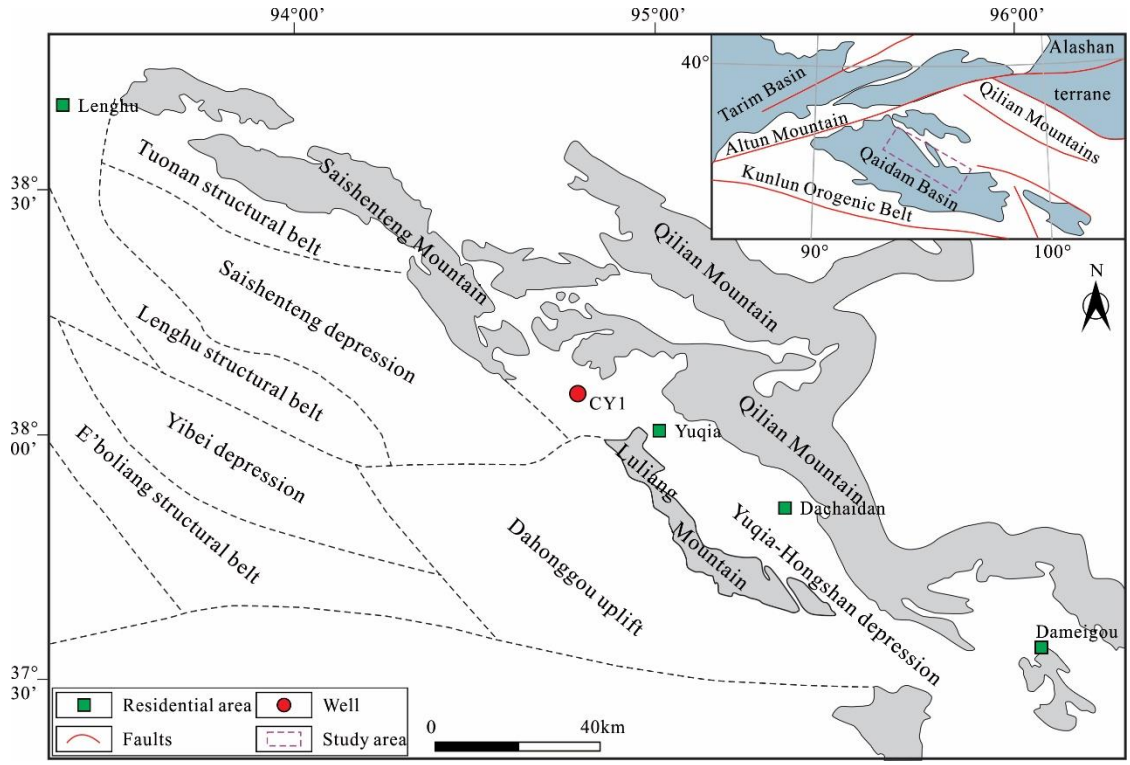

Figure 1.1 Studied well location and division of tectonic units in the northern margin of Qaidam Basin. (modified from Zhang et al., 2020).

The formation of the present Qaidam Basin is attributed to the convergent system in the northeastern Tibetan Plateau (Tapponnier et al., 2001; Jian et al., 2013). Significant tectonic events of the Qaidam Basin and its adjacent regions are illustrated in Fig. 1.2. The end of the Paleozoic marked the cessation of a transgressive period in the northern Qaidam Basin. Owing to the Indosinian

movement, the northern Qaidam Basin experienced a consistent stage of uplift, leading to a lack of sediment deposition during this time (Li et al., 2016; Shang et al., 2018; Wang et al., 2021). The Mesozoic tectonic settings of the basin are frequently associated with the evolution of the Meso-Tethys, Neo-Tethys, and the Mongol–Okhotsk Ocean, as well as the collisions involving related blocks, while the Cenozoic tectonic evolution of the basin is linked with the India–Eurasia collision as well as associated rise, thickening, shortening, and lateral extrusion of the Tibetan Plateau (Jian et al., 2013). In the initial stages of the Jurassic, crustal subsidence ensued, driven by the influences of regional extension and stress relaxation (Wang et al., 2006). The depocenters gradually shifted towards the southwestern and eastern regions of the northern Qaidam Basin. As the Tarim plate underwent significant eastward migration relative to the Qaidam microplate at the end of the Early Jurassic, the regional extensional environment transitioned into a compressive setting, and the southern part of the northern Qaidam Basin started to uplift (Chen et al., 2012; Wang et al., 2021). Simultaneously, the depocenter during this period relocated eastward to the Yuqia Sag (Fig. 1.1).

1.2.2 Sedimentary fill

The Qaidam Basin is filled with Mesozoic–Cenozoic sediments derived from the surrounding mountains and primarily deposited within a fluvial-lacustrine depositional environment. These sediments have accumulated atop the pre-Mesozoic basement, which is composed of igneous and metamorphic rocks (Jian et al., 2013; Guo et al., 2017a; Fig. 1.2). Structurally, the western and southern regions represent two Cenozoic depressions, while the northern sector of the basin comprises a Mesozoic fault-block belt (Pang et al., 2005). From the lower to upper strata, the Jurassic System can be categorized into the Xiaomeigou Formation of the Lower Jurassic, the Dameigou Formation of the Middle Jurassic, and the Caishiling and Hongshuigou formations of the Upper Jurassic. The Lower Jurassic sediments are mainly observed in the western segment of the northern margin of the Qaidam Basin and the intersecting region of the Qilian Mountains and the Altun Mountains, with a distribution area of 22,000 km^2 and a maximum thickness of 2200 m. The distribution of Middle Jurassic sediments primarily occurs in the Saishiteng-Yuka region, encompassing an area of 4200 km^2, with the maximum thickness observed in the Yuka area at 800 m. The seventh member of the Dameigou Formation denoted as J_2d^7, formed during the Middle Jurassic Bathonian stage within the basin's depression phase. It is characterized by sandstones and carbonaceous mudstones in the lower section and shales in the upper section (Wang et al., 2021; Wu et al., 2022). From the Late Jurassic to Early Cretaceous, a set of red sand-dominant sediments dominated by alluvial-fluvial and shallow lacustrine facies were deposited. In the early Pleistocene, the deposition of fluvial-deltaic sediments occurred, characterized by the presence of abundant terrestrial debris. Subsequently, the lake basin reached its climax during the middle Pleistocene, marked by the predominant deposition of deep-water fine-grained argillaceous sediments. Eventually, the central region of the basin experienced continuous elevation influenced by tectonic movements in the late Pleistocene (Dang et al., 2008). The Quaternary sediments, known as

the Qigequan Formation, typically exhibit thickness ranging from 1.5 to 2.5 km (with an average of 1.7 km), reaching a maximum thickness of approximately 3.4 km (Qiao et al., 2022).

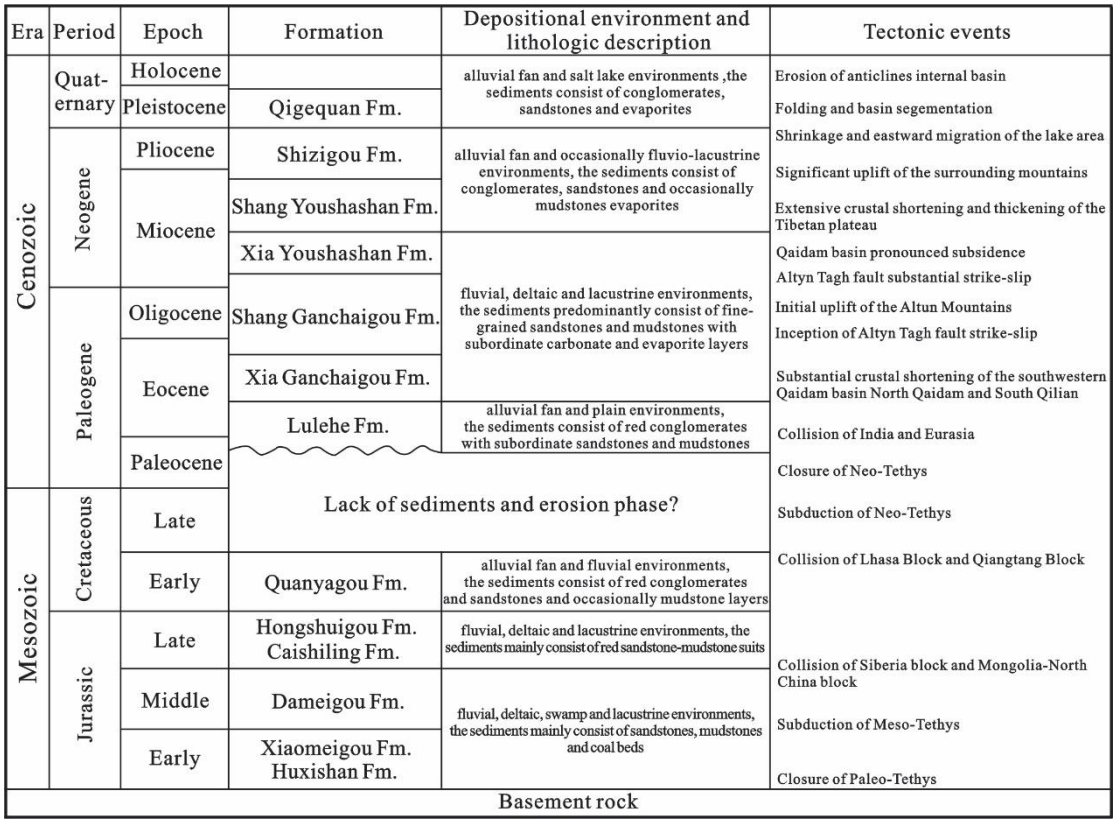

Figure 1.2 Stratigraphic division, depositional environment, and lithological description of the northern Qaidam basin and major tectonic events of this area (modified from Jian et al., 2013; Guo et al., 2017a).

1.3 Geology of Songliao Basin

1.3.1 Tectonic evolution

Situated in northeastern China, the Songliao Basin covers 260,000 km^2 and stands as one of the largest Mesozoic-Cenozoic intracontinental basins globally (Cao et al., 2021; Fig. 1.3a). The formation and filling of the Songliao Basin occurred through four tectonic stages: mantle upwelling, rifting, postrift thermal subsidence, and structural inversion (Feng et al., 2010). The first stage started during the Middle and Late Jurassic, marked by doming, extension, and extensive volcanism. Deposits from the Upper Jurassic through the Lower Cretaceous, categorized as pre-rift and syn-rift deposits (pre-rift and syn-rift tectonostratigraphic units), are found solely within isolated fault blocks, with a maximum thickness of 7000 m observed in the Shiwu and Dehui depressions (Xie et al., 2003). Post-rift deposits from the Lower to Upper Cretaceous (post-rift tectonostratigraphic unit) exhibit a thickness ranging from 3000 to 4000 m (with a maximum of 6000 m), and they unconformably overlay syn-rift strata,

extending beyond fault blocks to encompass the entire basin. Deposits from the Palaeocene and Eocene, identified as the structural inversion tectonostratigraphic unit, have a thickness ranging from 0 to 510 m and are limited to specific localities in the western sector of the basin.

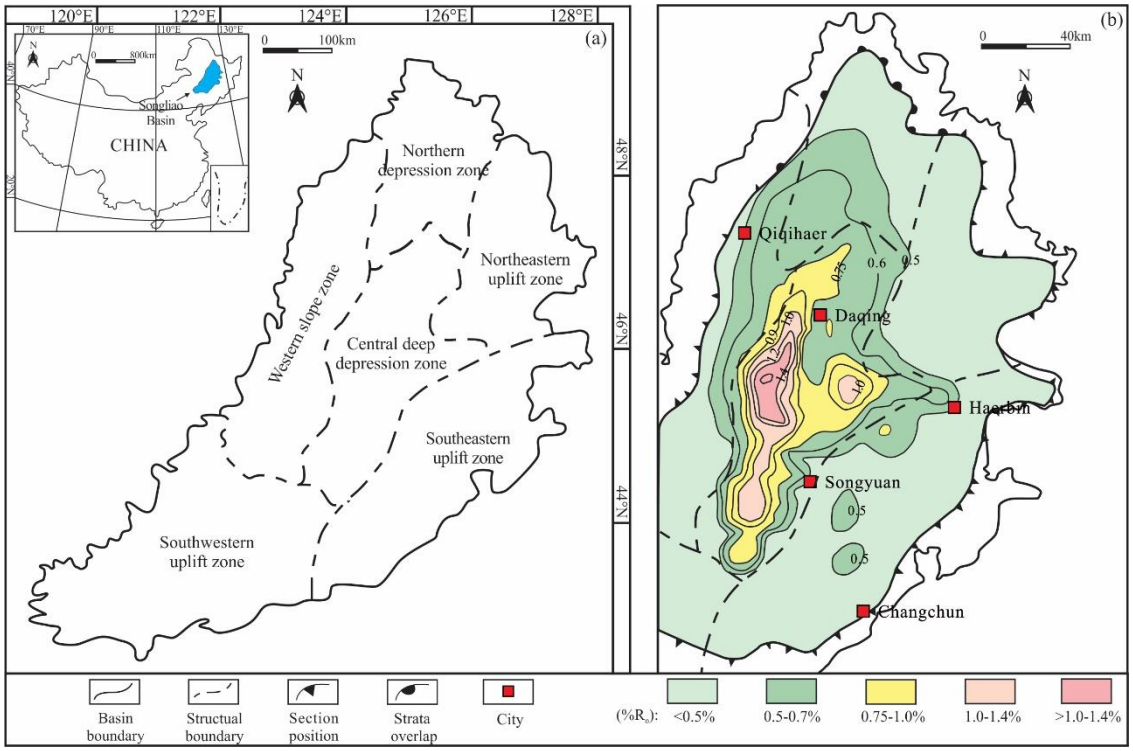

Figure 1.3 (a) Schematic map showing the location of the Songliao Basin in China and the distribution of first-order tectonic units of the Songliao Basin (modified after Gao et al., 2018); (b) Contour map of the vitrinite reflectance (VR_r) (modified after Liu et al., 2022a).

1.3.2 Sedimentary fill

The basin encompasses clastic deposits from the Jurassic, Cretaceous, Palaeogene, and Neogene periods, reaching a thickness of approximately 10 km at the basin center (Feng et al., 2010). These layers rest upon underlying Palaeozoic metamorphic, igneous, and volcanic rocks (Feng et al., 2010; Jia et al., 2013; Fig. 1.4). The oldest sedimentary layer in the basin is represented by the Upper Jurassic Huoshiling Formation. Above the Jurassic strata, there are the Lower Cretaceous Shahezi, Yingcheng, Denglouku, and Quantou formations. These, in turn, are overlain by the Upper Cretaceous Qinshankou, Yaojia, Nenjiang, Sifangtai, and Mingshui formations. The sedimentary succession concludes with an unconformity between the Cretaceous and Cenozoic, followed by the overlay of the Paleogene–Neogene Yi'an, Da'an, and Taikang formations (Wang et al., 2013a). The Huoshiling Formation is likely dated to the Late Jurassic Tithonian period. The sedimentary thickness ranges from 500 to 1600 m, encompassing strata that consist of volcanic flows (predominantly andesitic) and volcaniclastics intermingled with clastic fluvial, flood-plain, and swamp or mire facies. The Shahezi

Formation, deposited during the Berriasian–Valanginian, typically exhibits a thickness ranging from 400 to 1500 m.

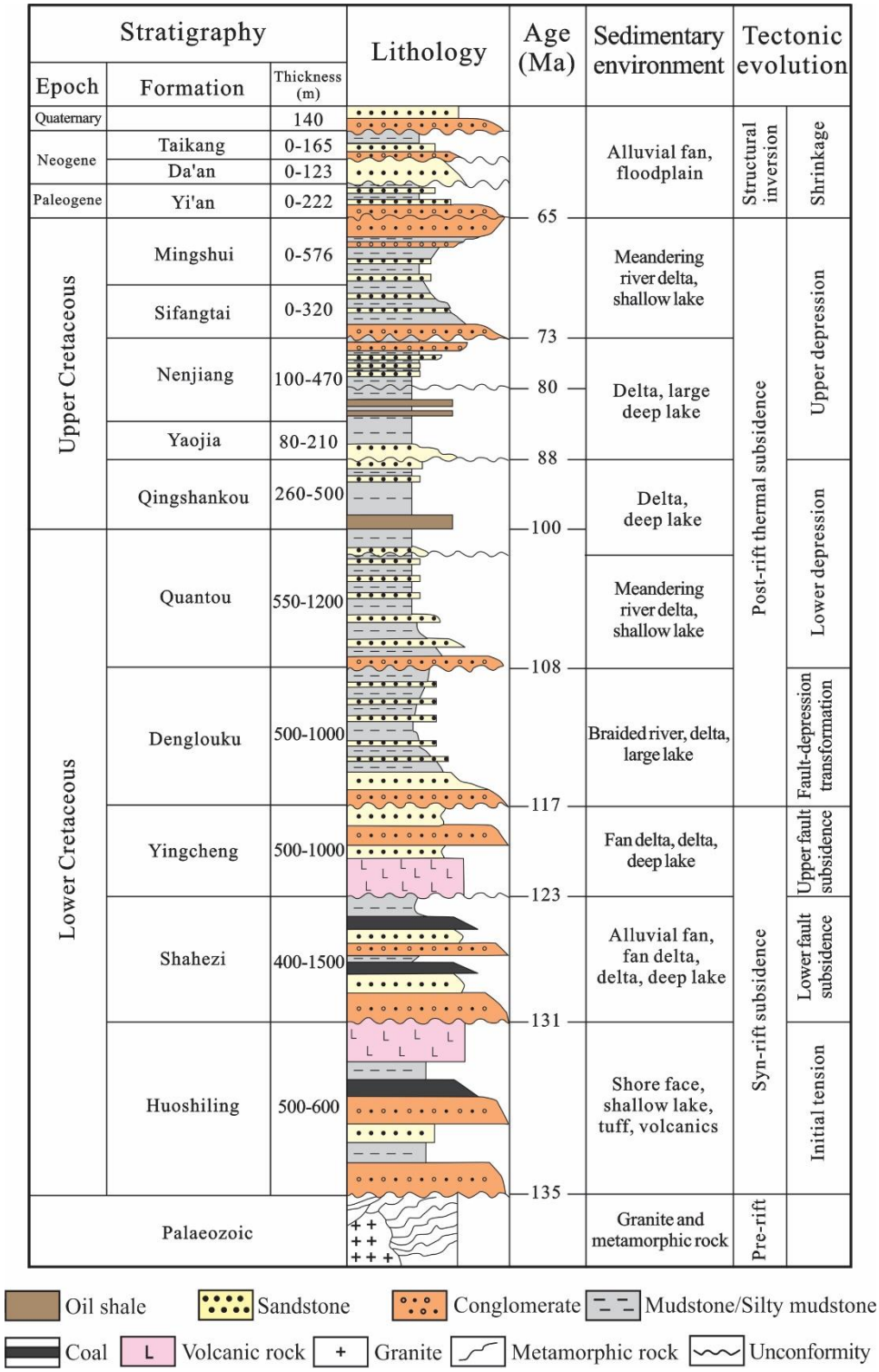

Figure 1.4 Integrated interpretation of stratigraphic column of the Songliao Basin (modified after Jia et al., 2013).

It is comprised of gray to black lacustrine and floodplain mudstone and siltstone interbedded with gray sandstone and conglomerate. Above the Shahezi Formation lies the Yingcheng Formation, which is predominantly composed of felsic volcanics that serve as the primary petroleum reservoirs. This formation is interbedded with clastic strata and contains several discontinuous coal beds, typically attaining a thickness ranging from 500 to 1000 m. The Denglouku Formation consists of interbedded sandstone and mudstone, conglomerate, and a thick argillite. The Quantou Formation is distinguished by mudstone, sandstone, and conglomerate with origins in fluvial and floodplain environments deposited under arid or semi-arid conditions. The Qingshankou Formation comprises gray, dark gray, and black mudstone interbedded with oil shale, as well as gray sandstone and siltstone. Organic-rich shales in the first member of the Qingshankou Formation (K_2qn^1) are the main oil source rocks, characterized by a VR_r within the range of 1.0%–1.6% in the central depression region (Liu et al., 2022a; Fig. 1.3b). The Yaojia Formation is composed of mudstone, siltstone, and sandstone of lacustrine, fluvial, and deltaic origin. In contrast, the Nenjiang Formation is characterized by deep-water lacustrine gray to black mudstone, marlstone, shelly limestone, and oil shale interbedded with gray siltstone and fine sandstone. During the deposition of the first member of the Nenjiang Formation, the lake rapidly expanded, reaching its maximum extent of 20×10^4 km^2, covering nearly the entire basin. Finally, the basin underwent regional compression during the deposition of the uppermost Sifangtai and Mingshui formations. These formations are present in the central and western sectors of the basin, predominantly comprising sandstone, siltstone, and shale deposited within fluvial, deltaic, and shallow lacustrine environments.

1.4 Geology of Lodève Basin

1.4.1 Tectonic evolution

The Lodève Basin, situated approximately 50 km northwest of Montpellier in the southern part of the French Massif Central, is a cuvette-shaped half-graben spanning an area of 180 km^2 (Laurent et al., 2020; Fig. 1.5).

The half-graben configuration is associated with a gravitational collapse along the Hercynian mountain chain during the Late Carboniferous to Late Permian (Echtler and Malavieille, 1990; Laurent et al., 2020). The sedimentary series displays an overall southward dip of 15–20°, filling the continental basin and delimited in the south by a north-dipping listric normal fault resulting from the inversion of a main thrust during the Late Hercynian collapse (Fig. 1.5). Middle Triassic terrestrial deposits unconformably seal an erosive surface truncating both the Late Carboniferous-Permian half-graben and its basement at the southern and northern basin margins. This post-rift unconformity signifies the end of the Late Hercynian tectonics, succeeded by a major regional erosion during which a minimum of 1500 m of Permian deposits was eroded, representing a gap of 15 Myr. This unconformity signifies the general uplift and erosion from the Late Permian to the Lower Triassic period along the shoulders of the newly developed Tethysian rift and, thus, the rejuvenation of basin

margins identified as the Lodève (in roll-over area) and Cabriéres Ridges (in the footwall of the listric Les Aires-Mas Blanc fault) (Laurent et al., 2020). During the Mesozoic, a significant shift in the

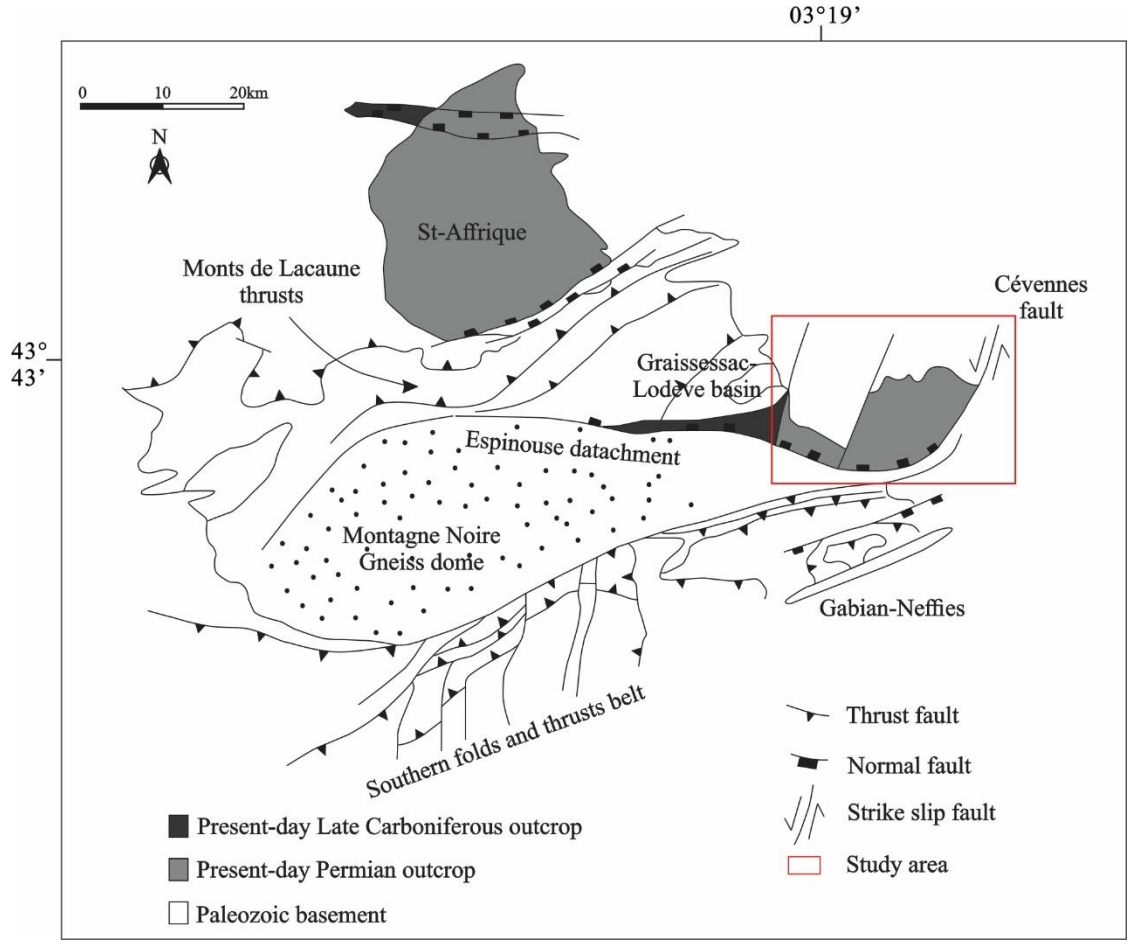

Figure 1.5 Structural map of the studied basin in the French southern Massif Central (modified after Pochat and Van Den Driessche, 2011).

tectonic regime occurred, as indicated by part of the western area controlled by NE-SW trending faults in the Lodève area. The comprehensive sealing of the remaining Paleozoic reliefs is associated with the overall extension of shallow marine carbonate deposits during the Jurassic. Presently, the Jurassic series is preserved on the Causse du Larzac plateau, which experienced an uplift during the Cenozoic (Laurent et al., 2020).

1.4.2 Sedimentary fill

The initial segment of the Graissessac–Lodève basin sequence, represented by the Croix de Mounis Formation, is characterized by a massive red shale-sand matrix supported gravel-rich conglomerate with angular pebbles and cobbles derived from Paleozoic basement (Pochat and Van Den Driessche, 2011; Fig. 1.6). The Pabau and Houilliere formations (Late Carboniferous) and the

Usclas and Loiras formations (Early Permian) mark the initiation and peak of a deep lacustrine environment.

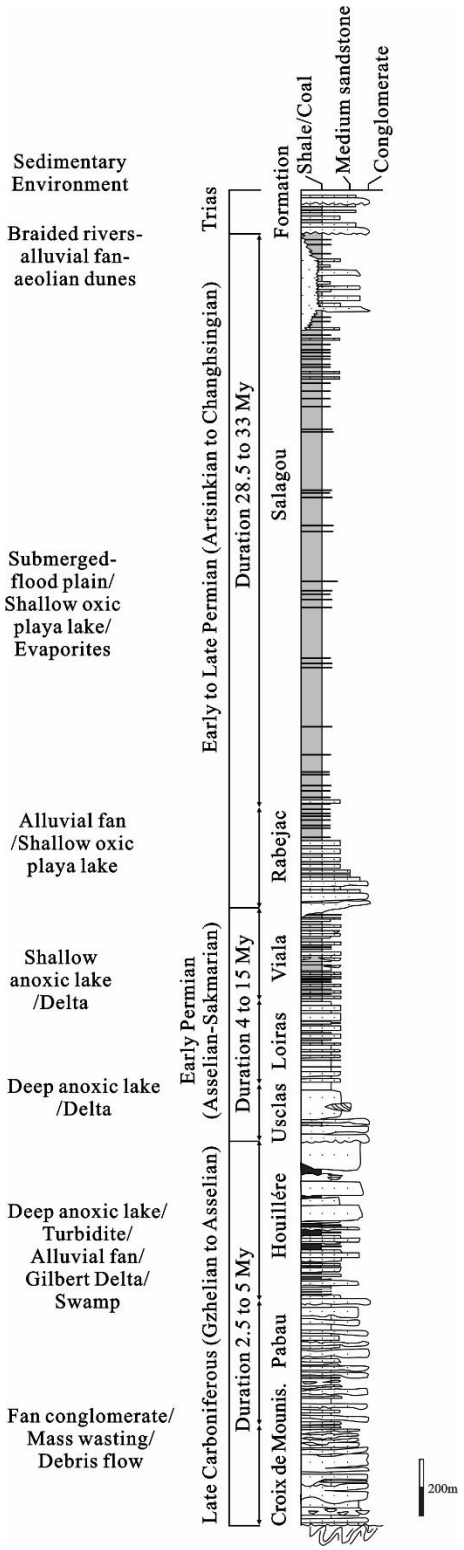

Figure 1.6 Sedimentological and stratigraphic log of the Late Carboniferous to Early Triassic in the Graissessac–Lodève basin (modified from Pochat and Van Den Driessche, 2011).

Within these formations, there are repetitive sequences featuring (1) sub-lacustrine fans to distal lacustrine facies, primarily controlled by sub-aqueous gravity processes (debris flow and turbidites) and black shale deposits, (2) high-energy wave processes manifesting as proximal coarse-grained wave ripples with meter-scale wavelengths, and (3) diverse environments including deltas, subaerial alluvial fans, and floodplains characterized by predominant allochthonous coal beds. The end of the deep lacustrine environments took place in the Early Permian. The Rabejac and Salagou formations represent a uniform sequence of red mudstones, featuring a growing prevalence of thin green silty-sandstone layers towards the top. These formations were deposited in a large shallow playa lake. The onset of the Early Triassic is marked by the introduction of a new supply of highly coarse and conglomeratic sediments. These sediments undergo a transformation, progressing from debris-flow processes on alluvial fans in the west to braided river plains intertonguing with Aeolian dune fields and finally transitioning to floodplain areas and small dispersed playa lakes towards the east.

1.5 Chapter overview

The presented thesis comprises an introduction and three main chapters, followed by a general conclusion and outlook chapter. The objectives and focus of each chapter are summarized in the following.

Chapter 2: *Organic petrologic and geochemical characterization of petroleum source rocks in the Middle Jurassic Dameigou Formation, Qaidam Basin, northwestern China: Insights into paleo-depositional environment and OM accumulation, was published as Wu, Z., Grohmann, S., Littke, R., Guo, T., He, S., Baniasad, A., 2022. Organic petrologic and geochemical characterization of petroleum source rocks in the Middle Jurassic Dameigou Formation, Qaidam Basin, northwestern China: Insights into paleo-depositional environment and organic matter accumulation. International Journal of Coal Geology, 259, 104038.*

This chapter applies organic petrography, inorganic geochemistry, and both bulk and molecular organic geochemistry to core samples from the CY1 well in the Yuqia Sag, northern Qaidam Basin. The objective is to examine the thermal maturity of the analyzed OM, assess the overall hydrocarbon generation potential, and elucidate the paleoclimate and depositional environments during the sedimentation of the Middle Jurassic Dameigou Formation. It was published in the "International Journal of Coal Geology" in 2022.

Chapter 3: *Geochemistry and petrology of petroleum source rocks in the Upper Cretaceous Qingshankou Formation, Songliao Basin, NE China, was published as Wu, Z., Littke, R., Baniasad, A., Yang, Z., Tang, Z., Grohmann, S., 2023. Geochemistry and petrology of petroleum source rocks in the Upper Cretaceous Qingshankou Formation, Songliao Basin, NE China. International Journal of Coal Geology, 270, 104222.*

This chapter mainly presents molecular organic geochemistry and major and trace element data of the K_2qn^1 in the southern part of the central depression, Songliao Basin. The objectives encompass

1) unraveling the depositional environments during the K_2qn^1 deposition, 2) ascertaining thermal maturity through biomarker analysis, 3) elucidating the pivotal factors governing the mechanisms of OM accumulation, and 4) evaluating weathering intensity and reconstructing the paleo-climatic conditions. It was published in the "International Journal of Coal Geology" in 2023.

Chapter 4: *Geochemistry and petrology of Early Permian lacustrine shales in the Lodève Basin, Southern France: depositional history, OM accumulation and thermal maturity, was published as Wu, Z., Grohmann, S., Littke, R., 2024. Geochemistry and petrology of Early Permian lacustrine shales in the Lodève Basin, Southern France: depositional history, organic matter accumulation and thermal maturity. International Journal of Coal Geology, 284, 104469.*

This chapter investigates organic petrology, stable carbon isotope, bulk and molecular geochemistry, as well as elemental geochemistry of the Early Permian shales in the Lodève Basin. The changes in the environmental conditions of the paleo-lake, the sources of OM, and the possible influence of variations in paleoclimatic conditions on the sedimentary environment are discussed. In addition, an OM accumulation model for the lacustrine fine-grained sediments is proposed. It was published in the "International Journal of Coal Geology" in 2024.

2 Organic petrologic and geochemical characterization of petroleum source rocks in the Middle Jurassic Dameigou Formation, Qaidam Basin, northwestern China: Insights into paleo-depositional environment and organic matter accumulation

Keywords: Middle Jurassic; Organic geochemistry; Organic petrology; Element geochemistry; Paleoclimate; Qaidam Basin

Abstract

The organic matter-rich mudstones of the Middle Jurassic Dameigou Formation in the northern Qaidam Basin are regarded as the principal petroleum source rocks for unconventional resource exploration in China. In this study, a detailed investigation on the organic petrography, inorganic geochemistry as well as bulk and molecular organic geochemistry is presented. Three different source rock units were identified with TOC contents and VR_r ranging from 1.5–39.2% and 0.35–0.57%, respectively. Carbonaceous mudstone and organic matter-rich mudstone in unit 1 with high Pr/Ph (4.79−7.25) and low Gam index (0.02−0.03) values mainly developed in an oxic freshwater column under warm and humid climatic conditions and strong weathering intensity. Organic matter in unit 1 with high proportions of C_{29} ααα 20R steranes (61−74%) is interpreted to be derived from terrestrial higher plants. By contrast, units 2 (Pr/Ph: 2.56−4.23; Gam index: 0.03−0.14) and 3 (Pr/Ph: 0.73; Gam index: 0.48) were deposited in sub-oxic to oxic freshwater and anoxic saline environments, respectively. Progressive aridification during the deposition of units 2 and 3 are reflected by decreasing CIA values (59.97−86.68) resulting in weakened weathering intensity and lower terrestrial influx. A mixture of terrestrial higher plants and algal biomass was the main source of organic matter in unit 2 with moderate C_{19}/C_{23} Tri (0.96–5.44), C_{20}/C_{23} Tri (1.28–3.87) and C_{24} Tet/C_{26} Tri (1.10–2.54) ratios, while unit 3 with the lowest C_{19}/C_{23} Tri (0.25), C_{20}/C_{23} Tri (0.95), and C_{24} Tet/C_{26} Tri (0.65) ratios and highest proportions of C_{27} ααα 20R steranes (69%) is characterized by a decrease in terrigenous organic matter content. The dominant source of organic matter is lake plankton, including halophilic algae and cyanobacteria. Organic matter accumulation in unit 1 is associated with a warm and humid climate, weathering intensity, and terrigenous organic matter input. Primary productivity is the most important factor controlling the enrichment of organic matter in units 2 and 3.

2.1 Introduction

During the last decade, great achievements have been made with respect to the exploration and development of unconventional hydrocarbons resources in marine and continental source rocks around the world (Jarvie et al., 2012; Klaver et al., 2012; Hackley et al., 2016; Zhang et al., 2019; Zhang, 2020; Qiao et al., 2021a, 2021b; Cichon-Pupienis et al., 2021). Continental basins are widely distributed in China, and developed extensive lacustrine shales that make up a large proportion of conventional resources (Katz, 1990; Wang et al., 2021). One prominent example for lacustrine organic matter-rich deposits is the seventh member of the Middle Jurassic Dameigou Formation (J_2d^7) in the Qaidam Basin, China. In comparison to source rocks deposited in relatively uniform marine settings, the formation of lacustrine shales is more complex and susceptible to multiple factors, including input of terrestrial material, variable water column conditions, lake level, and tectonic setting (Qiao et al., 2021a; Xie et al., 2021; Liu et al., 2022b). In particular, paleo-climatic conditions affect the depositional environment by controlling weathering intensity, water chemistry, primary productivity, and terrestrial input, which further influences the accumulation of organic matter in lacustrine sediments (Wang et al., 2021; Qiao et al., 2021b).

The Qaidam Basin is a petroliferous onshore basin in Northwest China that developed multiple sets of source rocks, among which J_2d^7 is composed of typical organic matter-rich lacustrine deposits (Fig. 2.1a). Previous climatic reconstructions of the Qaidam Basin focus on the investigation of palynological features and elemental geochemical proxies of sediments, indicating a variable paleoclimate during the late Middle to Late Jurassic (Wang et al., 2005; Xie et al., 2021). The sporopollen assemblage in the Dameigou Formation is dominantly characterized by *Coniopteris* and *Phoenicopsis*, indicating the existence of a warm and humid paleoclimate in the Yuqia Sag during the Middle Jurassic (Yang et al., 2006a; Liu et al., 2022b). However, the content of *Classopollis* displays a gradually increasing trend in the late Middle Jurassic and even rises up to 78% in the Caishiling Formation of the Upper Jurassic, reflecting a transformation to an arid paleoclimate upwards (Wang et al., 2005; Yang et al., 2007; Xie et al., 2021). The beginning of aridification in the late Middle Jurassic exerted significant impact on the sedimentary environments of lake systems and the formation of lacustrine source rocks (Wang et al., 2021; Xie et al., 2021; Liu et al., 2022b). Affected by this, the J_2d^7 displays strong heterogeneity with obvious manifestation in kerogen type and mineral composition. Different layers of J_2d^7 show a sharply varying proportion of organic matter derived from aquatic organisms and terrestrial sources (Qin et al., 2018; Wang et al., 2021; Xie et al., 2021). Organic petrology can precisely identify the various macerals and their percentages as well as thermal maturity based on micropetrographic parameters. Molecular organic geochemistry can reveal the organic matter source, depositional environment, and thermal maturity by analyzing biomarkers and related proxies (Peters et al., 2005). Elemental geochemistry can be applied to reconstruct the paleoclimate, indicate the weathering conditions, as well as investigate factors controlling organic matter accumulation.

In this study, organic petrography, inorganic geochemistry as well as bulk and molecular organic geochemistry were applied on core samples from the CY1 well in the Yuqia Sag, northern Qaidam Basin in order to (1) assess the thermal maturity of the analyzed organic matter and (2) the general hydrocarbon generation potential, as well as (3) reconstruct the paleoclimate and depositional environments prevailing during the deposition of the J_2d^7 and investigate their linkage to organic matter accumulation. This information can be helpful to reduce exploration uncertainties that are related to the type and distribution of the J_2d^7 source rock.

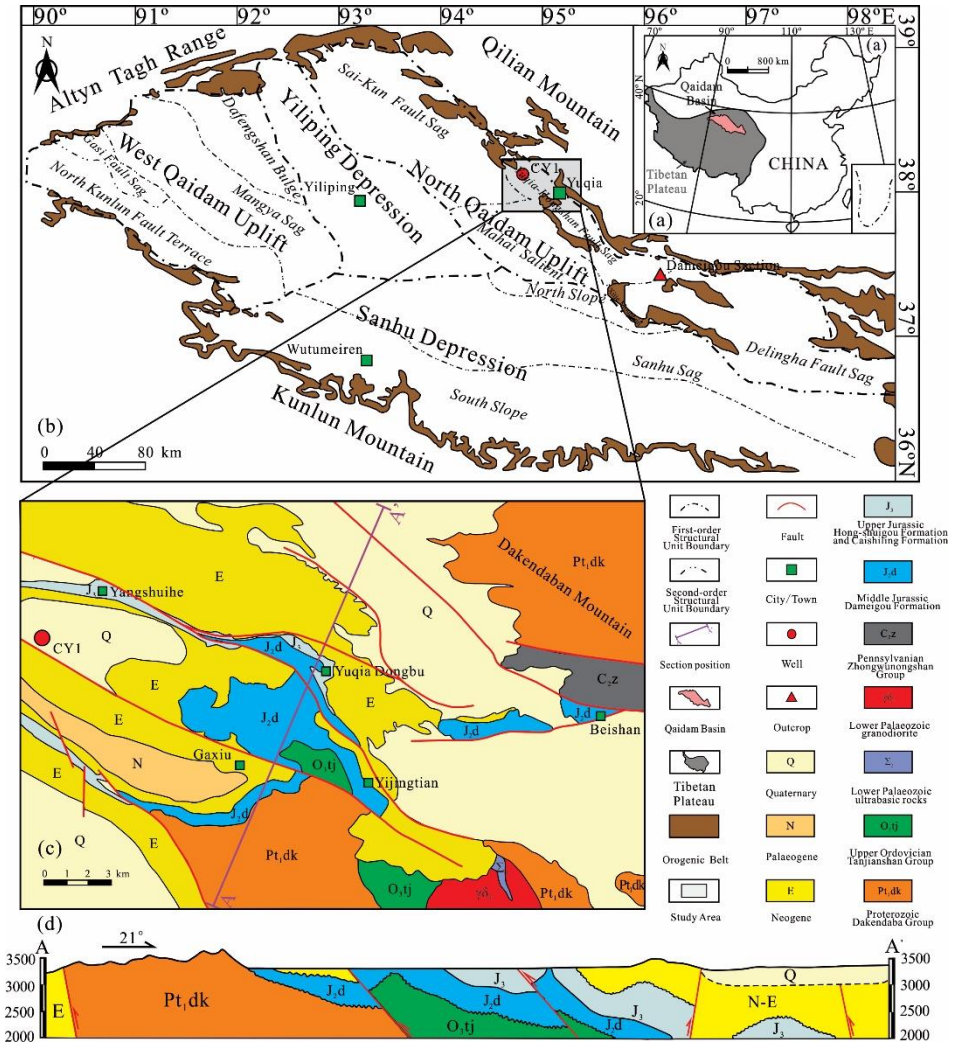

Figure 2.1 (a) Schematic map showing the location of the Qaidam Basin in China; (b) Geological setting of the Qaidam Basin and study area (modified after Bao et al., 2017; Qiao et al., 2021b); (c-d) Geological map of the Yuqia coalfield and well location with a northeast-oriented cross section (modified after Li et al., 2014).

2.2 Geological background

The Qaidam Basin, with an area of around 120,000 km^2, is located in the northeastern Qinghai-Tibet Plateau, NW China (Fig. 2.1a) and is an important oil- and coal-bearing basin in Northwest

China (Jian et al., 2013; Li et al., 2014; Wang et al., 2015). The Qaidam Basin that developed on the Precambrian crystalline basement evolved into an intracontinental basin in the Mesozoic and contains a thick Mesozoic−Cenozoic sedimentary succession of 3−16 km (Jian et al., 2013; Ren et al., 2017). The basin is a microplate surrounded by three mountain ranges, including the Eastern Kunlun Mountain in the south, the Qilian Mountain in the east, and the northwest Altyn Tagh Range (Fig. 2.1b). The northern Qaidam Basin with an area around of 3.4×10^4 km^2 is the primary structural unit and has long been regarded as promising area for petroleum resources exploration (Shao et al., 2014). The sampled well CY1 is located in the Yuqia sag, which is situated in the middle of the northern Qaidam Basin and shows excellent hydrocarbon potential in the J_2d^7 (Fig. 2.1c; Qin et al., 2018).

The formation of the Qaidam Basin is closely related to the convergent system in the northeastern Tibetan Plateau (Tapponnier et al., 2001). The combined effect of the Neo-Tethys, Meso-Tethys, and the Mongol-Okhotsk Ocean and the collisions of related blocks contribute to the basin's Mesozoic tectonic settings (Gehrels et al., 2011). The Triassic strata are not visible in outcrop or drilling in the northern Qaidam Basin, which might be owing to the strong extrusion, uplifting, and erosion caused by the Indosinian movement (Fig. 2.1d; Tang et al., 2000). Different from the western and southern parts that are Cenozoic depressions, the northern Qaidam Basin is a Mesozoic fault-block belt and was the depocentre during the Jurassic. At the beginning of the Jurassic, affected by the eastward compression stress by the Tarim plate, the Qaidam microplate started to differentially move northward associated with clockwise block rotation. These movements resulted in tectonic subsidence in the northern part of the basin (Dang et al., 2003; Li et al., 2014). During the Middle Jurassic, owing to stress relaxation and long-term tectonic extension in the Early Jurassic, the northern part of the Qaidam Basin developed the Yuqia sag, the study area, with abundant terrestrial debris input. Subsequently, the basin scaled down due to tectonic compression during the Late Jurassic (Jin et al., 2004). In the early Cretaceous, the northern Qaidam Basin was in a compressional tectonic state because of the collision of Lhasa Block and Qiangtang Block (Zhang, 2020). While the whole region was uplifted and mainly deposited coarse-grained clastic sediments, i.e., conglomerates and sandstones were deposited in delta, fluvial, and alluvial fan facies (Jian et al., 2013; Zhang, 2020). Upper Cretaceous strata are widely absent in the Qaidam Basin, but whether this was caused by a lack of sediments or erosion is unknown (Jian et al., 2013). During the Paleocene to Miocene, the depocentres of the basin were shifted to the western region (Jin et al., 2004). During the late Miocene, influenced by the intensification of intracontinental subduction of the Tibetan Plateau, the Kunlun tectonic belt began to thrust and nappe into the Qaidam Basin (Jin et al., 2004). The basin was uplifted in the western region and descended in the eastern region. During the Quaternary, the eastern area was strongly subsiding, leading to the deposition of Pleistocene lacustrine sediments in the Sanhu depression (Jin et al., 2004). The Dameigou Formation is divided into seven members (J_2d^1−J_2d^7, from base to top) based on lithology and depositional environment, among which the first to third members were deposited during the Early Jurassic, while fourth to seventh members were formed during the Middle Jurassic (Zhang

et al., 2020; Wang et al., 2021). The J_2d^1 was formed in the fault depression period of the basin and comprises shales and sandstones (Fig. 2.2; Wang et al., 2021). The J_2d^2–J_2d^3 of the Dameigou Formation are generally dominated by organic-lean mudstones and sandstone, while the J_2d^4 is characterized by sandstones that were deposited in braided river deltas (Fig. 2.2; Zhang et al., 2020; Wang et al., 2021). The lithology of the J_2d^5 is dominated by carbonaceous mudstones and coal seams that were deposited in a meandering river delta with abundant terrestrial higher land plant input, while the J_2d^6 comprises mudstones and sandy stones that were deposited in a shallow lake and meandering river delta (Fig. 2.2; Zhang et al., 2020; Wang et al., 2021). The J_2d^7, which was formed in the depression stage of the basin during the Middle Jurassic Bathonian, is dominated by sandstones and carbonaceous mudstones in the lower part and shales in the upper part (Fig. 2.2). The northern part of the Qaidam Basin, i.e., the study area, was covered by a meandering delta during the Early Jurassic. Later, lakes developed and a series of thick organic matter-rich mudstones and oil shales were deposited (Zhang et al., 2020; Xie et al., 2021; Wang et al., 2021).

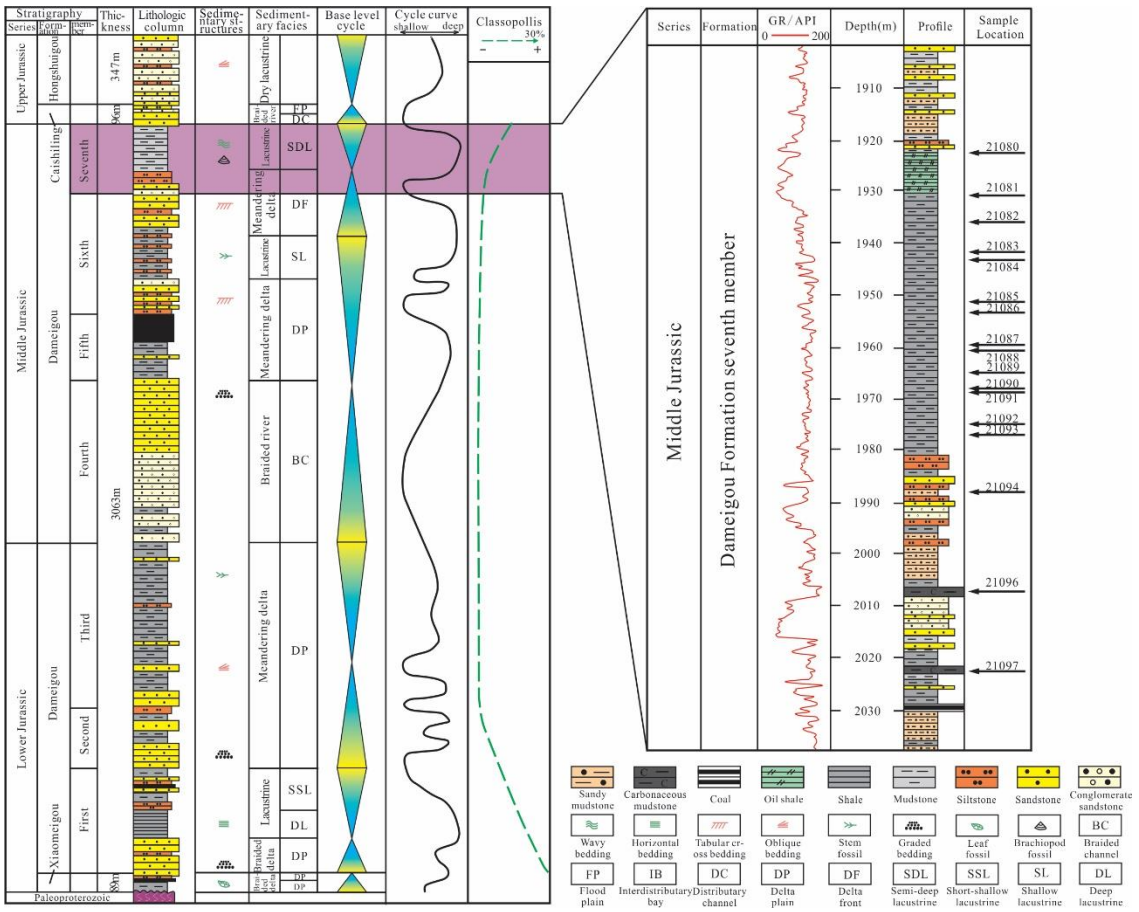

Figure 2.2 (a) Comprehensive stratigraphic units of the Jurassic at the northern margin of the Qaidam Basin (modified after Zhang et al., 2020); (b) Locations and lithology of the samples from the J_2d^7 in the CY1 Well (modified from Guo et al., 2017b).

2.3 Samples and methods

A total of 17 core samples were collected to be studied in detail from the CY1 well targeting the J_2d^7 (well position is shown in Fig. 2.1b). The depth of these samples varies between 1922.0−2023.5 m, including two carbonaceous mudstones, one sandy mudstone, 13 organic matter-rich mudstones, and one oil shale sample (Table 2.1).

Before the organic geochemical and microscopic investigations, each sample was cut into two halves after removing possibly weathered surfaces and subsequently dried at room temperature. One half was crushed and powdered for elemental carbon and sulfur analyses, Rock-Eval pyrolysis, biomarker analysis, X-ray diffraction (XRD), X-ray fluorescence spectrometry (XRF), and inductively coupled plasma mass spectrometry (ICP-MS). The other half was cut perpendicular to bedding planes to prepare polished sections for microscopic analysis.

2.3.1 Elemental carbon and sulfur analysis

Total organic (TOC) and total inorganic carbon (TIC) contents were determined on all samples using a liquid TOC II analyzer (Elementar). 100 mg pulverized sample was firstly combusted under a pure oxygen atmosphere at 550 °C for 600 s during which CO_2 is generated from the combustion of organic carbon. The residue was then combusted at 1000 °C for 400 s during which CO_2 is generated from the combustion of inorganic carbon bonds. The concentrations of CO_2 were detected by an IR detector and transferred to TOC and TIC, respectively, based on the sample weight and comparison to a standard.

The total sulfur (TS) contents were measured by combusting 100 mg of the pulverized sample under an oxygen atmosphere at 1800 °C using a S-200 Sulfur Analyzer (Leco). The generated SO_2 was detected by an IR detector and converted to the amount of TS.

2.3.2 Rock-Eval pyrolysis

In order to classify the kerogen type and determine the source rock potential of all analyzed samples, Rock-Eval pyrolysis was performed using a Rock-Eval VII instrument (Vinci Technologies) following the procedure described in detail in Behar et al. (2001). In a nitrogen atmosphere, approximately 50 mg of powdered sample was rapidly heated to 300 °C and held for 3 min to fully release S_1 (volatile hydrocarbon content, mg HC/g rock) fraction. Then the oven temperature was raised to 650 °C at 25°/min to measure the S_2 (remaining hydrocarbon generative potential, mg HC/g rock) fraction. Hydrogen (HI) and oxygen index (OI) were calculated from the S_2 and S_3 (CO_2 formed by thermal breakdown of kerogen, mg CO_2/g rock) peaks in relation to the TOC content determined by the elemental analyzer.

2.3.3 X-ray diffraction

The quantitative analysis of mineral composition was conducted on X'Pert PRO diffractometer using rock powder crushed by an agate mortar. 1−2 g powdered samples were placed in the groove of

a glass sheet and then scanned by X-Ray with a tube voltage of 35 kV, tube current of 30 mA, and scanning speed of 2°/min. The composition of minerals was determined by the intensity of the characteristic peaks of the different mineral crystals.

2.3.4 Organic petrography

Organic petrography was performed on all samples. Polished sections were prepared on bulk rock pieces (approximately 2.5 cm × 2.5 cm) cut perpendicular to bedding planes according to the procedures described in detail by Zieger and Littke (2019). For maceral analysis, the polished sections were investigated using a Zeiss Axio Imager incident light microscope operated with DISKUS Fossil software (Hilgers). Maceral identification was based primarily on their difference in reflectance color, structure, as well as their fluorescence intensity under ultra-violet light following the international standard ICCP system 1994 (ICCP, 1998 and 2001; Pickel et al., 2017; see also Taylor et al., 1998). Vitrinite reflectance (VR_r) was measured on at least 100 randomly oriented vitrinite particles per sample. Before measurement, a yttrium-aluminum-garnet standard (0.889% reflectance) was used for calibration.

2.3.5 Molecular geochemistry

Based on TOC contents, approximately 4 g of each pulverized sample was extracted by accelerated solvent extraction (ASE) using a DIONEX ASE 150 instrument and dichloromethane (DCM, 40 mL). Extraction was performed in a high-pressure cell at 100 °C and 100 bar for about 15 min. After extraction, sodium sulfate and activated copper powder were added to the extracts to eliminate excess water and elemental sulfur by fractionation. Consecutively, the extracts were subsequently separated into three fractions by column chromatography with silica gel (about 2 g) and eluents of different polarities: 5 mL *n*-pentane for the aliphatic hydrocarbons and 5 mL *n*-pentane/DCM (40:60, v:v) for the aromatic hydrocarbons.

Aliphatic and aromatic hydrocarbon fractions were analyzed by gas chromatography-flame-ionization detector (GC−FID) and gas chromatography-mass spectrometry (GC−MS). The GC−FID analysis was performed using a Fisons Instruments GC 8000 series, equipped with a split/splitless injector and a flame ionization detector (FID). 1 μL of the aliphatic fractions was injected into the GC−FID via split mode at an initial oven temperature of 60 °C, then programmed to 310 °C at 5 °C/min, which was kept for 20 min. GC−MS analyses of both fractions were performed using a Trace MS system coupled to a HRGC 5160 gas chromatograph. The MS was operated in electron impact ionization (EI+) mode at 70 eV electron energy in single ion monitoring (SIM) mode. The GC oven temperature was initially set at 80 °C (isothermal time 3 min), then heated to 320 °C with a rate of 3 °C /min, and finally held for 20 min.

2.3.6 Inorganic Geochemistry

Major elements concentrations were analyzed by XRF. After drying at 105 °C for 12 h, pulverized sample (about 1 g) was heated at 1000 °C in a muddle furnace for 2 h. The sample powders were then weighed to calculate the loss on ignition (LOI) at 400 °C. Finally, dried sample powders were mixed with lithium tetraborate ($Li_2B_4O_7$) for 8 times and fused into glass beads for the XRF analyses. Trace elements concentrations were measured by ICP−MS. After drying at 105 °C for 12 h, the sample powders were digested with 1 ml HNO_3 and 1 ml HF in a Teflon beaker. The sealed beaker was then heated to 190 °C in an oven for more than 12 h. After cooling, the Teflon beaker was opened and heated to 140 °C, and then was treated with 1 ml HNO_3. Finally, the reacted solutions were transferred to a polyethylene bottle and diluted to 100 g by the addition of 2% HNO_3 and then measured using ICP−MS.

The chemical index of alteration (CIA) is widely used to reflect the weathering intensity and reconstruct paleoclimate condition (Nesbitt and Young, 1982) and is calculated following the formula:

$$CIA = \text{molar } [Al_2O_3/(Al_2O_3 + CaO^* + Na_2O + K_2O)] \times 100$$

Here, CaO* represents the CaO in silicate minerals only and is corrected by subtracting Ca content in carbonates (calcite, dolomite) and phosphates (apatite) according to the equation as $CaO^* = CaO - Ca_{(calcite)} - Ca_{(dolomite)} - 10/3 \times P_2O_{5\,(apatite)}$ (Mclennan, 1993; Fedo et al., 1995). Na_2O, Al_2O_3, K_2O, and CaO* are molar concentrations, and Ca content in carbonates is obtained from XRD measurement.

2.4 Results

2.4.1 Lithology and mineralogy

Based on field observations, mineral composition, and TOC content, four lithofacies have been identified in the CY1 well, including carbonaceous mudstone, sandy mudstone, organic matter-rich mudstone, and oil shale. Mineralogically, the carbonaceous mudstone is characterized by low contents of quartz and clay minerals, with an average value of 4.1 wt% and 10.8 wt%, respectively (Table 2.2). The sandy mudstone is dominated by clay minerals (53.7 wt%), followed by quartz (35.9 wt%), potash feldspar (6.8 wt%), and plagioclase (3.6 wt%). Quartz (28.9−77.3 wt%, avg. 49.2 wt%) and clay minerals (13.2−61.1 wt%, aver. 37.2 wt%) are major components of the organic matter-rich mudstone (Table 2.2). In addition, a small amount of siderite was detected in mudstone. The oil shale is characterized by a high content of carbonate minerals (43.9 wt%) and a low content of quartz (8.7 wt%; Table 2.2).

2.4.2 Elemental carbon and sulfur composition

The results of TOC, TIC, and TS analyses are shown in Table 2.1. The TOC contents of carbonaceous mudstone are the highest, ranging from 27.0% to 39.2% (avg. 33.1%). The sandy mudstone has the lowest TOC content of 1.5%. The TOC contents of organic matter-rich mudstone

are highly variable, ranging from 3.1% to 15.2%, with an average value of 6.0%. Oil shale is characterized by relatively high TOC contents of 14.6%. Oil shale has high TIC content of 4.1%, while other samples are characterized by extremely low TIC contents. The TS contents of source rocks from the CY1 well are very low, ranging from 0.2% to 1.5%, with an average value of 0.4%.

OM* (organic matter content before sulfate reduction), CAR (carbonate content), and SIL (silicate content) were calculated following the equations presented by Littke (1993). As shown in Table 2.1, the carbonaceous mudstone shows high contents of OM* with values ranging from 36% to 52% (avg. 44%), while organic matter-rich mudstone was dominated by silicates with values ranging from 80% to 96% (avg. 92%). The CAR content exhibits an extremely high value of 34% in the oil shale.

2.4.3 Rock-Eval pyrolysis

As shown in Table 2.1, the HI values in the oil shale and organic matter-rich mudstone from the upper part are higher than those in organic matter-rich mudstone from the lower part and carbonaceous mudstone. T_{max} values (421–442°C, avg. 431°C) are similar for the selected samples. As shown in the HI vs.T_{max} diagram (Fig. 2.3), the oil shale and organic matter-rich mudstone from the upper part plot closer towards type I-II_1 kerogen, whereas organic matter-rich mudstone from the lower part and carbonaceous mudstone mainly comprise II_2-III kerogen.

2.4.4 Organic petrography

The VR_r measurement based on the autochthonous vitrinite particles indicated that the VR_r values of selected samples from the CY1 well range from 0.35% to 0.57% (avg. 0.48%; Table 2.2).

The carbonaceous mudstone is characterized by the highest volumetric percentage of organic matter and is especially enriched in vitrinite (36–62 vol%, avg. 49 vol%) and inertinite (17–18 vol%, avg. 17.5 vol%; Table 2.2), indicating abundant input of organic matter derived from terrestrial plants. Vitrinite occurs as massive and homogeneous phytoclasts, while inertinite appears as bright particles with detrital shape (Fig. 2.4a-h). Liptinite is mainly composed of sporinite (yellowish fluorescence; Fig. 2.4c-f), cutinite (bright yellow fluorescence; Fig. 2.4g and h) with serrated boundary, and resinite (bright yellow fluorescence; Fig. 2.4g and h) filling partly cellular pores in vitrinite. The sandy mudstone has the lowest volumetric percentage of organic matter of 1.6% and is dominated by vitrinite.

In organic matter-rich mudstone, liptinite is the dominant maceral group, with volume content increasing from the lower unit to the upper unit (1.2%–7.0%, avg. 3.5 vol%; Table 2.2). Lamalginite occurs as stripe-like lamellae and displays yellow fluorescence (Fig. 2.4i and j). Telalginite mainly occurs as structured *Botryococcus* with greenish-yellow fluorescence (Fig. 2.4k and l). Vitrinite and inertinite are visible but show a low volumetric percentage (excluding sample 21093).

The volumetric percentage of organic matter observed in oil shale is 5.8% (Table 2.2), with liptinite occurring as the dominant component and accounting for 5.5 vol% of the total macerals

counted. Exsudatinite with bright yellow fluorescence fills the camber of calcareous fossils (Fig. 2.4m and n). Lamalginite shows weak yellow fluorescence (Fig. 2.4o and p).

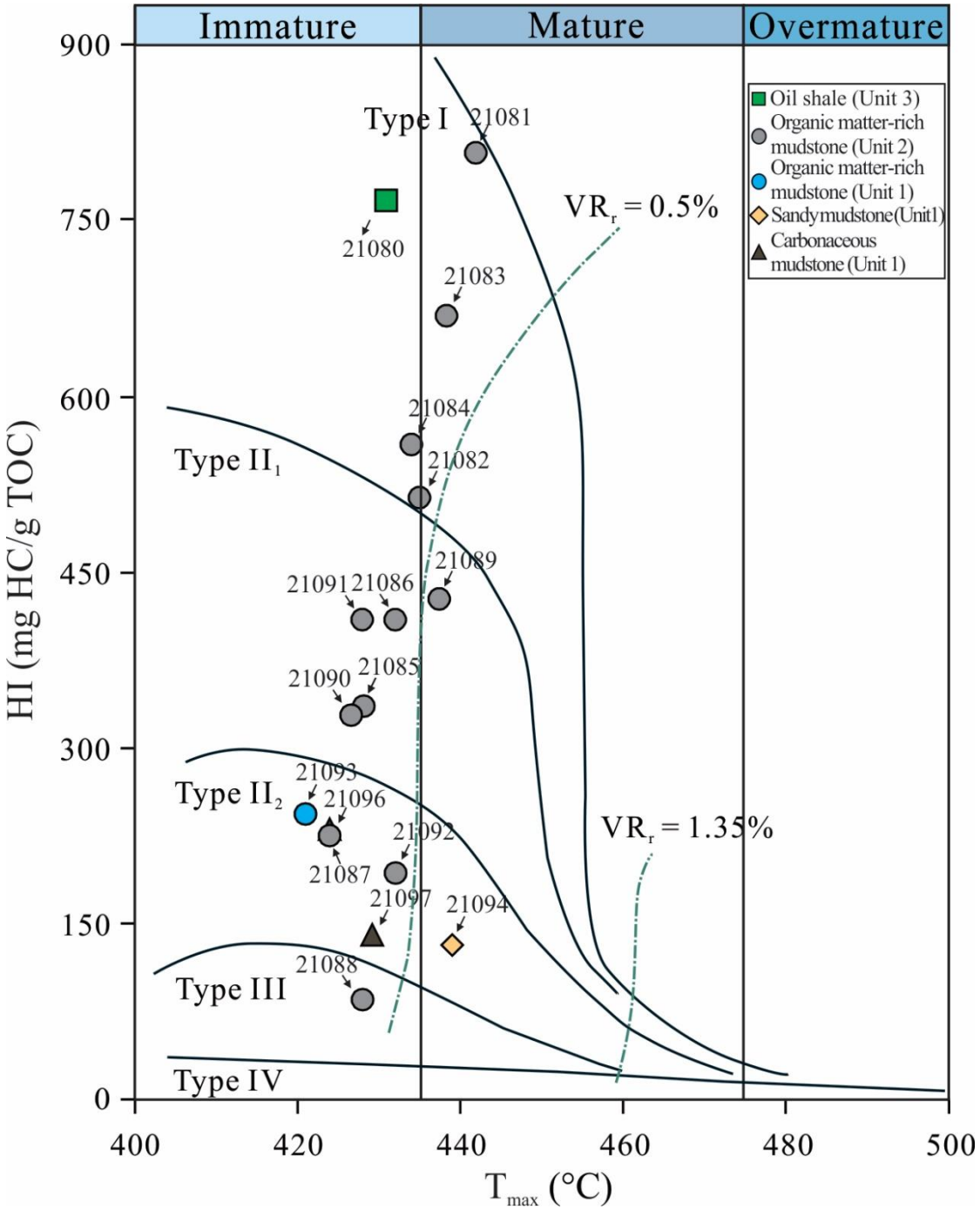

Figure 2.3 Cross-plot of HI versus T_{max} indicating the kerogen types of source rocks from the J_2d^7 in the CY1 Well. The organic matter-rich mudstones show a broad range of kerogen types. The oil shale is interpreted to contain type I kerogen, and the sandy mudstones, organic matter-rich mudstones at the bottom, and carbonaceous mudstones are interpreted to contain a type II-III kerogen.

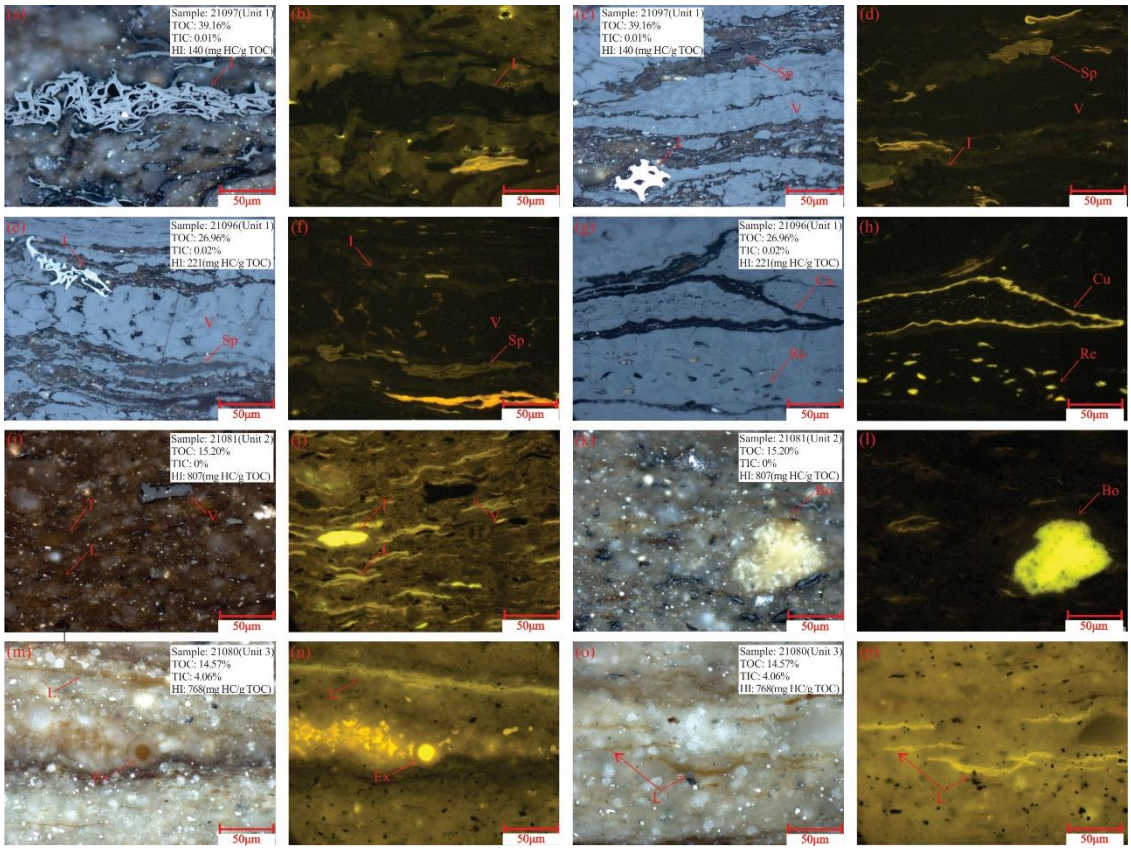

Figure 2.4 Microphotographs showing macerals in source rocks from the J_2d^7 in the CY1 Well under incident reflected white light (a, c, e, g, i, k, m, o) and in fluorescence mode (b, d, f, h, j, l, n, p). (a, b) semifusinite, sample 21097; (c, d) fusinite, vitrinite, and sporinite, sample 21097; (e, f) semifusinite, vitrinite, and sporinite, sample 21096; (g, h) resinite and cutinite, sample 21096; (i, j) lamalginite, telalginite, and vitrinite, sample 21081; (k, l) Botryococcus, sample 21081; (m, n) exsudatinite filling the space within minerals, sample 21080; (o, p) lamalginite, sample 21080; V-vitrinite, I-inertinite, L-lamalginite, T-telalginite, Cu-cutinite, Sp-sporinite, Re-resinite, Ex-exsudatinite, Bo-Botryococcus.

2.4.5 Molecular geochemistry

2.4.5.1 Acyclic alkanes, acyclic isoprenoids, and carotanes

Acyclic alkanes varying from *n*-C_9 to *n*-C_{31} are characterized by bimodal distributions with a predominance of at *n*-C_{15}, *n*-C_{17}, or *n*-C_{19} for the short-chain *n*-alkanes and between *n*-C_{23} to *n*-C_{25} for the middle-chain *n*-alkanes in the selected samples from the CY1 well (Fig. 2.5a-c).

Carbon preference index (CPI) and odd-to-even predominance (OEP) values of the carbonaceous mudstone are the highest, ranging from 1.76 to 2.33 (avg. 2.05) and 1.56 to 1.91 (avg. 1.73), while those of organic matter-rich mudstone are significantly lower, varying from 1.49 to 2.05 (avg. 1.69) and 1.41 to 1.75 (avg. 1.58; Table 2.3). CPI and OEP values of sandy mudstone are 1.57 and 1.45, while oil shale is characterized by the lowest values of 1.35 and 1.35. The pristane/phytane (Pr/Ph)

ratios of carbonaceous mudstone, sandy mudstone, organic matter-rich mudstone, and oil shale are 4.79–6.16 (avg. 5.47), 5.51, 2.56–7.25 (avg. 3.67), and 0.73, respectively (Table 2.3). Pr/*n*-C_{17} ratios of carbonaceous mudstone, sandy mudstone, organic matter-rich mudstone, and oil shale are 1.54–3.12 (avg. 2.33), 2.44, 0.48–6.83 (avg. 1.25), and 0.80, respectively, while the ratios of Ph/*n*-C_{18} display a reverse trend of 0.22–0.62 (avg. 0.42), 0.49, 0.14–1.15 (avg. 0.37), and 1.74, respectively.

β-carotane and γ-carotane, derived from pigments with a C_{40} carotenoid structure, were only detected in the oil shale. β-carotane is present in high, γ-carotane in low concentration (Fig. 2.5c).

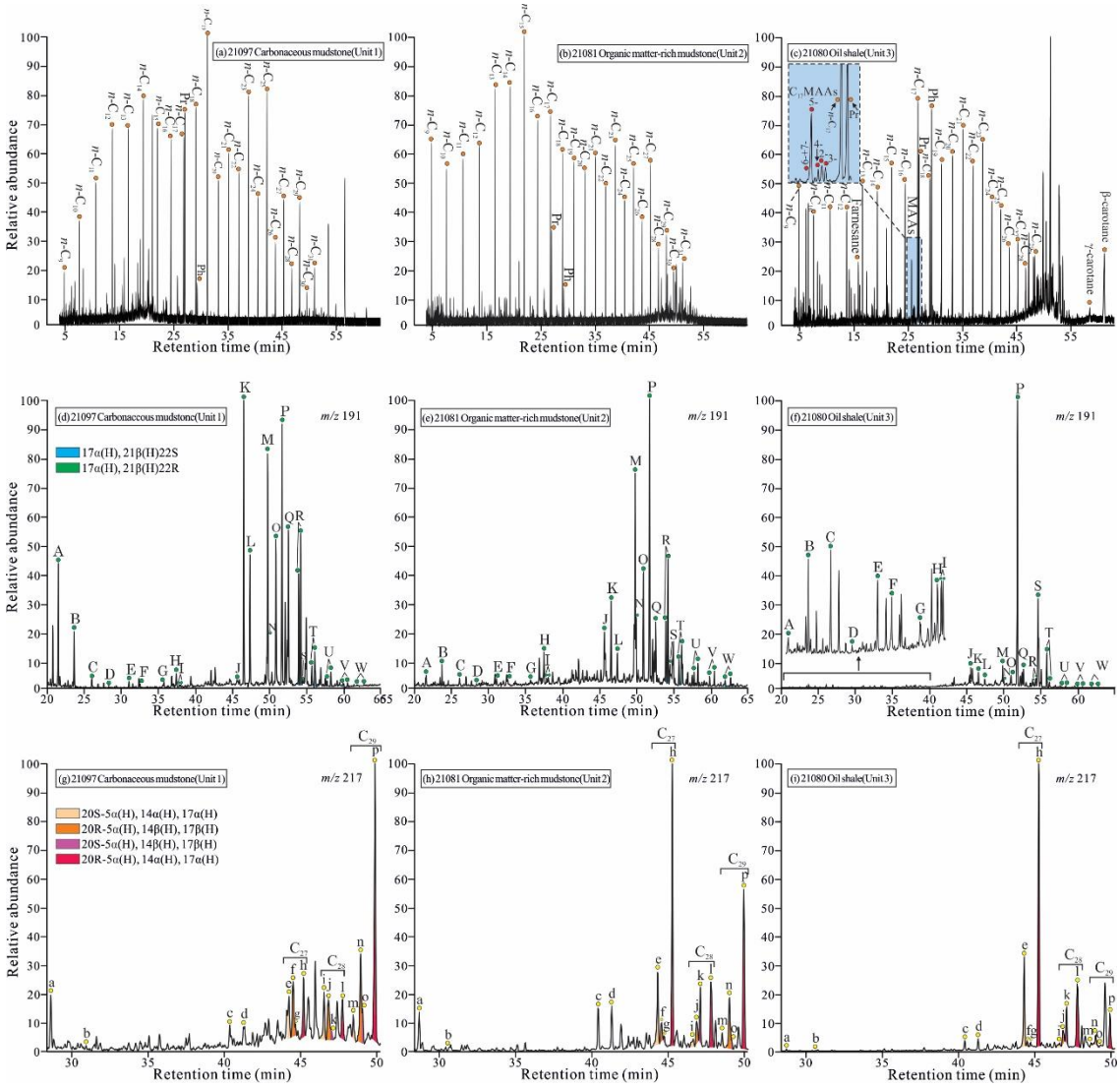

Figure 2.5 Distribution of partial gas and mass chromatograms of the aliphatic fraction in representative samples from the J_2d^7 in the CY1 Well. (a-c) Gas chromatograms; (d-f) Mass chromatograms (m/z 191) of the aliphatic fraction showing distribution of hopanes; (g-i) Mass chromatograms (m/z 217) of the aliphatic fraction showing distribution of steranes.

Table 2.1 TOC, TIC, and TS data, Rock-Eval pyrolysis data, as well as the three major primary sedimentary components calculated for the source rocks from the J_2d^7 in the CY1 Well.

Sample	Depth (m)	Lithology	TOC (%)	TIC (%)	TS (%)	S_1 (mg HC/g rock)	S_2 (mg HC/g rock)	S_3 (mg CO_2/g rock)	T_{max} (°C)	HI (mg HC/g TOC)	OI (mg CO_2/g TOC)	CAR (%)	OM* (%)	SIL (%)
21080	1922.0	Oil shale	14.57	4.06	0.47	6.91	111.88	1.16	431	768	8	34	19	47
21081	1931.1	Mudstone	15.20	0	0.47	1.31	122.68	0.61	442	807	4	0	20	80
21082	1936.5	Mudstone	5.88	0	0.32	0.12	30.07	0.36	435	511	6	0	8	92
21083	1941.5	Mudstone	3.98	0	0.23	0.11	26.56	0.33	438	667	8	0	5	95
21084	1943.5	Mudstone	4.65	0	0.23	0.15	25.87	0.32	434	556	7	0	6	94
21085	1951.5	Mudstone	5.60	0	0.27	0.24	18.71	0.52	428	334	9	0	7	93
21086	1953.5	Mudstone	3.52	0	0.22	0.09	14.35	0.35	432	408	10	0	5	95
21087	1959.9	Mudstone	6.86	0	0.25	0.20	15.42	0.73	424	225	11	0	9	91
21088	1960.9	Mudstone	6.70	0	0.19	0.07	5.74	0.82	428	86	12	0	9	91
21089	1965.2	Mudstone	3.12	0	0.26	0.09	13.28	0.31	437	426	10	0	4	96
21090	1968.2	Mudstone	5.88	0	0.34	0.28	19.28	0.54	427	328	9	0	8	92
21091	1968.4	Mudstone	5.61	0	0.36	0.37	23.02	0.49	428	410	9	0	8	92
21092	1975.1	Mudstone	4.18	0	0.26	0.06	8.04	0.52	432	192	12	0	6	94
21093	1977.3	Mudstone	7.16	0	0.36	0.25	17.39	1.11	421	243	16	0	10	90
21094	1988.0	Sandy mudstone	1.49	0	0.16	0.06	1.98	0.38	439	133	26	0	2	98
21096	2007.5	Carbonaceous mudstone	26.96	0.02	1.07	1.10	59.71	4.41	424	221	16	0	36	64
21097	2023.5	Carbonaceous mudstone	39.16	0.01	1.52	0.56	54.96	9.24	429	140	24	0	52	48

Table 2.2 TOC, VR_r, maceral composition (percentages based on whole rock samples), and mineralogical composition of the source rocks from the J_2d^7 in the CY1 Well.

Sample	TOC (%)	VR_r (%)	Maceral composition (vol%)				Mineralogical composition (wt%)								
			Vitrinite	Inertinite	Liptinite	Total OM	Quartz	Potash feldspar	Plagioclase	Calcite	Dolomite	Siderite	Pyrite	Amorphous matter	Clay
21080	14.57	0.46	0.1	0.2	5.5	5.8	8.7	0.3	0.7	42.8	1.1	3.9	1.0		41.5
21081	15.20	0.35	0.7	1.1	5.1	6.9	46.9	1.9	6.7			0.6	0.9		43.0
21082	5.88	0.43	0.6	1.0	7.0	8.6	40.6	1.9	7.4			7.2			42.9
21083	3.98	0.47	0.3	0.9	5.1	6.3	55.5	3.5	7.7	0.6	0.6	2.1			30.0
21084	4.65	0.42	0.9	1.0	5.7	7.6	66.9	2.0	6.8			0.3			24.0
21085	5.60	0.46	0.4	0.5	2.7	3.6	35.1	1.2	3.1			10.8			49.8
21086	3.52	0.47	0.6	0.9	4.3	5.8	60.6	2.6	5.8			6.3			24.7
21087	6.86	0.45	0.7	0.7	4.6	6.0	60.8	1.9	5.5			6.4			25.4
21088	6.70	0.48	0.6	0.5	2.2	3.3	28.9	1.0	2.1			15.1			52.9
21089	3.12	0.46	0.6	0.3	1.7	2.6	30.1	1.4	2.5			4.9			61.1
21090	5.88	0.50	0.6	0.5	1.2	2.3	37.4	1.9	2.9			8.1			49.7
21091	5.61	0.48	0.2	0.2	2.9	3.3	54.0		3.1			24.0			18.9
21092	4.18	0.53	1.8	0.4	1.4	3.6	45.3	1.5	1.7			4.1			47.4
21093	7.16	0.47	8.5	0.7	2.0	11.2	77.3	5.0	3.6		0.6	0.3			13.2
21094	1.49	0.51	1.1	0.2	0.3	1.6	35.9	6.8	3.6						53.7
21096	26.96	0.56	36.0	17.0	2.4	55.4	2.5							85.2	12.3
21097	39.16	0.57	62.0	18.0	2.4	82.4	5.7							85.1	9.2

Table 2.3 Biomarker parameters of acyclic alkanes of the source rocks from the J_2d^7 in the CY1 Well.

Sample	Pr/Ph	Pr/*n*-C_{17}	Ph/*n*-C_{18}	CPI	OEP
21080	0.73	0.80	1.74	1.35	1.35
21081	2.71	0.48	0.22	1.49	1.42
21082	3.87	0.58	0.17	1.55	1.62
21083	4.23	0.55	0.14	1.49	1.59
21084	4.02	0.63	0.19	1.54	1.62
21085	3.18	0.72	0.28	1.79	1.66
21086	3.68	0.53	0.18	1.56	1.56
21087	3.77	0.56	0.18	1.49	1.47
21088	3.47	0.62	0.19	1.73	1.63
21089	2.78	0.56	0.23	1.81	1.59
21090	2.77	1.63	0.72	1.90	1.75
21091	2.56	1.08	0.56	1.67	1.57
21092	3.45	1.54	0.56	2.05	1.70
21093	7.25	6.83	1.15	1.85	1.41
21094	5.51	2.44	0.49	1.57	1.45
21096	4.79	3.12	0.62	1.76	1.56
21097	6.16	1.54	0.22	2.33	1.91

Pr = pristane; Ph = phytane; CPI =2 × Σodd *n*-$C_{23–29}$/(Σeven *n*-$C_{22–28}$ + Σeven *n*-$C_{24–30}$); OEP = (*n*-C_{21} + 6 × *n*-C_{23} + *n*-C_{25})/(4 × *n*-C_{22} + 4 × *n*-C_{24}).

2.4.5.2 Terpanes

Tricyclic terpanes (Tri; *m/z* 191) in the range of C_{19} to C_{26}, C_{24} tetracyclic terpane (C_{24} Tet; *m/z* 191), and pentacyclic terpanes (hopanes; *m/z* 191) were identified in all the selected samples from CY1 well (Fig. 2.5d-f). The C_{19}/C_{23} Tri (0.25–32.23, avg. 7.04), C_{20}/C_{23} Tri (0.95–10.17, avg. 3.63), and C_{24} Tet/C_{26} Tri (0.65–4.96, avg. 2.31) ratios are characterized by decreasing values from the bottom to the top unit. The Ts/(Ts + Tm) ratio is commonly applied to indicate thermal maturity, ranging from 0.02 to 0.40 (avg. 0.23). In addition, the ratios of C_{29} Ts/(C_{29} Ts + C_{29} H) and 22S/(22S + 22R) ratios for C_{31} homohopane range from 0.09 to 0.36 (avg. 0.23) and 0.25 to 0.44 (avg. 0.35), respectively (Table 2.4). The oil shale is characterized by a high abundance of C_{30} hopane (C_{30} H) and gammacerane (Gam) with a Gam index of 0.48, while Gam is present in low abundances in the carbonaceous mudstone, sandy mudstone, and organic matter-rich mudstone with Gam index varying from 0.02 to 0.14. (Fig. 2.5d-f; Table 2.4). The C_{35} 22S/C_{34} 22S homohopane ratio also shows the highest value of 0.77 in the oil shale (Table 2.4).

2.4.5.3 Steroids

Steranes were detected by *m/z* 217 ion chromatogram and showed lower concentration than hopanes with steranes/hopanes ratios of 0.13–0.94 (avg. 0.28; Table 2.4). The distribution of steranes is displayed in Fig. 2.5g-i. The carbonaceous mudstone and sandy mudstone are dominated by high proportions of C_{29} ααα 20R steranes of 74% and 61%, respectively. In the organic matter-rich mudstone, the proportions of C_{29} ααα 20R steranes (34–73%, avg. 44%) are slightly more abundant than C_{27} ααα 20R steranes (9–48%. avg. 37%) and C_{28} ααα 20R steranes (15–22%, avg. 19%) is the lowest, except for sample 21093 with a high concentration of C_{29} ααα 20R steranes of 73% (Table 2.4). The oil shale is characterized by a high proportion of C_{27} (69%) compared to C_{28} (22%) and C_{29}

(10%) ααα 20R steranes. The C_{29} ααα 20S/(20S + 20R) and C_{29} ββ/(ββ + αα) ratios range from 0.06 to 0.17 and 0.24 to 0.41, respectively (Table 2.4).

2.4.5.4 Bicyclic alkanes and 13α(*n*-alkyl)-tricyclic terpanes

Abundant bicyclic sesquiterpanes were detected in the selected samples with peaks ranging from *n*-C_{14} to *n*-C_{16} on the mass chromatogram of *m/z* 123 (Fig. 2.6). The bicyclic sesquiterpanes in

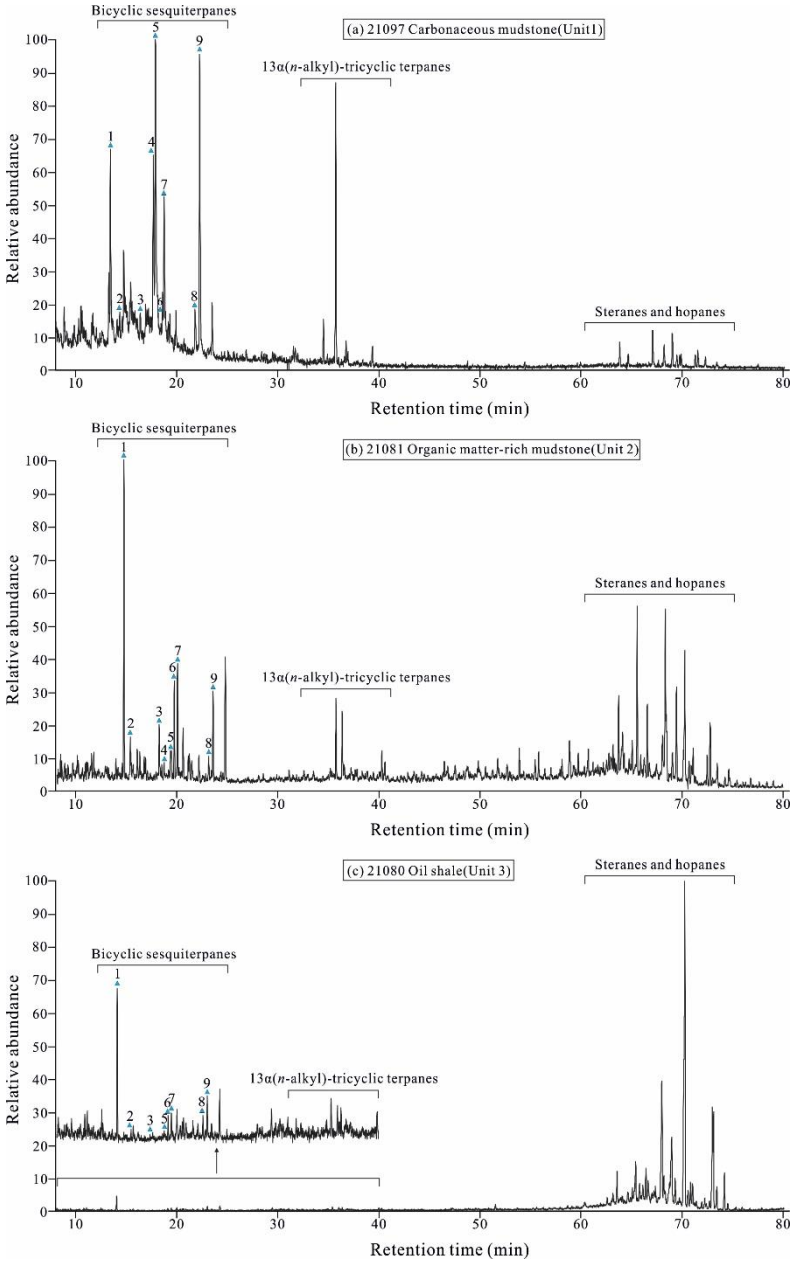

Figure 2.6 Distribution of partial mass chromatograms (m/z 123) of the aliphatic fraction in representative samples from the J_2d^7 in the CY1 Well showing the distribution of bicyclic sesquiterpanes and 13α(n-alkyl)-tricyclic terpanes. 1-2: C_{14} sesquiterpane; 3-6: C_{15} sesquiterpane; 7: 8β(H)-drimane; 8: C_{16} sesquiterpane; 9: 8β(H)-homodrimane.

hydrocarbon source rocks exhibit three distribution patterns. Bicyclic sesquiterpanes are very abundant in the carbonaceous mudstone, while steranes and hopanes are enriched in the oil shale (Fig. 2.6). C_{14} bicyclic sesquiterpanes are present in a high abundance in all the selected samples, while C_{15}-C_{16} sesquiterpanes exhibit relatively higher abundance in the carbonaceous mudstone and organic matter-rich mudstone compared to the oil shale. A novel 13α(*n*-alkyl)-tricyclic terpanes was identified in the selected samples based on mass spectra interpretation (Song et al., 2021).

2.4.5.5 Aromatic hydrocarbons

Trimethylnaphthalenes (TMNs; *m/z* 170), cadalene (Cad; *m/z* 183), tetramethylnaphthalenes (TeMNs; *m/z* 184), phenanthrene (P, *m/z* 178), and methylphenanthrenes (MPs; *m/z* 192) were identified in the aromatic fractions occuring in high abundance, while fluorene (FL; *m/z* 166), dibenzofuran (DBF; *m/z* 168), and dibenzothiophene (DBT; *m/z* 184) occur in low abundance (Fig. 2.7). Other aromatic hydrocarbons of biological origin, including tetrahydroretene (Tet; *m/z* 223), 6-isopropyl-1-isohexyl-2-methylnaphthalene (ip-iHMN; *m/z* 197), simonellite (Sim; *m/z* 237) and retene (Ret; *m/z* 219) show relatively low concentrations (Fig. 2.7). The concentrations of aromatic hydrocarbons show significant differences with respect to the lithofacies. Cad and P have high abundances compared to other compounds in the carbonaceous mudstone, while the TMNs are the most abundant compounds in organic matter-rich mudstone and oil shale (Fig. 2.7). Further, the log (1-MP/9-MP) and log (1,2,5-TMN/1,3,6-TMN) ratios show the lowest values in oil shale of –0.18 and –0.69, while those of carbonaceous mudstone (–0.11–0.12, avg. 0; –0.04–0.19, avg. 0.08), sandy mudstone (–0.01; –0.22), and organic matter-rich mudstone (–0.19–0.14, avg. 0.03; –0.29–0.49, avg. 0.25) are significantly higher (Table 2.5). By contrast, DBT shows high abundance in the normalized distribution of FL, DBF, and DBT in oil shale, while relative DBT contents in carbonaceous mudstone are the lowest (Table 2.5).

Methylated isoprenoid chromans with a methylated 2-methyl-2-(4,8,12-trimethyltridecyl) chromans (MTTCs) structure were detected in the aromatic hydrocarbon fractions from oil shale and organic matter-rich mudstone (Fig. 2.8). The isomers of dimethyl (β-MTTC and γ-MTTC; *m/z* 135) and trimethyl (α-MTTC; *m/z* 149) homologues are present in oil shale and organic matter-rich mudstone (Fig. 2.8a), while monomethyl isomer (δ-MTTC; *m/z* 121), a compound closely related to environments with high salinity, is only found in oil shale (Fig. 2.8b). The α/δ-MTTC ratios of oil shale is 14.79.

Moreover, 4-ring polycyclic aromatic hydrocarbons (PAHs) including fluoranthene (Fla) and pyrene (Py; *m/z* =202), methylfluoranthenes, benzo[*a*]fluorene, benzo[*b*]fluorene, 2-methylpyrene, 4-methylpyrene and 1-methylpyrene (*m/z* =216), and benzo[*a*]anthracene (BaA) and chrysene (Ch; *m/z* =228); 5-ring PAHs including benzo[*a*]pyrene, benzo[*e*]pyrene, perylene, benzo[*b*]fluoranthene and benzo[*k*]fluoranthene (*m/z* =252); and 6-ring PAHs including indeno[1,2,3-*cd*]pyrene (InPy) and

benzo[*ghi*]perylene (BghiP; *m/z* =276) are detected in the selected samples (Fig. 2.9). Compared to the 6-ring PAHs, both 4-ring and 5-ring PAHs exhibit relatively high abundance.

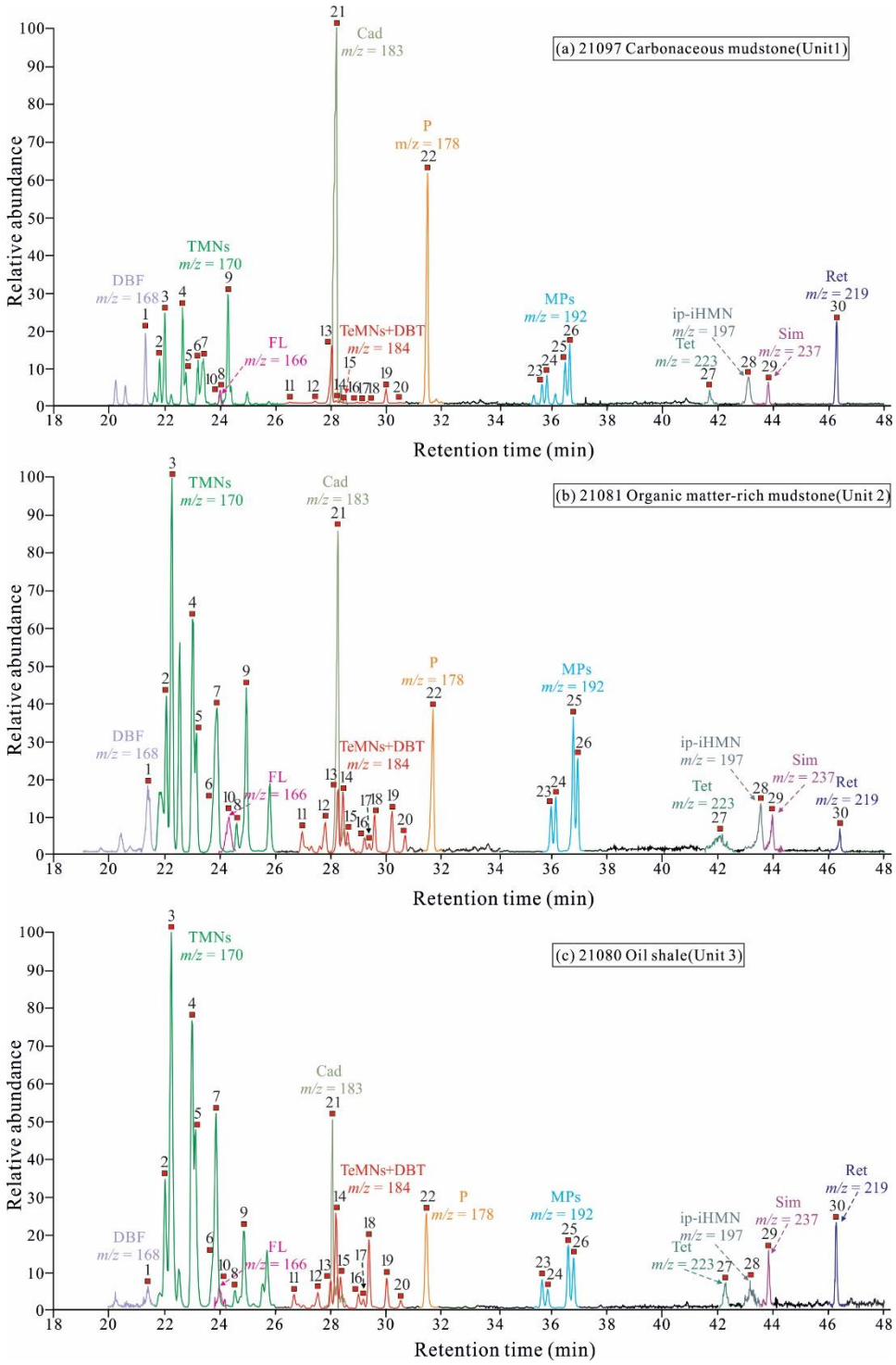

Figure 2.7 Total ion chromatogram (TIC) of the aromatic hydrocarbons in representative samples from the J_2d^7 in the CY1 Well.

Table 2.4 Biomarker parameters of tricyclic and tetracyclic terpanes, hopanes, and steranes of the source rocks from the J_2d^7 in the CY1 Well.

Sample	Tricyclic and tetracyclic terpanes				Hopanes				Steranes/ hopanes	Steranes					
	C_{19}/ C_{23} Tri	C_{20}/ C_{23} Tri	C_{24} Tet/ C_{26} Tri	Ts/ (Ts + Tm)	C_{29} Ts/ (C_{29} Ts + C_{29} H)	Gam/ C_{30} H	C_{31} H 22S/ 22(S + R)	C_{35} H 22S/ C_{34} H 22S		C_{29} ααα S/ (R + S) steranes	C_{29} ββ/ (ββ + αα) steranes	C_{29}/C_{27} regular steranes	Sterane ααα 20R distribution (%)		
													C_{27}	C_{28}	C_{29}
21080	0.25	0.95	0.65	0.34	0.21	0.48	0.31	0.77	0.47	0.16	0.32	0.18	69	22	10
21081	1.15	1.40	1.98	0.40	0.26	0.14	0.34	0.53	0.94	0.10	0.27	0.66	48	18	35
21082	3.46	2.29	1.84	0.29	0.27	0.06	0.30	0.45	0.27	0.09	0.29	0.91	33	19	47
21083	3.58	2.96	1.78	0.23	0.22	0.05	0.25	0.37	0.15	0.10	0.31	1.22	31	20	49
21084	4.58	3.37	1.54	0.21	0.21	0.04	0.25	0.19	0.31	0.06	0.26	0.98	36	15	48
21085	3.87	3.41	2.15	0.25	0.24	0.03	0.35	0.35	0.19	0.09	0.26	0.93	37	20	43
21086	5.44	3.87	1.84	0.25	0.20	0.04	0.31	0.17	0.26	0.08	0.25	0.97	35	19	45
21087	2.71	2.29	2.18	0.22	0.20	0.03	0.35	0.39	0.35	0.13	0.29	0.64	47	19	34
21088	3.66	2.79	2.54	0.25	0.22	0.06	0.37	0.32	0.24	0.09	0.25	0.76	41	22	38
21089	3.11	2.77	2.13	0.21	0.20	0.06	0.37	0.35	0.24	0.10	0.24	0.77	42	21	37
21090	1.54	1.81	1.49	0.17	0.17	0.05	0.36	0.30	0.16	0.09	0.25	0.85	38	19	43
21091	0.96	1.28	1.10	0.40	0.36	0.04	0.37	0.37	0.22	0.12	0.25	0.63	43	18	38
21092	4.36	3.44	1.73	0.18	0.34	0.04	0.38	0.19	0.26	0.09	0.26	0.70	43	20	37
21093	20.37	4.83	3.66	0.25	0.17	0.03	0.41	0.19	0.31	0.17	0.41	1.40	9	18	73
21094	11.46	5.56	3.16	0.10	0.09	0.03	0.37	0.39	0.13	0.16	0.39	1.54	18	21	61
21096	32.23	10.17	4.56	0.07	0.20	0.02	0.44	0.15	0.16	0.09	0.33	2.27	12	15	74
21097	16.96	8.50	4.96	0.02	0.30	0.02	0.42	0.07	0.16	0.07	0.30	2.65	14	12	74

Tri = tricyclic terpane; Tet = tetracyclic terpane; H = hopane; Gam = gammacerane; Steranes/hopanes = C_{27}-C_{29} regular steranes/C_{29}-C_{35} 17α-hopanes.

Table 2.5 Biomarker parameters of aromatic fractions of the source rocks from the J_2d^7 in the CY1 Well.

Sample	Log (1-MP/9-MP)	Log (1,2,5-TMN/1,3,6-TMN)	Ret/(Ret+ Cad)	DBT/(DBF + FL	DBT/P	Normalized distribution of DBT, DBF and FL (%)			Fla/(Fla + Py)	BaA/(BaA + Ch)	InPy/(InPy + BghiP)
						DBT	DBF	FL			
21080	–0.18	–0.69	0.27	0.91	0.14	47.6	42.7	9.7	0.36	0.33	0.31
21081	–0.19	–0.29	0.05	0.19	0.09	15.8	69.2	15.0	0.51	0.34	0.37
21082	0.05	0.24	0.08	0.25	0.11	20.2	53.5	26.3	0.60	0.35	0.12
21083	–0.02	0.11	0.06	0.23	0.11	18.4	64.6	17.0	0.61	0.30	0.32
21084	0.03	0.28	0.11	0.34	0.11	25.2	49.8	25.0	0.59	0.25	0.34
21085	0.00	0.38	0.11	0.25	0.10	20.1	56.7	23.2	0.65	0.33	0.22
21086	0.01	0.35	0.11	0.29	0.12	22.3	54.2	23.6	0.61	0.30	0.22
21087	0.13	0.34	0.09	0.18	0.08	15.2	71.8	13.0	0.58	0.29	0.29
21088	0.14	0.45	0.16	0.27	0.13	21.0	59.1	20.0	0.63	0.34	0.29
21089	0.06	0.49	0.12	0.16	0.08	13.9	64.6	21.5	0.61	0.37	0.25
21090	0.10	0.49	0.09	0.26	0.15	20.5	61.3	18.2	0.61	0.34	0.19
21091	0.05	0.31	0.13	0.24	0.14	19.3	65.0	15.7	0.55	0.34	0.28
21092	0.04	0.22	0.10	0.15	0.10	13.2	48.6	38.2	0.57	0.60	0.31
21093	–0.08	–0.07	0.34	0.19	0.13	16.0	54.8	29.2	0.56	0.50	0.43
21094	–0.01	–0.22	0.18	0.16	0.03	14.1	55.8	30.1	0.61	0.39	0.26
21096	–0.11	–0.04	0.35	0.05	0.02	4.6	71.8	23.6	0.68	0.43	0.48
21097	0.12	0.19	0.11	0.07	0.01	6.3	85.5	8.2	0.62	0.60	0.55

TMN: trimethylnaphthalene; MP: methylphenanthrene; DBT: dibenzothiophene; P: phenanthrene; FL: fluorene; DBF: dibenzofuran. Ret: retene; Cad: Cadalene; Fla: fluoranthene; Py: pyrene; BaA: benzo[*a*]anthracene; Ch: chrysene; InPy: indeno[1,2,3-*cd*]pyrene; BghiP: benzo[*ghi*]perylene.

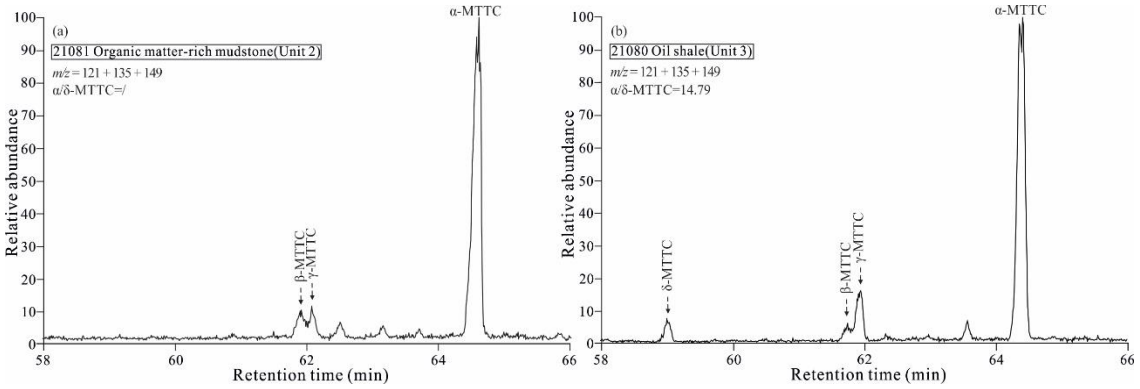

Figure 2.8 Distribution of partial mass chromatograms (m/z 121 + 135 + 149) of the aromatic hydrocarbons showing the distribution of MTTCs in representative samples from the J_2d^7 in the CY1 Well.

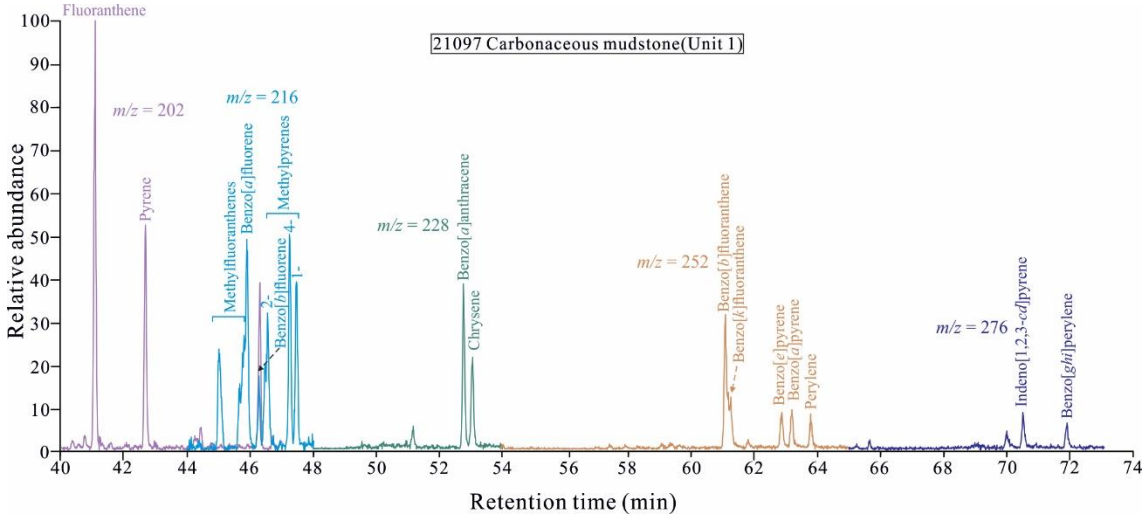

Figure 2.9 Ion chromatograms (m/z 202, 216, 228, 252, and 276) of the aromatic hydrocarbons showing the distribution of PAHs in representative sample from the J_2d^7 in the CY1 Well.

2.4.6 Major and trace elements

The results of multiple inorganic geochemical proxies are listed in Table 2.6. The oil shale shows a high ratio of U/Th of 0.49, while significantly lower ratios are observed in the carbonaceous mudstone, sandy mudstone, and organic matter-rich mudstone of 0.31–0.43, 0.29, and 0.19–0.31, respectively. Similarly, the P/Al (17.43–158.00), Ba/Al (32.72–101.73), and 100* MgO/Al_2O_3 (2.08–32.25) ratios show similar patterns that are characterized by an increasing trend from the carbonaceous mudstone to the oil shale. Zr/K (105.00–197.06) and Zr/Rb (1.23–2.12) ratios of carbonaceous mudstone, sandy mudstone, and sample 21093 are higher than those of organic matter-rich mudstone and oil shale (Zr/K: 41.86–102.56; Zr/Rb: 0.54–1.23; Table 2.6). The CIA (84.35–89.23) and

ln(Al_2O_3/Na_2O) (3.60–3.85) values also exhibit a decreasing trend upward from the carbonaceous mudstone, sandy mudstone, and sample 21093 to the organic matter-rich mudstone and oil shale (CIA: 59.97–86.68; ln(Al_2O_3/Na_2O): 2.31–3.71; Table 2.6).

Table 2.6 Inorganic geochemical proxies of the source rocks from the J_2d^7 in the CY1 Well.

Sample	U/Th	100*MgO/Al_2O_3	P/Al (10^{-4})	Ba/Al (10^{-4})	CIA	In(Al_2O_3/Na_2O) (molar)	Zr/K (10^{-4})	Zr/Rb
21080	0.49	32.25	158.00	101.73	59.97	2.37	41.86	0.54
21081	0.21	11.01	154.25	90.07	74.50	2.31	69.77	0.95
21082	0.23	9.05	59.44	70.86	77.74	2.58	73.94	0.93
21083	0.28	8.04	33.82	63.00	83.03	2.75	74.07	0.95
21084	0.26	6.94	39.81	62.22	81.92	2.95	76.96	1.04
21085	0.23	6.29	61.40	53.49	84.03	3.25	75.69	0.85
21086	0.25	5.95	49.57	59.83	85.03	3.31	73.56	0.92
21087	0.31	6.37	34.60	45.49	84.65	3.18	76.62	0.98
21088	0.23	5.57	65.18	51.61	83.95	3.33	76.17	0.94
21089	0.19	4.54	35.38	44.92	86.27	3.66	66.08	0.78
21090	0.21	4.54	60.91	43.70	86.68	3.63	83.15	0.97
21091	0.21	4.64	67.47	45.46	85.18	3.68	69.76	0.82
21092	0.20	3.96	41.53	45.59	86.23	3.71	102.56	1.23
21093	0.24	4.06	56.62	49.34	85.86	3.78	157.39	2.12
21094	0.29	2.72	17.43	51.56	84.35	3.60	105.00	1.23
21096	0.31	2.08	28.68	32.72	88.47	3.75	197.06	1.74
21097	0.43	2.46	57.14	36.19	89.23	3.85	188.24	1.91

2.5 Discussion

2.5.1 Thermal maturity

Both the T_{max} and VR_r results (Tables 2.1 and 2.2) indicate that the J_2d^7 in the CY1 Well is thermally immature to early mature with average values of 431 °C and 0.48%, respectively.

The cross-plot of C_{29} ααα 20S/(20S + 20R) versus C_{29} ββ /(ββ + αα) ratios (Fig. 2.10a) shows that the selected samples from the J_2d^7 plot far away from the equilibrium area, which indicates a low maturity (Peters et al., 2005). It is also supported by the closer plotting to the well studied immature

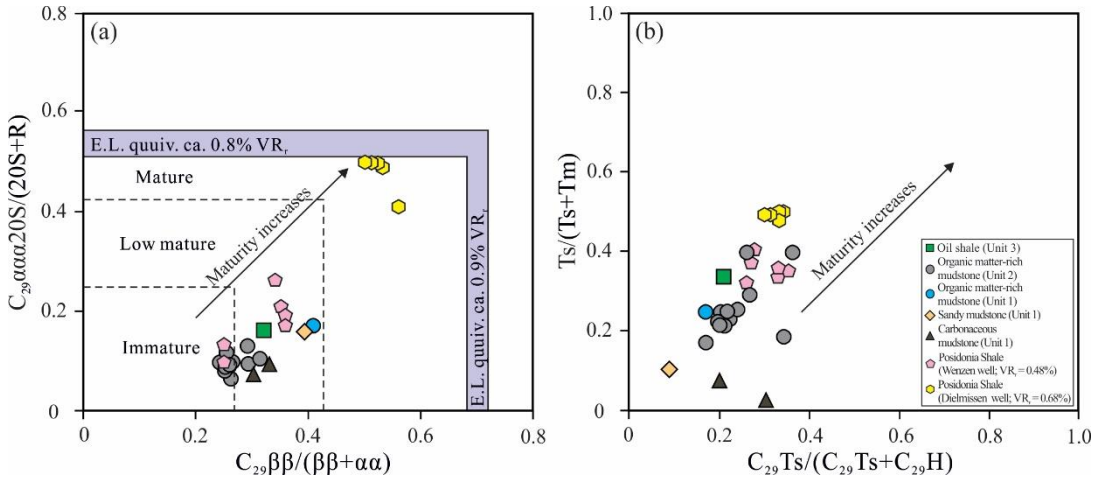

Figure 2.10 Molecular thermal maturity indicators of source rocks from the J_2d^7 in the CY1 Well. (a) Cross-plot of C_{29} ααα 20S/(20S +20R) versus C_{29} ββ/(ββ + αα); (b) Cross-plot of Ts/(Ts + Tm) versus C_{29} Ts/(C_{29} Ts + C_{29} H). E.L. equiv. = equilibration levels equivalent to vitrinite reflectance values (taken from Peters et al., 2005). Data of Posidonia shale are taken from Fang et al. (2019).

Posidonia with VR_r values of 0.48% as compaed to the same rock at 0.68% VR_r. C_{31} 22S/(22S + 22R) homohopanes ratios of 0.50–0.54 generally indicate the onset of maturation corresponding to VR_r values of approximately 0.6% (Seifert and Moldowan, 1980). Therefore, the ratios of 0.25–0.44 in this study illustrate immature conditions (Table 2.4). Furthermore, C_{29} Ts/(C_{29} Ts + C_{29} hopane) and Ts/(Ts + Tm) ratios were reported to increase with increasing thermal maturity, while the latter ratio is susceptible to the variations in the organic matter facies (Peters et al., 2005; Fang et al., 2019; Qiao et al., 2021a). The plots of Ts/(Ts + Tm) versus C_{29} Ts/(C_{29} Ts + C_{29} hopane) also indicate a low thermal maturity (Fig. 2.10b). Song et al. (2021) proposed that C_{14} bicyclic sesquiterpanes are enriched in immature samples and their concentrations decrease with increasing maturity. In this study, the C_{14} bicyclic sesquiterpanes are present in a high abundance in all the selected samples, clearly indicating that the studied samples from the J_2d^7 in the CY1 Well are immature (Fig. 2.6).

2.5.2 Paleo-depositional environment

The TOC/TS ratios indicate that the selected samples are placed in a non-marine setting (Fig. 2.11a). The Pr/*n*-C_{17} versus Ph/*n*-C_{18} plot indicates that oxic conditions prevailed in the bottom water during the deposition of carbonaceous mudstone, organic matter-rich mudstone, and sandy mudstone, while the oil shale was deposited in oxygen-deficient bottom water (Fig. 2.11b). This conclusion is consistent with variation in C_{35} 22S/C_{34} 22S homohopane ratios that are commonly used to reveal the redox conditions (Table 2.4; Peters et al., 2005). β-carotane and γ-carotane were widely observed in sources rocks deposited in anoxic and saline water and also accumulated in evaporitic and carbonate-rich environments (Ding et al., 2020; Xie et al., 2021). The occurrence of β-carotane and γ-carotane in the oil shale reflects a change from oxic and freshwater to anoxic and saline environments. Furthermore, Gam is thought to be a reduction product of tetrahymanol in bacterivorous ciliates existing (ten Haven et al., 1989; Venkatesan, 1989). Abundant Gam and δ-MTTC are commonly regarded as an indicator of hypersaline environment, water column stratification, and anoxic conditions (ten Haven et al., 1987; Sinninghe Damsté et al., 1995; Hanson et al., 2000, 2001). The high Gam index and low α/δ-MTTC values of the oil shale reflect anoxic and saline lacustrine environment (Figs. 2.8b, 2.11c). This is consistent with the former observation that the organic matter-rich mudstone is enriched in *Botryococcus*, which lives in brackish-freshwater water. The pattern of the organic matter-rich mudstone and carbonaceous mudstone rich in bicyclic sesquiterpanes and poor in steranes and hopanes occurs commonly in sediments deposited in fresh-brackish lacustrine or swamp environments (Fig. 2.6a and b; Luo et al., 1991; Ji et al., 2016). By contrast, the high abundance of steranes and hopanes and scarceness of bicyclic sesquiterpanes in the oil shale indicate a more saline environment (Fig. 2.6c; Luo et al., 1991). Furthermore, the decreasing relative abundance of C_{15}-C_{16} bicyclic sesquiterpanes and increasing relative abundance of C_{14} bicyclic sesquiterpanes from the carbonaceous mudstone to the oil shale indicates an evolution from fresh-brackish water to saline environment (Fig. 2.6; Ji et al., 2016). A cross-plot of DBT/P versus Pr/Ph is widely used to indicate

source rock depositional environments and lithologies (Hughes et al., 1995; Song et al., 2017; Zheng et al., 2022). Based on the plot, carbonaceous mudstone, sandy mudstone, and organic matter-rich mudstone (No. 21093) fall into the field of Zone 4, associating with a fluvial/deltaic environment. By contrast, organic matter-rich mudstone and oil shale plot into the field of Zone 3−4 and Zone 2, respectively, revealing evolution from fluvial/deltaic environment to lacustrine environment (Fig. 2.12a). Song et al. (2019) suggested that FL is prone to convert to DBF in oxic condition while forming DBT in anoxic conditions. Therefore, relatively high contents of DBT in the normalized distribution of FL, DBF, and DBT is indicative of reducing condition (Quan et al., 2017; Song et al., 2019). In this study, the relatively high percentage of DBT in the oil shale suggests anoxic conditions during deposition. According to the plots of biomarker parameters above (Figs. 2.11 and 2.12), three units were identified in the J_2d^7 (Figs. 2.13 and 2.14). Unit 1 belongs to fluvial systems, while Units 2 and 3 were deposited in freshwater and saline lacustrine environments, respectively.

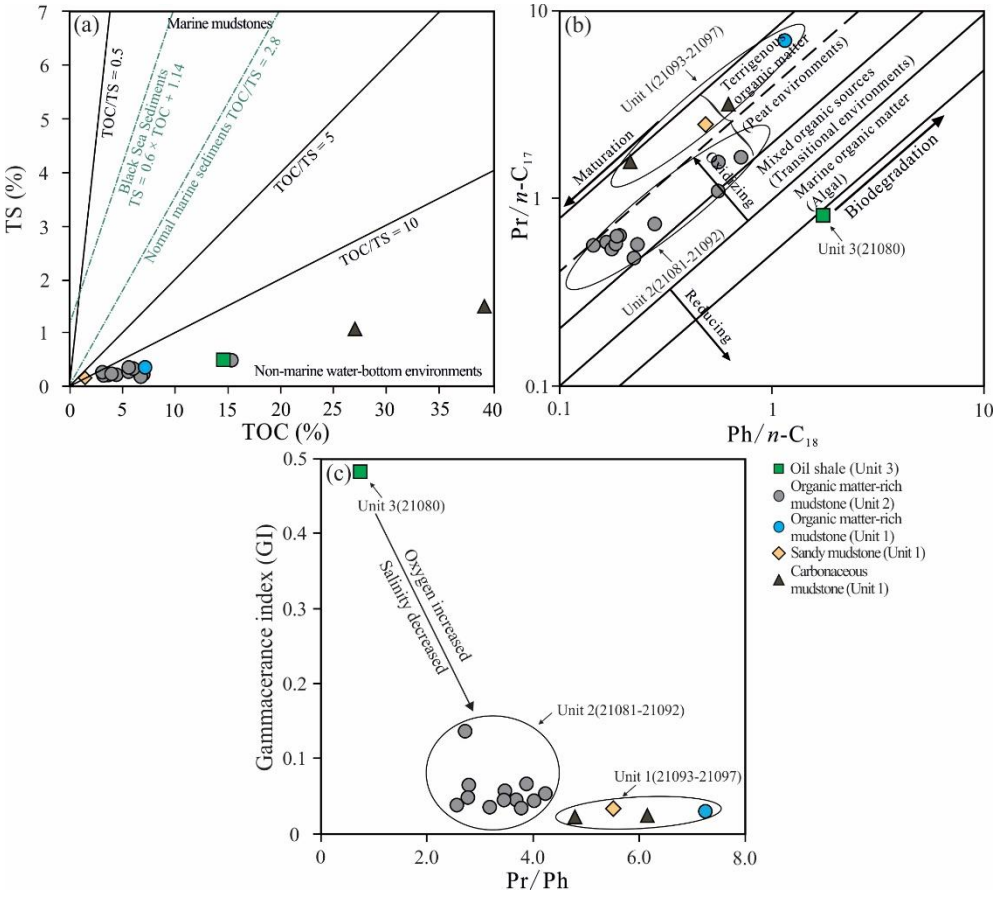

Figure 2.11 (a) Cross-plot of TS versus TOC; (b) Cross-plot of pristane/n-C_{17} (Pr/n-C_{17}) versus phytane/n-C_{18} (Ph/n-C_{18}) (modified after Littke, 1993); (c) Cross-plot of gammacerane index (GI) versus Pristane/Phystane (Pr/Ph). Data of normal marine sediments and Black Sea sediments are taken from Berner and Raiswell (1983) and Leventhal (1983), respectively.

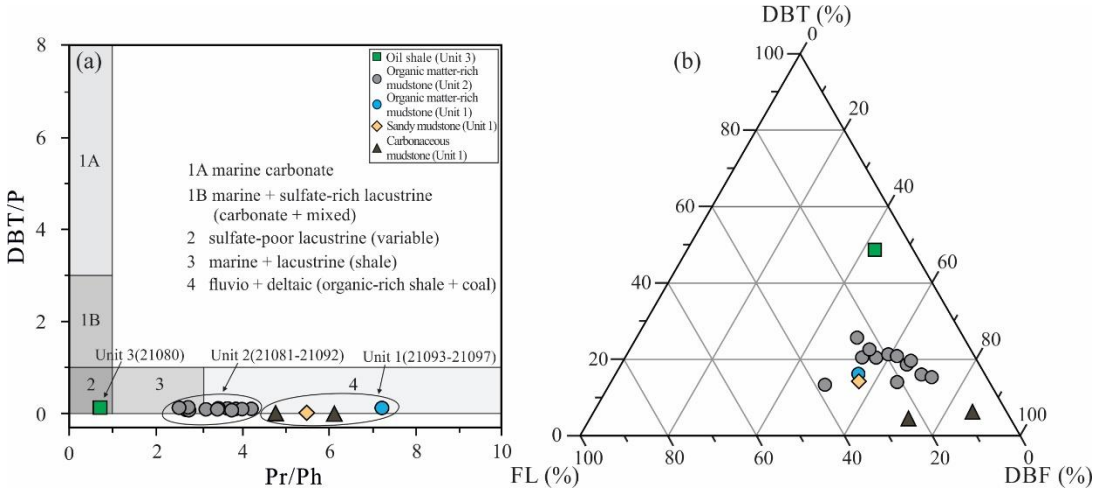

Figure 2.12 (a) Cross-plot of dibenzothiophene/phenanthrene (DBT/P) versus Pristane/Phystane (Pr/Ph) (modified after Hughes et al., 1995); (b) Ternary plot showing relative proportions of fluorene (FL), dibenzofuran (DBF), and dibenzothiophene (DBT).

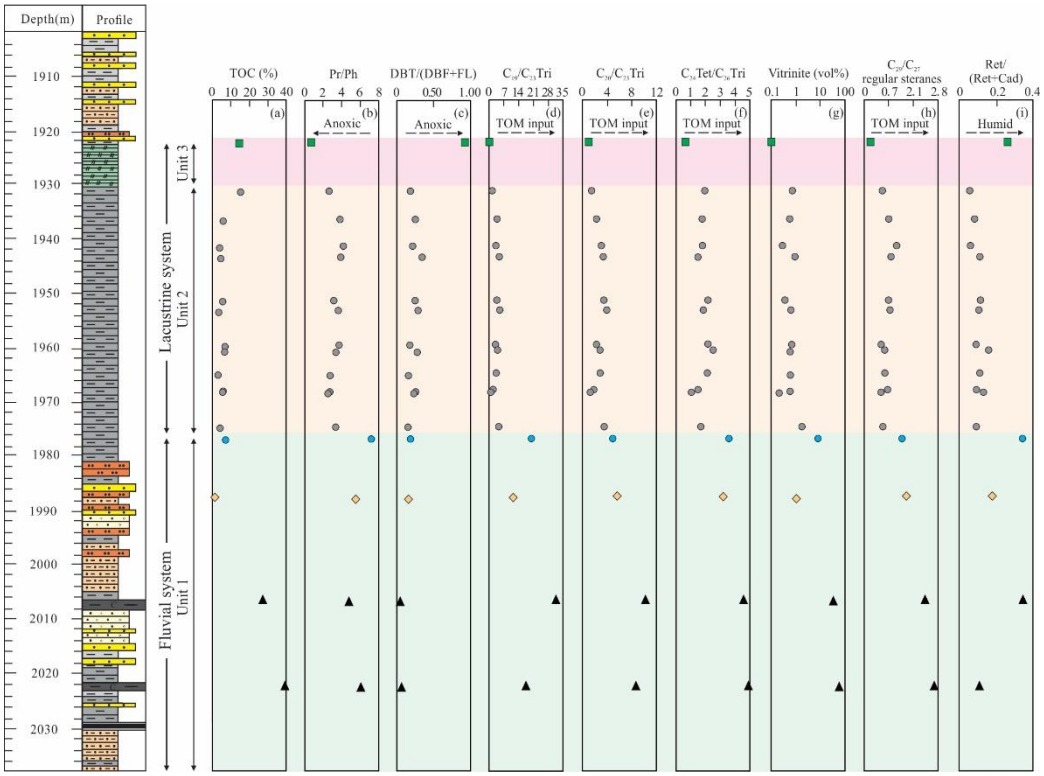

Figure 2.13 Vertical variations of major biomarker parameters and maceral composition. (a) TOC (wt%); (b) Pristane/Phystane (Pr/Ph); (c) dibenzothiophene/(dibenzofuran + fluorene) (DBT/(DBF + FL)); (d) C_{19}/C_{23} tricyclic terpane (C_{19}/C_{23} Tri); (e) C_{20}/C_{23} tricyclic terpane (C_{20}/C_{23} Tri); (f) C_{24} tetracyclic/C_{26} tricyclic terpane (C_{24} Tet/ C_{26} Tri); (g) Vitrinite content; (h) C_{27}/C_{29} steranes; (i) Retene/(retene + cadalene) (Ret/(Ret + Cad)).

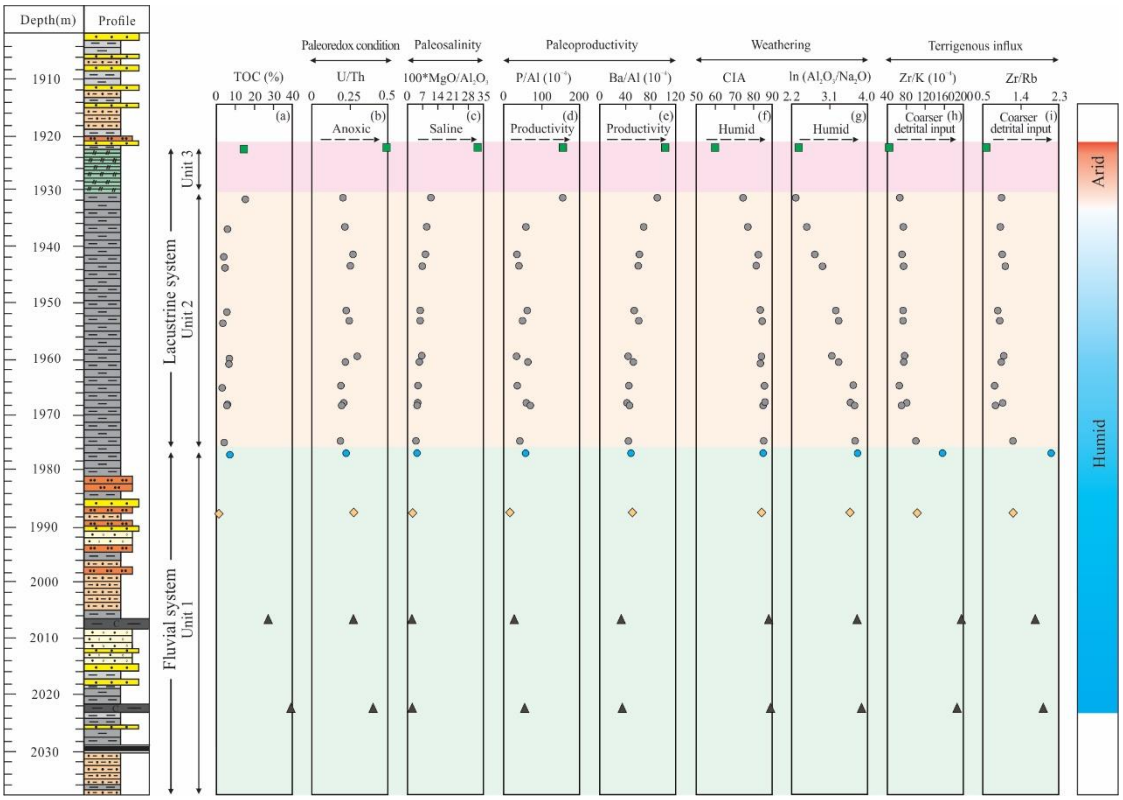

*Figure 2.14 Vertical variations of paleoredox, palaeosalinity, paleoproductivity, weathering, and terrigenous influx parameters. (a) TOC (wt%); (b) U/Th; (c) 100*MgO/Al_2O_3; (d) P/Al (10^{-4}); (e) Ba/Al (10^{-4}); (f) CIA; (g) ln (Al_2O_3/Na_2O) ; (h) Zr/K (10^{-4}); (i) Zr/Rb.*

Redox sensitive trace element ratios U/Th display a high value in sediments deposited under reducing conditions (Jones and Manning, 1994). In this study, the U/Th ratios reveal an inverse trend as compared to the stratigraphic distribution of Pr/Ph and a similar trend as DBT/(DBF+FL) along with the well profile (Figs. 2.13b and c, 2.14b). The U/Th ratios suggest that suboxic to oxic conditions prevailed during sedimentation of units 1 and 2, while unit 3 was deposited in anoxic conditions. MgO is strongly associated with marine environments, while Al_2O_3 indicates continental environments. Therefore, a high 100*MgO/Al_2O_3 ratio indicates saline condition (Xu et al., 2021). In this study, the 100*MgO/Al_2O_3 ratios show an increasing trend upward from unit 1 to unit 2 and reach the maximum value in unit 3 (Fig. 2.14c), suggesting a change in water salinity from freshwater to saline water.

2.5.3 Origin of organic matter and paleoproductivity

The tricyclic and tetracyclic terpane parameters are widely used to reflect terrigenous organic matter input (Peters et al., 2005). C_{23} Tri often occurs in crude oils derived from marine sources, while the C_{19} and C_{20} Tri are reported to be associated with terrigenous organic matter (Aquino Neto et al., 1983; Peters and Moldowan, 1993). High concentrations of C_{24} Tet commonly indicate input of terrigenous organic matter (Philp and Gilbert, 1986; George et al., 2004; Hao et al., 2011). In this study, unit 1 is characterized by the highest C_{19}/C_{23} Tri, C_{20}/C_{23} Tri and C_{24} Tet/C_{26} Tri ratios,

indicating high terrestrial organic matter input (Fig. 2.13d-f). This conclusion is consistent with the occurrence of abundant vitrinite and inertinite particles in unit 1 (Figs. 2.4a-h, 2.13g). The C_{19}/C_{23} Tri, C_{20}/C_{23} Tri and C_{24} Tet/C_{26} Tri ratios exhibit a decreasing trend upward from unit 2 to unit 3, suggesting a decline in the contribution of terrigenous organic matter (Fig. 2.13d-f). It is usually believed that C_{27} steranes derive mainly from phytoplankton and metazoans (Volkman and Maxwell, 1986), while C_{28} steranes mainly originate from diatoms, green algae, and chrysophytes (Huang and Meinschein, 1979). C_{29} steranes are typically indicative of terrigenous higher plants (Huang and Meinschein, 1979), although other origins from diatoms, red algae, and brown/green algae are possible (Idler et al., 1968; Patterson, 1971; Volkman et al., 1998). As shown in the ternary plot of C_{27}-C_{29} ααα 20R steranes, unit 1 falls in the land plants zone indicating strong terrigenous organic matter input, while the organic matter in unit 2 is derived from algae, higher land plants, and bacteria (Fig. 2.15a). This conclusion is consistent with the ratios of C_{29}/C_{27} regular steranes and cross-plot of Pr/Ph versus C_{27}/C_{29} ααα 20R steranes, in which significant terrigenous organic matter input together with an oxic environment is indicated for unit 1, while a mixed organic matter origin deposited in a sub-oxic to oxic environment are interpreted for unit 2 (Figs. 2.13h, 2.15b). Only the oil shale in unit 3 falls into the planktonic/algal zone, indicating a significant input of plankton and metazoans (Fig. 2.15). Steranes are mainly derived from eukaryotes, e.g., algae and higher plants, while hopanes originate from bacterio-hopanepolyols which exist in bacteria membranes (Huang and Meinschein, 1979; Kodner et al., 2008). Therefore, a high sterane/hopane value indicates a strong input of eukaryotic organisms. In this study, extremely low values of steranes/hopanes in unit 1, combined with high C_{19}/C_{23} Tri, C_{20}/C_{23} Tri, and C_{24} Tet/C_{26} Tri ratios, are attributed to abundant terrigenous organic matter input (Fig. 2.13d-f; Table 2.4,). Steranes/hopanes show a high value for sample 21081 at the top of unit 2 but drop to a low value in unit 3. The relatively high steranes/hopanes value for sample 21081 co-occurs with relatively low C_{19}/C_{23} Tri, C_{20}/C_{23} Tri, and C_{24} Tet/C_{26} Tri ratios and high C_{27} sterane abundances (Fig. 2.13d-f; Table 2.4), and therefore indicates a contribution from algal biomass. In contrast, the low sterane/hopane value, combined with low C_{19}/C_{23} Tri, C_{20}/C_{23} Tri, and C_{24} Tet/C_{26} Tri ratios, indicate a significant contribution from bacterial biomass in unit 3. This conclusion is consistent with Xie et al. (2021), who suggested that salinity tolerant cyanobacteria began to bloom during this period. The occurrence of monomethylalkanes (MMAs) with methyl group at position 4, 5, 6 or 7 (Fig. 2.5c) also indicates OM derived from cyanobacteria living in microbial mats (Kenig, 2000; Bauersachs et al., 2009; Pawlowska et al., 2013). The precursor of 13α(*n*-alkyl)-tricyclic terpanes is still unclear, and probably associated with some specific prokaryote or thermogenic origin from preexisting triterpenoids (Fig. 2.6; Wang and Simoneit, 1995).

Aromatic hydrocarbon 1-MP is considered to derive from conifers and is dominant in type III kerogen, while 9-MP is more abundant in type II and type I kerogens (Alexander et al., 1988; Heppenheimer et al., 1992; Budzinski et al., 1995). 1,2,5-TMN is generally associated with conifers and the log ratio of 1,2,5-TMN/1,3,6-TMN is widely used to indicate contribution to the organic matter

from coniferous higher plants (Alexander et al., 1988; Strachan et al., 1988). In this study, Unit 3 and sample 21081 at the top of unit 2 show the lowest values of 1-MP/9-MP and 1,2,5-TMN/1,3,6-TMN, indicating a reduction in the flux of terrigenous organic matter into the lacustrine systems (Table 2.5). Ret, Cad, Sim, Tet, and ip-iHMN are present in relatively small concentrations (Fig. 2.7). Ret is widely considered to derive from bioditerpenoids synthesized by conifers (Simoneit, 1985; Hautevelle et al., 2006), although it may originate from algal and bacterial resources (Wen et al., 2000). Cad is derived from cadinenes and cadinols, which exist widely in vascular resins, while algae (van Aarssen et al., 2000), bryophytes, and fungi are suggested to be the possible origin (Bordoloi et al., 1989). Sim and Tet are associated with conifers (Simoneit, 1977; Hautevelle et al., 2006). Ip-iHMN is possibly associated with vascular plant (Ellis et al., 1996).

PAHs with ≥4 rings, including Fla, Py, BaA, Ch, InPy, and BghiP are widely regarded as combustion markers and are present in all the selected samples (Grimalt et al., 2004; Lima et al., 2005; Yunker et al., 2011; Huang et al., 2015; Xu et al., 2019a). The PAHs ratios of Fla/(Fla + Py), BaA/(BaA + Chy), and InPy/(InPy + BghiP) can be used as indices to assess the relative contributions of combustion-derived versus petrogenic-derived organic matter in source rocks (Grice et al., 2007; Zakir Hossain et al., 2013; Yunker et al., 2015; Xu et al., 2019a). Ratios of Fla/(Fla + Py) < 0.4, BaA/(BaA + Chy) < 0.2, and InPy/(InPy + BghiP) < 0.2 are regarded as typical of petrogenic sources, while Fla/(Fla + Py) > 0.5, BaA/(BaA + Chy) > 0.35, and InPy/(InPy + BghiP) > 0.5 are typical of combustion-related sources. In this study, unit 1 is characterized the highest Fla/(Fla + Py) (avg. 0.62), BaA/(BaA + Chy) (avg. 0.48), and InPy/(InPy + BghiP) (avg. 0.43) values, indicating a dominant combustion source for the PAHs (wildfires), while unit 2 shows the moderate values, with the average contents of 0.59, 0.34, and 0.27, respectively, suggesting a mixture of petrogenic and combustion source. These three parameters show the lowest values in unit 3 (Table 2.5).

Primary productivity is a crucial factor that controls the enrichment of organic matter in sediments. Major element P is an essential nutrient for organism growth and biological metabolism and is widely used to reflect planktonic primary productivity (Tribovillard et al., 2006; Ross and Bustin, 2009). Similarly, trace element Ba can be incorporated by phytoplankton, and subsequently precipitated as barite during the decay of organic matter (Liao et al., 2019). By eliminating the influence of terrigenous clastic materials, P/Al and Ba/Al ratios were selected as indicators of paleoproductivity (Dean et al., 1997; Gonneea and Paytan, 2006; Tribovillard et al., 2006; Ross and Bustin, 2009). In the late Middle Jurassic sequence studied, both P/Al and Ba/Al ratios increase upward and show the highest values in unit 3, indicating increasing paleoproductivity from unit 1 to unit 3 (Fig. 2.14d and e). This conclusion is consistent with the presence of abundant lamalginite and telalginite in units 2 and 3 (Fig. 2.4j, l, p). The occurence of β-carotane and γ-carotane in unit 3 may be associated with cyanobacterial blooms, which are regarded as the most likely precursor of β-carotane and γ-carotane; they are commonly enriched in evaporitic and carbonate-rich sediments (Fig. 2.5c; Ding et al., 2020; Xie et al., 2021).

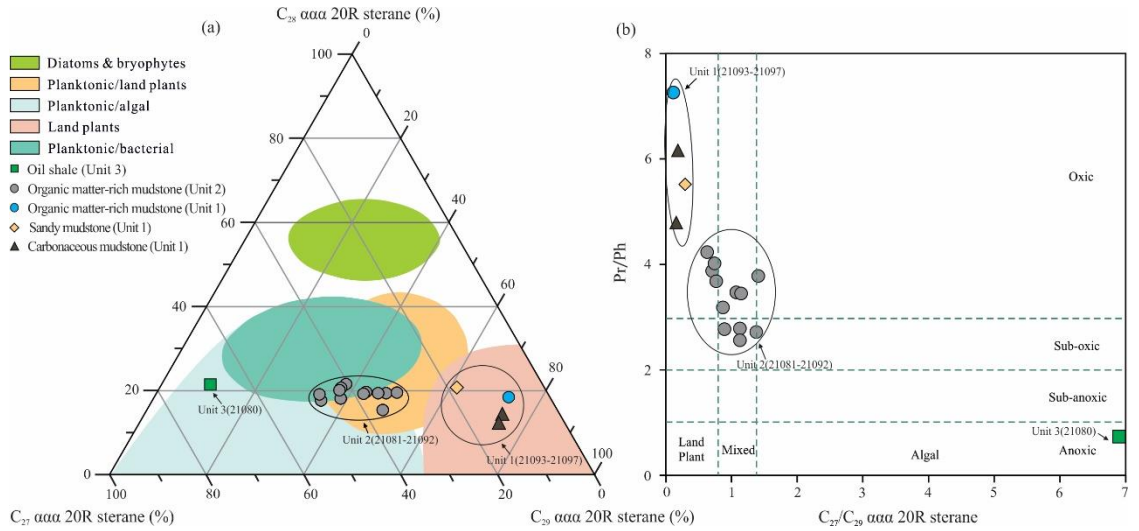

Figure 2.15 Ternary plot showing the distribution of C_{27}, C_{28}, and C_{29} ααα 20R steranes (modified after Huang and Meinschein, 1979); (b) Cross-plot of the C_{27}/C_{29} ααα 20R sterane versus the pristane/phytane (Pr/Ph) (modified after Gorter, 2001).

2.5.4 Paleoclimate, weathering, and terrigenous influx

Climate is the crucial factor controlling physical/chemical weathering intensity at the source area and further influencing the terrigenous detrital flux to the depositional site. Strong weathering intensity is caused by moist environments and rising temperatures, while weathering intensity is weak in arid and cold climates (Nesbitt, 2003; Wang et al., 2020). In this study, paleoclimate was reconstructed by multiple biomarkers and elemental proxies. The CIA is widely used to reflect the chemical weathering intensity of sediments and also evaluate variations in paleoclimate (Nesbitt and Young, 1982; Wang et al., 2020; Xie et al., 2021). Low CIA value is explained as weak weathering under an arid climate, while a high CIA value indicates strong weathering under a warm and humid tropical climate (Nesbitt and Young, 1982; Goldberg and Humayun, 2010; Wang et al., 2020). As shown in Fig. 2.14f, the stratigraphic profile of CIA values exhibits a descending trend upward, suggesting gradual aridification. Unit 1 and samples from the bottom of unit 2 are characterized by high CIA values, indicating the carbonaceous mudstone, sandy mudstone, and part of organic matter-rich mudstone were deposited under humid and warm conditions. By contrast, the lower CIA values of samples from the top of unit 2 and unit 3 suggest a more arid climate during the deposition of part of the organic matter-rich mudstone and oil shale units. The ratio of $\ln(Al_2O_3/Na_2O)$ is widely used to indicate the degree of chemical weathering conditions (Montero-Serrano et al., 2015; Cichon-Pupienis et al., 2021). It exhibits similar stratigraphic variations as CIA values that display decreasing trends from unit 1 to unit 3, indicating weaker weathering conditions and a transition from humid to arid climate upward (Fig. 2.14g). A predominance of Ret is generally associated with hot and humid conditions, while Cad shows a high abundance in land plants that grow in an arid climate (van Aarssen et al.,

2000; Cesar and Grice, 2019; Zakrzewski et al., 2020). Therefore, the Ret/(Ret + Cad) ratio is applied as a proxy of climatic variation (van Aarssen et al., 2000; Hautevelle et al., 2006; Cesar and Grice, 2019; Jiang et al., 2019; Zakrzewski et al., 2020). As shown in Fig. 2.13i, Ret/(Ret + Cad) ratios decrease from unit 1 to unit 2, indicating a more arid climate. However, the remarkable increase of Ret/(Ret + Cad) ratio in unit 3 might be explained by the contribution of bacterial to the organic matter because bacterial biomass is a possible source of Ret (Wen et al., 2000).

The high content of carbonate minerals in unit 3 may be attributed to the evaporation of lakes in an arid climates (Warren, 2016; Xie et al., 2021). Overall, unit 1was deposited under a warm and humid climate, but the climate transitioned into more arid conditions during the deposition of units 2 and 3. Jian et al. (2013) suggested that a warm and humid climate prevailed during the Early-Middle Jurassic which might be associated with strong monsoonal circulation and global warming due to an increased atmospheric CO_2 content. The climatic transition from humid to arid starting in the late Middle Jurassic was probably attributed to changes in global atmospheric circulation patterns in response to the breakup of Pangea and the orogenic rejuvenation of the Qilian Mountains (Jian et al., 2013). Ritts and Biffi (2001) and Jian et al. (2013) suggested that the uplift of the Qilian Mountains produced a rain shadow, which further gave rise to arid conditions.

Zr is an inert element that mainly resides in coarse silt or the very fine-grained sand fraction in siliciclastic sediments and almost only exists in zircons (Fralick and Kronberg, 1997; Bábek et al., 2016). Rb and K are mainly enriched in fine-grained siliciclastic fractions, especially in clay minerals (Kalugin et al., 2007; Clift et al., 2008; Bábek et al., 2016; Xu et al., 2021). Zr/Rb and Zr/K ratios, therefore, can be used to indicate detrital influx, with higher ratios corresponding to coarser detrital input (Dypvik and Harris, 2001; Bábek et al., 2016; Bom et al., 2021; Cichon-Pupienis et al., 2021). As the average grain size of sediments is associated with water depth, a decline in the Zr/Rb and Zr/K ratios generally indicates increasing water depth (Cao et al., 2020). In this study, the Zr/Rb and Zr/K ratios show a declining trend from unit 1 to unit 3, reflecting decreasing terrigenous detrital input and finer grain size due to the aridification and weaker weathering strength (Fig. 2.14h and i). Furthermore, the abrupt decrease of Zr/Rb and Zr/K ratios from unit 1 to unit 2 also indicates a rapidly increasing water depth during the transition from fluvial to lacustrine environment (Fig. 2.14h and i).

2.5.5 Mechanisms of organic matter accumulation in the J_2d^7

The accumulation of organic matter in continental shales is controlled by multiple factors, among which the primary factors are climate, palaeoproductivity, and redox conditions (Fig. 2.16; Tyson, 2001, 2005; Algeo et al., 2013; Wang et al., 2021; Xie et al., 2021).

The carbonaceous mudstone interbedded with sandstone and sandy mudstone in unit 1 is derived from fluvial deposition (Qin et al., 2018; Wang et al., 2021), which took place under warm and humid climate conditions coupled to a high degree of weathering in the hinterland. The shallow water column

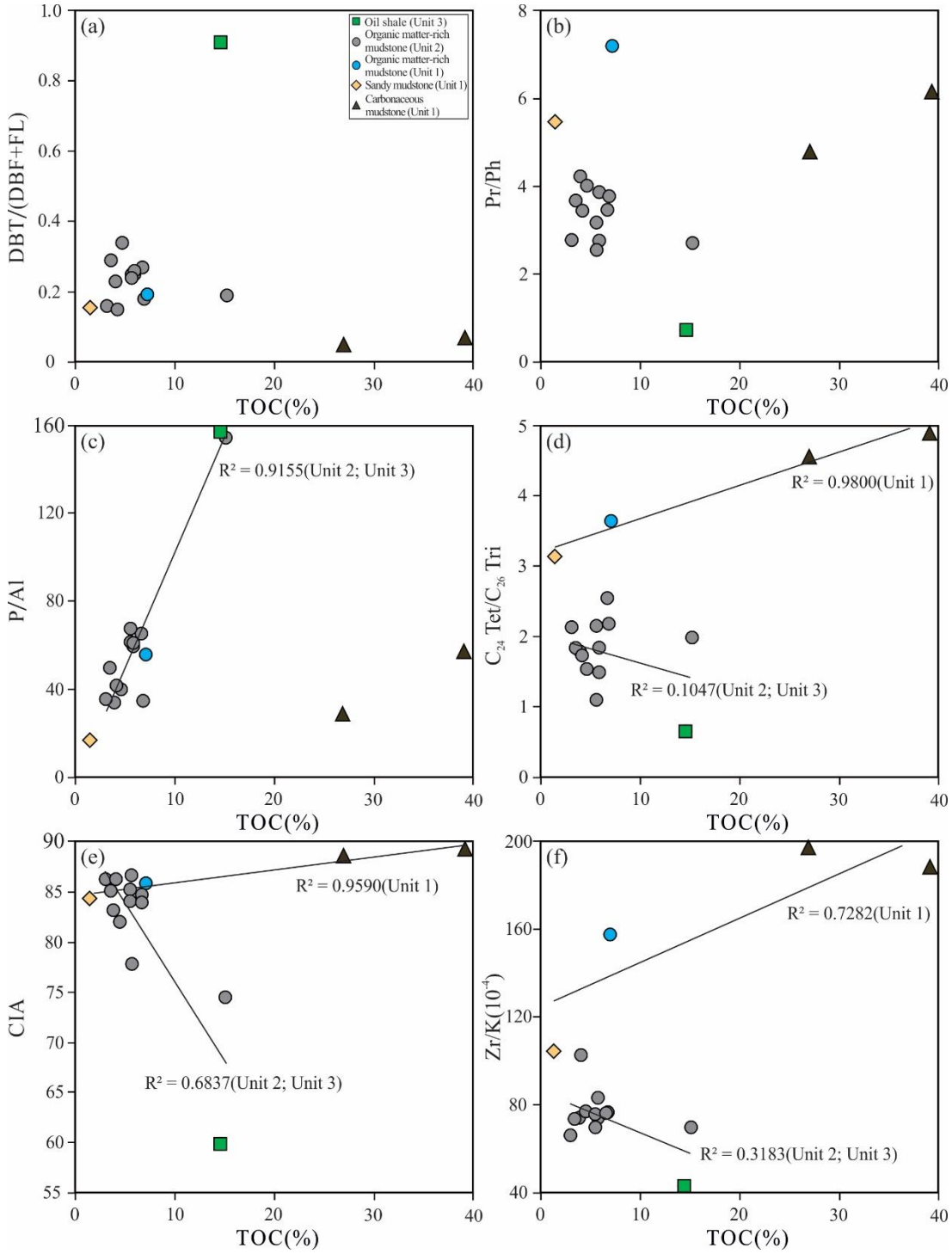

Figure 2.16 Cross-plot of (a) dibenzothiophene/(dibenzofuran + fluorene) (DBT/(DBF + FL)) versus TOC; (b) pristane/phytane (Pr/Ph) versus TOC; (c) P/Al versus TOC; (d) C_{24} tetracyclic/C_{26} tricyclic terpane (C_{24} Tet/C_{26} Tri) versus TOC; (e) CIA versus TOC; (f) Zr/K versus TOC.

resulted in oxic bottom water conditions, which is generally regarded as an adverse factor for the preservation of organic matter due to oxidative decomposition. Accordingly, vitrinite and inertinite that are less sensitive to weathering are the dominant macerals in unit 1. The warm and humid climate

is a favor to the growth of terrigenous higher plants. Meanwhile, the strong weathering leads to abundant terrestrial organic matter debris together with the terrigenous clastics being transported to the depositional site. This process results in the positive correlations between TOC contents and proxies of terrigenous organic matter input (C_{24} Tet/C_{26} Tri), weathering intensity (CIA), and terrigenous influx (Zr/K) in unit 1 (Fig. 2.16d-f). The organic matter-rich mudstone and oil shale in units 2 and 3 were deposited in a gradually deepened lacustrine system. Under moderately warm-humid paleoclimate, the organic matter-rich mudstone in unit 2 was deposited in suboxic-oxic and freshwater conditions with moderate organic terrigenous debris input. The increasing of P/Al and Ba/Al ratios and gradually pervasive presence of alginite upward indicate a moderate to short-term high paleoproductivity in unit 2, which is characterized by mixed organic matter composed of terrestrial higher plants and algal biomass. Due to the subsequent aridification of climate, freshwater supply to the Yuqia Lake Basin declined, resulting in lake salinization and stratification of the water column (Wang et al., 2021; Xie et al., 2021). As a result, the oil shale in unit 3 was deposited in anoxic and highly saline conditions with a low terrigenous influx. The high P/Al and Ba/Al ratios indicate elevated paleoproductivity, which may be ascribed to halophilic algal and cyanobacteria blooms (Wang et al., 2021; Xie et al., 2021). As shown in Fig. 2.16a and b, there is no correlation between the TOC contents and the DBT/(DBF+FL) and Pr/Ph ratios, suggesting that redox conditions are not the controlling factor for the accumulation of organic matter in lacustrine source rocks. In contrast, the TOC contents of units 2 and 3 display a positive correlation with P/Al ratios, indicating that paleoproductivity exerts a profound impact on the organic matter enrichment (Fig. 2.16c). Terrigenous organic matter input (C_{24} Tet/C_{26} Tri), weathering intensity (CIA), and terrigenous influx (Zr/K) proxies were negatively correlated with TOC contents of units 2 and 3, which may be attributed to adverse dilution effect on organic matter accumulation by detrital input (Fig. 2.16d-f; Tyson, 2001; Sageman et al., 2003).

2.6 Conclusions

This study presents a large set of new data on elemental carbon and sulfur content, Rock-Eval pyrolysis, organic petrography, as well as organic and inorganic geochemistry on the J_2d^7 of the northern Qaidam Basin. The following conclusions concerning maturity and origin of organic matter, depositional environments, paleoclimate conditions, and organic matter accumulation mechanisms are drawn:

1) Source rocks from J_2d^7 are generally rich in organic matter and thermally immature to early mature with TOC contents and VR_r ranging from 1.5–39.2% and 0.35–0.57%, respectively. Based on multiple geochemical proxies, three units were identified in the J_2d^7 from bottom to top, which were deposited in fluvial, freshwater lacustrine, and saline lacustrine environments, respectively.

2) Unit 1 having high Pr/Ph (4.79−7.25), low Gam index (0.02−0.03) and high CIA values (84.35−89.23) was deposited in an oxic environment under warm and humid climatic and strong weathering conditions. Affected by the aforementioned factors, abundant terrigenous clastics were

transported to the depositional site. Units 2 (Pr/Ph: 2.56−4.23; Gam index: 0.03−0.14) and 3 (Pr/Ph: 0.73; Gam index: 0.48) were deposited in sub-oxic to oxic freshwater and anoxic saline environments, respectively. Progressive aridification during the deposition of units 2 and 3 are reflected by decreasing CIA values (59.97−86.68) resulting in weakened weathering intensity and lower terrigenous influx.

3) Organic matter in unit 1 with high proportions of C_{29} ααα 20R steranes (61−74%) is primarily sourced from terrigenous higher plants, while a mixture of terrestrial higher plant and algal biomass was the main source of organic matter in unit 2. The latter unit is characterized by moderate C_{19}/C_{23} Tri (0.96–5.44), C_{20}/C_{23} Tri (1.28–3.87) and C_{24} Tet/C_{26} Tri (1.10–2.54) ratios. Unit 3 with the lowest C_{19}/C_{23} Tri (0.25), C_{20}/C_{23} Tri (0.95), and C_{24} Tet/C_{26} Tri (0.65) ratios and highest proportions of C_{27} ααα 20R steranes (69%) is characterized by a decrease in terrigenous organic matter content. The dominant source of organic matter is lake plankton, including halophilic algae and cyanobacteria.

4) Organic matter accumulation in unit 1 is related to a warm and humid climate, strong weathering intensity, and terrigenous organic matter input. Primary productivity is the most critical factor controlling the enrichment of organic matter in units 2 and 3.

Table 2.7 Identification of terpanes, steranes, and aromatic compounds in Figs. 2.5 and 2.7.

Compound group	Peak	Abbreviation	Biomarker	*m/z*
Terpanes	A	C_{19} Tri	C_{19}-tricyclic terpane	191
	B	C_{20} Tri	C_{20}-tricyclic terpane	
	C	C_{21} Tri	C_{21}-tricyclic terpane	
	D	C_{22} Tri	C_{22}-tricyclic terpane	
	E	C_{23} Tri	C_{23}-tricyclic terpane	
	F	C_{24} Tri	C_{24}-tricyclic terpane	
	G	C_{25} Tri	C_{25}-tricyclic terpane	
	H	C_{24} Tet	C_{24}-tetracylic terpane	
	I	C_{26} Tri R	C_{26}-R tricyclic terpane	
		C_{26} Tri S	C_{26}-S tricyclic terpane	
Hopanes	J	Ts	C_{27}-18α(H)-22,29,30-trisnorneohopane	
	K	Tm	C_{27}-17α(H)-22,29,30-trisnorhopane	
	L	C_{27} β	C_{27}-17β(H)-22,29,30-trisnorhopane	
	M	C_{29} H	C_{29}-17α(H),21β(H)-norhopane	
	N	C_{29} Ts	C_{29}-18α(H)-30-norneohopane	
	O	C_{29} M	C_{29}-17β(H),21α(H)-30-normoretane	
	P	C_{30} H	C_{30}-17α(H),21β(H)-hopane	
	Q	C_{30} M	C_{30}-17β(H),21α(H)-moretane	
	R	C_{31} H S	C_{31}-17α(H),21β(H),22S-homohopane	
		C_{31} H R	C_{31}-17α(H),21β(H),22R-homohopane	
	S	Gam	Gammacerane	
	T	C_{32} H S	C_{32}-17α(H),21β(H),22S-homohopane	
		C_{32} H R	C_{32}-17α(H),21β(H),22R-homohopane	
	U	C_{33} H S	C_{33}-17α(H),21β(H),22S-homohopane	
		C_{33} H R	C_{33}-17α(H),21β(H),22R-homohopane	
	V	C_{34} H S	C_{34}-17α(H),21β(H),22S-homohopane	
		C_{34} H R	C_{34}-17α(H),21β(H),22R-homohopane	
	W	C_{35} H S	C_{35}-17α(H),21β(H),22S-homohopane	
		C_{35} H R	C_{35}-17α(H),21β(H),22R-homohopane	
Steranes	a	pregnane	5α,14β,17β(H)-pregnane (diginane)	217
	b	homopregnane	5α,14β,17β(H)-homopregnane (20-methyldiginane)	
	c	C_{27} βα dia20S	20S-13β(H),17α(H)-diacholestane	
	d	C_{27} βα dia20R	20R-13β(H),17α(H)-diacholestane	
	e	C_{27} ααα 20S	20S-5α(H),14α(H),17α(H)-cholestane	
	f	C_{27} αββ 20R + C_{29}dβα20S	20R-5α(H),14β(H),17β(H)-cholestane +13β,17α,20S-diastigmastane	
	g	C_{27} αββ 20S	20S-5α(H),14β(H),17β(H)-cholestane	
	h	C_{27} ααα 20R	20R-5α(H),14α(H),17α(H)-cholestane	
	i	C_{28} ααα 20S	20S-24-Methyl-5α(H),14α(H),17α(H)-cholestane	
	j	C_{28} αββ 20R	20R-24-Methyl-5α(H),14β(H),17β(H)-cholestane	
	k	C_{28} αββ 20S	20S-24-Methyl-5α(H),14β(H),17β(H)-cholestane	
	l	C_{28} ααα 20R	20R-24-Methyl-5a(H),14a(H),17a(H)-cholestane	
	m	C_{29} ααα 20S	20S-24-Ethyl-5α(H),14α(H),17α(H)-cholestane	
	n	C_{29} αββ 20R	20R-24-Ethyl-5α(H),14β(H),17β(H)-cholestane	
	o	C_{29} αββ 20S	20S-24-Ethyl-5α(H),14β(H),17β(H)-cholestane	
	p	C_{29} ααα 20R	20R-24-Ethyl-5α(H),14α(H),17α(H)-cholestane	
Aromatic hydrocarbons	1	DBF	dibenzofuran	168
	2	1,3,7-TMN	1,3,7-trimethylnaphthalene	170
	3	1,3,6-TMN	1,3,6-trimethylnaphthalene	
	4	1,4,6- + 1,3,5-TMN	1,4,6- + 1,3,5-trimethylnaphthalene	
	5	2,3,6-TMN	2,3,6-trimethylnaphthalene	
	6	1,2,7- + 1,6,7-TMN	1,2,7- + 1,6,7-trimethylnaphthalene	
	7	1,2,6-TMN	1,2,6-trimethylnaphthalene	
	8	1,2,4-TMN	1,2,4-trimethylnaphthalene	
	9	1,2,5-TMN	1,2,5-trimethylnaphthalene	
	10	FL	fluorene	166
	11	1,3,5,7-TeMN	1,3,5,7-tetramethylnaphthalene	184
	12	1,3,6,7-TeMN	1,3,6,7-tetramethylnaphthalene	
	13	1,4,6,7- + 1,2,4,6- + 1,2,4,7-TeMN	1,4,6,7- + 1,2,4,6- + 1,2,4,7-tetramethylnaphthalene	
	14	1,2,5,7- + 1,3,6,8-TeMN	1,2,5,7- + 1,3,6,8-tetramethylnaphthalene	
	15	2,3,6,7-TeMN	2,3,6,7-tetramethylnaphthalene	
	16	1,2,6,7-TeMN	1,2,6,7-tetramethylnaphthalene	
	17	1,2,3,7-TeMN	1,2,3,7-tetramethylnaphthalene	

Continued

18	1,2,3,6-TeMN	1,2,3,6-tetramethylnaphthalene	
19	1,2,5,6- + 1,2,3,5-TeMN	1,2,5,6- + 1,2,3,5-tetramethylnaphthalene	
20	DBT	dibenzothiophene	
21	Cad	cadalene	183
22	P	phenanthrene	178
23	3-MP	3-methylphenanthrene	192
24	2-MP	2-methylphenanthrene	
25	9-MP	9-methylphenanthrene	
26	1-MP	1-methylphenanthrene	
27	Tet	tetrahydroretene	223
28	ip-iHMN	6-isopropyl-1-isohexyl-2-methylnaphthalene	197
29	Sim	simonellite	237
30	Ret	retene	219

3 Geochemistry and petrology of petroleum source rocks in the Upper Cretaceous Qingshankou Formation, Songliao Basin, NE China

Keywords: Upper Cretaceous; Molecular organic geochemistry; Organic petrology; Major and trace elements; Organic matter accumulation; Songliao Basin

Abstract

The Upper Cretaceous Qingshankou Formation in the Songliao Basin, NE China is known to contain excellent petroleum source rocks. In addition, it serves as a valuable record to study depositional conditions within the water column and climatic change. In this study, a large set of organic petrography, major and trace element geochemistry, as well as bulk and molecular organic geochemistry data obtained on 38 core samples of the first member of the Qingshankou Formation (K_2qn^1) in the south central depression is reported. All rocks are thermally oil-mature, reaching the early to peak oil generation stage, indicated by the vitrinite reflectance (VR_r) of approximately 0.8%. Two different types of lacustrine source rocks (units I and II) and two OM-rich layers within unit I are identified in the studied well. Basically, there is a lower unit 1, characterized by lower organic carbon (TOC) content and an upper unit 2 characterized by higher TOC content. Furthermore, within unit 1, thin marine transgressive layers of approximately 1-2 meters were identified. Generally, unit 1 is characterized by the lowest TOC and sulfur contents with average values of 1.31 wt% and 0.56 wt%, respectively. By contrast, unit 2 samples have significantly higher TOC (avg. 2.39 wt%) and sulfur contents (avg. 1.24 wt%). Samples, which represent the postulated marine transgressive events show the highest TOC (avg. 2.82 wt%) and sulfur contents (avg. 2.01 wt%). Unit 1 was mainly deposited in oxic-dysoxic and freshwater-brackish water column conditions based on multiple organic and inorganic geochemical proxies. By contrast, unit 2 and marine transgressive layers were deposited in less oxygenated and more saline environments. Source rocks from the K_2qn^1 generally show only minor terrestrial organic matter input. However, unit 1, containing type II-III kerogen, shows indications for a slightly more pronounced contribution from terrigenous higher plants than unit 2 and the marine transgressive layers, where the kerogen is almost exclusively derived from planktonic/algal and microbial organic matter. The low TOC content in unit 1 is attributed to multiple adverse factors for organic matter accumulation, including a relatively shallow, oxic-dysoxic, and weakly stratified water column and high dilution by terrigenous mineral matter. By contrast, more favorable conditions persisted during the deposition of marine transgressive layers and unit 2, e.g., a more reducing and stratified water column and lower dilution by terrigenous mineral matter.

3.1 Introduction

As the largest continental petroliferous basin in China, the Songliao Basin is characterized by Cretaceous sediments with a thickness of approximately 7000 m (Jia et al., 2013; Zhao et al., 2020; Zhang et al., 2022). Among these sediments, the organic matter (OM)-rich Qingshankou and the Nenjiang Formations are regarded as major petroleum source rocks and represent research hotspots and exploration targets since the discovery of the Daqing oilfield in the 1950s (Zhou and Littke, 1999; Feng et al., 2010; Wang et al., 2013a; Xu et al., 2019b; Zhang et al., 2022). Besides the economic value, the lacustrine sediments throughout almost the whole Cretaceous section act as a detailed record of paleo-climatic change and paleo-environmental evolution (Bechtel et al., 2012; Wang et al., 2013a). The Qingshankou and Nenjiang formations represent excellent source rocks and are generally suggested to be associated with high paleo-bioproductivity reflected by the occurrence of various aquatic organisms (e.g., dinoflagellates, green algae, botryococcus) and a stratified water column of the paleo-lake (Bechtel et al., 2012; Zhang et al., 2022). The Qingshankou Formation is generally divided into three members based on lithology and biological assemblages (Feng et al., 2010; Huang et al., 2013; Cao et al., 2021). As the major source rock, the first member of the Qingshankou Formation (K_2qn^1) was deposited during a period of large-scale lake expansion when the lake had its maximum depth and covered the largest area of 87,000 km^2 (Feng et al., 2010). Deep lacustrine fine-grained siliciclastic rocks with a thickness of 60–100 m in the K_2qn^1 are characterized by high total organic carbon (TOC) content and a wide distribution across the entire central depression (Fig. 3.1a; Liu et al. 2019). By contrast, the second and third members of the Qingshankou Formation mainly consist of large deltaic systems with deep-water lacustrine shale of 200–300 m thickness, which is attributed to the decreasing lacustrine strata area of 41,000 km^2 (Feng et al., 2010).

Compared to marine settings, lacustrine sediments are generally deposited in a more complex environment and are more susceptible to terrestrial influx. Paleo-climate changes and fluctuations of paleo-lake level can result in unstable water column conditions and variations of preservation conditions and, thus, control OM accumulation. Previous studies suggested that the formation of source rocks in the K_2qn^1 is closely related to marine incursion events (Hou et al., 2000; Huang et al., 2013; Hu et al., 2015; Xu et al., 2019b). Hou et al. (2000) observed abundant C_{30} 4-desmethylsteranes (24-*n*-propylcholestanes) derived from marine alga *Sarcinochrysidales* in the K_2qn^1 and proposed that the Songliao paleo-lake was connected to the East Asiatic Ocean during the Late Cretaceous and thus marine transgressional events periodically occurred in the gigantic freshwater paleo-lake. Hu et al. (2015) detected in few samples in the lower part of the Qingshankou Formation significant peaks of marine-origin C_{30} steranes and explained this phenomenon as marine organic input owing to seawater incursion. However, the reported concentrations of the above-mentioned biomarkers are low and they are absent in layers above, suggesting that the seawater incursion was not continuous. In addition, the high TOC content of the corresponding sediments was attributed to the high bio-productivity during the marine transgression. Xu et al. (2019b) proposed a high-resolution model of OM accumulation in

the K_2qn^1, which suggests that marine ingression during the deposition of the K_2qn^1 lower part may have influenced bottom water salinity and redox conditions providing favorable conditions for the preservation of OM. Zhang et al. (2022) suggested that seawater ingression from the southeastern uplift and a relatively high lake level occurred during the deposition of the lowermost member of the Qingshankou Formation. However, Jones et al. (2018) argued that there is no persuasive evidence for the existence of marine incursions during the deposition of K_2qn^1 based on osmium ratios ($^{187}Os/^{188}Os$). The authors suggested that lake stratification associated with strong temperature and/or salinity gradients and OM remineralization resulted in anoxic bottom water conditions favorable for the enrichment of OM in the K_2qn^1. Cao et al. (2021) stated that the osmium data could be influenced by the neutralization of nonradiogenic Osi signals of marine flux by radiogenic river input in the climatically sensitive lake system. The authors observed a significant $\delta^{34}S$ negative excursion in the basal K_2qn^1 and explained it as a result of intense sulfate isotope fractionation by microbial sulfate reduction owing to high sulfate contents in the paleo-lake during marine transgression. Therefore, the existence of marine incursion events during the deposition of K_2qn^1 remains controversial.

Although there are many publications on the Qingshankou Formation (e.g., Jia et al., 2013; Wang et al., 2013c; Xu et al., 2015, 2019b; Liu et al., 2017a; Zhu et al., 2017; Liu et al., 2019; Zhang et al., 2021a), previous studies primarily focus on the wells situated closer to the central part of the central depression (e.g., Xu et al., 2015, 2019b; Zhang et al., 2022) or in the Qijia-Gulong sag located in the western part of the central depression (e.g., Zhu et al., 2017; Liu et al., 2019), whereas locations proximal to the southwest depression margin have not received much attention so far. In addition, investigations on organic and elemental geochemical characterization are still scant, especially for the wells located in the southern part of the central depression (Fig. 3.1a), although thermal maturity is low there and thus favorable for detailed paleo-environmental research. Additionally, previous studies generally applied a single approach, e.g., solely organic geochemical (Bechtel et al., 2012; Zhang et al., 2022) or inorganic geochemical (Xu et al., 2015) analysis, for reconstructing the paleo-depositional environment prevailing during deposition of the K_2qn^1. However, this approach may lead to inaccurate evaluations of the target source rocks due to the possible influence of factors such as thermal maturity and detrital siliciclastic flux or trace-element mobility during diagenesis on the precision of biomarker and trace-metal proxies, respectively (Peters et al., 2005; Tribovillard et al., 2006). Owing to the wide distribution of the Qingshankou Formation in the Songliao Basin and the heterogeneity of lacustrine sediments, the paleo-redox conditions, water salinity, type of kerogen, origin of OM, paleo-productivity, detrital flux, and OM accumulation mechanisms of source rock deposited close to the shallow paleo-lake in the southern part of the central depression (Fig. 3.1b) need in-depth investigations based on both organic and inorganic geochemistry data. Some major and trace-element geochemical proxies,e.g., Ga/Rb, Sr/Cu, and chemical index of alteration (CIA), are widely used to evaluate the chemical weathering conditions and reconstruct paleo-climate of sedimentary basins (Roy and Roser, 2013; Jian et al., 2013; Cichon-Pupienis et al., 2021; Qiao et al., 2022; Xu et al., 2022). So

far, Wang et al. (2013a) and Zhao (2014) have applied spore and pollen data to reconstruct the paleo-climate of the Songliao Basin during the Late Cretaceous. However, only a few studies selected a small number of inorganic geochemical parameters (e.g., Fe/Mn) to indicate paleo-climatic conditions using core samples collected from the east central depression and south-eastern uplift (Jia et al., 2013; Xu et al., 2015, 2019b). A comprehensive and systematic elemental geochemical analysis of sediments can provide more robust evidence of chemical weathering history and compensate for the shortage in the study of climate change during the deposition of the K_2qn^1.

This study presents molecular organic geochemistry and major and trace element data of the K_2qn^1 in the southern part of the central depression, Songliao Basin based on 38 core samples. Organic petrography, TOC and total sulfur (TS) contents, and Rock-Eval pyrolysis data are also presented and discussed. The goals are to 1) decipher the depositional environments during deposition of the K_2qn^1 and provide detailed information on the biological origin of OM and 2) determine the thermal maturity by biomarker analysis to enhance the understanding of maturation levels of the source rocks from the southern part of the central depression, as well as (3) elucidate the key factors controlling the mechanisms of OM accumulation. Besides, this study utilizes major and trace element parameters to evaluate weathering intensity and reconstruct the paleo-climatic conditions of the Songliao Basin.

3.2 Geological setting

The Songliao Basin, with a total area of 26×10^4 km^2, is a non-marine continental rift basin superimposed on a Paleozoic basement (Feng et al., 2010; Xu et al., 2022). The basin comprises of six structural units, among which the central depression is the main oil and gas-producing area (Fig. 3.1a). Jurassic, Cretaceous, Palaeogene, and Neogene clastic sediments with a thickness of approximately ten kilometers were deposited in the center of the basin thinning towards the basin margin (Fig. 3.1c). The subduction and movement of Pacific Rim tectonic systems resulted in the formation of the Songliao Basin (Li et al., 2021a). During the Late Cretaceous, sinistral slip fault systems resulted from regional tectonic events and the high global sea level may have led to marine water influx into the gigantic Songliao paleo-lake, causing a mixture of fresh and marine waters (Hu et al., 2015). This mixing was suggested to be the possible reason for two Late Cretaceous lacustrine anoxic events and the formation of OM-rich source rocks in the Qingshankou and Nengjiang Formations (Wang et al., 2013b).

The basin experienced four tectonic stages (Feng et al., 2010). During the pre-rift stage (before 155 Ma), mantle doming led to uplift and erosion (Wang et al., 2013a). Subsequently, the Huoshiling, Shahezi, and Yingcheng Formations were deposited during the synrift stage from the Late Jurassic to the Early Cretaceous (Wang et al., 2013a). The Huoshiling Formation consists of volcanic flows and volcaniclastics intercalated with fluvial-deltaic sediments (Fig. 3.1c; Feng et al., 2010). The overlying Shahezi Formation mainly consists of lacustrine and floodplain mud- and siltstones interbedded with sandstones, while the Yingcheng Formation mainly comprises felsic volcanics. During the late Early Cretaceous and Late Cretaceous, the basin experienced down warping caused by thermal subsidence.

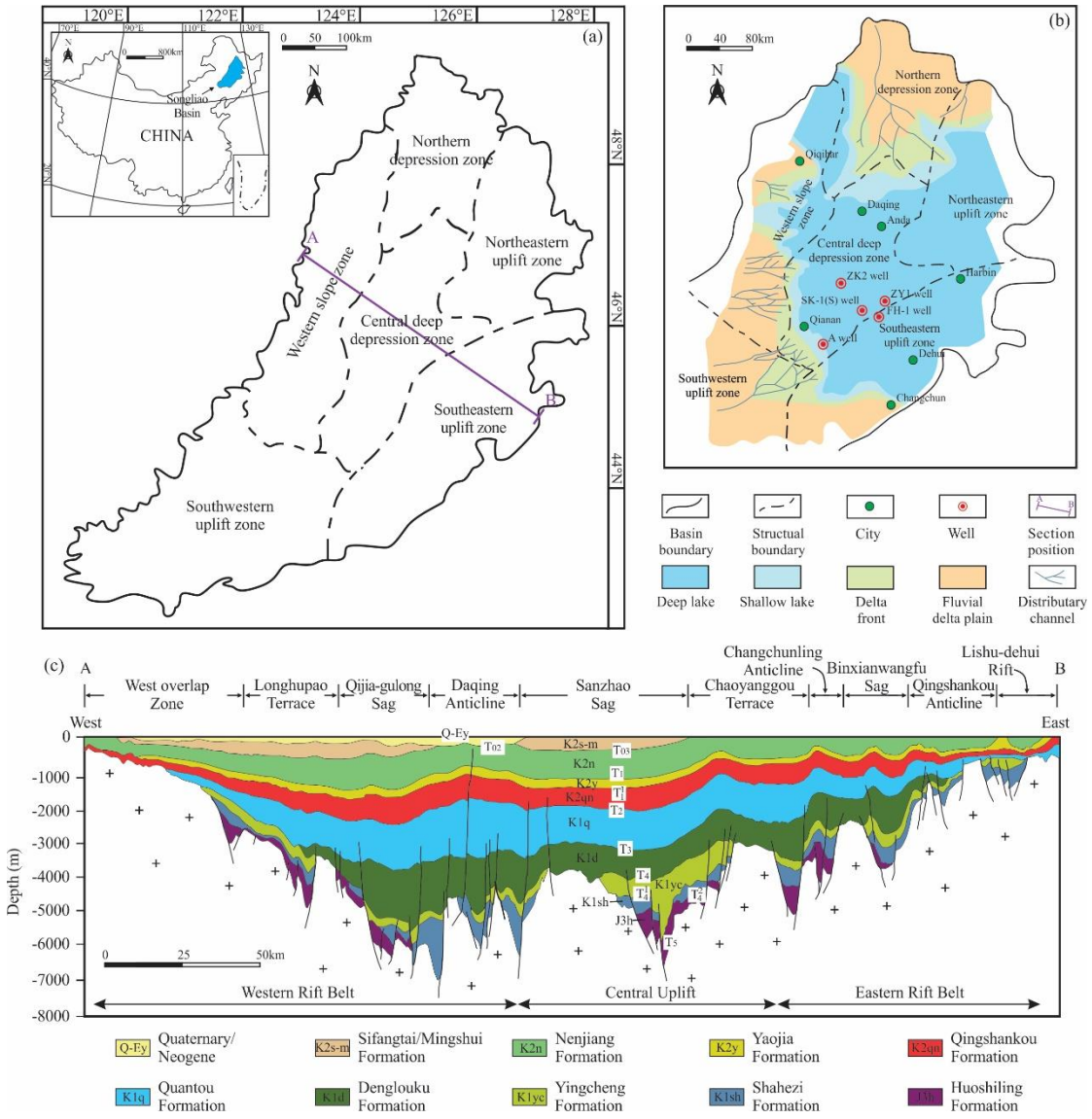

Figure 3.1 (a) Schematic map showing the location of the Songliao Basin in China and the distribution of first-order tectonic units of the Songliao Basin (modified after Gao et al., 2018). (b) Sedimentary facies map of the K_2qn^1 in the Songliao Basin (modified after Feng et al., 2010). (c) Structural cross section across the central part of the Songliao Basin (modified after Feng et al., 2010). For age information of the individual layers, see Fig. 3.2.

The most important oil-prone source rocks in the Qingshankou and Nenjiang formations were deposited during this period (Wang et al., 2013a). The Qingshankou Formation is characterized by fine-grained lacustrine mudstones and unconformably overlies the Quantou Formation that was mainly deposited in fluvial and floodplain environments (Feng et al., 2010). The lake was deepest and most extensive during the deposition of the lower part of the Qingshankou Formation but significantly shrank during the deposition of the upper unit of the Qingshankou Formation (Feng et al., 2010; Zhang et al., 2022). Similarly, the first and second members of the Nenjiang Formation are dominated by

mudstone deposited during a lacustrine transgressive phase (Feng et al., 2010; Bechtel et al., 2012; Liu et al., 2022c). The paleo-lake, with an area of 20 × 10^4 km^2, reached its maximum extent and almost covered the whole basin during the deposition of the first member of the Nenjiang Formation (Feng et al., 2010). Finally, the basin experienced regional compression during deposition of the uppermost Sifangtai and Mingshui formations (Fig. 3.1c). These two formations exist in the central and western area of the basin and mainly consist of sandstone, siltstone, and shale deposited in fluvial, deltaic, and shallow lacustrine environments (Feng et al., 2010).

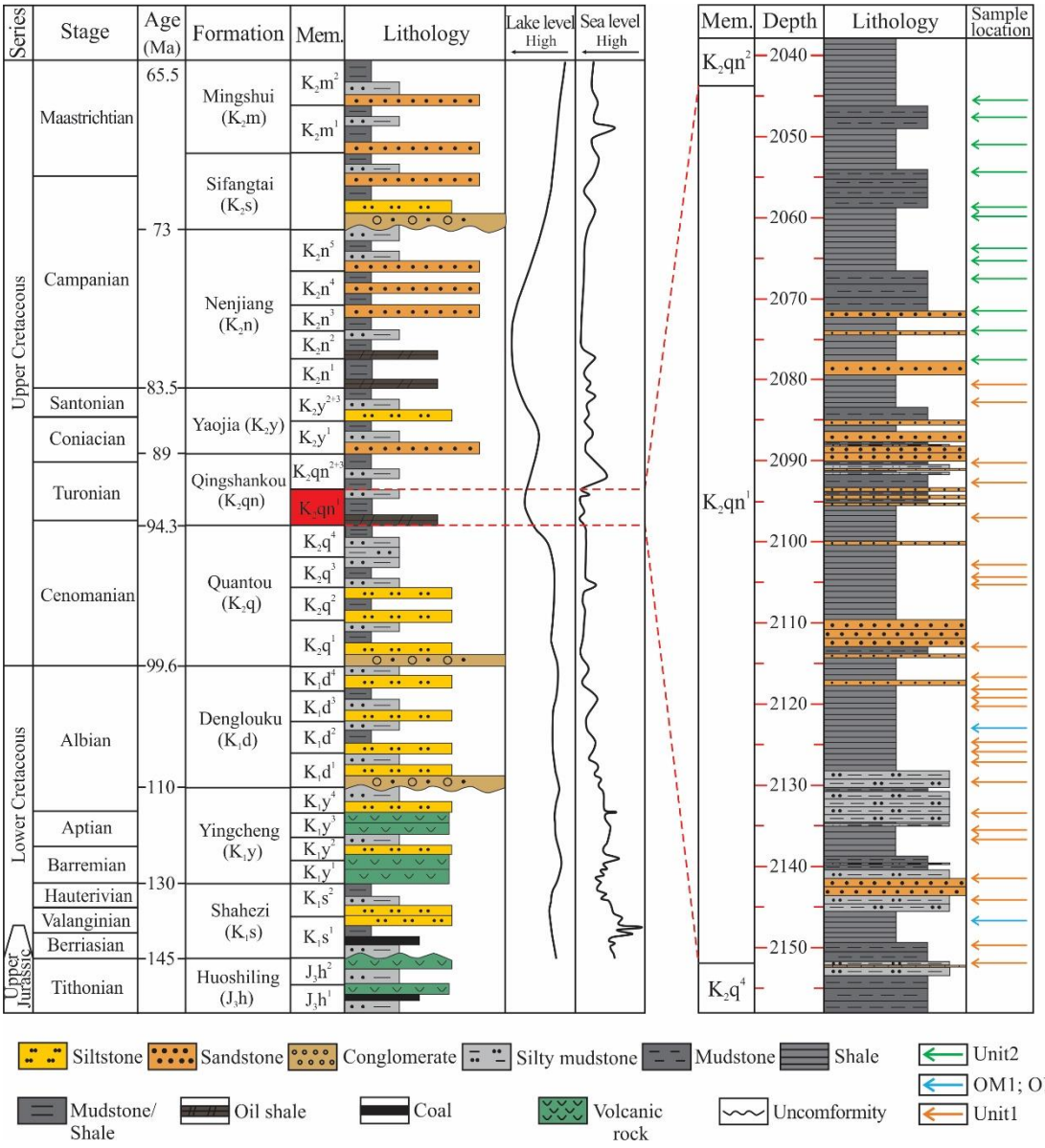

Figure 3.2 Stratigraphic column of the Songliao Basin showing simplified lithology, change in lake level during the Upper Jurassic to Cretaceous, and depth and lithology of the samples from well A (modified after Wu et al., 2009).

3.3 Samples and methods

A total of 38 core samples were collected for the present study from the well A targeting the K_2qn^1 at depths between 2045.4 and 2152.2 m in the southern part of the central depression (Fig. 3.2). Table 3.1 gives an overview of the depth and lithology of selected samples. Prior to analyses, core samples with a thickness of approximately 5 cm were cut into two parts. One part was ground into powder by a tungsten carbide ball mill and dried. The other part was cut perpendicular to the bedding and embedded in epoxy resin for the organic petrological analysis.

3.3.1 Elemental analysis

TOC and total inorganic carbon (TIC) contents were measured by a Liquid TOC II (Elementar) instrument. TOC and TIC contents were calculated from the detected CO_2 released during combustion in a pure oxygen atmosphere at 550 °C and 1000 °C, respectively. For CO_2 detection a non-dispersive infrared detector was used. Similarly, total sulfur (TS) contents were measured by combusting sample powder at 1800 °C using a Leco S-200 Sulfur Analyzer and detecting the generated SO_2. Major elements concentrations were analyzed using a PANalytical PW2424 X-ray fluorescence spectrometry device. Trace elements concentrations were determined by an Agilent 7900 inductively coupled plasma mass spectrometer and Agilent 5110 inductively coupled plasma atomic emission spectrometer.

The CIA, proposed by Nesbitt and Young (1982), is widely used to indicate the chemical weathering intensity of soils and sediments, with further implications for the evaluation of paleo-climate conditions (McLennan et al., 1993; Fedo et al., 1995; Wang et al., 2020; Qiao et al., 2022). CIA is calculated by the following equation:

$$CIA = \text{molar } [Al_2O_3/(Al_2O_3 + CaO^* + Na_2O + K_2O)] \times 100$$

CaO* represents only the CaO content in the silicate fraction. According to the correction method proposed by Fedo et al. (1995), the CaO* is calculated as:

$$CaO^* = CaO - CO_{2\,(calcite)} - 0.5 \times CO_{2\,(dolomite)} - 10/3 \times P_2O_{5\,(apatite)}$$

In this study, a value of 0.6 is adopted as the calcite/dolomite ratio (average ratio of the K_2qn^1 in the central depression based on XRD data; Zhang et al., 2021a) and CO_2 yields are acquired from TIC data. Subsequently, $CO_{2\,(calcite)}$ and $CO_{2\,(dolomite)}$ values are determined using calcite/dolomite ratios.

The C-value is commonly used to reconstruct paleo-climate based on the hypothesis that Fe, Mn, Cr, Ni, V, and Co are enriched in humid conditions, whereas Ca, Mg, Sr, Ba, K, and Na are concentrated under arid conditions (Moradi et al., 2016; Deng et al., 2019; Doner et al., 2019; Li et al., 2020). The C-value is defined as:

$$\text{C-value} = \Sigma (Fe + Mn + Cr + Ni + V + Co)/\Sigma (Ca + Mg + Sr + Ba + K + Na) \text{ (presented as ppm)}$$

The enrichment factor (EF) is used to characterize the enrichment and depletion degree of the element and calculated as (Tribovillard et al., 2006):

$$\text{Element } X_{EF} = (X/Al)_{sample}/(X/Al)_{PAAS}$$

Element X_{EF} represents the enrichment factor of element X. It is normalized using Post Achaean Australian Shale (PAAS) data (Taylor and McLennan, 1985).

3.3.2 Rock-Eval pyrolysis

Rock-Eval pyrolysis was carried out on the powdered rock samples (50–150 mg) using a Rock-Eval VII instrument (Vinci Technologies) following the methodology described by Behar et al. (2001). The S_1 (volatile hydrocarbon content) fraction was measured at 300 °C for 3 min. Subsequently, the oven temperature increased to 650 °C at 25 °C/min to measure the S_2 (remaining hydrocarbon generative potential) fraction, also as mg HC/g rock, and T_{max} (calibrated temperature of maximum pyrolysis yield, °C). Hydrogen (HI) and oxygen index (OI) were determined from the S_2 and S_3 (CO_2 formed by thermal breakdown of kerogen) peaks in relation to the TOC content.

3.3.3 Petrography

All the core samples were prepared as polished sections for organic petrography analysis according to the methods described by Zieger and Littke (2019). Maceral counting and identification were performed on a Zeiss Axio Imager microscope. The macerals were identified according to the principles described in Taylor et al. (1998), using the nomenclature of the ICCP System 1994 (ICCP, 1998, 2001; Pickel et al., 2017). Before the reflectance measurement, a yttrium-aluminum-garnet standard (0.89% reflectance) was used for calibration. For each sample, 30 to 50 vitrinite particles were randomly selected. In addition, the morphology and size of pyrite framboids were described in detail using the measuring tool in the Fossil software. More than 100 pyrite framboids were randomly selected for diameter measurement for each measured sample.

3.3.4 Molecular organic geochemistry

Extractable OM of 23 samples was gained by mixing about 5 g of powdered rock with 15 mL pure dichloromethane and activated copper flake; the mixture was constantly stirred for 24 h. Subsequently, the extracts were treated with sodium sulfate to remove water. Fractionation was performed on a Baker micro column filled with 2 g activated silica gel to separate extracts into aliphatic, aromatic, and polar compounds, using 5 mL of *n*-pentane, mixture of *n*-pentane and dichloromethane (40:60, v:v), and methanol, respectively.

Aliphatic and aromatic fractions were first analyzed by a Fisons Instruments gas chromatograph (GC 8000) equipped with a 30 m ZB-1 silica capillary column, split/splitless injector and flame ionization detector (FID). One µL of solvent was injected with a splitless time of 60 s at setup conditions of 270 °C injector temperature and an initial GC temperature of 60 °C. Following 3 min isothermal, the temperature was raised to 310 °C at 5 °C/min and remained isothermal for 20 min. Gas chromatography–mass spectrometry (GC–MS) analysis was performed on a Mega Series HRGC 5160 gas chromatograph equipped with a 30 m ZB-5-MS fused silica capillary column linked to a Trace MS mass spectrometer (Thermoquest). The chromatographic conditions were set to 270 °C injector

temperature and an initial GC temperature of 80 °C and 3 min isothermal. Subsequently, the temperature was raised to 160 °C at a rate of 10 °C/min and then to 320 °C at 3 °C/min and final isothermal of 20 min. For the measurement of aliphatic fractions, the MS was set to selected ion monitoring of *m/z* 85, 177, 191, 205, 217, 218, 259, 370, 372, 386, 398, 400, and 412, while the aromatic fractions were analyzed in full scan mode (see Fang et al., 2019). The biomarker ratios in this study were acquired by calculating the peak areas in the specific ion chromatograms.

3.4 Results

3.4.1 Elemental analysis

TOC, TIC, and TS contents of the analyzed samples are shown in Table 3.1. Two units of source rocks are identified in the studied well based on the TOC and TS contents and lithology. Generally, unit 1, consisting of shale, mudstone and, silty mudstone, is characterized by low TOC and TS contents, while unit 2 is comprised of shale and mudstone with significantly higher TOC and TS contents (Table 3.1). It is noteworthy that samples No. 22/099 and 22/117 show higher TOC and TS contents, ranging from 2.62–3.03 wt% and 1.27–2.74 wt%, respectively, compared with other samples in unit 1. The TOC and TS contents of samples from unit 1 vary from 0.55 to 2.16 (avg. 1.31) wt% and 0.08 to 2.21 (avg. 0.56) wt%, while those of unit 2 range from 1.41 to 2.96 (avg. 2.39) wt% and 0.63 to 2.52 (avg. 1.24) wt%. Two exceptional OM-rich samples in unit 1 (OM1 and OM2) are also characterized by high TIC contents, ranging from 1.04 to 2.18 wt% (Table 3.1).

OM* (organic matter content before sulfate reduction), CAR (carbonate content), and SIL (silicate content) were calculated using the equations proposed by Littke (1993). As shown in Table 3.1, silicate is the dominant component in all the samples. Two exceptional OM-rich samples in unit 1 are characterized by significantly higher CAR with values ranging from 8.7 to 18.2 wt%. Unit 1 has the lowest OM* content, ranging from 0.8 to 3.9 wt%, with an average value of 2.2 wt%.

3.4.2 Rock-Eval pyrolysis

Rock-Eval pyrolysis was used to indicate kerogen type, hydrocarbon generation potential, and thermal maturity. As shown in Table 3.1 and Fig. 3.3, the S_2 and HI values of unit 1 range from 0.10 to 8.66 (avg. 3.16) mg HC/g rock and from 18 to 449 (avg. 198) mg HC/g TOC, respectively, which are lower than those of unit 2, varying from 4.04 to 13.60 (avg. 10.56) mg HC/g rock and 287 to 510 (avg. 434) mg HC/g TOC, respectively. Two exceptional OM-rich samples in unit 1 have relatively similar values as compared to unit 2, ranging from 8.37 to 13.29 mg HC/g rock and 320 to 439 mg HC/g TOC, respectively. T_{max} values of the studied samples show lower variability and range between 431 °C and 450 °C with an average of 440 °C.

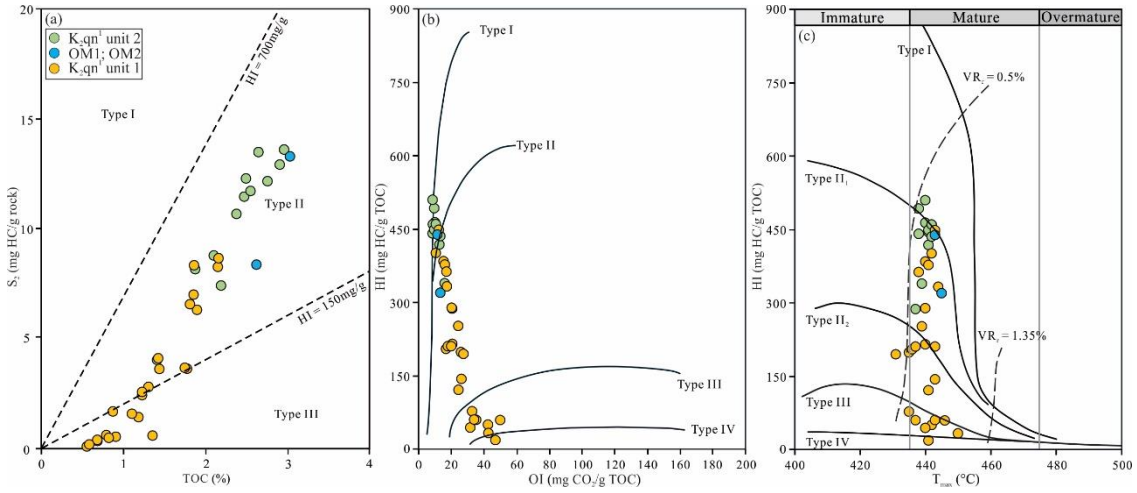

Figure 3.3 Rock Eval data: (a) Cross-plot of TOC versus S_2. (b) Cross-plot of OI versus HI. (c) Cross-plot of HI versus T_{max}.

3.4.3 Organic petrography

Organic petrographic analysis revealed that unit 2 and two exceptional OM-rich samples in unit 1 have a higher volumetric percentage of OM compared with unit 1, which is consistent with the TOC result (Fig. 3.4, Table 3.2). Semifusinite appears in grey-white color with a vague cellular structure (Fig. 3.4a), while fusinite is brighter with higher relief and clear lumens (Fig. 3.4b). Vitrinite is observed as small and grey detrital particles dispersed in the mineral matrix (Fig. 3.4c). These terrigenous macerals make up a higher relative volumetric percentage in unit 1 as compared to unit 2 and two exceptional OM-rich samples in unit 1 (Table 3.2). Liptinite, mainly as lamalginite and telalginite, is the dominant maceral group in most analyzed samples (Fig. 3.4d, f, h, j, l). Lamalginite is present as stripe-like lamellae and shows orange fluorescence under UV light excitation (Fig. 3.4e–l). Telalginite was found as structured algal bodies with large size and mainly occurs in unit 2 (Fig. 3.4f, h). Generally, vitrinite and inertinite account for very low relative volumetric percentage of the total macerals in unit 2 and two exceptional OM-rich samples in unit 1 (Table 3.2). Vitrinite reflectance (VR_r) of the studied samples varies between 0.80% and 0.88% (avg. 0.83%, Table 3.2).

3.4.4 Petrographic features of pyrite

Polished section observation suggests that pyrite framboids can be found in approximately half of the samples of unit 1 but are generally more frequent in unit 2 and two exceptional OM-rich samples in unit 1 (Table 3.2). As an effective proxy to indicate paleo-redox conditions, framboid size distribution was characterized by multiple parameters (Table 3.2) in this study. Pyrite framboids in unit 1 (2.8–25.6 μm; avg. diameter range of 7.8–10.8 μm) have a larger diameter than those in unit 2 (1.5–16.8 μm; avg. diameter range of 5.9–7.4 μm) and two exceptional OM-rich samples in unit 1 (2.0–15.8 μm, avg. 6.1–6.4 μm; Fig. 3.4c, g, k).

Table 3.1 TOC, TIC, and TS data, Rock-Eval pyrolysis data, as well as the three major primary sedimentary components calculated for the source rocks from the K_2qn^1.

Sample	Depth (m)	Lithology	TOC (wt%)	TIC (wt%)	TS (wt%)	S_1 (mg HC/g rock)	S_2 (mg HC/g rock)	S_3 (mg CO_2/g rock)	T_{max} (°C)	HI (mg HC/g TOC)	OI (mg CO_2/g TOC)	OM* (wt%)	CAR (wt%)	SIL (wt%)
Unit 2														
22/055	2045.4	Shale	2.47	0.56	1.49	1.07	11.46	0.25	440	464	10	4.6	4.6	90.8
22/056	2047.6	Mudstone	1.41	0.40	2.52	0.51	4.04	0.29	437	287	21	4.2	3.3	92.4
22/058	2051.1	Shale	2.49	0.57	1.35	1.23	12.29	0.24	438	493	10	4.5	4.8	90.7
22/061	2054.4	Mudstone	2.64	0.34	0.86	1.52	13.49	0.23	440	510	9	4.2	2.8	93.0
22/063	2058.7	Mudstone	2.75	0.36	0.79	1.22	12.16	0.24	438	441	9	4.3	3.0	92.7
22/064	2059.8	Shale	2.10	0.23	1.13	0.76	8.78	0.27	441	418	13	3.8	1.9	94.3
22/066	2063.9	Shale	2.19	0.80	0.63	0.77	7.42	0.35	439	339	16	3.4	6.7	89.9
22/067	2065.3	Shale	2.96	0.87	1.55	0.81	13.60	0.26	442	460	9	5.3	7.3	87.4
22/068	2067.6	Mudstone	2.90	1.08	1.05	1.06	12.92	0.32	441	445	11	4.7	9.0	86.3
22/070	2071.7	Mudstone	2.37	0.26	1.25	1.14	10.67	0.23	441	449	10	4.2	2.2	93.6
22/072	2074.0	Shale	2.55	0.93	1.00	0.71	11.72	0.27	442	460	11	4.2	7.8	88.0
22/074	2077.9	Shale	1.87	1.01	1.27	0.26	8.16	0.25	442	436	13	3.6	8.4	88.0
Unit 1														
22/075	2080.7	Shale	0.90	0.16	0.60	0.12	0.54	0.32	437	60	35	1.7	1.3	97.0
22/076	2082.8	Shale	1.18	0.22	0.12	0.23	1.43	0.29	441	121	25	1.6	1.8	96.5
22/080	2090.3	Mudstone	1.42	0.23	0.44	0.58	4.11	0.29	440	289	20	2.2	1.9	95.9
22/081	2092.8	Mudstone	1.10	0.29	0.13	0.29	1.58	0.29	443	143	26	1.5	2.4	96.0
22/083	2097.0	Shale	1.86	0.14	1.07	0.65	8.34	0.23	443	449	12	3.4	1.2	95.4
22/086	2103.0	Shale	1.44	0.71	0.15	0.63	3.62	0.35	439	252	24	2.0	5.9	92.1
22/087	2104.4	Shale	1.23	0.60	1.30	0.60	2.43	0.32	435	198	26	2.8	5.0	92.2
22/088	2105.2	Shale	0.87	0.25	2.21	0.40	1.69	0.24	431	194	28	3.2	2.1	94.7
22/092	2112.5	Mudstone	0.68	0.23	0.17	0.06	0.34	0.29	442	50	43	1.0	1.9	97.0
22/094	2116.9	Shale	0.68	0.13	0.10	0.08	0.40	0.34	446	59	50	1.0	1.1	97.9
22/095	2118.2	Shale	1.77	0.16	0.09	0.42	3.63	0.30	436	205	17	2.4	1.3	96.3
22/096	2119.2	Shale	2.15	0.35	0.27	0.52	8.26	0.33	440	384	15	3.0	2.9	94.0
22/097	2120.3	Shale	1.85	0.38	0.99	0.41	7.00	0.30	441	378	16	3.3	3.2	93.5
22/099(OM2)	2122.9	Shale	3.03	2.18	1.27	1.01	13.29	0.35	443	439	12	5.1	18.2	76.7
22/100	2124.8	Shale	1.90	0.90	0.81	0.34	6.31	0.33	444	333	17	3.2	7.5	89.3
22/102	2126.0	Shale	1.30	0.16	0.68	0.23	2.80	0.27	440	215	21	2.3	1.3	96.3
22/103	2127.3	Shale	2.16	0.15	1.16	0.51	8.66	0.23	442	401	11	3.9	1.2	94.9
22/105	2129.6	Silty mudstone	0.55	0.27	0.08	0.02	0.10	0.26	441	18	47	0.8	2.2	97.0
22/107	2133.4	Silty mudstone	1.23	0.17	0.12	0.08	2.58	0.22	443	210	18	1.7	1.4	96.9
22/109	2135.6	Shale	0.58	0.20	0.21	0.02	0.19	0.25	450	33	43	0.9	1.7	97.4
22/110	2136.7	Shale	0.79	0.37	0.55	0.11	0.61	0.26	435	77	33	1.5	3.1	95.4
22/113	2141.5	Silty mudstone	1.81	0.24	1.03	0.58	6.57	0.31	438	363	17	3.3	2.0	94.7
22/115	2144.1	Silty mudstone	1.35	0.14	0.09	0.05	0.59	0.43	440	44	32	1.8	1.2	97.0
22/117(OM1)	2146.8	Shale	2.62	1.04	2.74	0.35	8.37	0.35	445	320	13	6.0	8.7	85.3
22/120	2149.7	Mudstone	1.75	0.58	0.67	0.27	3.67	0.35	437	210	20	2.9	4.8	92.3
22/122	2152.2	Silty mudstone	0.82	0.11	0.50	0.05	0.49	0.28	443	60	34	1.5	0.9	97.6

Table 3.2 TOC, VR_r, maceral composition, and minimum (min.), maximum (max.) as well as average (ave.) diameters of pyrite framboids of the source rocks from the K_2qn^1. Std = standard deviation, sk = skewness, n = number of measured framboids. "–" indicates the complete absence, "o" indicates a low relative volumetric percentage (< 1%) compared to all macerals, "+" indicates a moderate relative volumetric percentage (1–10%), "++" indicates a high relative volumetric percentage (10–50%), "+++" indicates an extremely high relative volumetric percentage (>50%).

Sample	TOC (wt%)	VR_r (%)	Maceral composition				Framboidal pyrite diameters (μm)					
			Vitrinite (%)	Inertinite (%)	Liptinite (%)	Total OM (vol%)	min.	max.	ave.	std	sk	n
Unit 2												
22/055	2.47	0.80	+	o	+++	7.4	/	/	/	/	/	/
22/056	1.41	0.80	+	–	+++	8.8	/	/	/	/	/	/
22/058	2.49	0.81	+	o	+++	13.6	2.8	15.3	6.2	2.2	1.8	110
22/061	2.64	0.81	+	o	+++	5.7	2.8	13.5	6.7	2.3	1.0	122
22/063	2.75	0.81	o	o	+++	9.1	4.0	13.1	7.4	1.8	0.3	108
22/064	2.10	0.80	o	–	+++	12.5	2.5	14.7	6.7	2.2	1.4	109
22/066	2.19	0.81	o	o	+++	12.5	2.8	15.7	7.1	2.1	0.9	118
22/067	2.96	/	o	+	+++	3.7	2.1	14.1	6.3	2.4	1.0	194
22/068	2.90	0.81	o	o	+++	7.6	1.5	15.6	5.9	2.9	1.4	135
22/070	2.37	0.82	+	+	+++	7.1	2.7	16.8	6.8	2.4	1.7	115
22/072	2.55	0.81	+	o	+++	14.0	2.8	15.9	6.1	2.4	2.3	111
22/074	1.87	0.82	o	o	+++	9.2	2.8	14.9	6.6	2.4	1.3	111
Unit 1												
22/075	0.90	0.84	++	+	+++	1.8	3.8	24.1	8.4	3.0	1.6	190
22/076	1.18	0.82	++	+	+++	2.0	4.7	24.3	8.9	2.7	2.3	104
22/080	1.42	0.81	+	+	+++	3.5	/	/	/	/	/	/
22/081	1.10	0.83	++	+	++	1.1	4.2	21.8	8.5	3.4	2.0	107
22/083	1.86	0.84	+	+	+++	3.4	/	/	/	/	/	/
22/086	1.44	0.84	++	+	+++	0.9	/	/	/	/	/	/
22/087	1.23	0.88	++	+	+++	0.6	5.8	20.0	10.8	2.7	1.2	165
22/088	0.87	0.82	++	+	+++	1.3	3.4	21.9	9.0	3.8	1.4	143
22/092	0.68	0.84	++	–	+++	0.6	/	/	/	/	/	/
22/094	0.68	0.84	++	+	+++	1.4	/	/	/	/	/	/
22/095	1.77	0.84	++	–	+++	1.2	4.3	20.9	9.0	3.1	1.2	130
22/096	2.15	0.83	++	+	+++	2.4	3.1	20.7	9.3	3.8	0.9	130
22/097	1.85	0.82	++	+	+++	1.9	/	/	/	/	/	/
22/099(OM2)	3.03	/	o	+	+++	5.0	2.1	14.3	6.1	2.8	0.8	354
22/100	1.90	0.84	+	+	+++	2.0	3.5	25.6	8.6	2.7	2.5	143
22/102	1.30	0.83	+	++	+++	1.4	2.8	24.3	8.5	2.7	1.6	332
22/103	2.16	0.87	++	+	+++	1.1	/	/	/	/	/	/
22/105	0.55	0.86	++	–	+++	0.8	/	/	/	/	/	/
22/107	1.23	0.86	++	+	+++	1.1	/	/	/	/	/	/
22/109	0.58	0.86	++	–	+++	1.2	/	/	/	/	/	/
22/110	0.79	0.86	++	+	+++	0.8	4.1	25.6	9.7	3.8	1.4	158
22/113	1.81	0.86	+	o	+++	6.3	3.5	21.8	8.1	3.1	1.9	139
22/115	1.35	0.86	++	+	+++	1.3	/	/	/	/	/	/
22/117(OM1)	2.62	0.86	+	+	+++	4.5	2.0	15.8	6.4	3.1	0.9	239
22/120	1.75	0.86	+	–	+++	5.5	3.2	22.7	7.8	2.8	2.0	132
22/122	0.82	0.86	++	+	+++	1.1	/	/	/	/	/	/

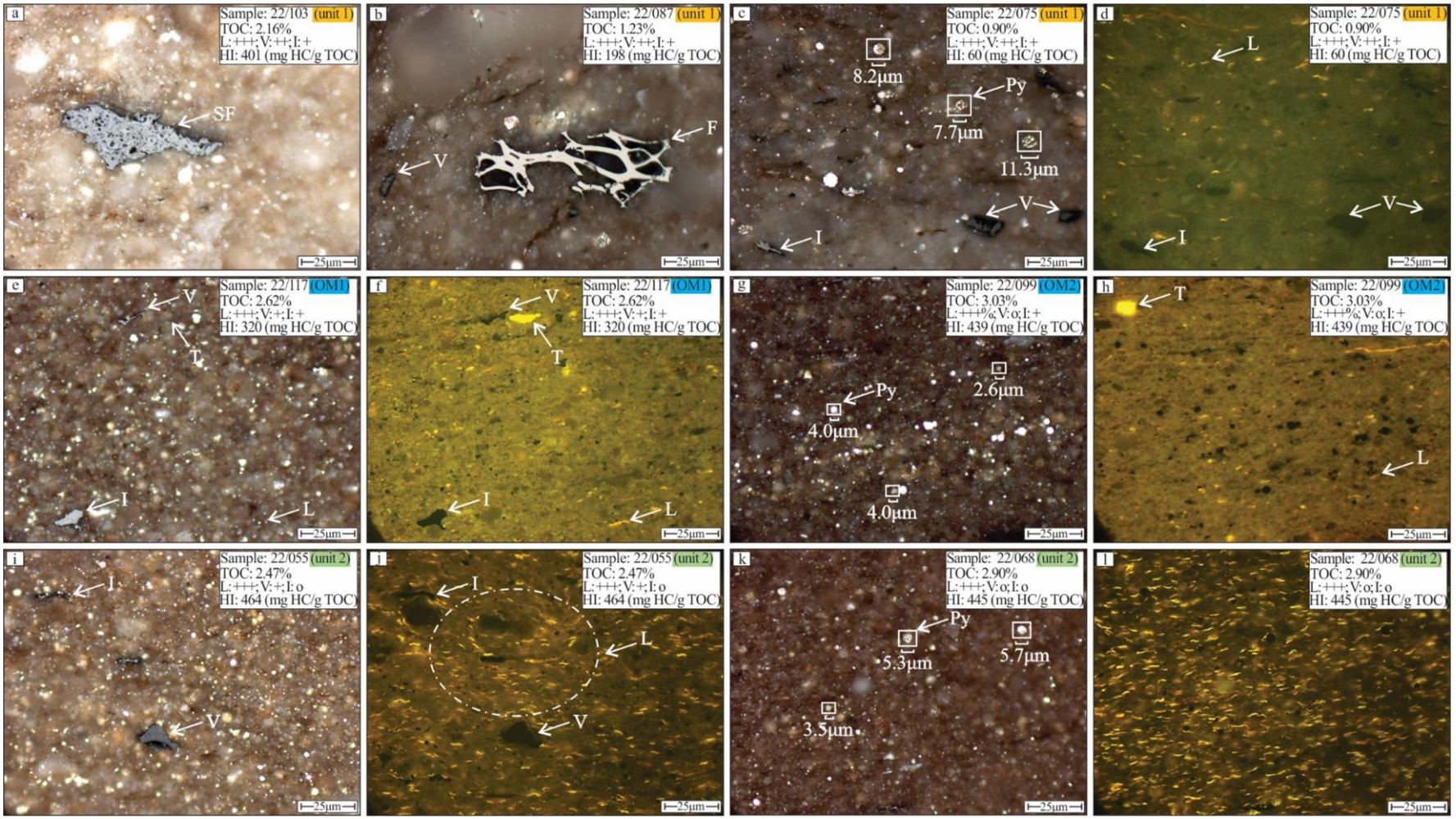
a
Sample: 22/103 (unit 1)
TOC: 2.16%
L: +++; V: ++; I: +
HI: 401 (mg HC/g TOC)
SF
25µm
b
Sample: 22/087 (unit 1)
TOC: 1.23%
L: +++; V: ++; I: +
HI: 198 (mg HC/g TOC)
F
V
25µm
c
Sample: 22/075 (unit 1)
TOC: 0.90%
L: +++; V: ++; I: +
HI: 60 (mg HC/g TOC)
8.2µm
Py
7.7µm
11.3µm
V
I
25µm
d
Sample: 22/075 (unit 1)
TOC: 0.90%
L: +++; V: ++; I: +
HI: 60 (mg HC/g TOC)
L
V
I
25µm
e
Sample: 22/117 (OM1)
TOC: 2.62%
L: +++; V: +; I: +
HI: 320 (mg HC/g TOC)
V
T
I
L
25µm
f
Sample: 22/117 (OM1)
TOC: 2.62%
L: +++; V: +; I: +
HI: 320 (mg HC/g TOC)
V
T
I
L
25µm
g
Sample: 22/099 (OM2)
TOC: 3.03%
L: +++%; V: o; I: +
HI: 439 (mg HC/g TOC)
Py
2.6µm
4.0µm
4.0µm
25µm
h
Sample: 22/099 (OM2)
TOC: 3.03%
L: +++%; V: o; I: +
HI: 439 (mg HC/g TOC)
T
L
25µm
i
Sample: 22/055 (unit 2)
TOC: 2.47%
L: +++; V: +; I: o
HI: 464 (mg HC/g TOC)
I
V
25µm
j
Sample: 22/055 (unit 2)
TOC: 2.47%
L: +++; V: +; I: o
HI: 464 (mg HC/g TOC)
I
L
V
25µm
k
Sample: 22/068 (unit 2)
TOC: 2.90%
L: +++; V: o; I: o
HI: 445 (mg HC/g TOC)
Py
5.3µm
5.7µm
3.5µm
25µm
l
Sample: 22/068 (unit 2)
TOC: 2.90%
L: +++; V: o; I: o
HI: 445 (mg HC/g TOC)
25µm

Figure 3.4 Microphotographs representative of the OM in the source rocks from the K_2qn^1 under reflected white light (a, b, c, e, g, i, k) and in fluorescence mode (d, f, h, j, l). (a) Semifusinite, sample 22/103, shale, unit 1. (b) Fusinite and vitrinite, sample 22/087, shale, unit 1. (c) Vitrinite, inertinite, and pyrite framboids with relatively large diameter, sample 22/075, shale, unit 1. (d) Lamalginite in Fig. 3.4c. (e) Inertinite, sample 22/117, shale, OM1. (f) Lamalginite and telalginite in Fig. 3.4e. (g) Pyrite framboids with relatively small diameter, sample 22/099, shale, OM2. (h) Lamalginite and telalginite in Fig. 3.4g. (i) Vitrinite and inertinite, sample 22/055, shale, unit 2. (j) Lamalginite in Fig. 3.4i. (k) Pyrite framboids with relatively small diameter, sample 22/068, mudstone, unit 2. (l) Lamalginite in Fig. 3.4k. V-vitrinite, I-inertinite, F-fusinite, SF-semifusinite, L-lamalginite, T-telalginite, Py-pyrite framboid.

3.4.5 Molecular geochemistry

3.4.5.1 Acyclic alkanes

The normal alkanes in the extracted samples show a unimodal distribution (Fig. 3.5a–c). Unit 1 is characterized by a high abundance of low-molecular-weight *n*-alkanes with maximum peaks occurring at *n*-C_{15} and *n*-C_{16} (Fig. 3.5a). Unit 2 and two exceptional OM-rich samples in unit 1 have a higher proportion of *n*-alkanes of intermediate (*n*-C_{21}–*n*-C_{25}) and long (> *n*-C_{27}) chain length (Fig. 3.5b and c, Table 3.3). Further differences are indicated by the proxies of acyclic aliphatic compounds.

Table 3.3 Biomarker parameters of acyclic alkanes of the source rocks from the K_2qn^1.

Sample	Pr/Ph	*n*-C_{17}/*n*-C_{27}	*n*-C_{17}/*n*-C_{23} + *n*-C_{25} + *n*-C_{25}	CPI	OEP	WI	TAR
Unit 2							
22/055	1.13	1.46	0.35	1.10	1.10	1.50	0.53
22/056	1.22	1.80	0.46	1.10	1.08	1.23	0.47
22/058	1.06	1.67	0.39	1.11	1.08	1.39	0.48
22/061	1.45	1.87	0.44	1.08	1.08	1.27	0.43
22/063	1.48	2.52	0.55	1.08	1.08	1.11	0.35
22/064	1.28	2.03	0.45	1.08	1.06	1.26	0.39
22/066	1.32	1.56	0.37	1.08	1.09	1.39	0.47
22/067	1.62	3.18	0.67	1.11	1.10	0.85	0.24
22/068	1.33	1.78	0.42	1.07	1.08	1.29	0.43
22/070	1.31	1.54	0.36	1.11	1.09	1.49	0.53
22/072	1.43	2.34	0.56	1.06	1.07	1.07	0.36
22/074	1.35	3.07	0.71	1.06	1.07	0.79	0.23
Unit 1							
22/075	2.08	3.37	0.90	1.08	1.09	0.72	0.28
22/076	2.49	7.89	2.00	1.06	1.07	0.33	0.11
22/086	1.38	1.90	0.40	1.06	1.08	1.28	0.38
22/094	1.97	7.26	2.04	1.05	1.02	0.36	0.13
22/097	1.27	3.03	0.54	1.09	1.12	1.00	0.22
22/099(OM2)	1.26	2.52	0.49	1.10	1.12	1.10	0.29
22/102	1.69	8.13	1.67	1.07	1.10	0.40	0.10
22/107	1.65	3.10	0.55	1.08	1.10	1.00	0.23
22/109	1.70	1.42	0.35	1.09	1.13	1.32	0.47
22/113	1.39	1.71	0.39	1.08	1.08	1.40	0.47
22/117(OM1)	1.49	3.53	0.79	1.06	1.08	0.77	0.22

Pr = pristane; Ph = phytane; CPI = 2 × Σodd *n*-$C_{23–29}$/(Σeven *n*-$C_{22–28}$ + Σeven *n*-$C_{24–30}$); OEP = (*n*-C_{21} + 6 × *n*-C_{23} + *n*-C_{25})/(4 × *n*-C_{22} + 4 × *n*-C_{24}); WI = Σ*n*-C_{21-31}/Σ*n*-C_{15-20}; TAR = (*n*-C_{27} + *n*-C_{29} + *n*-C_{31})/(*n*-C_{15} + *n*-C_{17} + *n*-C_{19}).

As shown in Table 3.3, the Pr/Ph values of unit 1 vary from 1.27 to 2.49 (avg. 1.74), which are higher than those of unit 2 (1.06–1.62, avg. 1.33) and two exceptional OM-rich samples in unit 1 (1.26–1.49). Proxies used to indicate the OM sources, including waxiness index (WI; Peters et al., 2005) and terrigenous/aquatic ratio (TAR; Bourbonniere and Meyers, 1996) show significantly lower values in unit 1, while *n*-C_{17}/*n*-C_{27} (Eglinton and Hamilton, 1967; Guenther et al., 2013; Qiao et al., 2021a) exhibits a higher value in unit 1 (Table 3.3). CPI (carbon preference index; Bray and Evans 1961) and OEP (odd-to-even predominance; Peters and Moldowan, 1993) values show minor differences in all of the samples, ranging from 1.05 to 1.11 (avg. 1.08) and 1.02 to 1.13 (avg. 1.09), respectively (Table 3.3). Monomethylalkanes (MMAs) with the methyl group at position 4, 5, 6 or 7 were detected in all samples (Fig. 3.5c).

3.4.5.2 Terpanes

Tricyclic terpanes (Tri) ranging from C_{19} to C_{26}, C_{24} tetracyclic terpane (C_{24} Tet), and pentacyclic terpanes (hopanes) are detected in all samples (Fig. 3.5d–f). The C_{19}/C_{23} Tri ratio shows similar values for units 1 and 2, ranging from 0.10 to 0.90 (avg. 0.52) and 0.38 to 1.07 (avg. 0.78), respectively, whereas two exceptional OM-rich samples in unit 1 are characterized by the lowest values of 0.14–0.16 (Table 3.4). Besides, C_{24} Tet/C_{26} Tri ratio exhibits similar result with the lowest values in two exceptional OM-rich samples in unit 1 (Table 3.4).

Gradually decreasing concentrations of C_{31} to C_{35} homohopanes and low homohopane index values (HHI, Peters and Moldowan, 1991) are observed in all of the samples (Fig. 3.5d–f, Table 3.4). Biomarker proxies of thermal maturity, including Ts/(Ts + Tm) and C_{29} Ts/(C_{29} Ts + C_{29} H), range from 0.63 to 0.84 (avg. 0.76) and 0.23 to 0.60 (avg. 0.47), respectively. Gammacerane (Gam) is present in relatively high abundance in unit 2 and two exceptional OM-rich samples in unit 1 with Gam index varying from 0.10 to 0.17 (avg. 0.14) and 0.17 to 0.20, respectively. By contrast, Gam index is lower in unit 1 at 0.04–0.15 with an average value of 0.09 (Table 3.4).

3.4.5.3 Steroids

The concentration of steranes is much lower than that of hopanes with steranes/hopanes ratios of 0.03–0.13 (avg. 0.06; Table 3.4). The distribution of steranes is shown in Fig. 3.5g–i. Unit 2 and two exceptional OM-rich samples in unit 1 are characterized by a higher proportion of C_{27} ααα 20R sterane (39–59%, avg. 49%) compared with that of unit 1 (39–48%, avg. 44%). C_{29} ααα 20R sterane is more enriched in unit 1 with a proportion of 24–43% (avg. 35%; Table 3.4). C_{29} ααα 20S/(20S + 20R) and C_{29} ββ/(ββ + αα) ratios vary from 0.48 to 0.63 (avg. 0.56) and 0.48 to 0.57 (avg. 0.53).

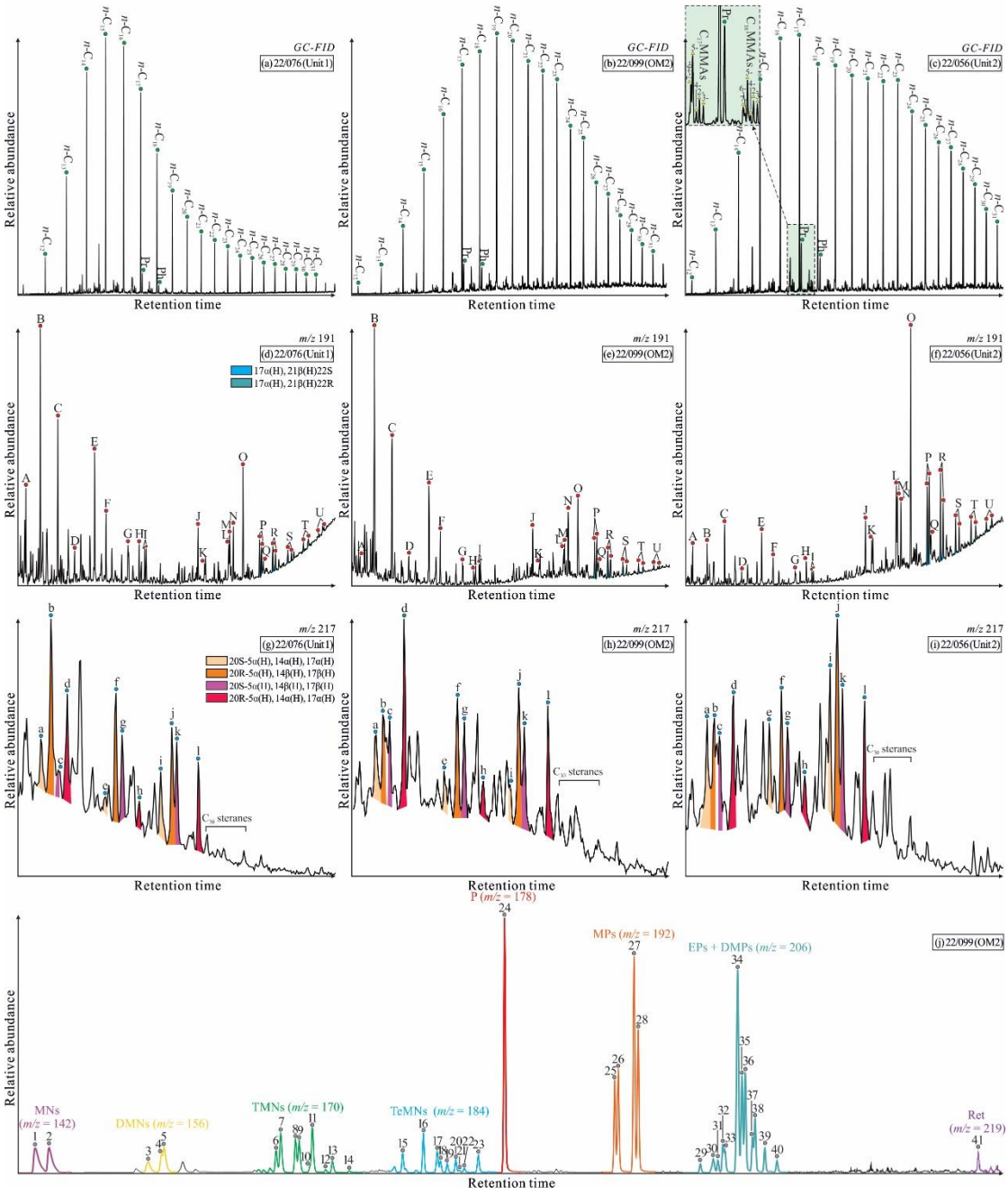

Figure 3.5 (a–c) Gas chromatograms; (d–f) m/z 191 mass fragmentograms showing the hopanes distributions; (g–i) m/z 217 mass fragmentograms showing the steranes distributions of the aliphatic fraction (samples 22/056, 22/076, and 22/099) and (j) total ion chromatogram of the aromatic fraction (sample 22/099). See Appendix (Table 3.7) for detailed peak identification.

Table 3.4 Biomarker parameters of tricyclic and tetracyclic terpanes, hopanes, and steranes of the source rocks from the K_2qn^1.

Sample	Tricyclic and tetracyclic terpanes		Hopanes				Steranes/ hopanes	Steranes					
	C_{19}/ C_{23} Tri	C_{24} Tet/ C_{26} Tri	Ts/ (Ts + Tm)	C_{29} Ts/ (C_{29} Ts + C_{29} H)	Gam/ (C_{30} H + Gam)	HHI		C_{29} ββ/ (ββ + αα) steranes	C_{29} ααα S/ (R + S) steranes	C_{29}/C_{27} regular steranes	Sterane ααα 20R distribution (%)		
											C_{27}	C_{28}	C_{29}
Unit 2													
22/055	0.38	0.82	0.71	0.43	0.17	0.04	0.07	0.54	0.62	0.52	52	29	19
22/056	0.63	0.89	0.63	0.43	0.14	0.05	0.04	0.56	0.61	1.01	45	26	28
22/058	0.82	1.05	0.73	0.48	0.15	0.03	0.08	0.54	0.60	0.69	39	43	18
22/061	0.83	0.68	0.75	0.58	0.14	0.04	0.09	0.54	0.56	1.17	55	19	26
22/063	1.07	0.83	0.73	0.58	0.13	0.06	0.05	0.50	0.63	0.65	55	27	18
22/064	1.03	1.02	0.70	0.53	0.12	0.05	0.06	0.51	0.60	0.44	53	33	14
22/066	0.94	0.70	0.80	0.53	0.16	0.05	0.06	0.49	0.53	0.82	59	19	23
22/067	0.73	0.55	0.78	0.54	0.14	0.05	0.03	0.53	0.57	1.20	44	26	30
22/068	0.76	0.52	0.78	0.52	0.15	0.06	0.04	0.55	0.53	1.04	41	26	33
22/070	0.73	0.79	0.72	0.49	0.11	0.06	0.04	0.52	0.59	0.98	40	39	21
22/072	0.82	0.64	0.79	0.60	0.10	0.05	0.04	0.57	0.56	0.76	57	22	21
22/074	0.58	0.45	0.79	0.52	0.14	0.04	0.04	0.53	0.52	1.18	44	25	31
Unit 1													
22/075	0.87	0.83	0.79	0.38	0.13	0.04	0.05	0.49	0.48	1.73	42	15	43
22/076	0.90	0.71	0.76	0.55	0.11	0.04	0.08	0.48	0.53	1.90	45	16	39
22/086	0.32	0.54	0.84	0.46	0.10	0.06	0.05	0.56	0.60	1.41	45	31	24
22/094	0.71	1.17	0.75	0.28	0.08	0.06	0.06	0.54	0.56	1.64	44	19	37
22/097	0.17	0.51	0.82	0.40	0.07	0.05	0.06	0.56	0.54	1.16	39	30	32
22/099(OM2)	0.16	0.31	0.78	0.48	0.20	0.05	0.08	0.48	0.49	0.75	59	16	25
22/102	0.37	0.67	0.81	0.45	0.08	0.06	0.04	0.56	0.52	1.15	47	19	35
22/107	0.33	0.56	0.82	0.36	0.04	0.06	0.05	0.50	0.58	1.27	43	23	35
22/109	0.10	0.51	0.75	0.23	0.04	0.08	0.07	0.53	0.60	1.44	48	18	34
22/113	0.90	0.85	0.74	0.51	0.15	0.05	0.05	0.52	0.60	1.99	46	19	35
22/117(OM1)	0.14	0.38	0.78	0.41	0.17	0.08	0.13	0.57	0.48	0.55	46	37	18

Tri = tricyclic terpane; Tet = tetracyclic terpane; Gam index = gammacerance index: Gam/(C_{30} H + Gam); HHI = homohopane index: C_{35}/ ΣC_{31}–C_{35} 22S and 22R homohopanes; H = hopane; Steranes/hopanes = C_{27}-C_{29} regular steranes/C_{29}-C_{35} 17α-hopanes.

3.4.5.4 Aromatic hydrocarbons

As shown in the distribution of aromatic hydrocarbons (Fig. 3.5j), phenanthrene (P, *m/z* 178), methylphenanthrenes (MPs; *m/z* 192), and dimethylphenanthrenes (DMPs, *m/z* 206) have high abundances, while methylnaphthalenes (MNs; *m/z* 142), dimethylnaphthalenes (DMNs, *m/z* 156), trimethylnaphthalenes (TMNs; *m/z* 170), tetramethylnaphthalenes (TeMNs; m/z 184), ethylphenanthrenes (EPs, *m/z* 206), and retene (Ret; *m/z* 219) are present in relatively low concentrations. Dibenzothiophene (*m/z* 184) occurs in low concentration, approaching the detection limit of the instrument. Thermal maturity proxies of TNR-1, TNR-2, TMNr, and MPI-1 vary from 0.7 to 1.5 (avg. 1.04), 0.55 to 0.83 (avg. 0.71), 0.57 to 0.81 (avg. 0.67), and 0.31 to 0.67 (avg. 0.42), respectively (Table 3.5). VR_{TNR-2}, the calculated corresponding vitrinite reflectance from TNR-2 ranges from 0.73% to 0.90% (avg. 0.83%). 9-MP is the predominant compound in the MP homologues with low Log (1-MP/9-MP) ratios ranging from –0.30 to –0.10 (avg. –0.18) in most samples (Table 3.5). Similarly, Log (1,2,5-TMN/1,3,6-TMN) and Log (1,2,7-TMN/1,3,7-TMN) ratios exhibit low values varying from –0.94 to –0.46 (avg. –0.62) and –0.79 to –0.30 (avg. –0.57), respectively (Table 3.5). Among DMPs, the Log (1,7-DMP/ 1,3- + 3,9- + 2,10- + 3,10-DMP) ratios range from –0.46 to –0.23 (avg. –0.34).

3.4.6 Major and trace elements

The major and trace elemental concentrations and multiple proxies are listed in Table 3.6. The concentrations of Al and Ti, used as indicators of terrigenous input, are the highest in unit 1 with an average content of 8.77% and 0.39%, respectively. The detrital input for the two exceptional OM-rich samples in unit 1 is the lowest with an average content of 7.68% Al and 0.29% Ti. Above these layers, the terrigenous detrital proxies exhibit an increasing trend upward in unit 2 with an average content of 8.35% Al and 0.35% Ti (Table 3.6). Stratigraphically, the Zr/Al ratio exhibits a similar variation pattern that is characterized by the highest value in unit 1 (avg. 26.17) but lower value in the two exceptional OM-rich samples in unit 1 (avg. 23.81) and gradually increasing values in unit 2 (avg. 22.82; Table 3.6). Indicators of paleo-redox conditions, including U/Th and Cu/Zn ratios, show the lowest values in unit 1, ranging from 0.15 to 0.31 (avg. 0.23) and 0.15 to 0.28 (avg. 0.23), respectively. Above, unit 2 shows higher ratios of U/Th and Cu/Zn, varying from 0.30 to 0.53 (avg. 0.37) and 0.21 to 0.34 (avg. 0.27), respectively. These two parameters show the highest values in two exceptional OM-rich samples in unit 1 of 0.47–0.67 and 0.35–0.42, respectively (Table 3.6). The paleo-salinity proxies, including Sr/Ba, Ca/Mg, and 100×(Mg/Al), also show similar patterns that are characterized by an increasing trend from units 1 to unit 2 and the highest values are observed in the two exceptional OM-rich samples in unit 1 (Table 3.6). Unit 1 shows the lowest ratio of Cu/Al (2.47–4.01, avg. 3.15), whereas higher ratios are observed in unit 2 (3.17–4.44, avg. 3.78) and two exceptional OM-rich samples in unit 1 (4.45–5.16). There are minor differences in the elemental proxies related to paleo-climate reconstruction, including C-value (0.28–0.59, avg. 0.47), CIA (54.32–67.52, avg. 63.27),

Sr/Cu (6.59–20.25, avg. 10.91), and Rb/Sr (0.24–0.88, avg. 0.54), among the studied samples. In detail, unit 1 has slightly higher average C-values (0.48), CIA (64.05), and Rb/Sr (0.61) values compared with those of unit 2 of 0.46, 62.44, and 0.44, respectively and two exceptional OM-rich samples in unit 1 of 0.39, 58.91, and 0.38, respectively (Table 3.6).

Table 3.5 Biomarker parameters of aromatic fractions of the source rocks from the K_2qn^1.

Sample	TNR -1	TNR -2	VR_{TNR-2} (%)	TMNr	MPI -1	Log (1-MP/9-MP)	Log (1,2,5-TMN/1,3,6-TMN)	Log (1,2,7-TMN/1,3,7-TMN)	Log (1,7-DMP/1,3- + 3,9- + 2,10- + 3,10-DMP)
Unit 2									
22/055	0.83	0.60	0.76	0.57	0.40	–0.17	–0.47	–0.66	–0.36
22/056	1.01	0.74	0.84	0.62	0.44	–0.13	–0.48	–0.62	–0.33
22/058	0.86	0.67	0.80	0.62	0.37	–0.19	–0.49	–0.52	–0.37
22/061	0.70	0.60	0.76	0.65	0.67	–0.19	–0.56	–0.41	–0.35
22/063	1.13	0.80	0.88	0.67	0.36	–0.20	–0.58	–0.62	–0.45
22/064	0.84	0.55	0.73	0.64	0.39	–0.17	–0.67	–0.51	–0.37
22/066	0.95	0.73	0.84	0.71	0.43	–0.19	–0.65	–0.60	–0.30
22/067	0.94	0.68	0.81	0.66	0.42	–0.30	–0.60	–0.62	–0.32
22/068	1.00	0.68	0.81	0.60	0.39	–0.21	–0.53	–0.45	–0.39
22/070	0.75	0.62	0.77	0.60	0.36	–0.19	–0.46	–0.49	–0.39
22/072	1.15	0.77	0.86	0.65	0.31	–0.21	–0.55	–0.45	–0.34
22/074	1.08	0.71	0.83	0.74	0.36	–0.17	–0.77	–0.79	–0.30
Unit 1									
22/075	1.13	0.75	0.85	0.69	0.45	–0.12	–0.64	–0.61	–0.25
22/076	1.14	0.76	0.85	0.70	0.43	–0.28	–0.65	–0.60	–0.29
22/086	1.46	0.83	0.90	0.70	0.38	–0.16	–0.67	–0.56	–0.40
22/094	1.50	0.82	0.89	0.81	0.39	–0.20	–0.94	–0.71	–0.23
22/097	1.04	0.78	0.87	0.66	0.42	–0.16	–0.53	–0.67	–0.41
22/099 (OM2)	0.96	0.70	0.82	0.69	0.47	–0.25	–0.64	–0.48	–0.46
22/102	1.27	0.78	0.87	0.72	0.40	–0.14	–0.72	–0.68	–0.36
22/107	1.07	0.64	0.79	0.65	0.43	–0.10	–0.67	–0.67	–0.24
22/109	1.06	0.67	0.80	0.69	0.44	–0.12	–0.71	–0.67	–0.26
22/113	0.93	0.71	0.83	0.64	0.37	–0.22	–0.51	–0.33	–0.34
22/117 (OM1)	1.06	0.70	0.82	0.71	0.56	–0.11	–0.72	–0.30	–0.33

TNR-1: trimethylnaphthalene ratio 1 (2,3,6-TMN/[1,4,6- + 1,3,5-TMN]). Alexander et al. 1985.
TNR-2: trimethylnaphthalene ratio 2 (2,3,6- + 1,3,7-TMN/[1,4,6- + 1,3,5- + 1,3,6-TMN]). Radke et al. 1986.
VR_{TNR-2}: calculated reflectance from TNR-2 (0.60 × TNR-2 + 0.40). Radke et al. 1994.
TMNr: trimethylnaphthalene ratio (1,3,7-TMN/[1,3,7-TMN + 1,2,5-TMN]). van Aarssen et al. 1999.
MPI-1: methylphenanthrene index 1 (1.89 × [3-MP + 2-MP]/[P + 1.26 × (9-MP + 1-MP)]). Cassani et al. 1988.

Table 3.6 Inorganic geochemical proxies of the source rocks from the K_2qn^1.

Sample	SiO_2 (wt%)	Al_2O_3 + Na_2O + K_2O (wt%)	Al (wt%)	Ti (wt%)	U/Th	Cu/Zn	Sr/Ba	Ca/Mg	100×(Mg/Al)	Cu/Al (10^{-4})	C-value	CIA	Sr/Cu	Rb/Sr	Ga/Rb	Zr/Al (10^{-4})	U_{EF}	Mo_{EF}
Unit 2																		
22/055	55.55	22.08	8.13	0.33	0.32	0.29	0.98	1.71	16.36	4.44	0.46	64.33	9.28	0.46	0.17	20.79	5.08	4.96
22/056	56.69	21.22	7.78	0.31	0.36	0.21	0.65	2.67	12.60	3.17	0.59	59.12	15.67	0.38	0.16	23.01	5.88	6.28
22/058	56.42	22.41	8.00	0.38	0.33	0.34	0.26	1.79	15.00	4.36	0.45	61.83	8.48	0.47	0.18	23.50	5.46	5.13
22/061	59.22	23.09	8.66	0.36	0.37	0.23	0.51	1.00	13.39	3.18	0.48	65.21	8.40	0.61	0.19	20.32	4.99	7.60
22/063	57.52	22.64	8.41	0.37	0.32	0.30	0.82	1.51	12.96	4.00	0.51	61.33	10.03	0.39	0.19	22.00	4.15	5.29
22/064	57.24	23.96	9.12	0.34	0.33	0.26	0.72	1.13	12.94	3.40	0.51	64.64	9.19	0.55	0.18	20.61	4.45	8.68
22/066	52.99	22.06	8.24	0.33	0.30	0.28	1.04	2.37	16.50	4.21	0.48	60.26	12.39	0.32	0.18	23.67	4.74	7.45
22/067	53.59	22.32	8.22	0.35	0.39	0.29	0.88	1.67	19.46	4.20	0.41	64.31	8.35	0.51	0.17	23.24	6.20	6.01
22/068	52.02	21.69	7.97	0.35	0.53	0.26	1.23	3.83	14.43	3.58	0.36	56.17	20.25	0.24	0.17	24.22	7.18	9.88
22/070	57.44	23.14	8.62	0.34	0.38	0.27	0.75	1.31	12.76	3.82	0.51	63.25	8.66	0.55	0.17	23.43	5.34	6.60
22/072	53.84	21.94	8.15	0.34	0.37	0.25	1.01	2.39	16.69	3.61	0.39	61.35	14.08	0.36	0.17	24.54	6.51	6.92
22/074	51.36	24.00	8.86	0.39	0.42	0.25	0.90	1.56	20.32	3.40	0.38	67.52	14.12	0.39	0.16	24.49	6.22	5.91
Unit 1																		
22/075	61.98	22.71	8.07	0.39	0.22	0.20	0.49	0.82	13.01	2.47	0.56	63.76	11.66	0.66	0.17	28.87	3.89	4.05
22/076	60.18	23.78	8.44	0.40	0.20	0.22	0.52	0.92	14.45	3.82	0.46	64.40	8.79	0.59	0.17	29.15	3.64	2.52
22/080	58.92	23.47	8.62	0.38	0.23	0.25	0.53	0.96	14.85	3.31	0.49	63.35	9.82	0.56	0.17	26.10	3.64	2.60
22/081	58.08	23.81	9.00	0.39	0.21	0.19	0.58	1.03	14.89	3.48	0.50	64.18	9.94	0.53	0.16	25.67	3.30	1.21
22/083	57.71	25.43	9.28	0.37	0.25	0.28	0.48	0.44	13.58	4.01	0.50	67.46	6.59	0.76	0.15	23.06	3.64	2.63
22/086	54.36	23.18	8.72	0.36	0.22	0.24	0.77	1.86	16.86	3.30	0.41	61.81	15.35	0.39	0.16	23.28	3.42	2.71
22/087	56.53	21.68	8.22	0.35	0.25	0.23	0.78	1.87	16.18	3.20	0.52	59.95	15.25	0.38	0.15	23.72	3.83	5.68
22/088	59.42	22.31	8.19	0.34	0.25	0.22	0.62	1.80	11.60	3.04	0.58	59.52	14.34	0.43	0.16	27.23	3.71	9.26
22/092	58.91	23.98	9.20	0.42	0.21	0.21	0.60	0.99	15.33	2.99	0.48	63.56	10.98	0.55	0.17	25.87	3.45	1.60
22/094	61.00	24.63	8.97	0.43	0.20	0.23	0.47	0.65	12.26	3.18	0.47	65.96	8.91	0.72	0.16	29.88	3.67	0.85
22/095	57.51	24.18	9.21	0.35	0.24	0.21	0.48	0.60	16.07	2.74	0.56	64.85	9.72	0.68	0.16	22.80	3.05	4.96
22/096	58.49	23.10	8.28	0.35	0.24	0.20	0.57	1.23	14.61	2.81	0.46	61.88	12.02	0.54	0.16	25.00	3.32	5.27
22/097	58.53	22.90	8.39	0.36	0.22	0.20	0.57	1.47	14.06	2.82	0.47	61.27	12.66	0.52	0.16	24.55	3.16	3.74
22/099 (OM2)	46.62	19.36	7.32	0.26	0.47	0.42	1.40	3.71	24.59	5.16	0.28	54.32	13.12	0.27	0.16	23.09	8.27	12.16
22/100	54.38	23.03	8.44	0.36	0.26	0.21	0.72	1.65	18.36	2.65	0.40	63.99	15.18	0.46	0.16	23.34	3.54	2.63
22/102	60.79	24.18	8.87	0.36	0.25	0.20	0.47	0.73	11.72	2.57	0.50	64.96	9.91	0.73	0.15	24.46	3.18	1.98
22/103	59.97	24.36	8.92	0.38	0.31	0.25	0.50	0.73	11.21	3.36	0.50	64.92	7.47	0.71	0.17	24.55	4.14	3.78
22/105	58.21	24.98	9.29	0.45	0.15	0.27	0.58	0.93	14.75	3.89	0.48	65.83	7.53	0.69	0.16	26.59	2.81	0.46
22/107	59.71	26.61	9.46	0.46	0.21	0.23	0.58	0.76	10.99	3.31	0.35	66.45	8.27	0.73	0.18	28.86	3.81	0.52
22/109	61.08	24.18	8.76	0.40	0.22	0.15	0.55	0.87	11.87	2.50	0.44	64.92	10.46	0.77	0.16	28.42	3.92	0.66
22/110	60.22	24.21	8.82	0.44	0.23	0.27	0.74	1.41	10.66	2.99	0.42	64.25	10.27	0.60	0.18	28.80	3.78	1.55
22/113	60.26	22.86	8.53	0.36	0.28	0.27	0.68	1.25	12.43	3.83	0.53	63.65	8.84	0.51	0.17	25.44	4.18	3.29
22/115	58.69	24.53	8.79	0.38	0.20	0.20	0.54	0.59	12.51	2.67	0.59	66.50	9.06	0.88	0.15	26.17	3.60	0.78
22/117 (OM1)	50.09	22.74	8.03	0.33	0.67	0.35	1.02	1.97	18.93	4.45	0.49	63.49	9.33	0.50	0.15	24.53	10.56	5.97
22/120	56.54	22.72	8.45	0.38	0.28	0.27	0.84	1.75	14.91	3.44	0.47	63.05	11.27	0.48	0.16	25.92	4.53	3.58
22/122	60.51	26.92	9.65	0.48	0.22	0.22	0.64	0.61	7.36	3.10	0.36	66.82	9.00	0.69	0.18	30.36	3.64	0.84

3.5 Discussion

3.5.1 Thermal maturity

Rock-Eval T_{max} data (avg. 440 °C) suggest that the source rocks are within the (early-peak) oil window, which is consistent with the VR_r values. This maturity interpretation is further supported by aliphatic thermal maturity parameters, i.e., CPI and OEP1 ratios close to 1 (Table 3.3), owing to the presence of thermally generated even-numbered *n*-alkanes (Peters et al., 2005). The C_{29} Ts/(C_{29} Ts + C_{29} hopane) and Ts/(Ts + Tm) ratios increase with increasing thermal maturity and are widely used as maturity indicators (Peters et al., 2005; Fang et al., 2019; Qiao et al., 2021a). In the cross-plot of C_{29} Ts/(C_{29} Ts + C_{29} hopane) versus Ts/(Ts + Tm), the samples of this study plot close to the very well-studied samples of the Posidonia shale from the borehole Harderode (Germany) that corresponds to a VR_r of 0.88% (Fig. 3.6a). In addition, the cross-plot of C_{29} ααα 20S/(20S + 20R) versus C_{29} ββ /(ββ + αα) sterane ratios is effective in reflecting the thermal maturity of source rocks, with values reaching an equilibrium of approximate ca. 0.55 corresponding to about 0.8% VR_r and ca. 0.7 corresponding to about 0.9% VR_r, respectively (Fig. 3.6b; Seifert and Moldowan, 1986; Peters et al., 2005; Song et al., 2017; Qiao et al., 2021a; Zheng et al., 2022). The sterane maturity biomarker ratio C_{29} ααα 20S/(20S + 20R) plots in the equilibrium area, thus depicting oil window maturity (Seifert and Moldowan, 1986). However, it should be noted that only a minimum maturity can be estimated based on the equilibrium value of the sterane isomerization. Aromatic maturity proxies, including TNR-1, TNR-1, MPI-1, TMNr, and VR_{TNR-2}, also indicate that the samples are at the stage of oil generation (Table 3.5; Radke et al., 1994; George et al., 2001; Volk et al., 2005; Fang et al., 2019; Qiao et al., 2021a).

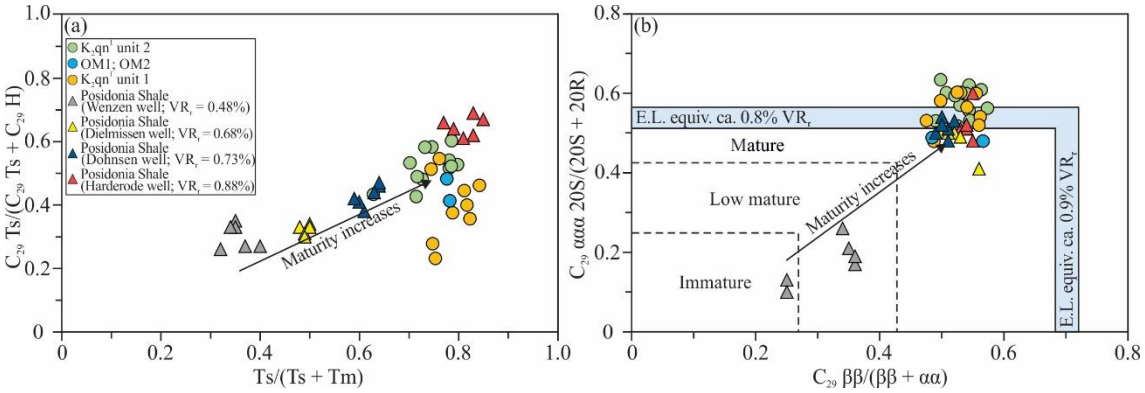

Figure 3.6 Molecular thermal maturity indicators of the source rocks from the K_2qn^1. (a) Cross-plot of C_{29} Ts/(C_{29} Ts + C_{29} H) versus Ts/(Ts + Tm). (b) C_{29} ααα 20S/(20S + 20R) versus C_{29} ββ/(ββ + αα). E.L. equiv. = equilibration levels equivalent to vitrinite reflectance values (taken from Peters et al., 2005). Data of Posidonia shale are taken from Fang et al. (2019) for comparison.

3.5.2 Paleo-salinity, paleo-redox conditions, and paleo-productivity

Salinity exerts a strong influence on aquatic organism communities composition in lacustrine systems (Romero-Viana et al., 2012), which is recorded in biomarker data. Additionally, high salinity is generally accompanied with density stratification in lakes creating oxygen-depleted bottom waters, which is beneficial to preservation of OM (Powell, 1986). Generally, sulfur can be transferred from an anoxic water column to source rocks, mainly as pyrite. Most sulfur transfer occurs, however, from anoxic pore water, where microbial sulfate reduction generates H_2S that reacts with Fe^{2+} in sediments to form pyrite/marcasite (Berner and Raiswell, 1983, 1984; Sim et al., 2011; Wei and Algeo, 2020). In iron-depleted environments, organic sulfur instead of pyrite can form leading to formation of type II or Type-I sulfur-rich kerogen (Zhao et al., 2022a). The freshwater environment is, however, usually characterized by low contents of aqueous sulfate, while marine settings have much higher sulfate concentrations (Wei and Algeo, 2020); accordingly, most freshwater sediments have low TS/TOC ratios. Wei and Algeo (2020) proposed a TS/TOC ratio of 0.1 as the boundary to separate freshwater sediments from brackish and marine sediments by analyzing hundreds of data points. The same authors also suggested that the TS/TOC range of 0.1–0.5 is the overlapping area for brackish and marine samples, while almost all marine samples are characterized by TS/TOC ratios higher than 0.5. The author explained the large overlapping area of brackish and marine samples by the availability of labile organic substrates to drive microbial sulfate reduction (Wei and Algeo, 2020). In this study, 9 samples from unit 1 plot close to the freshwater boundary, while 15 samples fall into the brackish-marine and marine zone (Figs. 3.7a, 3.8a). Unit 2 and two exceptional OM-rich samples in unit 1 plot in the transitional or even marine zones (Figs. 3.7a, 3.8a). It should be noted that sample No. 22088 (TOC = 0.87 wt%) from unit 1 is characterized by the highest TS/TOC ratio of 2.54 (Figs. 3.7a, 3.8a). Wei and Algeo (2020) suggested that TS/TOC ratio is arbitrarily variable in sediments with low TOC and TS concentrations, which can result in erroneous estimations of redox conditions. TS/TOC ratio is recommended to be applied in samples with at least 1.0 wt% TOC (Wei and Algeo, 2020). Overall, the TOC/TS relationship indicates that the sediments of unit 2 and two exceptional OM-rich samples in unit 1 do not represent typical sulfate-depleted freshwater, while this is the case for the remaining part of unit 1.

As an empirical element proxy, Sr/Ba ratio acts as an indicator of paleo-salinity in fine-grained siliciclastic sediments (Tao et al., 2017; Li et al., 2020; Wei and Algeo, 2020; Burnaz et al., 2022). Aqueous Sr with much higher concentrations in marine environments is easily adsorbed onto clay minerals (Wei and Algeo, 2020). Additionally, in terrestrial conditions, Sr is released more easily than Ba from sediments during chemical weathering (Yang et al., 2006b). Therefore, marine sediments are characterized by much higher Sr/Ba ratios compared to freshwater deposits. Sr/Ba ratios of < 0.2, 0.2–0.5, and > 0.5 are correlated to freshwater, brackish, and marine facies, respectively. In unit 1, Sr/Ba ratio ranges from 0.47 to 0.84, which suggests a brackish-marine depositional environment (Fig. 3.8b).

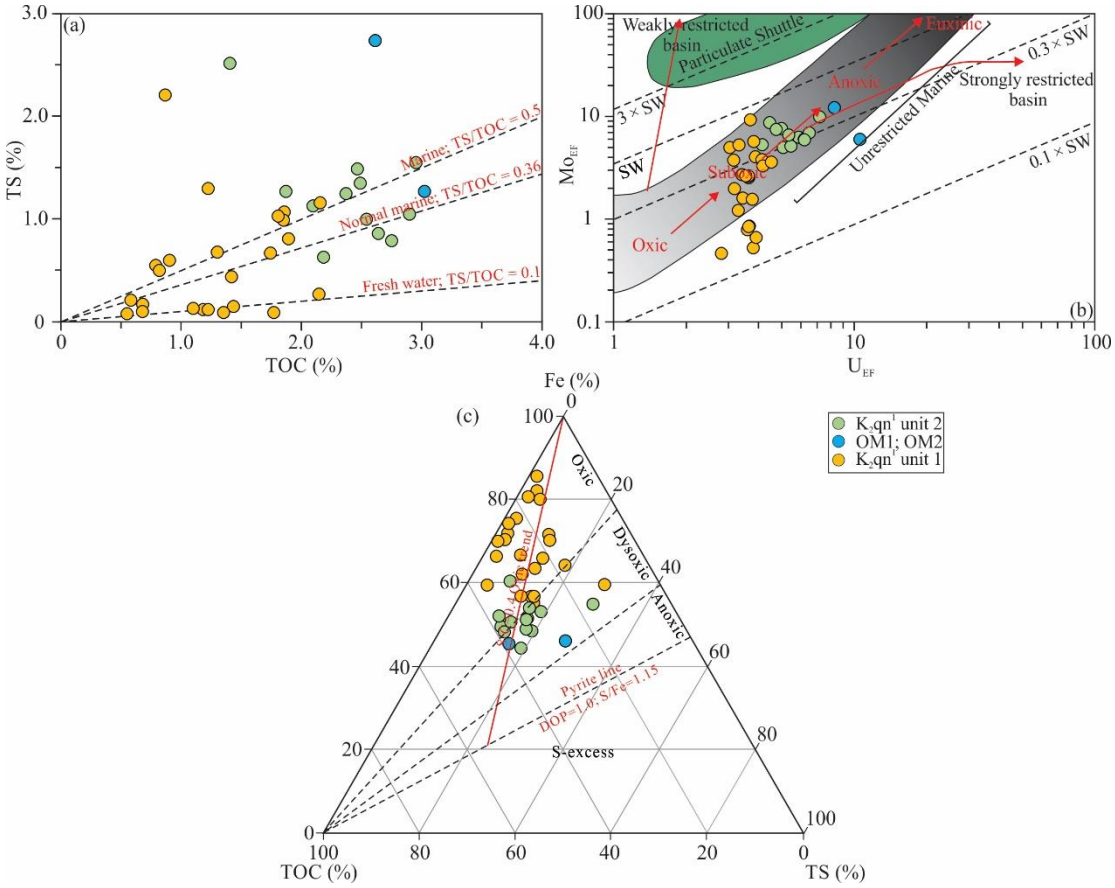

Figure 3.7 (a) Cross-plot of TS versus TOC. (b) Cross-plot of Mo_{EF} versus U_{EF} (modified from Algeo and Tribovillard, 2009; Tribovillard et al., 2012). The dashed lines represent the Mo/U molar ratios equal to the modern seawater value (1 × SW) and fractions thereof (3 × SW and 0.3 × SW). The black field refers to the variation of redox conditions in an unrestricted marine environment. The green field refers to the particulate shuttle trend, characteristic of depositional systems in which intense redox cycling of metal (especially Mn−) oxyhydroxides occurs within the water column. (c) Ternary diagram of relative concentrations of TOC, TS, and Fe.

Most samples from unit 2 and two exceptional OM-rich samples in unit 1 have even higher Sr/Ba ratios, with average values of 0.81 and 1.21, respectively. Thus, these samples were deposited probably in a more saline environment relative to unit 1. Li and Wang (1990) observed similar trends of Ca/Mg and Sr/Ba in the lacustrine source rocks deposited in the Biyang Basin, Gaoyou Basin, and Dongpu Basin, east China. Due to the close relation of MgO and Al_2O_3 to marine and continental environments, respectively, Lei et al. (2002) proposed 100×(Mg/Al) ratio > 10 indicates saline conditions, a ratio from 1 to 10 indicates brackish conditions and a ratio < 1 indicates freshwater conditions. The 100 × (Mg/Al) ratio was also successfully applied to reconstruct water salinity prevailing during the deposition of the Jurassic oil shales in the Qaidam Basin and the Cretaceous Nenjiang Formation in the Songliao Basin (Xu et al., 2015; Wu et al., 2022). In several studies, Ca/Mg and 100×(Mg/Al) ratios in sediments were reported to increase with increasing salinity (Li and Wang,

1990; Xu et al., 2015; Wu et al., 2022). As shown in Fig. 3.8c and Table 3.6, Ca/Mg and 100 × (Mg/Al) ratios exhibit similar trends as TS/TOC and Sr/Ba ratios, suggesting a higher water salinity during the deposition of unit 2 and two exceptional OM-rich samples in unit 1.

Gammcerance, possibly generated by the reduction of tetrahymanol (gammaceran-3β-ol) (ten Haven et al., 1989; Venkatesan, 1989), is widely used to reflect salinity changes (Peters et al., 2005). The occurrence of abundant gammacerane (Gam index > 0.1) is thought to be an indicator of a hypersaline environment and stratified water column during the deposition of the source rocks (Sinninghe Damsté et al., 1995; Sepúlveda et al., 2009; Song et al., 2017). As shown in Fig. 3.8d, the Gam index reflects the increasing salinity of the paleo-lake from unit 1 (avg. 0.09) to unit 2 (avg. 0.14) and the most saline environment during the deposition of two exceptional OM-rich samples in unit 1 (avg. 0.18). This is consistent with the results of the elemental proxies for salinity.

Wei et al. (2018) identified marine incursions into the Paleogene Bohai Bay Basin lake system by the occurrence of marine fossils and high values of salinity proxies, e.g., avg. Sr/Ba ratio of 1.95 in the fourth member of the Eocene Shahejie Formation. The presence of C_{30}-steranes with a 4-desmethyl structure is regarded as a marker for paleo-marine biotic input (Moldowan, 1984). Hou et al. (2000) observed abundant C_{30} 4-desmethylsteranes (24-*n*-propylcholestanes), derived diagenetically from 24-*n*-propylchoesterols present in the marine alga Sarcinochrysidales, in the K_2qn^1 samples, serving as one of the most powerful molecular parameters for identifying marine transgressional events in sedimentary records. In this study, C_{30} steranes show low concentrations in unit 1, while the two exceptional OM-rich samples in unit 1 and samples in unit 2 exhibit a higher abundance of this compound (Fig. 3.5g-i). The occurrence of C_{30} steranes as well as the significant positive excursion of the salinity proxies (e.g., Sr/Ba and Ca/Mg ratios and Gam index value) in the two exceptional OM-rich samples in unit 1 (Fig. 3.8) suggest the occurrence of marine transgressive events. Furthermore, the occurrence of the C_{30} steranes and range of the salinity proxies observed in unit 2 may suggest a permanent but weak marine influence, i.e. the lake probably was connected to the sea via a (narrow?) gateway.

Paleo-redox conditions play an important role in OM accumulation by controlling its preservation. Multiple molecular biomarkers and trace element proxies (e.g., Pr/Ph, HHI, and U/Th) and the size distribution of pyrite framboids are used as robust indicators of bottom water redox conditions (Peters and Moldowan, 1991; Jones and Manning, 1994; Peters et al., 2005). Algeo and Tribovillard (2009) suggested that the degree of enrichment of authigenic Mo and U is closely associated with the redox variation with high concentrations corresponding to more reducing conditions. In marines sediments, oxic environments have the lowest concentrations of Mo and U, while the suboxic and anoxic facies are characterized by moderate and strong enrichments with EFs of Mo and U < 10 and > 10, respectively (Algeo and Tribovillard, 2009; Tribovillard et al., 2012). In this study, there is a major difference in the Mo_{EF}-U_{EF} covariation pattern among the studied samples (Fig. 3.7b). The progressive degree of Mo and U enrichment from units 1 to 2 suggests a more reducing

water column during the deposition of unit 2. However, some samples in unit 1 also represent reducing conditions. Samples, which represent the postulated marine transgressive events show the highest level of Mo and U enrichment, which is indicative of deposition under the most reducing bottom-water conditions. This reducing depositional environment was possibly associated with the water density stratification caused by seawater incursion.

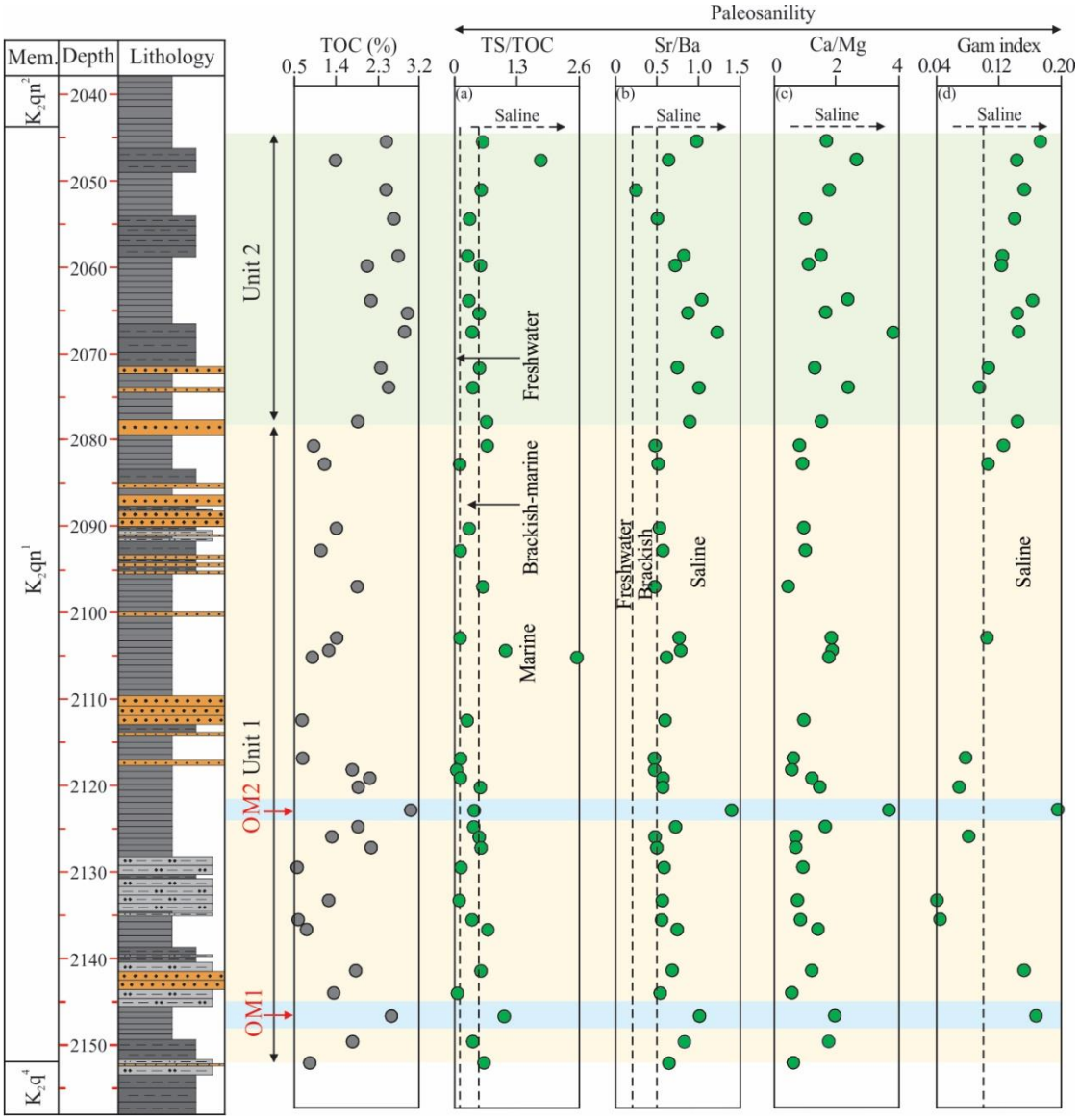

Figure 3.8 Stratigraphic profiles of palaeosalinity parameters. (a) TS/TOC. (b) Sr/Ba. (c) Ca/Mg. (d) Gam index.

The relative concentrations of TOC, TS, and Fe reflect mainly oxic bottom water conditions for unit 1 and dysoxic conditions for unit 2 and samples, which represent the postulated marine transgressive events (Fig. 3.7c). It should be noted that this plot has been developed originally for marine sediments, where sulfur contents are higher; therefore almost all lacustrine sediments are "too

oxic". Only the relative differences should be considered here, and they indicate that unit 2 samples are much more oxygen-depleted than those of unit 1 on average.

The ratio U/Th is widely used to assess paleo-redox conditions and shows high values in sediments derived from reducing bottom-water columns (Jones and Manning, 1994; Wignall and Twitchett, 1996; Kimura and Watanabe, 2001; Wang et al., 2017; Wu et al., 2022). However, the threshold values of the different redox conditions remain controversial. Jones and Manning (1994) proposed a U/Th ratio of 0.75 as the oxic-dysoxic boundary, while Wang et al. (2017) adopted the U/Th ratios of < 0.27, 0.27–0.50, and > 0.50 to indicate oxidizing, dysoxic, and anoxic conditions, respectively. Algeo and Liu (2020) suggested that one important problem in the calculation method for redox thresholds proposed by Jones and Manning (1994) is the use of DOP_T (degree of pyritization based on total sulfur and iron concentrations) instead of true DOP (degree of pyritization based on Fe speciation data) to determine the U/Th ratio. Besides, there is uncertainty about the relationship between redox conditions and elemental proxies in different formations owing to the complex depositional factors (Algeo and Liu, 2020). Similar to the varying patterns of the above-mentioned proxies, the U/Th ratio exhibits an increasing trend upward from units 1 to 2, suggesting the evolution towards more reducing conditions (Fig. 3.9a). Samples, which represent the postulated marine transgressive events also have high U/Th values. This trend is also consistent with the variation of the Cu/Zn ratio, which shows a rise in values in reducing bottom-water conditions and a decline in values in oxidizing conditions (Fig. 3.9b; Dypvik, 1984; Quan et al., 2017).

The molecular biomarker proxy Pr/Ph is commonly used as a robust indicator of redox conditions with low values (<1.0) implying anoxic conditions. In this study, most samples have Pr/Ph ratios higher than 1.0, indicating that relatively oxidizing conditions prevailed during the deposition. However, it should be noted that lower Pr/Ph ratios are observed on average in unit 2 (avg. 1.33) and samples, which represent the postulated marine transgressive events (avg. 1.37) relative to unit 1 (avg. 1.74), suggesting more reducing conditions in Unit 2 (Fig. 3.9c). Besides, the size distribution of pyrite framboids (Figs. 3.9d, 3.10a–f) as well as the relation between standard deviation/skewness values and mean diameters of pyrite framboids further confirm that relatively less oxygen-rich conditions occurred during the deposition of unit 2 (Fig. 3.10g and h). Similar to the triangular plot of Fe-TS-TOC (Fig. 3.7c), the absolute values are of little interest here, because the original plots were developed for marine environments with higher sulfur contents.

Cu is mainly delivered to the sediments associated with organometallic complexes and can serve as an effective indicator of paleo-productivity (Tribovillard et al., 2006). A high concentration of Cu suggests that abundant OM flux delivered this element to the sediments. In order to compensate for the dilution effect of terrigenous clastic materials, Cu/Al ratio rather than absolute Cu contents is commonly presented and discussed. It tends to increase though with much scatter upward from units 1 to 2, while the highest value is recorded for one of the two in samples, which represent the postulated marine transgressive events, indicating a relatively enhanced paleo-productivity (Fig. 3.9e).

In conclusion, major and trace elements data, molecular biomarkers, as well as the pyrite framboid size distribution suggest that unit 1 was mainly deposited under oxic-dysoxic and fresh-brackish water column conditions, while unit 2 and samples, which represent the postulated marine transgressive events were deposited in less oxygenated and more saline as well as more sulfate-rich environments (Figs. 3.8–3.10).

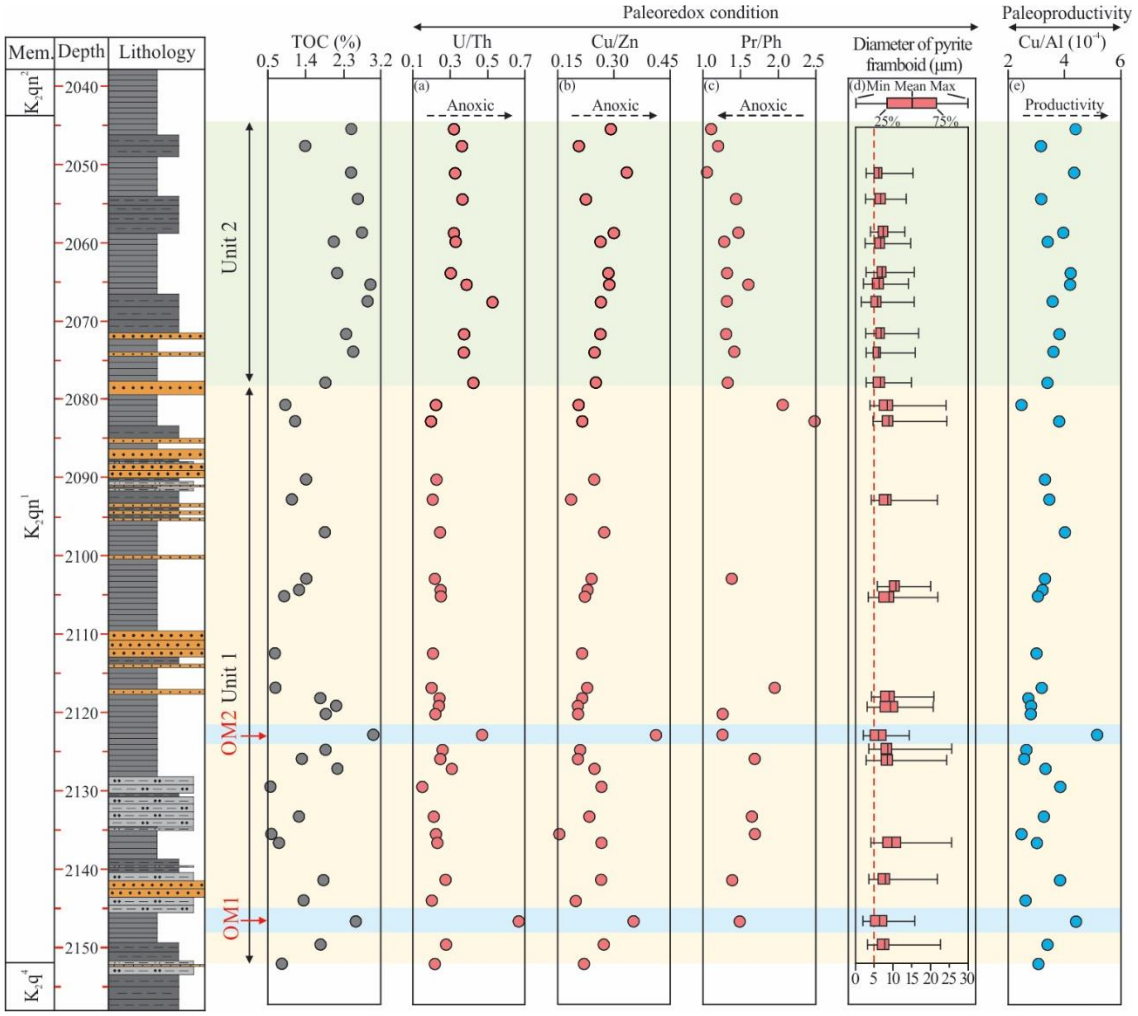

Figure 3.9 Stratigraphic profiles of paleoredox and paleoproductivity parameters. (a) U/Th. (b) Cu/Zn. (c) Pr/Ph. (d) size distributions of pyrite framboids. (e) Cu/Al (10^{-4}).

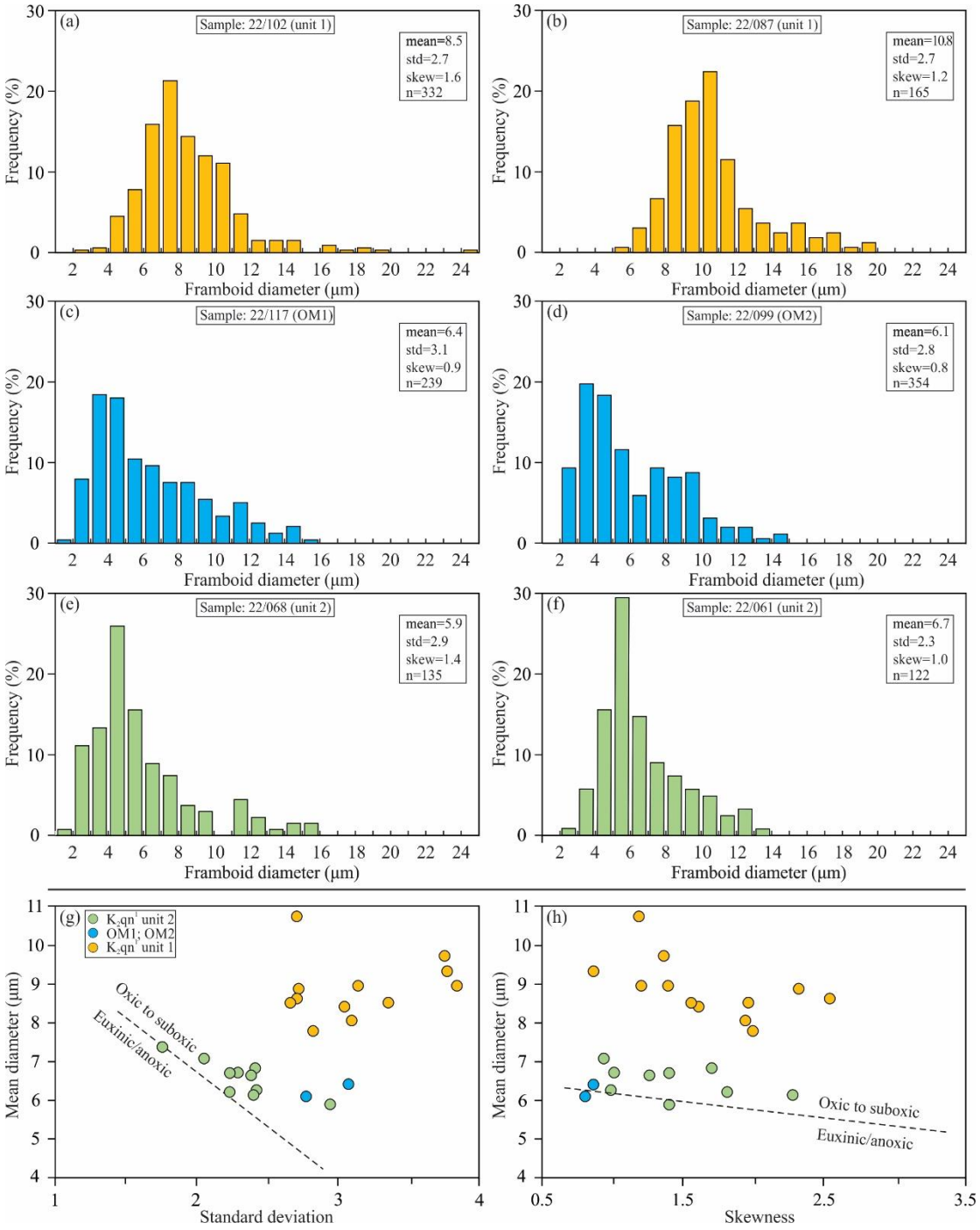

Figure 3.10 (a–f) Histograms showing the distribution of pyrite framboid diameters of the representative samples (samples 22/061, 22/068, 22087, 22/099, 22/102, and 22/117). (g) Cross-plot of the mean framboid diameters versus the standard deviation and (h) skewness of diameter distribution (after Wilkin et al., 1996).

3.5.3 Paleo-climate, detrital input and weathering

The reconstruction of palaeoclimatic conditions is an important topic in earth sciences. Furthermore, paleo-climate influenced weathering intensity and thus input of terrigenous materials into the lake system as well as plant communities. Zhao et al. (2014) suggested that a semi-humid and subtropical climate prevailed during the deposition of K_2qn^1 based on the analysis of fossils, although these occur in low abundance only. In contrast, Li (2019) suggested that the paleo-climate evolved from arid to humid and finally back to arid during the depositional process by studying the elemental geochemistry of the Qingshankou Formation from the well Songke 1 in the southern part of the central depression. In addition, Zhu et al. (2017) studied cores, well logs, and seismic sedimentology of the Qingshankou Formation in the Qijia area, Songliao Basin, and proposed a sedimentary model suggesting an arid climate for sediments of the Qingshankou Formation. The cross-plot of Ga/Rb versus K_2O/Al_2O_3 ratios can be used as a paleo-climate indicator, because the enrichment of Al and Ga is associated with kaolinite representing warm and humid conditions. In contrast, the elements K and Rb are related to illite representing rather dry and cool climatic conditions (Ratcliffe et al., 2004, 2010; Roy and Roser, 2013; Qiao et al., 2022). As shown in Fig. 3.11a, most studied samples plot within an area indicative of arid/cold conditions with weak chemical weathering.

This conclusion is further supported by the binary diagram of SiO_2 versus $Al_2O_3 + K_2O + Na_2O$ (Fig. 3.11b; Suttner and Dutta, 1986). CIA is commonly used to reveal the weathering intensity by the quantitative calculation of the removal of labile components relative to stable residual constituents in sediments and also serves as a robust geochemical proxy of variations in paleo-climate (Nesbitt and Young, 1982; Fedo et al., 1995; Wang et al., 2020). Kaolinite, with a CIA value of 100, reflects the highest weathering intensity, while fresh minerals and parent rocks are characterized by lower values, e.g., feldspars with a CIA value of 50. As shown in Table 3.6, the CIA exhibits a value lower than 70, reflecting weak chemical weathering intensity related to arid or semi-arid climate. Influenced by the diagenetic K-metasomatism on K_2O content in rocks, the A–CN–K ($Al_2O_3 – CaO^* + Na_2O – K_2O$) ternary diagram was applied to correct CIA values (Fedo et al., 1995; Yan et al., 2010; Wang et al., 2020). The corrected CIA values are relatively consistent and mainly cluster between 50 and 70, pointing to a predominantly cold and dry climate where sediments experienced weak weathering (Fig. 3.11c). This result is in line with the CIA values (58–68) of K_2qn^1 reported by Xu et al. (2019b).

As another climate-sensitive trace element proxy, the Sr/Cu ratio is often applied. Values > 5 (Yandoka et al., 2015; Pan et al., 2020a; Yang and Guo, 2021) or > 10 (Jia et al., 2013; Li et al., 2021b) are regarded as indicative of an arid climate. In this study, samples from the K_2qn^1 with Sr/Cu ratio higher than 5 and even higher values of > 10 characterize approximately half of the samples (Fig. 3.12a), indicating generally arid or at least semi-arid paleo-climate conditions. Xu et al. (2015) observed similar Sr/Cu ratios in K_2qn^1 (avg. 6.33). A similar result is also deduced from the high Sr/Cu

ratios (up to 15.6) of mudstones in K_2qn^1 from the south-east uplift, Songliao Basin, reported by Jia et al. (2013). This is the highest Sr/Cu value of K_2qn^1 in the Songliao Basin reported so far.

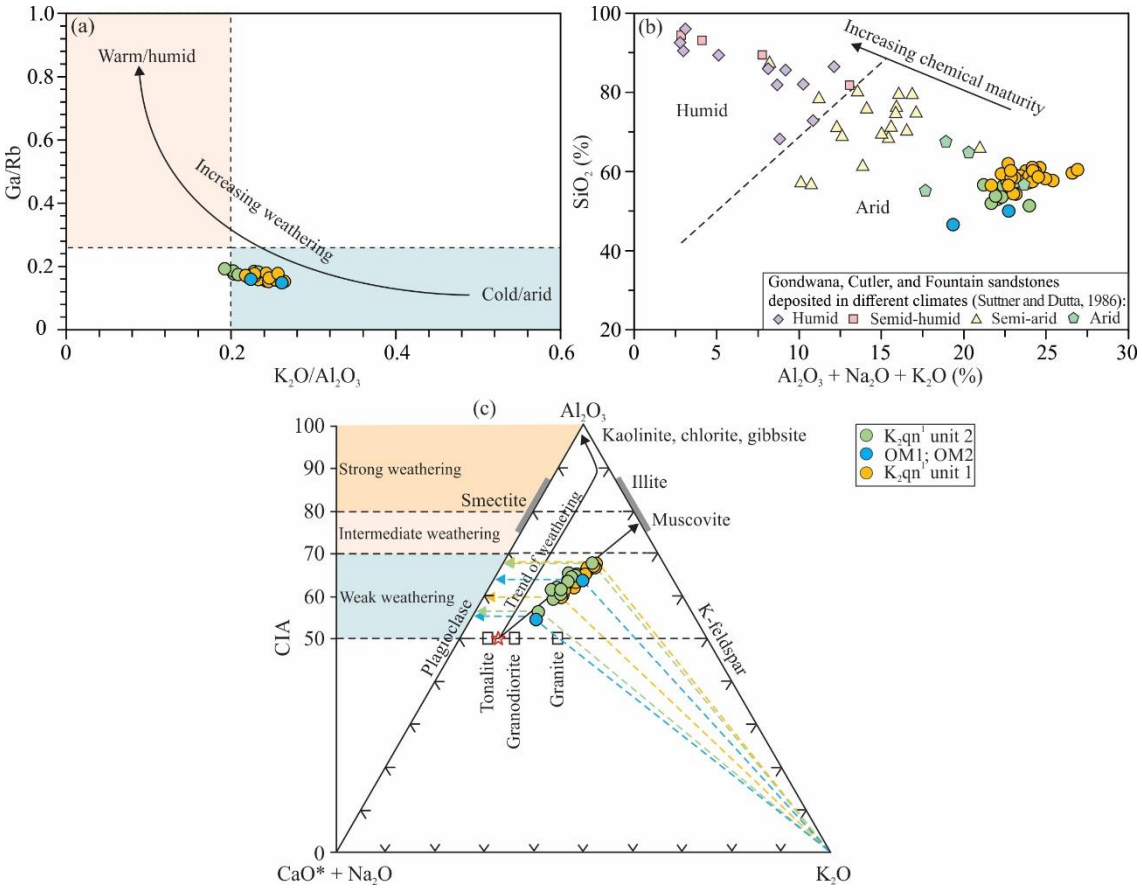

Figure 3.11 (a) Discrimination diagrams of Ga/Rb versus K_2O/Al_2O_3 (after Roy and Roser, 2013) and (b) SiO_2 versus ($Al_2O_3 + K_2O + Na_2O$) (after Suttner and Dutta, 1986). (c) A–CN–K ternary diagrams for K metasomatism correction, showing corrected CIA value and composition of unweathered source rock (after Yan et al., 2010).

Arid conditions are further supported by the measured low Rb/Sr ratio (0.24–0.88, avg. 0.54) based on the differences in the mobility of these elements from parent rocks during chemical weathering (Fig. 3.12b; Yang et al., 2006b; Tao et al., 2017; Li et al., 2021b). This result is consistent with the previous study of Jia (2012), in which an even lower Rb/Sr ratio of 0.25 was reported for the oil shale in the Qingshankou Formation, while mudstone had a higher Rb/Sr ratio of 0.42.

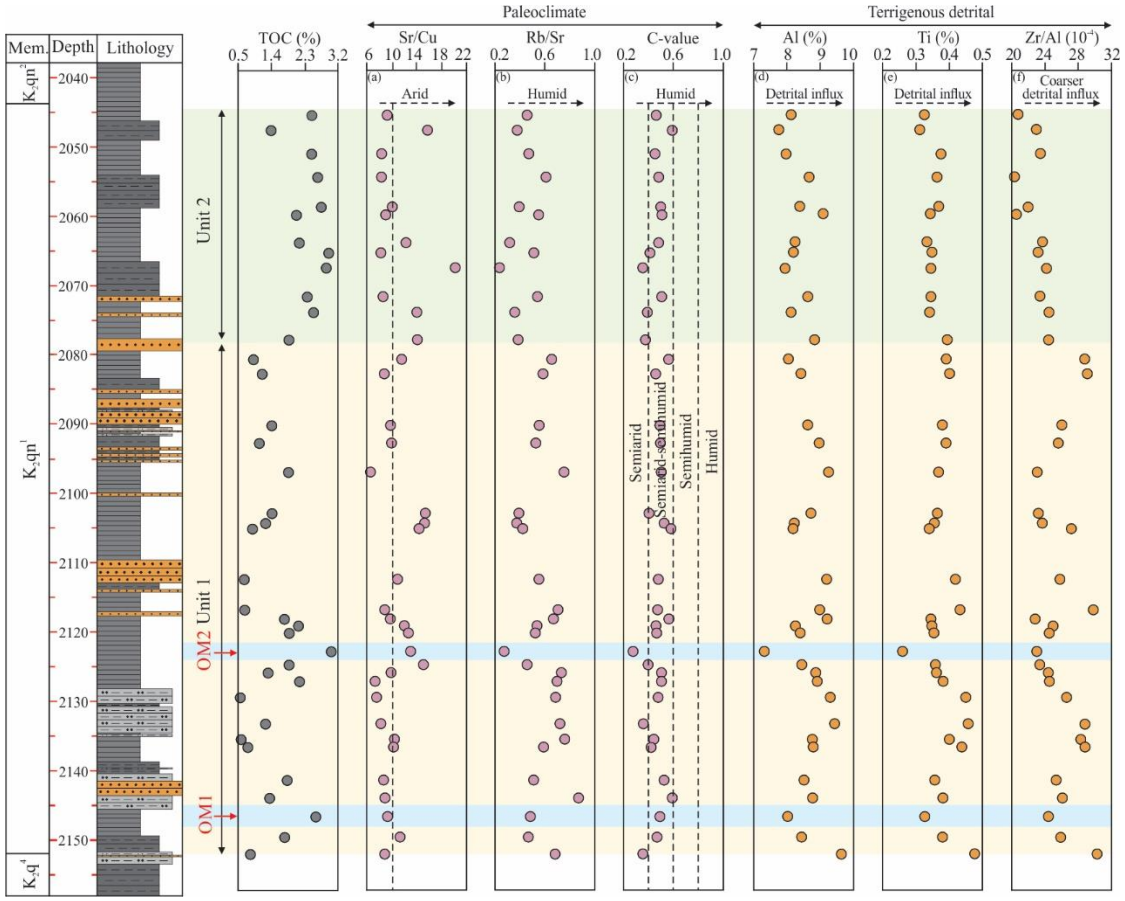

Figure 3.12 Stratigraphic profiles of paleoclimate and terrigenous influx parameters. (a) Sr/Cu. (b) Rb/Sr. (c) C-value. (d) Al (%). (e) Ti (%). (f) Zr/Al (10^{-4}).

Zhao et al. (2007) first used the C-value to reflect the paleoclimate conditions during the deposition of source rocks in the Junggar Basin, China. Subsequently, C-value was widely applied as an indicator to reconstruct paleoclimate changes (Moradi et al., 2016; Doner et al., 2019; Li et al., 2020). C-values of > 0.8, 0.6−0.8, 0.4−0.6, 0.2−0.4, and < 0.2 are correlated to a humid, semi-humid, semi-arid to semi-humid, semi-arid, and arid paleoclimate, respectively (Zhao et al., 2007). In this study, the C-values (0.28–0.59, avg. 0.47) indicate a semiarid to semiarid-semihumid paleo-climate according to the thresholds in the previous publications (Fig. 3.12c). However, based on the large variety of multiple geochemical proxies used in this study, the overall climatic conditions are interpreted as mainly arid or semi-arid coupled to a low degree of weathering during the deposition of the K_2qn^1 (Fig. 3.12a and b). It should be noted that unit 1 is characterized by somewhat higher values of these proxies, e.g., Rb/Sr ratio, relative to unit 2 and samples, which represent the postulated marine transgressive events, indicating a slightly warmer and/or more humid environment during deposition of unit 1.

Al is derived from clay minerals, while Ti is principally present in both clay minerals and heavy minerals (Rimmer et al., 2004; Calvert and Pedersen, 2007). The concentrations of Al and Ti are

extensively used as indicators of clastic influx, owing to the relatively immobile chemical properties during diagenesis (Rimmer, 2004; Burnaz et al., 2022). Stratigraphically, Al and Ti contents show the highest values in unit 1, reflecting the high terrigenous detrital input (Fig. 3.12d and e). Zr mainly occurs in coarse silt or the very fine-grained sand fraction in siliciclastic sediments and almost only exists in zircons (Bábek et al., 2016). Since an increase in the Zr/Al ratio indicates a coarser detrital input, it can sometimes be correlated with the water depth (El-Shafeiy et al., 2016; Cao et al., 2020; Shang et al., 2020). In this study, Zr/Al ratios show a declining trend upward, suggesting an increasing water depth from units 1 to 2 (Fig. 3.12f).

3.5.4 Origin of organic matter

Rock-Eval data exhibit a lower HI for samples from unit 1 than for unit 2 thus variable kerogen composition ranging from type III to II, suggesting a mixed source of OM (Figs. 3.3, 3.13a). This result is in accordance with the microscopy data. Microscopic observation shows that vitrinite accounts for a higher relative volumetric percentage of the total macerals in unit 1 relative to samples of unit 2 and samples, which represent the postulated marine transgressive events (Table 3.2), indicating the contribution of more terrestrial OM (Fig. 3.13b). In contrast, OM in unit 2 and samples, which represent the postulated marine transgressive events mainly consists of liptinite (lamalginite and telalginite). However, as shown in Fig. 3.5a–c, *n*-alkane distributions suggest that unit 1 shows predominantly short-chain *n*-alkanes (*n*-$C_{10–20}$), whereas unit 2 and samples, which represent the postulated marine transgressive events are characterized by higher concentrations of long-chained alkanes (> *n*-C_{27}), which is a pattern generally associated with higher land plants (Peter et al., 2005). Previous studies, however, suggested that long-chained alkanes (*n*-$C_{27–31}$) may be derived from certain non-marine algae (e.g., *Botryococcus braunii*; Moldowan et al., 1985; Derenne et al., 1988). Volkman et al. (1998) proposed a possible source of long-chain saturated fatty acids from microalgae. A similar pattern of *n*-alkane distributions with a proportion of long-chain *n*-alkanes accounting for > 40% was also observed by Bechtel et al. (2012) in the lower unit of K_2qn^1, which may be associated with microalgae and bacteria.

It is generally accepted that a high abundance of C_{27} steranes is indicative of algal input, while the enrichment of C_{29} steranes is associated with the input of terrigenous OM (Huang and Meinschein, 1979; Volkman, 1986; Bechtel et al., 2012; Jiang and George, 2018; Qiao et al., 2021a). The relatively high Pr/Ph, C_{29}/C_{27} regular steranes, and low C_{27}/C_{29} ααα 20R steranes ratios in unit 1 suggest more terrigenous OM input and/or deposition under oxidizing conditions (Figs. 3.13c, 3.14a). This result is further supported by the ternary plot of C_{27}–C_{29} ααα 20R steranes, in which unit 1 plots closer to the planktonic/land plants zone suggesting a higher abundance of terrigenous plants. In contrast, OM in unit 2 and the samples, which represent the postulated marine transgressive events have an origin from planktonic/algal or planktonic/bacterial biomass according to this diagram (Fig. 3.14b). However, it should be noted that the difference in OM origin among samples from K_2qn^1 is relatively small. In

addition, the low vitrinite content further points towards a generally minor terrestrial OM input into the paleo-lake, which may result in the minor differences in the C_{19}/C_{23} Tri and C_{24} Tet/C_{26} Tri ratios (Fig. 3.13d, Table 3.4), which are also commonly used as indicators of terrigenous OM input (Volk et al., 2005; Hao et al., 2011; Tian et al., 2014; Wu et al., 2022). Therefore, although K_2qn^1 in well A was deposited in proximity to the deltaic facies (Fig. 3.1b), the minor influx of terrigenous OM implies a negligible influence from the deltaic environment.

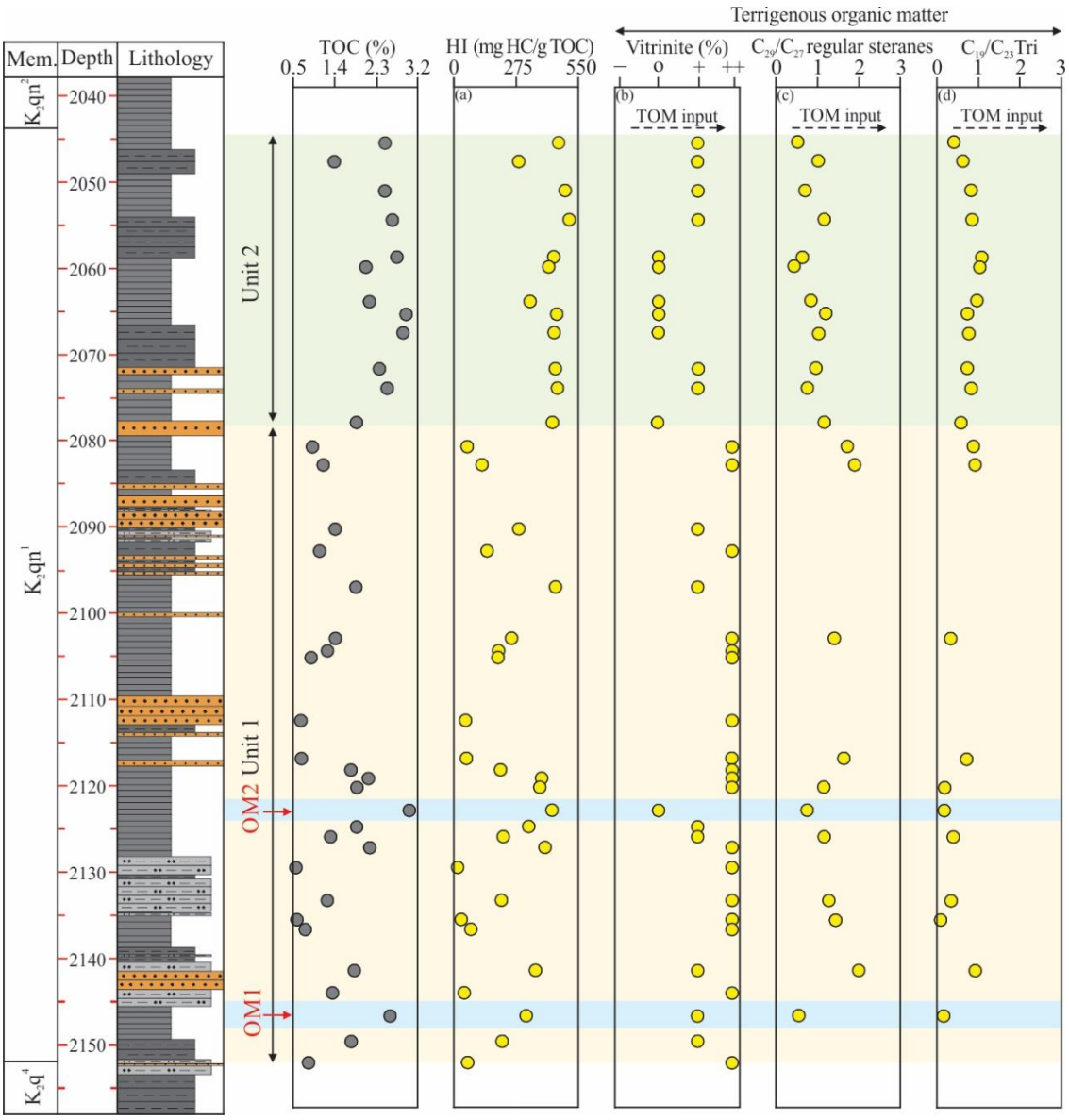

Figure 3.13 Stratigraphic profiles of OM biomarker parameters, HI, and vitrinite relative volumetric percentage. (a) HI. (b) Vitrinite relative volumetric percentage. (c) C_{29}/C_{27} steranes. (d) C_{19}/C_{23} Tri. TOM: terrestrial organic matter.

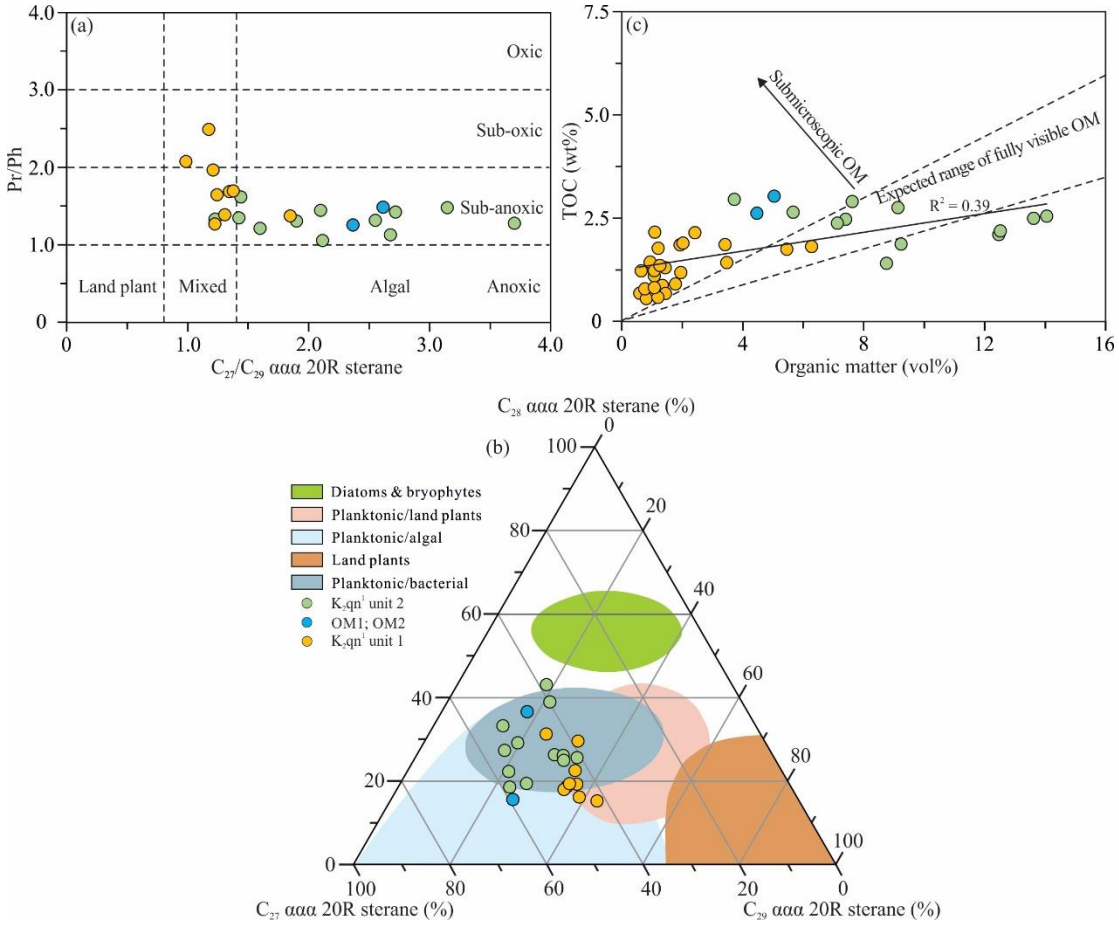

Figure 3.14 (a) Cross-plot of the Pr/Ph versus the C_{27}/C_{29} ααα 20R sterane (modified after Gorter, 2001). (b) Ternary plot showing the distribution of C_{27}, C_{28}, and C_{29} ααα 20R steranes (modified after Huang and Meinschein, 1979). (c) Cross-plot of the TOC (wt%) versus OM volume (vol%) (modified after Ghassal et al. 2016).

Steranes/hopanes ratio is regarded as an indicator of eukaryotic versus prokaryotic input with a high value (≥ 1) indicative of marine OM derived from planktonic and/or benthic algae, whereas a low value characterizes terrigenous and/or microbially reworked OM (Moldowan et al., 1985; Peters et al., 2005). In this study, the low steranes/hopanes ratio suggests a predominant contribution of prokaryotes (bacteria) to OM (Table 3.4). This is consistent with the rather poor positive correlation between TOC content and the volume percentage of macerals (R^2 = 0.39; Fig. 3.14c), suggesting the existence of abundant submicroscopic OM in most samples, which is probably almost entirely derived from microbial biomass (Ghassal et al. 2016).

The occurrence of monomethyl alkanes (MMAs; Fig. 3.5c) indicates the presence of OM derived from cyanobacteria living in microbial mats (Kenig, 2000; Bauersachs et al., 2009; Pawlowska et al., 2013; Ding et al., 2020). Furthermore, 1,3,6,7-TeMN, which is a typical compound of microbial origin (Jiang et al., 1998; Cesar and Grice, 2017), was observed in all the analyzed samples in this study (Fig. 3.5j).

The aromatic hydrocarbon 1,2,5-TMN might be derived from degradation and aromatization of bicyclic diterpane widely distributed in conifers, while 1,2,7-TMN may be derived from oleanane-type triterpenoids in angiosperms (Strachan et al., 1988). 1-MP and 1,7-DMP are possibly derived from conifers, e.g., Araucariaceae resins, as suggested by the relatively high concentrations in Jurassic samples from the Eromanga Basin, Australia (Alexander et al., 1988), while 9-MP is more enriched in type II and type I kerogens (Budzinski et al., 1995). In this study, the relatively low abundances of these compounds, e.g., 1,2,5-TMN and 1-MP, suggest a minor contribution of coniferous plant species (Fig. 3.5j). In addition, log ratios of 1-MP/9-MP, 1,7- DMP/(1,3- + 3,9- + 2,10- + 3,10-DMP), 1,2,5-TMN/1,3,6-TMN, and 1,2,7-TMN/1,3,7-TMN are significantly lower than the threshold values proposed by Alexander et al. (1988) and Strachan et al. (1988), suggesting a minor flux of terrigenous OM into the lake sediments (Table 3.5). In summary, terrigenous OM derived from higher land plants is scarce in the studied sediments, but slightly more abundant in unit 1 as compared to unit 2. The bulk of the OM is derived from the lake system itself, i.e., algal and microbial biomass.

3.5.5 Factors controlling OM enrichment and source rocks depositional model

Marine incursions into the lake system could have promoted OM enrichment by increasing the nutrients influx with further influence on primary productivity and/or leading to more reducing conditions generally associated with stratified water columns (Katz, 1995; Erbacher et al., 2001; Wei et al., 2018). The change of subduction direction of the Pacific Plate at 90 Ma may have formed a few sinistral slip fault systems, which probably led to the seawater influx to the study area (Yang, 2013; Cao et al., 2021). Paleontological data and organic geochemical markers, e.g., the occurrence of planktonic foraminifera, shark teeth, and C_{30} 4-desmethylsteranes, also imply a strong influence of seawater incursion events to the paleo-lake during the deposition of the Upper Cretaceous strata in the Songliao Basin (Chang and Chow, 1978; Hou et al., 2000; Xi et al., 2011). Such marine influence increased sulfate concentrations and favored salinization of the paleo-lake (Huang et al., 2013), which amplified the lake stratification and contributed to anoxic bottom waters during the deposition of K_2qn^1 (Cao et al., 2021). Cao et al. (2021) suggested that the sulfate input from marine transgression events is the most important factor controlling redox conditions of the paleo-lake by accelerating OM remineralization and releasing iron-sorbed phosphate from sediments. The enhanced nutrient cycling efficiency resulted in high primary productivity and then accelerated the consumption of oxygen in the bottom water.

Based on the results from this study, the TOC contents of the K_2qn^1 exhibit positive and negative correlations with U/Th and Pr/Ph ratios, respectively, suggesting that reducing conditions contribute to OM enrichment (Fig. 3.15a and b). In contrast, the Zr/Al ratio and proportion of C_{29} regular steranes are negatively associated with TOC contents, indicating that the detrital influx exerts an adverse impact on the TOC content (Fig. 3.15c and d). There are weak to moderate positive correlations

between the TOC contents and the Cu/Al and Gam index values, which suggests that both enhanced paleo-productivity and salinity in the water column favor the OM accumulation in the K_2qn^1 (Fig. 3.15e and f).

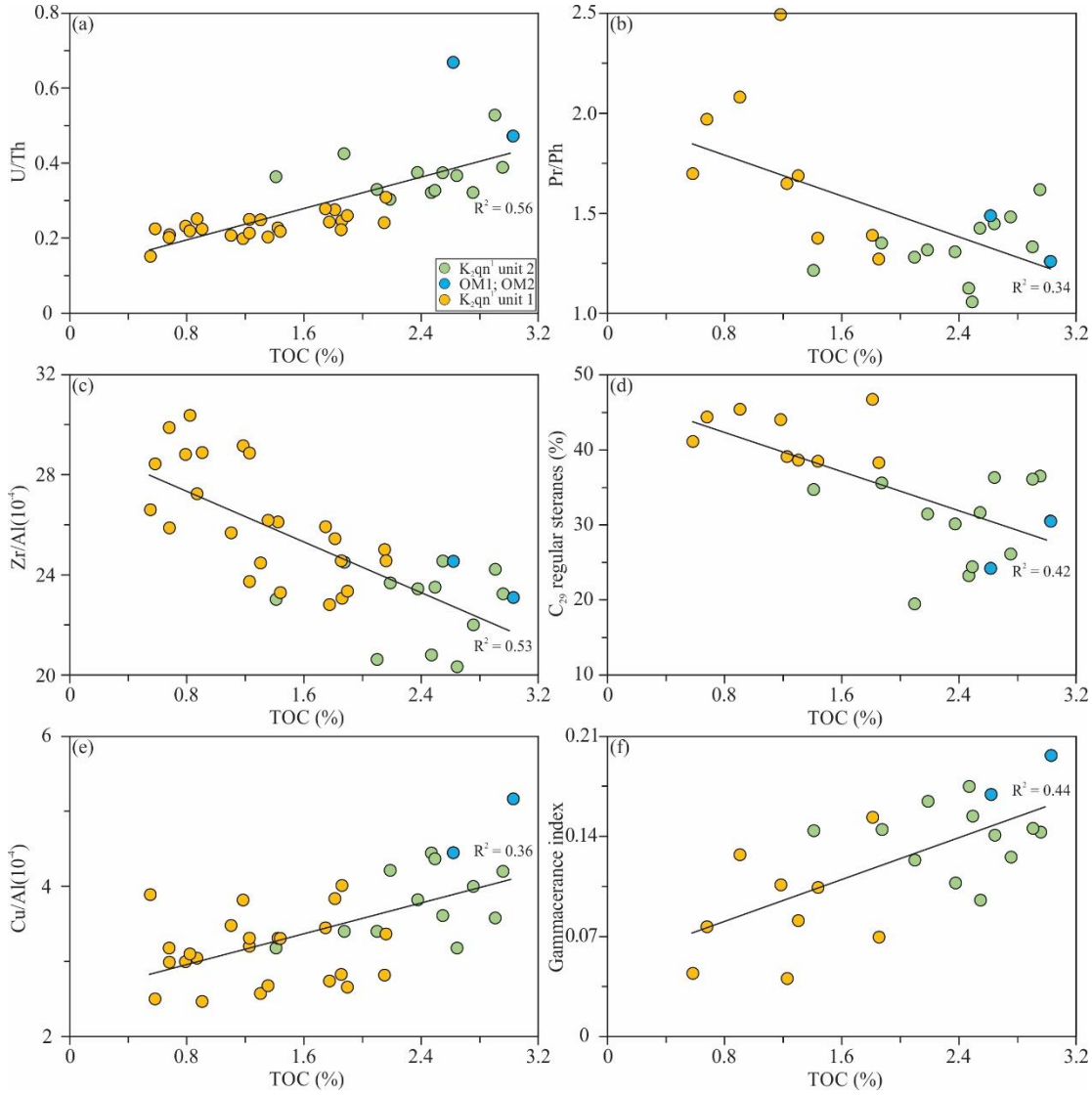

Figure 3.15 (a) Cross-plot of U/Th versus TOC; (b) Cross-plot of Pr/Ph versus TOC; (c) Cross-plot of Zr/Al versus TOC; (d) Cross-plot of C_{29} regular steranes versus TOC; (e) Cross-plot of Cu/Al versus TOC; (f) Cross-plot of Gammacerance index versus TOC.

A relatively shallow and oxic-dysoxic water column is assumed to have prevailed during the deposition of the less TOC-rich sediments in unit 1 based on the multiple proxies discussed above (Fig. 3.16a). The lower values of salinity indicators suggest a freshwater-brackish environment with a weakly or not permanently stratified water column compared to unit 2 and samples, which represent the postulated marine transgressive events. Such shallow lake environments or depositional settings with gravity flows and freshwater inflows are generally characterized by i) reduced salinity

stratification, increasing vertical ventilation of the water column, and ii) rather high dissolved oxygen content (Li et al., 2021c). These factors are typically adverse to the preservation of OM due to oxidative decomposition.

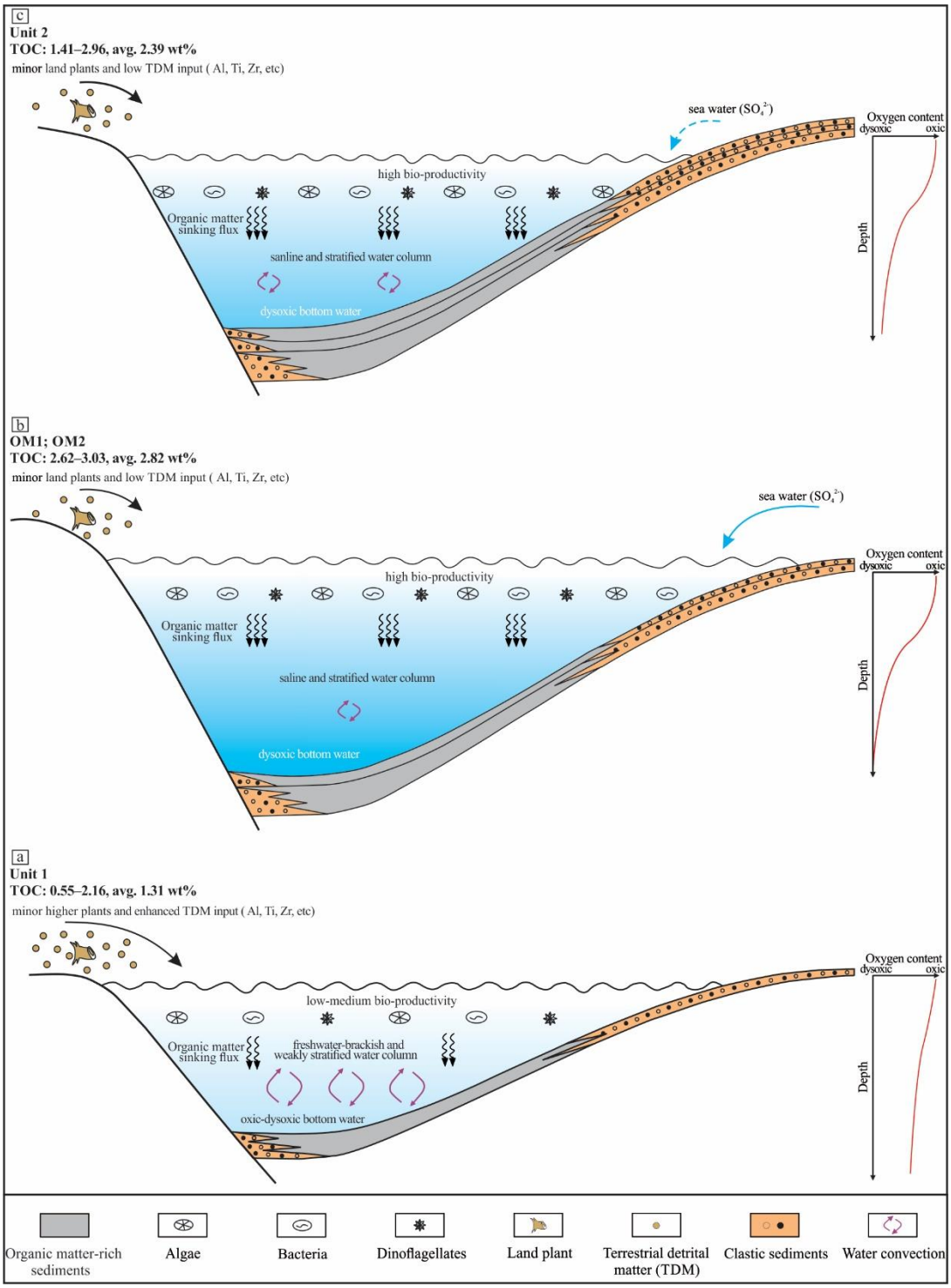

Figure 3.16 Depositional model of lacustrine source rocks of the K_2qn^1 based on high-resolution geochemical data.

Although the K_2qn^1 was deposited in overall arid or semiarid climatic conditions coupled to a low degree of weathering, the relatively warmer and more humid climate prevailing during the deposition of unit 1 resulted in a stronger weathering intensity. Therefore, more terrigeneous detrital materials accompanied by little terrigenous OM were transported into the depositional site, which exerted an unfavorable effect on OM accumulation by the dilution due to detrital influx. By contrast, marine incursions into the paleo-lake may have led to enhanced salinity and water column stratification. The reduced oxygen content in bottom waters is conducive to preserving OM and contributes to the high TOC content in the samples, which represent the postulated marine transgressive events. The high primary productivity associated with algae and microbial communities would result in the transportation of excess OM to the bottom water, further intensifying the water column oxygen deficiency. In addition, the arid climate, weak weathering intensity, as well as increasing water depth make the source rocks less susceptible to land plant detritus, terrigenous clastic materials, and fluvial freshwater influx. As a result, owing to the combined effect of the above favorable factors, samples, which represent the postulated marine transgressive events with high TOC contents were deposited in dysoxic and saline environments with a low terrigenous influx (Fig. 3.16b). Subsequently, unit 2 was deposited in overall less oxygenated bottom water environments than unit 1, probably associated with a rise in lake level (Fig. 3.16c).

3.5.6 Comparison to the K_2qn^1 from other wells in the Songliao Basin

Here, a comparison of the data of this study with those of previous studies is presented (Figs. 3.17 and 3.18; Huang et al., 2013; Xu et al., 2015, 2019b; Cao et al., 2021; Zhang et al., 2022). Rock-Eval pyrolysis data of the K_2qn^1 in the ZY1 and ZK2 wells suggested similar thermal maturity within the oil window (Fig. 3.17a and b). Samples of the K_2qn^1 from the ZY1 well (TOC: 5.46–18.25, avg. 8.66 wt%), located in the east central depression, exhibit the highest HI values, which suggests the dominance of type I OM (Fig. 3.17a). In contrast, samples of the K_2qn^1 from the ZK2 well (TOC: 1.29–3.69, avg. 2.51 wt%), located in the central part of the depression, show significantly lower HI values, indicating mainly type II OM (Fig. 3.17b). The data of the K_2qn^1 from the ZK2 well are similar to the geochemical results present in this study (Zhang et al., 2022). However, the magnitude of variation in the TOC and HI values of K_2qn^1 in the ZK2 well is not as apparent as that observed in the ZY1 and A wells (Fig. 3.17a and b). This discrepancy may be attributed to the varying impacts of the postulated marine transgressive events. Zhang et al. (2022) suggested that seawater incursion was more intense in the southeastern uplift than in the central depression. Thus, the extent to which marine transgressions have impacted the TOC and HI values of K_2qn^1 in the Songliao Basin may vary, with the central part of the central depression likely experiencing the least influence.

Similarly, samples of the K_2qn^1 from the FH-1 well in the southeastern uplift are characterized by higher TS/TOC ratios than those from the SK-1 (S) well in the southeastern uplift (Fig. 3.17c and d), suggesting enhanced salinity eastward in the paleo-lake during the deposition of the K_2qn^1. For

each well, samples at the bottom part, e.g., samples in the 493-500 m interval in the FH-1 well, show the highest TS/TOC ratios, whereas samples above this unit are characterized by the lowest TS/TOC ratios, e.g., samples in the 477-493 m interval in the FH-1 well. This trend is consistent with the

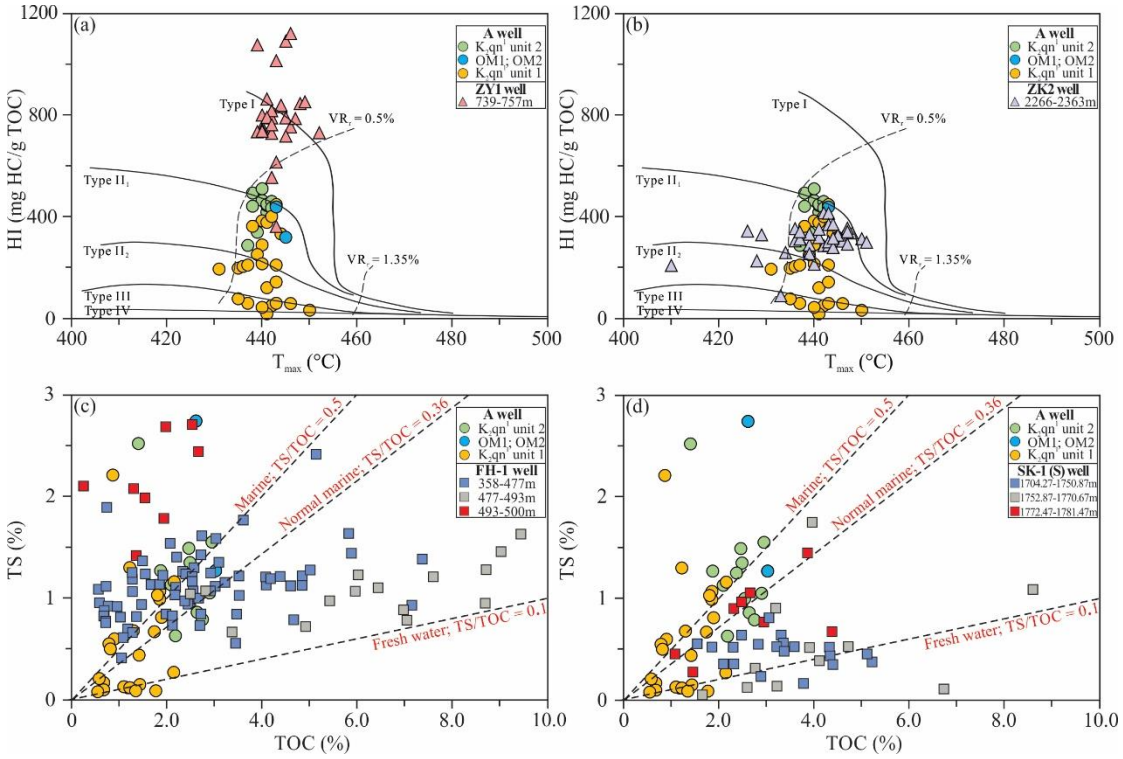

Figure 3.17 (a–b) Cross-plot of HI versus T_{max} of the K_2qn^1 from the ZY1 and ZK2 wells (HI and T_{max} data are taken from Xu et al., 2015 and Zhang et al., 2022); (c–d) Cross-plot of TS versus TOC of the K_2qn^1 from the FH-1 and SK-1(S) wells (TS and TOC data are taken from Cao et al., 2021 and Huang et al., 2013). Well positions are shown in Fig. 3.1b. Sulfur data from SK-1(S) well represent pyrite sulfur and might be slightly lower than TS.

variation of the TOC/TS ratios in Fig. 3.8a in this study. TOC contents of samples from the ZY1 well exhibit similar trends as the variation of TOC contents of samples from well A (Fig. 3.18a and b). Xu et al. (2019b) proposed that marine ingression had influenced the deposition of the lower phase of K_2qn^1, while the data presented in this study suggest that the impact of postulated marine transgressive events on unit 1 was limited to two thin layers. As shown in Fig. 3.18a and b, three samples at the bottom part with the highest TOC contents may be influenced by the possible marine transgression events. The remaining samples in the bottom part generally show lower TOC values than those in the upper part. In addition, the salinity proxies of the K_2qn^1 from the ZY1 well show a similar variation trend as those of the A well in this study (Fig. 3.18c–e). Samples, which represent the postulated marine transgressive events are characterized by the highest Ca/Mg and Sr/Ba ratios and Gam index values, suggesting the highest water salinity during the deposition. The other samples in the bottom

part exhibit lower values of the proxies mentioned above than those in the upper part, suggesting the increasing water salinity of the paleo-lake in ascending order. Marine ingressions during deposition of the lower unit were probably related to short-term transgressions leading to high salinity and stratification. In contrast, deposition of the upper unit took place under more constant, brackish conditions. Probably a more or less permeable connection existed at that time between the sea and the lake allowing for water exchange. For the redox conditions (Fig. 3.18f–g), Samples, which represent the postulated marine transgressive events from the ZY1 well, also show the lowest Pr/Ph ratios, indicating the most reducing bottom-water conditions, which is consistent with the conclusion in this study.

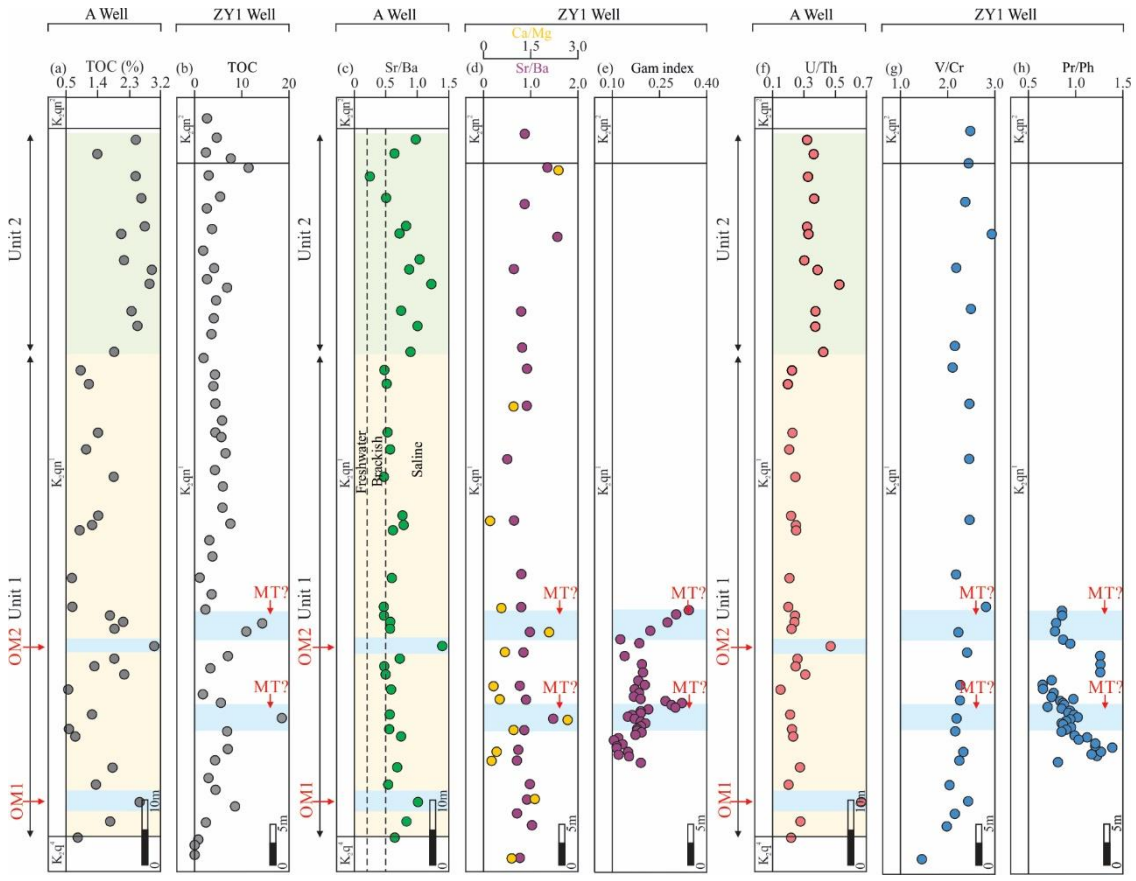

Figure 3.18 Stratigraphic profiles of TOC and paleosalinity and paleoredox parameters of the K_2qn^1 from the ZY1 well (TOC, Ca/Mg, Sr/Ba, Gam index, V/Cr, and Pr/Ph values of the K_2qn^1 from the ZY1 well are taken Xu et al., 2015, 2019b). Well position is shown in Fig. 3.1b. MT: Intervals enriched in organic carbon, possible marine transgression events.

3.6 Conclusions

By integrating molecular organic geochemistry, major and trace elements, organic petrography, elemental carbon and sulfur composition, and Rock-Eval pyrolysis analyses on the K_2qn^1 in the

Songliao Basin, this study presents a large set of new data concerning the maturity and origin of OM, depositional environments, reconstruction of paleo-climate conditions, as well as factors controlling OM enrichment. The following conclusions can be drawn:

1) Sediments from the K_2qn^1 in the southern part of the central depression, Songliao Basin, contain three different types of lacustrine source rock within the (early-peak) oil window with VR_r ranging from 0.80% to 0.88% (avg. 0.83%). Unit 1 is characterized by low TOC (avg. 1.31 wt%) and TS (avg. 0.56 wt%) contents, while unit 2 has significantly higher TOC (avg. 2.39 wt%) and TS contents (avg. 1.24 wt%). Samples, which represent the postulated marine transgressive events show the highest TOC and TS contents with average contents of 2.82 wt% and 2.01 wt%, respectively.

2) Unit 1 having the highest Pr/Ph (1.27–2.49, avg. 1.74) ratio and the lowest U/Th (0.15–0.31, avg. 0.23) ratio and Gam index value (0.04–0.15, avg. 0.09) was deposited under oxic-dysoxic and fresh-brackish water column conditions. By contrast, unit 2 (Pr/Ph: 1.06–1.62, avg. 1.33; U/Th: 0.30–0.53, avg. 0.37; Gam index: 0.10–0.17, avg. 0.14) and samples, which represent the postulated marine transgressive events (Pr/Ph: 1.26–1.49; U/Th: 0.47–0.67; Gam index: 0.17–0.20) were deposited in less oxygenated and more saline environments. Based on multiple geochemistry proxies, the overall climatic conditions were arid coupled to a low degree of weathering during the deposition of the K_2qn^1. However, the relatively warmer and more humid environment climate prevailing during the deposition of unit 1 resulted in a stronger weathering intensity and higher terrigenous influx.

3) Source rocks from the K_2qn^1 have a low vitrinite content indicative of a generally minor terrestrial OM input. Unit 1 with type II-III kerogen and low C_{27}/C_{29} ααα 20R steranes values have, however, a slightly higher relative content of terrigenous higher plants. OM in Unit 2 and samples, which represent the postulated marine transgressive events originate almost exclusively from planktonic/algal and microbial biomass. The low steranes/hopanes ratio in the studied samples suggests a major OM source from prokaryotes (bacteria and archaea).

4) A series of adverse factors for OM accumulation, including a relatively shallow, oxic-dysoxic, and weakly stratified water column and diluting by the high terrigenous mineral influx, resulted in the formation of less TOC-enriched sediments in the lower unit 1. The environments prevailing during deposition of the upper unit 2 and of short-term marine transgression events were more favorable compared with those of unit 1, leading to a higher TOC content and more hydrogen-enriched kerogen.

Table 3.7 Identification of terpanes, steranes, and aromatic compounds in Fig. 3.5.

Compound group	Peak	Abbreviation	Biomarker	*m/z*
Terpanes	A	C_{19} Tri	C_{19}-tricyclic terpane	191
	B	C_{20} Tri	C_{20}-tricyclic terpane	
	C	C_{21} Tri	C_{21}-tricyclic terpane	
	D	C_{22} Tri	C_{22}-tricyclic terpane	
	E	C_{23} Tri	C_{23}-tricyclic terpane	
	F	C_{24} Tri	C_{24}-tricyclic terpane	
	G	C_{25} Tri	C_{25}-tricyclic terpane	
	H	C_{24} Tet	C_{24}-tetracylic terpane	
	I	C_{26} Tri R	C_{26}-R tricyclic terpane	
		C_{26} Tri S	C_{26}-S tricyclic terpane	
Hopanes	J	Ts	C_{27}-18α(H)-22,29,30-trisnorneohopane	
	K	Tm	C_{27}-17α(H)-22,29,30-trisnorhopane	
	L	C_{29} H	C_{29}-17α(H),21β(H)-norhopane	
	M	C_{29} Ts	C_{29}-18α(H)-30-norneohopane	
	N	C_{30} DiaH	C_{30}-17α-diahopane	
	O	C_{30} H	C_{30}-17α(H),21β(H)-hopane	
	P	C_{31} H S	C_{31}-17α(H),21β(H),22S-homohopane	
		C_{31} H R	C_{31}-17α(H),21β(H),22R-homohopane	
	Q	Gam	Gammacerane	
	R	C_{32} H S	C_{32}-17α(H),21β(H),22S-homohopane	
		C_{32} H R	C_{32}-17α(H),21β(H),22R-homohopane	
	S	C_{33} H S	C_{33}-17α(H),21β(H),22S-homohopane	
		C_{33} H R	C_{33}-17α(H),21β(H),22R-homohopane	
	T	C_{34} H S	C_{34}-17α(H),21β(H),22S-homohopane	
		C_{34} H R	C_{34}-17α(H),21β(H),22R-homohopane	
	U	C_{35} H S	C_{35}-17α(H),21β(H),22S-homohopane	
		C_{35} H R	C_{35}-17α(H),21β(H),22R-homohopane	
Steranes	a	C_{27} ααα 20S	20S-5α(H),14α(H),17α(H)-cholestane	217
	b	C_{27} αββ 20R + C_{29}dβα20S	20R-5α(H),14β(H),17β(H)-cholestane +13β,17α,20S-diastigmastane	
	c	C_{27} αββ 20S	20S-5α(H),14β(H),17β(H)-cholestane	
	d	C_{27} ααα 20R	20R-5α(H),14α(H),17α(H)-cholestane	
	e	C_{28} ααα 20S	20S-24-Methyl-5α(H),14α(H),17α(H)-cholestane	
	f	C_{28} αββ 20R	20R-24-Methyl-5α(H),14β(H),17β(H)-cholestane	
	g	C_{28} αββ 20S	20S-24-Methyl-5α(H),14β(H),17β(H)-cholestane	
	h	C_{28} ααα 20R	20R-24-Methyl-5a(H),14a(H),17a(H)-cholestane	
	i	C_{29} ααα 20S	20S-24-Ethyl-5α(H),14α(H),17α(H)-cholestane	
	j	C_{29} αββ 20R	20R-24-Ethyl-5α(H),14β(H),17β(H)-cholestane	
	k	C_{29} αββ 20S	20S-24-Ethyl-5α(H),14β(H),17β(H)-cholestane	
	l	C_{29} ααα 20R	20R-24-Ethyl-5α(H),14α(H),17α(H)-cholestane	
Aromatic hydrocarbons	1	2-MN	2-methylnaphthalene	142
	2	1-MN	1-methylnaphthalene	
	3	2,6- + 2,7-DMN	2,6- + 2,7-dimethylnaphthalene	156
	4	1,3- + 1,7-DMN	1,3- + 1,7-dimethylnaphthalene	
	5	1,6-DMN	1,6-dimethylnaphthalene	
	6	1,3,7-TMN	1,3,7-trimethylnaphthalene	170
	7	1,3,6-TMN	1,3,6-trimethylnaphthalene	
	8	1,4,6- + 1,3,5-TMN	1,4,6- + 1,3,5-trimethylnaphthalene	
	9	2,3,6-TMN	2,3,6-trimethylnaphthalene	
	10	1,2,7- + 1,6,7-TMN	1,2,7- + 1,6,7-trimethylnaphthalene	
	11	1,2,6-TMN	1,2,6-trimethylnaphthalene	
	12	1,2,4-TMN	1,2,4-trimethylnaphthalene	
	13	1,2,5-TMN	1,2,5-trimethylnaphthalene	
	14	1,4,5-TMN	1,4,5-trimethylnaphthalene	
	15	1,3,5,7-TeMN	1,3,5,7-tetramethylnaphthalene	184
	16	1,3,6,7-TeMN	1,3,6,7-tetramethylnaphthalene	
	17	1,4,6,7- + 1,2,4,6- + 1,2,4,7-TeMN	1,4,6,7- + 1,2,4,6- + 1,2,4,7-tetramethylnaphthalene	
	18	1,2,5,7- + 1,3,6,8-TeMN	1,2,5,7- + 1,3,6,8-tetramethylnaphthalene	
	19	2,3,6,7-TeMN	2,3,6,7-tetramethylnaphthalene	
	20	1,2,6,7-TeMN	1,2,6,7-tetramethylnaphthalene	
	21	1,2,3,7-TeMN	1,2,3,7-tetramethylnaphthalene	
	22	1,2,3,6-TeMN	1,2,3,6-tetramethylnaphthalene	

Continued

23	1,2,5,6- + 1,2,3,5-TeMN	1,2,5,6- + 1,2,3,5-tetramethylnaphthalene	
24	P	phenanthrene	178
25	3-MP	3-methylphenanthrene	192
26	2-MP	2-methylphenanthrene	
27	9-MP	9-methylphenanthrene	
28	1-MP	1-methylphenanthrene	
29	3-EP	3-ethylphenanthrene	206
30	9- + 2- + 3,6-DMP	9- + 2- + 3,6-dimethylphenanthrene	
31	1-EP	1-ethylphenanthrene	
32	2,6- + 3,5-DMP	2,6- + 3,5-dimethylphenanthrene	
33	2,7-DMP	2,7-dimethylphenanthrene	
34	1,3- + 3,9- + 3,10- + 2,10-DMP	1,3- + 3,9- + 3,10- + 2,10-dimethylphenanthrene	
35	1,6- + 2,9- + 2,5-DMP	1,6- + 2,9- + 2,5-dimethylphenanthrene	
36	1,7-DMP	1,7-dimethylphenanthrene	
37	1,9- + 4,9- + 4,10-DMP	1,9- + 4,9- + 4,10-dimethylphenanthrene	
38	2,3-DMP	2,3-dimethylphenanthrene	
39	1,8-DMP	1,8-dimethylphenanthrene	
40	1,2-DMP	1,2-dimethylphenanthrene	
41	Ret	retene	219

4 Geochemistry and petrology of Early Permian lacustrine shales in the Lodève Basin, Southern France: depositional history, organic matter accumulation and thermal maturity

Keywords: Biomarkers; Major and trace elements; Paleoenvironmental conditions; Organic matter accumulation; Early Permian; Lodève Basin

Abstract

The lacustrine shales in the Lodève Basin, southern France, serve as excellent archives of paleo-lake development as well as climatic evolution during the Early Permian. In this study, an extensive dataset is presented encompassing organic petrographic data, major and trace element quantification, bulk and molecular organic geochemical proxies, as well as compound-specific stable carbon isotope data derived from the analysis of 36 black shale outcrop samples originating from the Usclas-St. Privat Formation (USPF), Tuilières-Loiras Formation (TLF), and Viala Formation (VF). All sample are thermally oil-mature, as evident from a vitrinite reflectance (VR_r) of around 0.8%. The lower section of the USPF, characterized by notably higher total sulfur (TS) concentrations, displays total organic carbon (TOC) and TS contents spanning from 2.69 to 7.83 (avg. 4.28) wt% and 0.42–1.55 (avg. 1.09) wt%, respectively. In contrast, the upper section of the USPF (average TOC of 2.59 wt%), TLF (average TOC of 2.66 wt%), and VF (average TOC of 3.17 wt%) exhibit considerably lower TS contents of 0.26 wt%, 0.22 wt%, and 0.17 wt%, respectively. The lower section of the USPF, characterized by the lowest pristane/phytane (Pr/Ph) ratio and the highest TS/TOC ratios and chemical index of alteration (CIA) values, was deposited in oxygen-depleted and saline lacustrine environments. These conditions prevailed under more humid climatic conditions and were probably related to marine incursions. In contrast, the upper section of the USPF, the TLF, and the VF display elevated Pr/Ph ratios but reduced TS/TOC and CIA values, signifying deposition within oxic-dysoxic and freshwater-brackish bottom water conditions with a significant change towards arid conditions. All samples are characterized by low vitrinite and inertinite contents together with consistently similar average values of Al_2O_3 and TiO_2. The biomarker analysis suggests that the organic matter (OM) in most samples mainly originates from planktonic/algal biomass with additional microbial OM. Only the lower section of the USPF displays a slightly enhanced contribution of terrestrial OM input and also more detrital elements. It is concluded that the structural evolution of the basin from narrow deep towards wider and shallower settings as well as the postulated marine transgressive events during early stages played a crucial role in shaping the deposition environments of the two distinct sets of lacustrine shales, thereby influencing the OM accumulation mechanisms. In contrast, the substantial climatic aridification seems to have a relatively minor impact on the sources of OM and the conditions prevailing within the water column.

4.1 Introduction

Lacustrine organic matter (OM)-rich shales are important source rocks for conventional petroleum, contributing probably to over 20% of the global hydrocarbon production (Bohacs et al., 2000). Well studied examples include the Murta Formation in the Eromanga Basin, central Australia and the Qingshankou Formation in the Songliao Basin, northeast China (Röth et al., 2023; Wu et al., 2023). Additionally, such OM-rich lacustrine shales can be applied to decipher detailed information concerning paleoenvironmental conditions and paleoclimate, rendering them invaluable geological archives for basic geological and geochemical research. Lacustrine systems have been categorized into overfilled, balanced-filled, and underfilled lake basins based on the accommodation capacity within the basin (primarily dictated by tectonics) compared to the volume of sediment and water supplied (Carroll and Bohacs, 1999; Bohacs et al., 2000). All these sequences are highly variable, e.g. with respect to lithological composition, desiccation and flooding records, and fluvial inflow (Harris et al., 2004). Among these, the balanced-filled lakes, characterized by near parity between accommodation space and the flux of sediment and water, are considered the most favorable for developing superior, oil-prone source rocks (Bohacs et al., 2000). In light of the escalating number of detailed geochemical and geological studies of such lacustrine sequences partly triggered by the need to understand them in detail as petroleum source rocks, a multifarious range of depositional models has emerged (e.g., the hypersaline lake model proposed by Kirkland and Evans 1981).

The development of high-quality lacustrine source rocks is intricately shaped by the complex interaction of external factors, encompassing climate evolution and nutrient input, alongside internal elements, such as water chemistry and biological productivity (Gonçalves, 2002). These elements collectively modulate the equilibrium between OM generation and degradation. Furthermore, as a result of their sedimentary setting within relatively smaller water reservoirs, the deposition of lacustrine sediments experiences increased rates of environmental fluctuation, e.g., fluctuations in water chemistry and salinity within lake systems over relatively brief periods owing to the seasonal or periodic paleoclimatic conditions. In addition, variable weather conditions can lead to variable input of terrestrial minerals and plant debris (Gonçalves, 2002; Wu et al., 2023). Moreover, lake systems, as opposed to oceans, depend on extraneous nutrient sources to facilitate the proliferation of algae and bacteria (Harris et al., 2004). The variations in the paleoclimate could also result in changes in the depositional environments in lacustrine systems, thereby exerting a consequential influence on redox conditions, water salinity, OM sources, productivities, and lithofacies (e.g., Wu et al., 2022). Furthermore, the occurrences of marine incursions may lead to fluctuations of paleo-lake level, subsequently exerting a governing role over lake water chemistry and OM preservation conditions (Zhang et al., 2022; Wu et al., 2023).

However, it should be noted that within extensional continental rift basins, the stratigraphic sequences manifest a highly akin progression encompassing four consecutive phases: (1) an initial domain dominated by fluvial systems during the rift's initial stages, (2) a domain characterized by

deep-water lacustrine conditions within an elongated and deep basin, as subsidence surpasses infill rates, (3) a lacustrine domain gradually becoming shallower, possibly evolving into a shallow playa lake environment, as sedimentation rates eventually match and surpass subsidence, and (4) a renewed period of fluvial dominance, emerging as the rift basin experiences overfilling (Lambiase, 1990; Pochat and Van Den Driessche, 2011). This process occurs regardless the geological epochs and climatic zones. Based on the study of the stratigraphy of multiple rifts spanning geological epochs from Precambrian to Holocene across six continents, Lambiase (1990) proposed a typical pattern discernible within stratigraphic sequences. This pattern is typified by a basal fluvial-derived sandstone and the overlying lacustrine sediments. These lacustrine deposits are observed either in direct superposition atop the basal sandstone or overlying on the pre-rift rocks when the basal sandstone is absent. It is noteworthy that the entire geological progression, commencing with the initiation of faulting to the formation of sizable, deep lakes, occurs with remarkable celerity, which is reflected by the abrupt transition from the deposits in sediment origins, shifting from subaerial deposits to those characteristic of deep-water environments. The lacustrine sediments in the deepest water settings either develop into marine settings, if the initial rift develops into an oceanic setting or they are overlain by deposits from shallower waters. This latter transition is associated with a discernible increase in sediment grain size. The overlying deposits on the lacustrine shales comprise a combination of fluviodeltaic complex, synrift fluvial and postrift fluvial sediment (Lambiase, 1990). However, it is important to note that this overall stratigraphic pattern can be disrupted by renewed tectonic activity, as observed in continental rifts in Newark, southern Sudan, and West Africa. In addition, this pattern of stratigraphic sequences is also evident in the Lower Cretaceous synrift lacustrine shales in the Congo Basin (Harris et al., 2004). The lacustrine sediments, deposited within a balanced-fill lake system, often exhibit notable OM enrichment and are predominantly characterized by type I kerogen rich in hydrogen. However, the subsequent transition from a balanced fill to an overfilled lake results commonly in a reduction in total organic carbon (TOC) content, accompanied by a shift in kerogen type from Type I to Type III in the upper late rift section. Similarly, Gonçalves (2002) suggested that discrepancies in the subsidence rates and fault activity have led to diverse evolution of lake geometry and the associated topography, including water depth and surface area, within the Camamu rift basin.This tectonic evolutionary progression significantly influenced the patterns of OM accumulation in Early Cretaceous source rocks within the Camamu Basin, situated in Brazil.

In the Lodève Basin of southern France, fine-grained sedimentary rocks were discovered within Early Permian lacustrine rift sequences, e.g. Usclas-St. Privat Formation (USPF), Tuilières-Loiras Formation (TLF), and Viala Formation (VF). Recent research suggested that the formation of these lacustrine source rocks was controlled by basin expansion, utilizing sedimentological and structural analyses (Pochat and Van Den Driessche, 2011) or paleoclimatic variations inferred from fieldwork (Michel et al., 2015). However, comprehensive and systematic investigations concerning the evolution of the depositional environment, OM source, and paleoclimate conditions of these Early Permian

shales were scarce. Based on organic petrology, stable carbon isotope, bulk and molecular geochemistry, as well as elemental geochemistry data, the objective of this study is to decipher 1) changes in the environmental conditions of the paleo-lake during their deposition, 2) the sources of OM, be it algae, transported higher land plants or bacteria, 3) the possible influence of variations in paleoclimatic conditions on the sedimentary environment, 4) to construct an OM accumulation model for the lacustrine fine-grained sediments, and 5) to quantify thermal maturation and estimate maximum burial temperatures and depth of the lacustrine Early Permian shales.

4.2 Geological setting

The Lodève Basin, encompassing a southern-dipping continental infill with an inclination of 15-20° and spanning roughly 150 km^2, is a Permian half-graben positioned on the southern border of the Massif Central Basin (Lopez et al., 2008; Mujal and Marchetti, 2020; Fig. 4.1a). Thick, locally substantially eroded Paleozoic rocks are situated unconformably upon underlying Precambrian and Cambrian bedrocks consisting of schists, arkosic rocks, and volcaniclastics (Conrad and Odin, 1984; Michel, et al., 2015; Laurent et al., 2020; Fig. 4.1b and c). The basin is demarcated by the northern

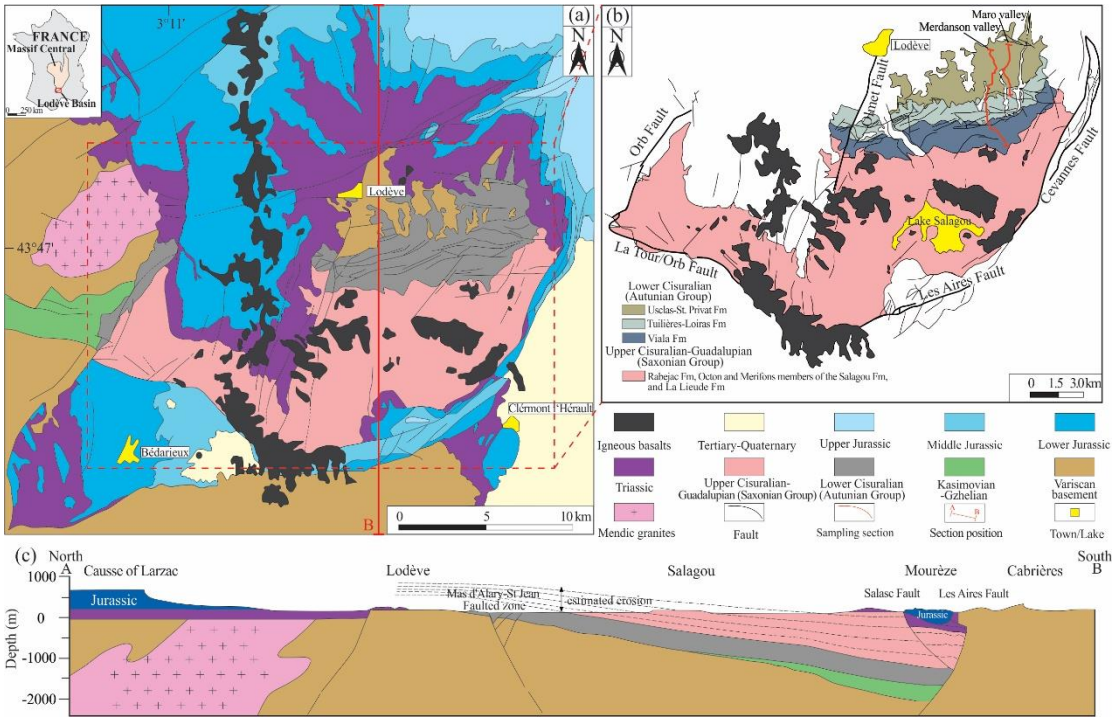

Figure 4.1 (a) Schematic map showing the location of the Lodève Basin in France and simplified geological map of the Lodève Basin (modified after Lopez et al., 2008 and Mujal and Marchetti, 2020). (b) Geologic map of the Lodève Basin showing the locations of the sampling section studied herein (modified after Michel et al., 2015). (c) A cross-section from north to south of the Lodève half-graben (modified after Laurent et al., 2020). The location of the cross section is indicated by the red line A-B in Fig. 4.1a.

"Causse du Larzac," characterized by a 400 m-thick succession of Mesozoic limestone deposits (Lopez et al., 2008; Fig. 4.1). To the west, there is a basaltic plateau of the Escandorgue extending in a north-south direction, while to the east, the NNE-SSW trending Cevennes Fault further defines the boundary. In a southwestern direction, the limit of the basin is delineated by the Cabrières hill. The E-W-oriented Les Aires faults (Espinouse detachment), which form the southern boundary, and exhibit vertical movements predominantly along its southern segment, played a pivotal role in generation of accommodation space for the sediment deposition during the Permian (Conrad and Odin, 1984; Michel et al., 2015; Fig. 4.1b and c). The basin developed within the hanging wall of the above-mentioned north-dipping detachment fault, exhibiting a listric geometry of a half-graben with a steep border fault along its southern edge and a ramp-like margin extending towards the north (Pochat and Van Den Driessche, 2011; Fig. 4.1c). The fault has been in an active state since the Late Carboniferous period, spanning a distance of 60–70 km, and governed the subsidence of the studied basin.

The Carboniferous–Permian siliciclastics, with an approximate thickness of 3000 m, were deposited within the studied basin (Schneider et al., 2006). Presently, only Permian outcrops are observable, whereas Carboniferous outcrops are found in the adjoining Graissessac Basin (Bruguier et al., 2003). The Permian deposits have been classified into two main megasequences: the Autunian sequence, comprising the USPF, TLF, and VF, with an approximate thickness of 730 m, and the Saxonian sequence, encompassing the Rabejac, Salagou, and La Lieude formations, with a thickness over 2000 m (Lopez et al., 2008; Michel et al., 2015; Figs. 4.1 and 4.2). These sequences lay unconformably ontop of the Upper Carboniferous strata.

During the Late Carboniferous (Gzhelian) and Early Permian (Early Cisuralian), the sedimentation within the Graissessac–Lodève basin started in an alluvial proximal fan-conglomerate system, which subsequently transitioned to an alluvial distal fan (Pochat and Van Den Driessche, 2011). The overlying Late Carboniferous Pabau and Houilliere formations, as well as the Early Permian USPF and TLF, were deposited at the commencement and the peak of the extension of lacustrine settings but still within represent a cyclical sequence of diverse facies, including deltas, sub-aerial alluvial fans, floodplains, and the transitions from sub-lacustrine fans to distal lacustrine facies. The presence of various depositional features in the VF, including decimeter-scale fine-grained wave ripples, desiccation cracks, xeromorphic calcisols, and red pelites is indicative of a shallow lake under semiarid conditions (Schneider et al., 2006; Michel et al., 2015; Fig. 4.2). Notably, exclusively within the lower part of the VF, grey lacustrine shales/siltstones still occur as intercalations (Schneider et al., 2006). During the Late Cisularian, the Rabejac and Salagou formations, characterized by a rather uniform sequence of red mudstones, were mainly deposited in a large shallow playa lake (Pochat and Van Den Driessche, 2011). Simultaneously, this lake underwent a gradual sedimentary infilling, primarily facilitated by the deposition of materials originating from the southern and western peripheries of the basin. The Late Permian and the Early Triassic strata mark the onset of a new influx of coarse, conglomeratic sediments, which were deposited in alluvial fans, braided river-plains,

floodplains, and playa lakes from west to east. The paleo-lake surface area showed a progressive expansion, with values ranging from 295 to 450 km² during the Late Carboniferous, 600–750 km² in the Early Permian, and 880–1150 km² in the Late Permian. A similar pattern was observed with respect

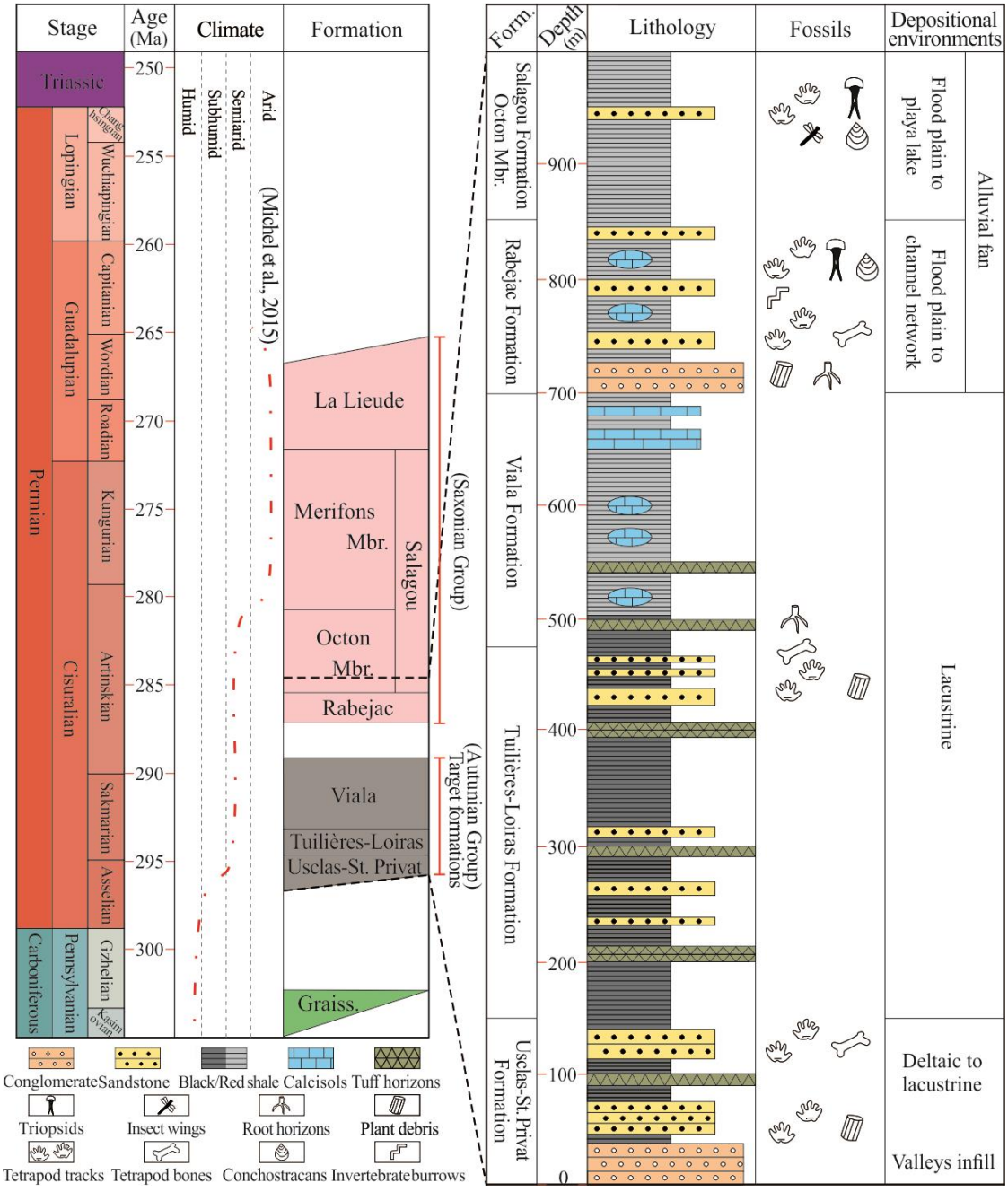

Figure 4.2 Generalized stratigraphic column of the Lodève Basin showing typical lithology, fossil content, and change in paleoclimate (modified after Schneider et al., 2006; Lopez et al., 2008; Michel et al., 2015; Mujal and Marchetti, 2020).

to sediment accumulation within the basin, with volumes ranging from 150 to 800 km³ during the Late Carboniferous expanding to 740–4210 km³ in the Late Permian (Pochat and Van Den Driessche, 2011). Nevertheless, sedimentation rates in the paleo-lake suffered a significant decline. This change was a result of the shift from an initial rapid stretching with associated tectonic subsidence to a later stage characterized by thermally induced subsidence as well as a consistent supply of sediment to a gradually expanding sedimentation area. A trend of decreasing maximum lake depth was also discernible (Pochat and Van Den Driessche, 2011).There has been a long debate regarding the presence of marine influence within the Carboniferous-Permian non-marine basins of France (Gottfried, 1987; Poplin et al., 2001; Schultze, 2009; Luccisano et al., 2023). The "endemic" Aeduelliform specimens, typically associated with the Lower Permian deposits (Autunian) in France, have been discovered in marine calcareous shale within the Kinney Clay Pit in New Mexico, North America (Gottfried, 1987). This finding suggests that Aeduelliforms had the capacity for movement in marine environments and were not confined solely to the freshwater basins of the Upper Carboniferous/Lower Permian period in France. This discovery also marks the first recorded instance of the presence of this specimen beyond the boundaries of Europe. Therefore, Schultze (2009) raised the possibility of a marine connection between these two geographic locations. In addition to the Early Permian strata related to this study, several fossils originated from the Late Carboniferous in the Massif Central, France, have been ascribed to a new taxonomic classification of fossil hagfish (Poplin et al., 2001). This finding implies a resemblance to modern hagfish, which are exclusively associated with marine environments, as the living hagfishes cannot thrive in freshwater conditions. Even slight fluctuations in salinity have been observed to significantly affect the living hagfishes (Poplin et al., 2001). However, during the Pennsylvanian and Permian, possibly separated by a range of Hercynian Mountains, the Lodève Basin was approximately 400 km inland from the Tethys ocean (Schneider et al., 2006; Michel et al., 2015). Thus, whether marine incursions occurred in the early stages of the Lodève Basin remains controversial.

4.3 Samples and methods

A set of 36 outcrop black shale samples was meticulously gathered following the stratigraphic ages, ranging from old (BS-1) to young (BS-34), from two sedimentological sections comprising the Early Permian USPF, TLF, and VF in the Lodève Basin for this study (Fig. 4.1b, Table 4.1). Notably, samples denoted as BS-4, BS-7, BS-9, BS-10, BS-12–18, and BS-23–25 were gathered in or close to the Maro Valley, whereas the remaining samples were collected along the Merdanson river (Fig. 4.1b, Table 4.1). For shale layers with thickness > 50 cm, two outcrop samples were collected from the bottom and top with the corresponding addition “A” and “B” following the sample number. Prior to measurement, the weathered surface of each sample was removed. In addition, each sample was separated into two sections: one was subjected to pulverization, while the other was for petrological observations, following the methodologies elucidated by Zieger and Littke (2019).

4.3.1 Elemental analysis and Rock-Eval pyrolysis

TOC and total inorganic carbon (TIC) contents were determined utilizing a Liquid TOC II (Elementar) apparatus. Values were calculated based on the detected CO_2 released during combustion in an oxygen atmosphere at up to 550 °C and 1000 °C, respectively. The total sulfur (TS) content was determined by subjecting the sample powder to combustion at a temperature of 1800 °C in a Leco S-200 Sulfur Analyzer and measuring the released SO_2. In both cases, standards of known TOC, TIC, and TS contents were used for calibration.

Rock-Eval pyrolysis was executed utilizing a Rock-Eval VII instrument (Vinci Technologies) adhering to the principles initially described by Espitalié et al. (1977), as well as the comprehensive procedural description outlined in Behar et al. (2001). The S_1 (volatile hydrocarbon content) fraction was measured at 300 °C for 3 min. The oven temperature was progressively raised to 650 °C to measure the S_2 (remaining hydrocarbon generative potential) fraction and T_{max} (calibrated temperature of maximum pyrolysis yield). The hydrogen (HI) and oxygen index (OI) were determined based on the S_2 and S_3 (CO_2 formed by thermal breakdown of kerogen) peaks relative to the TOC content.

4.3.2 Organic petrology

Maceral counting and identification were performed using a Zeiss Axio Imager microscope. The identification of macerals adhered to the guidelines delineated by Taylor et al. (1998), employing the terminology outlined in the ICCP System (ICCP, 1998, 2001; Pickel et al., 2017). Before conducting vitrinite reflectance measurements, calibration was achieved using an yttrium-aluminum-garnet standard. For each section, 30 to 50 randomly selected vitrinite particles were analyzed. Details of the polished section preparation and of the analytical instruments and procedures are described in Zieger and Littke (2019).

4.3.3 Molecular organic geochemistry

Approx.2-3 g of finely ground sample was extracted utilizing a DIONEX ASE 150 apparatus, with around 10 mL of dichloromethane (DCM) at a temperature of 100 °C and a pressure of 10 bar. Fractionation was carried out by liquid chromatography on a micro column packed with 2 g of activated silica gel to separate the extracts into aliphatic and aromatic fractions, using 5 mL of *n*-pentane and a mixture of *n*-pentane and DCM (40:60, v:v), respectively. Subsequently, the two fractions were examined by GC-MS on a HRGC 5160 gas chromatograph (GC) connected to a quadrupole mass spectrometer (Trace MS). For analysis of the aliphatic fraction, the initial GC oven temperature was kept at 80 °C for 3 min. Subsequently, it was raised to 160 °C at 10 °C/min, and further elevated to 320 °C at a rate of 3 °C/min, and maintained isothermal for 20 min. The MS was operated in electron impact ionization (EI) mode at 70 eV in single ion monitoring (SIM) mode. The measured ions are described in (Fang et al., 2019). For analysis of the aromatic fractions, the full scan mode was employed, with the GC temperature initially set at 80 °C held for 3 min; it was then

progressively increased to 320 °C at a rate of 3 °C/min and ultimately held constant for 20 min. The identification of compounds was performed by comparison of retention times and elution orders with those of reference substances and published chromatograms. For samples measured in full scan mode, compound identification was conducted by utilizing relative retention times and mass spectra. The calculated biomarker ratios were derived from the peak areas in the specific ion chromatograms.

4.3.4 Compound specific stable carbon isotope analyses (CSIA)

CSIA was performed by gas chromatography–isotope ratio monitoring-mass spectrometry (GC–irmMS) using a Finnigan Delta Plus XL mass spectrometer that was equipped with a GCC III combustion interface and connected to a gas chromatograph 6980A (Fisons Instruments). The chromatographic parameters were set with an initial oven temperature of 60 °C, maintained for 3 min, followed by a programmed ramp of 2°/min up to 300 °C. The oxidation process for the eluting substances was performed at a temperature of 940 °C. All the presented data have been normalized with respect to the VPDB standard. A more comprehensive description of the applied experimental methodology is provided by Schwarzbauer et al. (2013).

4.3.5 X-ray fluorescence (XRF)

The analysis of major and trace elements was executed using a SPECTRO XEPOS XRF spectrometer. To minimize moisture content, the sample was dried at 105 °C for 12 h prior to analysis. A blend of 8 g finely ground sample and 2 g of wax was thoroughly mixed to ensure homogeneity. To enhance accuracy, concentrations were corrected through comparison with standard samples incorporated within the system. A more comprehensive description of the applied experimental methodology is provided by Obreht et al. (2015).

The chemical index of alteration (CIA), proposed by Nesbitt and Young (1982), is calculated by the following equation:

$$CIA = \text{molar } [Al_2O_3/(Al_2O_3 + CaO^* + Na_2O + K_2O)] \times 100$$

CaO* refers to the CaO content within the silicate fraction. Following the correction approach outlined by McLennan (1993), the CaO* undergoes an initial correction using P_2O_5 data ($CaO' = CaO - 10/3 \times P_2O_5$). Subsequently, when CaO' exceeds Na_2O, the ultimate CaO* value is equated to Na_2O; conversely, when CaO' falls short of Na_2O, the ultimate CaO* value is set equal to CaO'.

Given that K may accumulate in the weathering residues, a chemical index of weathering (CIW) was introduced by removing the K component in the CIA equation (Harnois, 1988). However, the calculation of CIW may overlook the presence of Al associated with the K-feldspar in the examined materials (Fedo et al., 1995). To address the limitation of the CIW, the plagioclase index of alteration (PIA) was introduced and has since been widely utilized to assess the extent of weathering experienced by siliciclastic sediments across diverse climatic settings (Fedo et al., 1995). The PIA is defined as:

$$PIA = \text{molar } (Al_2O_3 - K_2O)/(Al_2O_3 + CaO^* + Na_2O - K_2O) \times 100$$

To correct the plot of data that deviates from the theoretical weathering trend in the A-CN-K (Al_2O_3-CaO* + Na_2O-K_2O) ternary diagram resulting from K-metasomatism, Panahi et al. (2000) proposed an equation to calculate the K_2O addition to the weathered sample as:

$K_2O_{corr} = [m \times Al_2O_3 + m \times (CaO^* + Na_2O)]/(1 - m)$

m is calculated by the following equation using major element data of the parent (protolith):

$m = K_2O/(Al_2O_3 + CaO^* + Na_2O + K_2O)$

Here, the Lower Crust beneath the Bournac pipe of the Massif Central, Franc (Dupuy et al., 1979) is adopted as the protolith.

The calculation of the index of compositional variability (ICV), employed to assess compositional maturity, can be performed using the following formula (Cox et al., 1995):

$ICV = (Fe_2O_3 + K_2O + Na_2O + CaO + MgO + MnO + TiO_2)/Al_2O_3$

The equations for the mafic–felsic–RW (robust weathering) ternary plot are as follows (Cho and Ohta, 2022): Mafic apex = exp.(m)/[exp.(m) + exp.(f) + exp.(rw)], Felsic apex = exp.(f)/[exp.(m) + exp.(f) + exp.(rw)], RW apex = exp.(rw)/[exp.(m) + exp.(f) + exp.(rw)], where $m = 0.051 \times \ln(TiO_2) - 0.120 \times \ln(Al_2O_3) + 0.018 \times \ln(Fe_2O_3) + 0.33 \times \ln(MgO) + 0.193 \times \ln(Na_2O) - 0.392 \times \ln(K_2O) + 0.330$, $f = -0.204 \times \ln(TiO_2) - 0.000 \times \ln(Al_2O_3) - 0.166 \times \ln(Fe_2O_3) - 0.177 \times \ln(MgO) + 0.311 \times \ln(Na_2O) + 0.236 \times \ln(K_2O) + 0.176$, and $rw = 0.152 \times \ln(TiO_2) + 0.198 \times \ln(Al_2O_3) + 0.148 \times \ln(Fe_2O_3) - 0.152 \times \ln(MgO) - 0.503 \times \ln(Na_2O) + 0.156 \times \ln(K_2O) - 0.506$. The value of the RW apex is used as the RW index.

4.4 Results

4.4.1 Elemental analysis and Rock-Eval pyrolysis

Generally, TOC and TS contents exhibit significant variability within each formation (Table 4.1). Specifically, within the USPF, the TOC and TS contents vary from 0.78 to 7.83 (avg. 3.03) wt% and 0.04 to 1.55 (avg. 0.48) wt%. It is worth highlighting that samples from the lower section of the USPF (sample No. BS-1A–BS-4) exhibit higher TS contents, spanning from 0.42 to 1.55 (avg. 1.09) wt%, in comparison to other samples. The TOC and TS contents of the TLF vary from 0.97 to 5.52 (avg. 2.66) wt% and 0.06 to 0.68 (avg. 0.22) wt%, while those of VF range from 1.49 to 4.04 wt% and 0.05 to 0.39 wt%, respectively, with average values of 3.17 wt% for TOC and 0.17 wt% for TS. The VF is also distinguished by comparatively elevated TIC contents, ranging from 2.54 to 5.65 wt%. OM* (OM content before sulfate reduction), CAR (carbonate content), and SIL (silicate content) were determined utilizing the equations proposed by Littke (1993). Silicate, composed mainly of the weathering products from the sounding area, is the predominant constituent across all analyzed samples (Table 4.1). The lower section of the USPF is characterized by higher OM* content, with an average content of 6.54 wt%.

Rock-Eval pyrolysis results reveal that most samples are characterized by relatively low S_1 values, ranging from 0.07 to 2.01 (avg. 0.68) mg HC/g rock. A pronounced variability is observed in

the S_2 and HI values within the USPF, spanning a range of 1.00 to 54.40 (avg. 14.17) mg HC/g rock and from 129 to 694 (avg. 413) mg HC/g TOC, respectively (Fig. 4.3, Table 4.1). The TLF displays a slightly lower average in S_2 and HI values, measuring at 11.18 mg HC/g rock and 395 mg HC/g TOC, respectively, which are evidently lower than those of the VF with 18.80 mg HC/g rock and 542 mg HC/g TOC, respectively. Additionally, the T_{max} values of the analyzed samples exhibit relatively limited variability, ranging between 432 °C and 447 °C (avg. 439 °C) (Fig. 4.3, Table 4.1).

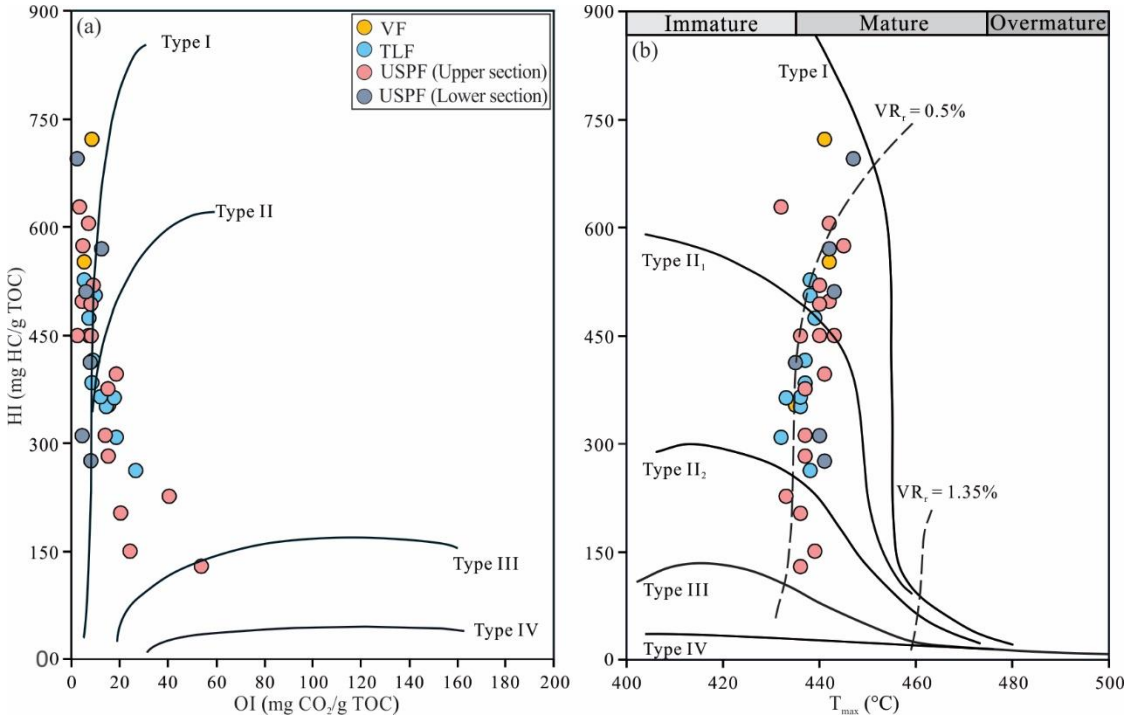

Figure 4.3 Rock-Eval data: (a) Cross-plot of HI versus OI. (b) Cross-plot of HI versus T_{max}.

4.4.2 Organic petrography

Based on organic petrographic analysis, inertinite, distinguished by its bright white color and high relief, occurs in the majority of samples, while vitrinite is observed in the form of small grey detrital particles (Fig. 4.4). Solid bitumen (SB) exhibits the typical pore-filling characteristics, occupying certain void spaces within the mineral grains (Fig. 4.4a, c), or occupying cell lumens within fusinite (Fig. 4.4g). Overall, the terrigenous macerals and SB occur in almost all samples but constitute a relatively small volumetric proportion within the analyzed samples (Table 4.2). Liptinite, characterized by the presence of lamalginite and liptodetrinite, exhibits strong orange fluorescence and represents the predominant maceral group (Fig. 4.4b, d, f, h, j, l). Notably, the lower section of the USPF exhibits a higher volumetric concentration of OM, aligning with the elevated TOC content (Table 4.2). Vitrinite reflectance (VR_r) values in the examined samples range from 0.72% to 0.79% (avg. 0. 75%, Table 4.2). The results of the VR_r measurements are generally consistent with the T_{max} values derived from Rock-Eval pyrolysis (Tables 4.1, 4.2).

Table 4.1 TOC, TIC, and TS contents, Rock-Eval pyrolysis data, and the three major primary sedimentary components calculated for the shales from the Lodève Basin.

Sample	Formation	TOC (wt%)	TIC (wt%)	TS (wt%)	S_1 (mg HC/g rock)	S_2 (mg HC/g rock)	S_3 (mg CO_2/g rock)	T_{max} (°C)	HI (mg HC/g TOC)	OI (mg CO_2/g TOC)	OM* (wt%)	CAR (wt%)	SIL (wt%)
BS-34		1.49	5.65	0.05	0.32	5.26	0.23	435	352	15	1.96	47.07	50.97
BS-33	VF	4.04	2.54	0.08	0.62	29.15	0.34	441	722	8	5.26	21.13	73.61
BS-32		3.99	2.92	0.39	0.87	21.99	0.21	442	551	5	5.49	24.29	70.22
BS-31		0.97	4.51	0.23	0.37	2.55	0.26	438	262	27	1.47	37.59	60.95
BS-30		1.61	2.25	0.09	0.25	4.95	0.30	432	308	19	2.15	18.78	79.07
BS-29		1.90	3.16	0.28	0.43	7.30	0.16	437	383	8	2.71	26.36	70.93
BS-28		2.24	3.33	0.24	0.39	11.30	0.22	438	505	10	3.10	27.76	69.15
BS-27	TLF	3.59	2.99	0.20	0.62	14.88	0.32	437	415	9	4.79	24.89	70.31
BS-26		5.52	3.70	0.27	0.76	26.14	0.40	439	473	7	7.34	30.83	61.83
BS-25		2.15	2.55	0.68	0.49	7.53	0.31	436	351	14	3.41	21.22	75.37
BS-24		3.61	6.09	0.06	0.72	19.02	0.19	438	526	5	4.69	50.78	44.53
BS-23		2.48	2.51	0.08	0.25	9.00	0.44	433	363	18	3.25	20.95	75.80
BS-22		2.50	3.79	0.08	0.50	9.08	0.30	436	364	12	3.28	31.60	65.12
BS-21		1.37	3.70	0.27	0.43	2.77	0.28	436	202	20	2.01	30.80	67.19
BS-20		3.89	7.06	0.16	0.32	20.16	0.35	440	519	9	5.14	58.80	36.06
BS-19		1.65	2.09	0.14	0.89	7.42	0.12	440	449	7	2.25	17.40	80.35
BS-18		1.73	0.02	0.08	0.86	3.90	0.70	433	226	41	2.29	0.18	97.53
BS-17		0.78	4.03	0.04	0.30	1.00	0.42	436	129	54	1.03	33.59	65.37
BS-16		0.98	4.07	0.25	0.53	2.76	0.15	437	282	15	1.50	33.93	64.58
BS-15	USPF	4.49	4.02	0.95	1.18	22.30	0.20	442	496	4	6.67	33.53	59.80
BS-14		2.99	5.18	0.14	0.64	18.10	0.21	442	605	7	3.97	43.20	52.84
BS-13		3.79	4.51	0.55	0.74	21.74	0.18	445	574	5	5.39	37.58	57.03
BS-12		4.45	2.41	0.86	0.47	21.95	0.36	440	493	8	6.54	20.05	73.41
BS-11		1.13	6.37	0.05	0.55	4.46	0.21	441	396	19	1.50	53.08	45.42
BS-10		0.78	0.07	0.07	0.15	1.17	0.19	439	150	24	1.07	0.59	98.33
BS-9		6.62	0.46	0.33	0.67	24.86	1.00	437	375	15	8.81	3.84	87.36
BS-8		1.60	2.50	0.24	1.31	7.16	0.13	436	448	8	2.28	20.86	76.86
BS-7		1.64	3.21	0.05	1.08	5.09	0.23	437	311	14	2.15	26.78	71.07
BS-6		2.08	0.01	0.17	1.92	13.06	0.07	432	628	3	2.83	0.05	97.12
BS-5		4.05	0.13	0.13	2.01	18.19	0.10	443	449	2	5.32	1.12	93.56
BS-4		2.69	5.74	0.42	1.07	13.72	0.16	443	510	6	3.86	47.82	48.32
BS-3		2.86	3.39	1.41	0.97	11.76	0.22	435	412	8	5.02	28.26	66.72
BS-2B		7.83	0.34	1.07	0.69	54.40	0.18	447	694	2	11.07	2.80	86.13
BS-2A		4.90	2.12	0.60	0.07	27.91	0.61	442	570	12	6.86	17.67	75.47
BS-1B		4.57	0.05	1.55	0.54	14.16	0.20	440	310	4	7.35	0.43	92.22
BS-1A		2.86	3.88	1.47	0.59	7.86	0.23	441	275	8	5.08	32.34	62.58

OM* = OM content before sulfate reduction; CAR = carbonate content; SIL = silicate content.

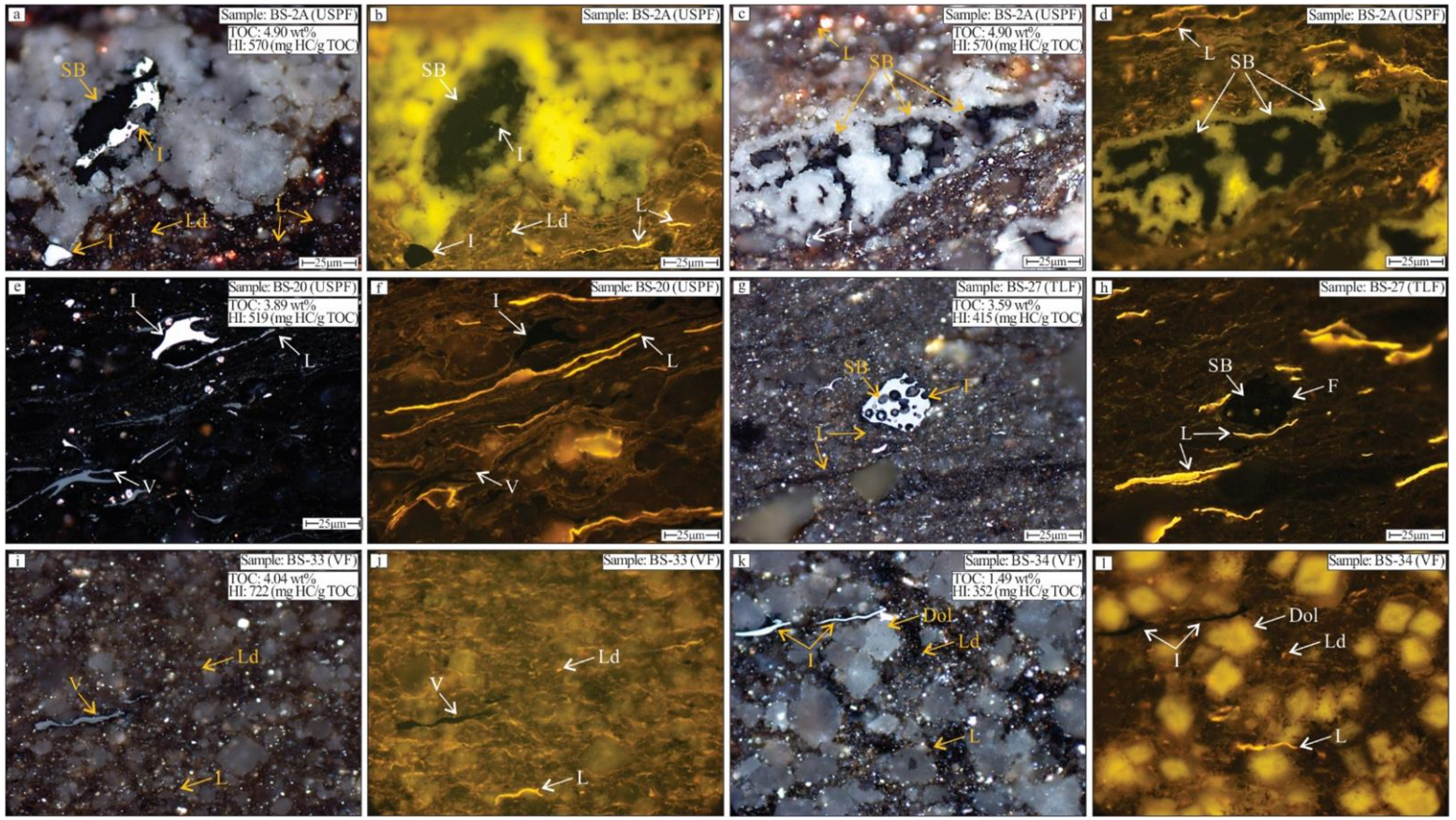

Figure 4.4 Microphotographs representative of the organic matter (OM) in the shales from the Lodève Basin under reflected white light (a, c, e, g, i, k) and in fluorescence mode (b, d, f, h, j, l). (a) Inertinite and SB, sample BS-2A, USPF. (b) Lamalginite and liptodetrinite in Fig. 4.4a. (c) SB infilling the voids within mineral particles, sample BS-2A, USPF. (d) Lamalginite in Fig. 4.4c. (e) Inertinite and vitrinite, sample BS-20, USPF. (f) Terrigenous OM without fluorescence in Fig. 4.4e. (g) SB infilling the voids within fusinite, sample BS-27, TLF. (h) Lamalginite in Fig. 4.4g. (i) Vitrinite, sample BS-33, VF. (j) Lamalginite and liptodetrinite in Fig. 4.4i. (k) Inertinite, sample BS-34, VF. (l) Lamalginite, liptodetrinite, and dolomite with orange fluorescence in Fig. 4.4k. V-vitrinite, I-inertinite, F-fusinite, L-lamalginite, Ld-liptodetrinite, SB-solid bitumen, Dol-dolomite.

Table 4.2 TOC, vitrinite reflectance (VR_r), and maceral compositions of the shales from the Lodève Basin.

Sample	Formation	TOC (wt%)	VR_r (%)	Maceral composition (vol%)				
				Vitrinite	Inertinite	Liptinite	Solid bitumen	Total OM
BS-34		1.49	0.73	0.1	0.1	2.5	0.0	2.7
BS-33	VF	4.04	0.74	0.0	0.3	7.1	0.0	7.4
BS-32		3.99	0.73	0.1	0.2	7.0	0.3	7.5
BS-31		0.97	0.73	0.0	0.0	0.3	0.3	0.7
BS-30		1.61	0.74	0.0	0.1	1.1	0.1	1.3
BS-29		1.90	0.72	0.0	0.2	2.8	0.0	3.1
BS-28		2.24	0.76	0.1	0.2	8.3	0.1	8.6
BS-27	TLF	3.59	0.75	0.1	0.7	6.7	0.2	7.8
BS-26		5.52	0.74	0.0	0.6	13.5	0.4	14.5
BS-25		2.15	0.76	0.0	0.2	2.5	0.2	2.8
BS-24		3.61	0.72	0.0	0.3	6.8	1.7	8.8
BS-23		2.48	0.75	0.1	0.5	4.5	0.2	5.2
BS-22		2.50	0.76	0.1	0.2	2.7	0.0	3.1
BS-21		1.37	0.75	0.2	0.1	3.6	0.0	3.9
BS-20		3.89	0.77	0.2	0.4	2.3	0.5	3.3
BS-19		1.65	0.76	0.2	0.1	1.2	0.0	1.6
BS-18		1.73	0.76	0.2	0.2	3.3	0.0	3.7
BS-17		0.78	0.74	0.4	0.2	2.8	0.0	3.4
BS-16		0.98	0.75	0.3	0.1	3.7	0.0	4.1
BS-15		4.49	0.74	0.4	0.5	8.5	0.1	9.5
BS-14		2.99	0.76	0.1	0.4	6.5	0.2	7.3
BS-13		3.79	0.73	0.2	0.3	7.4	0.0	7.8
BS-12		4.45	0.76	0.1	0.1	3.0	0.1	3.5
BS-11		1.13	0.76	0.0	0.0	3.2	0.0	3.3
BS-10	USPF	0.78	0.78	0.1	0.3	0.7	0.0	1.1
BS-9		6.62	0.75	0.2	0.8	7.0	0.4	8.4
BS-8		1.60	0.79	0.2	0.1	1.7	0.0	2.0
BS-7		1.64	0.76	0.1	0.1	3.1	0.0	3.3
BS-6		2.08	/	0.0	0.2	2.2	0.5	2.9
BS-5		4.05	0.77	0.1	0.3	1.1	0.0	1.6
BS-4		2.69	0.76	0.1	0.2	6.1	0.1	6.5
BS-3		2.86	0.78	0.2	0.5	5.4	0.0	6.0
BS-2B		7.83	0.76	0.1	0.2	12.7	0.1	13.1
BS-2A		4.90	0.79	0.1	0.5	9.8	0.7	11.1
BS-1B		4.57	0.79	0.4	0.3	1.3	0.2	2.1
BS-1A		2.86	0.78	0.3	0.1	0.4	0.0	0.8

4.4.3 Molecular geochemistry

4.4.3.1 Acyclic alkanes

The normal alkanes in most extracted samples show a unimodal pattern, prominently featuring higher proportions within the lower molecular weight *n*-alkanes, with distinct peaks observed at *n*-C_{14} and *n*-C_{16} (Fig. 4.5a-c). Additional distinctions emerge through the examination of acyclic aliphatic compound proxies (Table 4.3). The pristane/phytane (Pr/Ph) values of the USPF, TLF, and VF range from 0.98 to 1.89 (avg. 1.37), 1.30 to 1.89 (avg. 1.61), and 1.48 to 1.62 (avg. 1.57), respectively. Notably, the Pr/Ph ratio exhibits lower values of 0.98–1.20 (averaging at 1.13) for the low section of the USPF. CPI (carbon preference index; Bray and Evans, 1961) and OEP (odd-to-even predominance; Peters and Moldowan, 1993) values exhibit negligible distinctions across all analyzed samples, spanning a range from 0.92 to 1.22 (avg. 1.04) and 0.92 to 1.28 (avg. 1.04), respectively (Table 4.3). Proxies employed as indicators of OM sources, including waxiness index (WI; Peters et al., 2005) and terrigenous/aquatic ratio (TAR; Bourbonniere and Meyers, 1996) manifest comparatively elevated

values in some samples of the USPF (WI: 0.44–2.62, avg. 1.05; TAR: 0.06–0.88, avg. 0.28), when compared with those of the TLF (WI: 0.29–1.00, avg. 0.55; TAR: 0.03–0.26, avg. 0.10) and VF (WI: 0.51–0.64, avg. 0.59; TAR: 0.10–0.16, avg. 0.14) (Table 4.3). Conversely, the *n*-C_{17}/*n*-C_{27} and *n*-

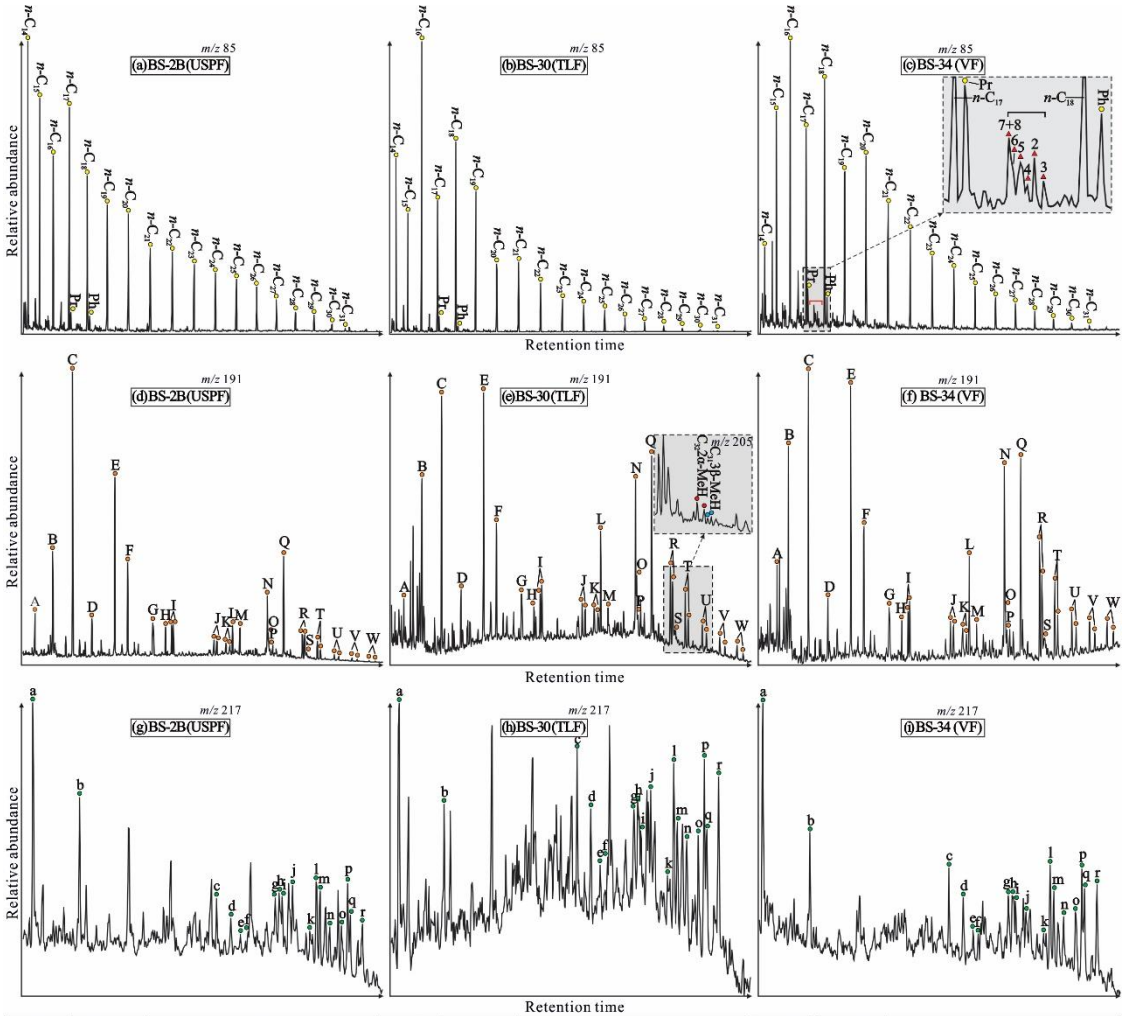

Peak	Abbreviation	Biomarker	Peak	Abbreviation	Biomarker	Peak	Abbreviation	Biomarker
A	C_{19} Tri	C_{19}-tricyclic terpane	O	C_{29} Ts	C_{29}-18α(H)-30-norneohopane	d	C_{21} βα dia20R	20R-13β(H),17α(H)-diacholestane
B	C_{20} Tri	C_{20}-tricyclic terpane	P	C_{30} DiaH	C_{30}-17α-diahopane	e	C_{27} αβ dia20S	20S-13α(H),17β(H)-diacholestane
C	C_{21} Tri	C_{21}-tricyclic terpane	Q	C_{30} H	C_{30}-17α(H),21β(H)-hopane	f	C_{27} αβ dia20R	20R-13α(H),17β(H)-diacholestane
D	C_{22} Tri	C_{22}-tricyclic terpane	R	C_{31} H S	C_{31}-17α(H),21β(H),22S-homohopane	g	C_{27} ααα 20S	20S-5α(H),14α(H),17α(H)-cholestane
E	C_{23} Tri	C_{23}-tricyclic terpane		C_{31} H R	C_{31}-17α(H),21β(H),22R-homohopane	h	C_{27} αββ 20R	20R-5α(H),14β(H),17β(H)-cholestane
F	C_{24} Tri	C_{24}-tricyclic terpane	S	Gam	Gammacerane	i	C_{27} αββ 20S	20S-5α(H),14β(H),17β(H)-cholestane
G	C_{25}Tri	C_{25}-tricyclic terpane	T	C_{32} H S	C_{32}-17α(H),21β(H),22S-homohopane	j	C_{29} ααα 20R	20R-5α(H),14α(H),17α(H)-cholestane
H	C_{24} Tet	C_{24}-tetracyclic terpane		C_{32} H R	C_{32}-17α(H),21β(H),22R-homohopane	k	C_{29} ααα 20S	20S-24-Methyl-5α(H),14α(H),17α(H)-cholestane
I	C_{26} Tri R	C_{26}-R tricyclic terpane	U	C_{33} H S	C_{33}-17α(H),21β(H),22S-homohopane	l	C_{29} αββ 20R	20R-24-Methyl-5α(H),14β(H),17β(H)-cholestane
	C_{26} Tri S	C_{26}-S tricyclic terpane		C_{33} H R	C_{33}-17α(H),21β(H),22R-homohopane	m	C_{29} αββ 20S	20S-24-Methyl-5α(H),14β(H),17β(H)-cholestane
J	C_{28} Tri R	C_{28}-R tricyclic terpane	V	C_{34} H S	C_{34}-17α(H),21β(H),22S-homohopane	n	C_{30} ααα 20R	20R-24-Methyl-5α(H),14α(H),17α(H)-cholestane
	C_{28} Tri S	C_{28}-S tricyclic terpane		C_{34} H R	C_{34}-17α(H),21β(H),22R-homohopane	o	C_{30} ααα 20S	20S-24-Ethyl-5α(H),14α(H),17α(H)-cholestane
K	C_{29} Tri R	C_{29}-R tricyclic terpane	W	C_{35} H S	C_{35}-17α(H),21β(H),22S-homohopane	p	C_{31} αββ 20R	20R-24-Ethyl-5α(H),14β(H),17β(H)-cholestane
	C_{29} Tri S	C_{29}-S tricyclic terpane		C_{35} H R	C_{35}-17α(H),21β(H),22R-homohopane	q	C_{31} αββ 20S	20S-24-Ethyl-5α(H),14β(H),17β(H)-cholestane
L	Ts	C_{27}-18α(H)-22,29,30-trisnorneohopane	a	Pregnane	5α,14β,17β(H)-pregnane (diginane)	r	C_{31} ααα 20R	20R-24-Ethyl-5α(H),14α(H),17α(H)-cholestane
M	Tm	C_{27}-17α(H)-22,29,30-trisnorhopane	b	Homopregnane	5α,14β,17β(H)-homopregnane (20-methyldiginane)			
N	C_{29} H	C_{29}-17α(H),21β(H)-hopane	c	C_{21} βα dia20S	20S-13β(H),17α(H)-diacholestane			

Figure 4.5 Exemplary mass chromatograms of the aliphatic fraction for the representative shale samples from the Lodève Basin. (a-c) Mass chromatograms (m/z 85) showing the n-alkanes and acyclic isoprenoids. Compounds 2–8 refer to monomethyl substituted heptadecanes. (d-f) Mass chromatograms (m/z 191 and 205) showing the hopanes and 2α- and 3β-methylhopane (MeH). (g-i) Mass chromatograms (m/z 217) showing the steranes

C_{17}/*n*-C_{27} and *n*-C_{17}/(*n*-C_{23} + *n*-C_{25} + *n*-C_{27}) values show a contrasting trend, exhibiting lower values in the USPF (Table 4.3).

4.4.3.2 Terpanes

Tricyclic terpanes (Tri) ranging from C_{19} to C_{29}, C_{24} tetracyclic terpane (C_{24} Tet), and pentacyclic terpanes (hopanes) have been detected across all samples (Fig. 4.5d–f). C_{32} 2α- and C_{31} 3β-methylhopanes show a low concentration in the analyzed samples (Fig. 4.5e). The C_{19}/C_{23} Tri and C_{24} Tet/C_{26} Tri ratios are low and rather uniform (Table 4.4). Gammacerane index values of the USPF (0.05–0.24, avg. 0.15), particularly the lower section samples No. BS-1A–BS-4 (0.10–0.24, avg. 0.17), are higher than those of the TLF (0.04–0.18, avg. 0.11) and VF (0.08–0.16, avg. 0.11) (Table 4.4). Similarly, the extended tricyclic terpane ratio (ETR) shows elevated values in the USPF (0.56–0.81, avg. 0.72) in comparison to the TLF (0.54–0.69, avg. 0.62) and VF (0.48–0.85, avg. 0.65) (Table 4.4). The values for Ts/(Ts + Tm) and C_{29} Ts/(C_{29} Ts + C_{29} H) within the analyzed samples encompass a range from 0.53 to 0.84 (avg. 0.67) and 0.27 to 0.54 (avg. 0.38), respectively. A gradual decline in the concentrations of C_{31} to C_{35} homohopanes and low homohopane index values (HHI, Peters and Moldowan, 1991) are evident throughout all samples (Fig. 4.5d-f, Table 4.4).

4.4.3.3 Steroids

The presence of steranes is notably diminished in comparison to the concentration of hopanes in the majority of the analyzed samples, as shown by steranes/hopanes ratios ranging from 0.09 to 0.90 (avg. 0.31; Table 4.4). The distribution of steranes is shown in Fig. 4.5g-i. Generally, the proportions of ααα 20R steranes of the C_{27}, C_{28}, and C_{29} exhibit similar values across the three formations (Table 4.4). C_{29} ααα 20S/(20S + 20R) and C_{29} ββ/(ββ + αα) ratios display a range from 0.34 to 0.55 (avg. 0.44) and from 0.44 to 0.61 (avg. 0.53), respectively (Table 4.4).

4.4.3.4 Aromatic hydrocarbons

The discernible peaks of the aromatic fractions are represented in Fig. 4.6a. Thermal maturity proxies of TNR-1, TNR-2, TMNr, MPI-1, and DNR-1 exhibit a range from 0.50 to 1.05 (avg. 0.85), 0.39 to 0.74 (avg. 0.61), 0.37 to 0.75 (avg. 0.59), 0.20 to 0.69 (avg. 0.55), and 1.92 to 3.43 (avg. 2.85), respectively (Table 4.5). These values correspond to calculated vitrinite reflectance values (VR_{TNR-2}, VR_{MPI-1}, and VR_{DNR-1}) spanning the range of 0.64 to 0.84 (avg. 0.76), 0.52 to 0.82 (avg. 0.73), and 0.66 to 0.80 (avg. 0.75), respectively (Table 4.5). 9-MP emerges as the predominant compound among the MP homologs, exhibiting consistently low log (1-MP/9-MP) ratios within the range of –0.27 to –0.06 (avg. –0.18) across the majority of samples (Table 4.5). Similarly, log (1,2,5-TMN/1,3,6-TMN), log (1,2,7-TMN/1,3,7-TMN), and log (1,7-DMP/1,3- + 3,9- + 2,10- + 3,10-DMP) ratios consistently exhibit low values spanning from –0.86 to –0.26 (avg. –0.49), –1.05 to –0.39 (avg. –0.70), and –0.50 to –0.13 (avg. –0.34), respectively (Table 4.5). TA(I)/TA(I + II) ratios, derived from the detected

triaromatic steroids (Fig. 4.6b), exhibit a range spanning from 0.21 to 0.49 (avg. 0.40, Table 4.5). The aryl isoprenoids (AIs) were detected in the lower section of the USPF fragmentograms (Fig. 4.6c).

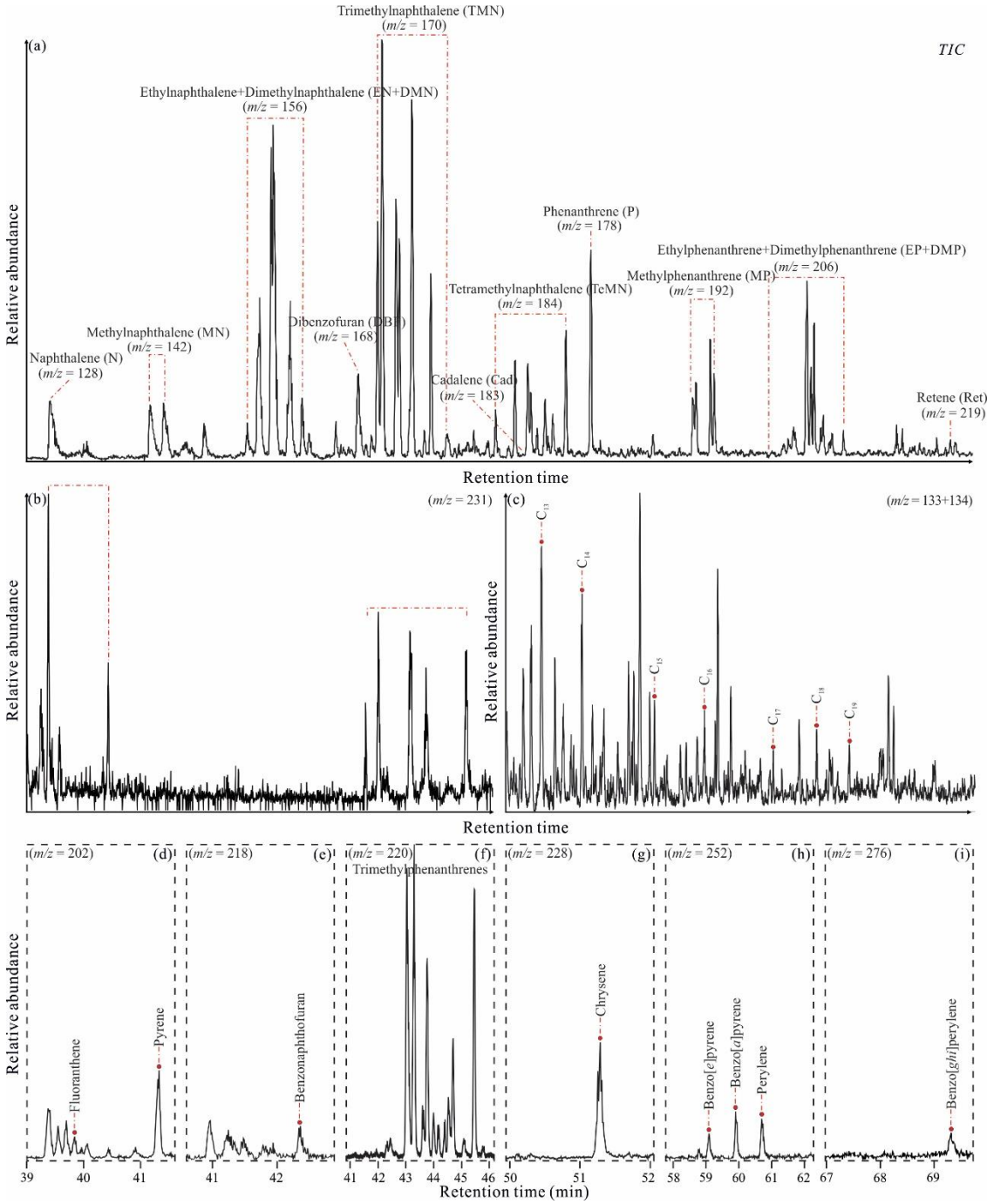

Figure 4.6 (a) TIC for the aromatic fraction (sample No. BS-16). (b) m/z 231 mass fragmentograms for triaromatic steranes (sample No. BS-16). (c) m/z 133 + 134 mass fragmentograms for aryl isoprenoids (AIs) (sample No. BS-2B). (d-i) Ion chromatograms (m/z 202, 218, 220, 228, 252, and 276; sample No. BS-16).

Furthermore, a range of polycyclic aromatic hydrocarbons (PAHs) was identified, such as fluoranthene (Fla) and pyrene (Py) (*m/z* 202), trimethylphenanthrenes (*m/z* 220), chrysene (*m/z* 228), and benzo[*e*]pyrene and benzo[*a*]pyrene (*m/z* 252) (Fig. 4.6d, f, g, h, i). The ratios of Fla/(Fla + Py) exhibit a range of values spanning from 0.04 to 0.21 (avg. 0.12) (Table 4.5). In addition to the PAHs, the analysis also revealed the presence of another oxygen-containing aromatic compound, benzonaphthofuran (*m/z* 218) (Fig. 4.6e).

4.4.3.5 Carbon isotopes of *n*-alkanes and isoprenoids

The carbon isotopic data of *n*-alkanes and acyclic isoprenoids for the examined samples are presented in Table 4.6. The majority of the analyzed samples exhibit *n*-alkanes characterized by a prevailing downward-sloping trend with increasing carbon chain length (Fig. 4.7), with $\delta^{13}C$ values ranging between −39.55‰ and −27.83‰ vs. VPDB for the individual compounds (Table 4.6). Furthermore, it is noteworthy that Ph is more enriched in ^{13}C relative to Pr across the majority of the samples. Additionally, a similar variation in the $\delta^{13}C$ values is observed among the analyzed samples for acyclic isoprenoids (Pr and Ph) and *n*-alkanes (Fig. 4.7).

4.4.4 Major and trace elements

Indicators of paleo-productivity, including Cu/Al, Ni/Al, and P/Al ratios, generally exhibit similar values across the examined samples (Table 4.7). Paleo-climate proxies, such as Rb/Sr, ln (Al_2O_3/Na_2O), CIA, and PIA, manifest a discernible decreasing trend from the USPF to the VF (Table 4.7). The Al_2O_3 and TiO_2 contents, employed as indicators of terrigenous input, generally exhibit similar average values among the samples. However, some samples of the USPF stand out with the highest values, exemplified by sample No. BS-1B, having 19.15 wt% Al_2O_3, and BS-9, recording 0.98 wt% TiO_2. Stratigraphically, the Zr/K and Zr/Rb ratios, which serve as proxies for changes in sediment grain size, exhibit an overall increasing trend from the USPF to the VF. However, it is noteworthy that certain samples from the USPF show the highest values, as exemplified by sample No. BS-9, having a Zr/Rb ratio of 1.28 (Table 4.7).

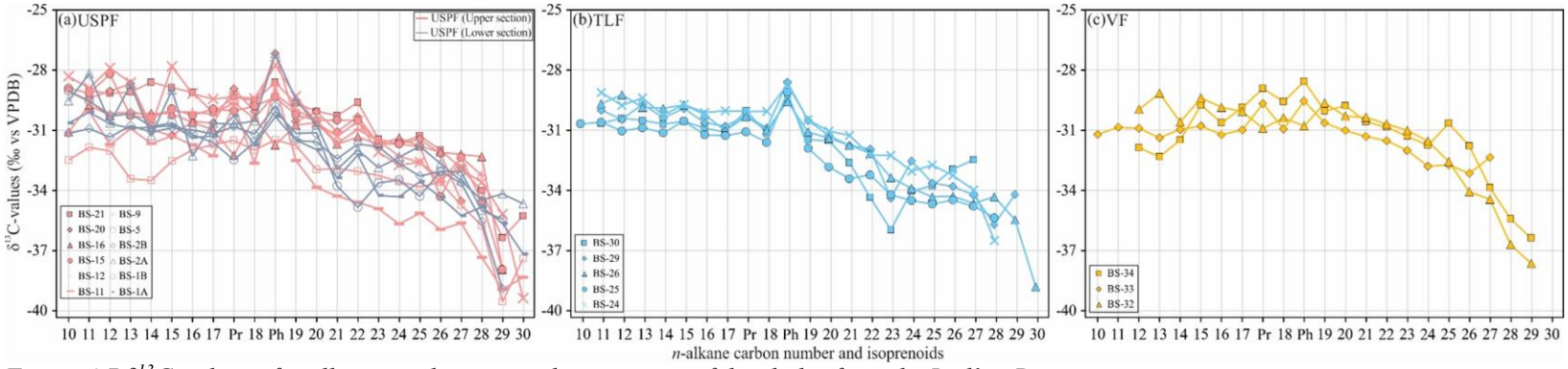

Figure 4.7 δ^{13}C-values of n-alkanes and isoprenoids in extracts of the shales from the Lodève Basin.

Table 4.3 Biomarker parameters of acyclic alkanes of the shales from the Lodève Basin.

Sample	Formation	Pr/Ph	n-C_{17}/n-C_{27}	n-C_{17}/(n-C_{23} + n-C_{25} + n-C_{27})	CPI	OEP	WI	TAR	10 × (7- + 8-methylhepadecanes /n-C_{17} + n-C_{18})
BS-34		1.48	6.28	1.18	1.00	1.00	0.51	0.10	0.67
BS-33	VF	1.62	4.29	0.97	1.03	1.02	0.61	0.16	0.43
BS-32		1.61	3.67	0.83	1.00	0.96	0.64	0.15	0.42
BS-30		1.76	14.86	2.20	1.02	1.06	0.29	0.04	0.18
BS-29		1.62	7.40	1.11	0.94	0.94	0.55	0.07	0.25
BS-26	TLF	1.51	9.31	1.28	0.98	1.03	0.59	0.07	0.32
BS-25		1.30	2.04	0.48	1.01	0.98	1.00	0.26	0.44
BS-24		1.89	15.98	2.03	0.98	1.01	0.32	0.03	0.25
BS-21		1.39	0.68	0.15	1.04	1.01	2.11	0.54	0.61
BS-20		1.44	3.35	0.67	1.00	1.07	0.90	0.24	0.33
BS-19		1.55	6.41	1.01	0.98	0.92	0.62	0.09	0.25
BS-16		1.38	1.01	0.28	1.11	1.04	1.85	0.66	0.34
BS-15		1.40	1.33	0.31	1.09	1.06	1.55	0.47	0.47
BS-14		1.42	9.33	1.44	0.95	0.95	0.44	0.06	0.14
BS-12		1.13	5.58	1.02	1.08	1.10	0.65	0.12	0.29
BS-11		1.89	8.31	1.23	0.92	0.96	0.53	0.07	0.14
BS-9	USPF	1.50	9.23	1.48	1.01	1.04	0.52	0.08	0.17
BS-8		1.80	3.04	0.50	1.22	1.28	0.82	0.13	0.58
BS-5		1.56	3.83	0.65	1.06	1.08	0.78	0.14	0.12
BS-4		1.20	0.80	0.24	1.10	1.05	2.09	0.79	1.06
BS-3		1.11	6.85	1.04	1.10	1.09	0.53	0.08	0.51
BS-2B		1.15	4.88	1.00	1.06	1.10	0.63	0.13	0.19
BS-2A		0.98	0.55	0.14	1.07	1.07	2.62	0.88	0.71
BS-1B		1.14	3.88	0.76	1.04	1.03	0.73	0.15	0.23
BS-1A		1.20	8.05	1.47	1.13	1.17	0.50	0.08	0.08

Pr = pristane; Ph = phytane; CPI = 2 × Σodd n-$C_{23–29}$/(Σeven n-$C_{22–28}$ + Σeven n-$C_{24–30}$); OEP = (n-C_{21} + 6 × n-C_{23} + n-C_{25})/(4 × n-C_{22} + 4 × n-C_{24}); WI = Σn-$C_{21\text{-}31}$/Σn-$C_{15\text{-}20}$; TAR = (n-C_{27} + n-C_{29} + n-C_{31})/(n-C_{15} + n-C_{17} + n-C_{19}).

Table 4.4 Biomarker parameters of tricyclic and tetracyclic terpanes, hopanes, and steranes of the shales from the Lodève Basin.

Sample	Tricyclic and tetracyclic terpanes			Hopanes				Steranes/ hopanes	Steranes				
	C_{19}/ C_{23} Tri	C_{24} Tet/ C_{26} Tri	ETR	Ts/ (Ts + Tm)	C_{29} Ts/ (C_{29} Ts + C_{29} H)	Gam/ (C_{30} H + Gam)	HHI		C_{29} ββ/ (ββ + αα) steranes	C_{29} ααα S/ (R + S) steranes	Sterane ααα 20R distribution (%)		
											C_{27}	C_{28}	C_{29}
VF													
BS-34	0.23	0.41	0.85	0.74	0.27	0.08	0.09	0.20	0.51	0.52	26	31	43
BS-33	0.38	0.53	0.48	0.70	0.34	0.09	0.12	0.21	0.52	0.45	26	38	37
BS-32	0.26	0.42	0.62	0.84	0.46	0.16	0.02	0.42	0.55	0.43	46	23	31
TLF													
BS-30	0.23	0.32	0.55	0.70	0.37	0.09	0.06	0.21	0.55	0.46	30	34	36
BS-29	0.25	0.33	0.65	0.74	0.35	0.15	0.03	0.38	0.49	0.39	32	19	48
BS-26	0.28	0.45	0.54	0.69	0.43	0.04	0.02	0.15	0.47	0.38	35	19	46
BS-25	0.08	0.17	0.69	0.70	0.47	0.18	0.01	0.11	0.58	0.44	52	21	27
BS-24	0.42	0.67	0.64	0.76	0.54	0.07	0.05	0.37	0.50	0.36	34	23	43
USPF													
BS-21	0.18	0.12	0.81	0.77	0.44	0.23	0.02	0.53	0.58	0.47	37	21	42
BS-20	0.39	0.30	0.62	0.65	0.31	0.08	0.08	0.20	0.56	0.50	36	26	38
BS-19	0.29	0.20	0.78	0.78	0.37	0.13	0.04	0.44	0.55	0.49	39	18	43
BS-16	0.25	0.53	0.56	0.82	0.41	0.20	0.04	0.90	0.61	0.55	34	29	37
BS-15	0.18	0.23	0.65	0.71	0.47	0.21	0.05	0.41	0.57	0.46	33	25	42
BS-14	0.31	0.38	0.66	0.61	0.37	0.05	0.02	0.47	0.54	0.43	36	26	38
BS-12	0.29	0.37	0.73	0.57	0.31	0.13	0.03	0.38	0.54	0.46	41	20	39
BS-11	0.52	0.24	0.69	0.73	0.42	0.08	0.02	0.18	0.44	0.34	42	12	46
BS-9	0.11	0.12	0.81	0.60	0.38	0.14	0.04	0.15	0.48	0.38	29	26	45
BS-8	0.55	0.55	0.79	0.67	0.49	0.19	0.02	0.77	0.54	0.37	32	18	50
BS-5	0.29	0.32	0.74	0.63	0.36	0.06	0.02	0.09	0.48	0.45	53	13	34
BS-4	0.20	0.28	0.76	0.62	0.39	0.15	0.02	0.26	0.57	0.49	37	26	37
BS-3	0.33	0.41	0.80	0.53	0.28	0.23	0.03	0.16	0.50	0.40	32	19	50
BS-2B	0.22	0.43	0.69	0.56	0.28	0.13	0.02	0.12	0.52	0.44	43	19	38
BS-2A	0.19	0.37	0.76	0.61	0.39	0.10	0.02	0.29	0.45	0.34	39	16	45
BS-1B	0.20	0.37	0.73	0.57	0.34	0.17	0.02	0.17	0.54	0.50	47	21	32
BS-1A	0.22	0.33	0.73	0.54	0.29	0.24	0.02	0.10	0.53	0.42	41	19	40

Tri = tricyclic terpane; Tet = tetracyclic terpane; Extended tricyclic terpane ratio (ETR) = (C_{28} Tri + C_{29} Tri)/(C_{28} Tri + C_{29} Tri + Ts); Gam index = gammacerane index: Gam/(C_{30} H + Gam); HHI = homohopane index: $C_{35}/\Sigma C_{31\text{-}35}$ 22S and 22R homohopanes; H = hopane; Steranes/hopanes = $C_{27\text{-}29}$ regular steranes/$C_{29\text{-}35}$ 17α-hopanes.

Table 4.5 Biomarker parameters of aromatic fractions of the shales from the Lodève Basin.

Sample	TNR-1	TNR-2	VR_{TNR-2} (%)	TMNr	MPI-1	VR_{MPI-1} (%)	DNR-1	VR_{DNR-1} (%)	TA(I)/TA(I + II)	Log (1-MP/9-MP)	Log (1,2,5-TMN/1,3,6-TMN)	Log (1,2,7-TMN/1,3,7-TMN)	Log (1,7-DMP/1,3- + 3,9- + 2,10- + 3,10-DMP)	Fla/(Fla + Py)
VF														
BS-34	0.79	0.57	0.74	0.61	0.48	0.69	2.42	0.71	0.37	-0.19	-0.56	-0.89	-0.44	0.17
BS-33	0.86	0.56	0.73	0.68	0.29	0.57	1.95	0.67	0.43	-0.16	-0.75	-0.58	-0.34	0.07
BS-32	0.80	0.59	0.75	0.63	0.65	0.79	3.38	0.79	0.45	-0.18	-0.56	-0.75	-0.38	0.07
TLF														
BS-30	0.99	0.56	0.74	0.71	0.56	0.73	2.78	0.74	0.36	-0.15	-0.86	-1.05	-0.30	0.12
BS-29	1.01	0.65	0.79	0.63	0.45	0.67	3.12	0.77	0.44	-0.13	-0.57	-0.81	-0.35	0.07
BS-26	1.05	0.68	0.81	0.70	0.63	0.78	2.87	0.75	0.48	-0.13	-0.68	-0.98	-0.23	0.06
BS-25	0.82	0.57	0.74	0.62	0.45	0.67	3.43	0.80	0.38	-0.17	-0.56	-0.57	-0.25	0.10
BS-24	0.89	0.64	0.79	0.60	0.47	0.68	2.75	0.74	0.44	-0.15	-0.49	-0.71	-0.32	0.08
USPF														
BS-21	0.75	0.66	0.79	0.68	0.67	0.80	1.92	0.66	0.38	-0.24	-0.56	-1.03	-0.30	0.12
BS-20	0.92	0.74	0.84	0.73	0.51	0.71	3.03	0.76	0.46	-0.26	-0.63	-0.93	-0.42	0.04
BS-19	0.86	0.67	0.80	0.75	0.61	0.77	3.43	0.80	0.44	-0.21	-0.73	-0.86	-0.40	0.07
BS-16	0.80	0.64	0.78	0.59	0.57	0.74	2.98	0.76	0.31	-0.17	-0.42	-0.74	-0.20	0.18
BS-15	0.88	0.63	0.78	0.56	0.63	0.78	3.29	0.79	0.43	-0.13	-0.41	-0.43	-0.22	0.18
BS-14	1.00	0.73	0.84	0.68	0.61	0.76	3.33	0.79	0.40	-0.20	-0.56	-0.86	-0.38	0.11
BS-12	0.74	0.58	0.75	0.57	0.56	0.73	2.83	0.74	0.43	-0.20	-0.43	-0.73	-0.40	0.09
BS-11	0.93	0.65	0.79	0.63	0.67	0.80	2.51	0.72	0.49	-0.20	-0.53	-0.78	-0.23	0.19
BS-9	0.50	0.39	0.64	0.37	0.20	0.52	2.13	0.68	0.32	-0.06	-0.26	-0.51	-0.13	0.14
BS-8	0.82	0.59	0.76	0.48	0.69	0.82	2.57	0.72	0.21	-0.18	-0.30	-0.61	-0.34	0.14
BS-5	0.87	0.63	0.78	0.57	0.58	0.75	2.80	0.74	0.44	-0.22	-0.42	-0.49	-0.44	0.12
BS-4	0.72	0.57	0.74	0.47	0.59	0.75	2.41	0.71	0.32	-0.13	-0.28	-0.47	-0.39	0.21
BS-3	0.67	0.50	0.70	0.45	0.56	0.73	3.20	0.78	0.37	-0.21	-0.31	-0.50	-0.46	0.11
BS-2B	0.87	0.64	0.79	0.48	0.55	0.73	2.97	0.76	0.47	-0.24	-0.27	-0.56	-0.36	0.07
BS-2A	0.69	0.51	0.70	0.50	0.47	0.68	2.78	0.74	0.42	-0.27	-0.41	-0.59	-0.38	0.11
BS-1B	1.04	0.69	0.82	0.54	0.62	0.77	2.99	0.76	0.36	-0.15	-0.39	-0.58	-0.50	0.19
BS-1A	0.88	0.55	0.73	0.47	0.56	0.74	3.28	0.78	0.47	-0.17	-0.37	-0.39	-0.44	0.18

TNR-1: trimethylnaphthalene ratio 1 (2,3,6-TMN/[1,4,6- + 1,3,5-TMN]). Alexander et al. 1985.
TNR-2: trimethylnaphthalene ratio 2 (2,3,6- + 1,3,7-TMN/[1,4,6- + 1,3,5- + 1,3,6-TMN]). Radke et al. 1986.
VR_{TNR-2}: TNR-2 (0.60 × TNR-2 + 0.40). Radke et al. 1994.
TMNr: trimethylnaphthalene ratio (1,3,7-TMN/[1,3,7-TMN + 1,2,5-TMN]). van Aarssen et al. 1999.
MPI-1: methylphenanthrene index 1 (1.89 × [3-MP + 2-MP]/[P + 1.26 × (9-MP + 1-MP)]). Cassani et al. 1988.
VR_{MPI-1}: MPI-1 (0.60 × MPI-1 + 0.40). Radke and Welte 1983.
DNR-1: dimethylnaphthalene ratio 1 ([2,6- + 2,7-DMN]/1,5-DMN). Radke et al. 1982.
VR_{DNR-1}: DNR-1 (0.49 + 0.09 × DNR-1). Jiang and George, 2020.

Table 4.6 Compound specific stable carbon isotope data of n-alkanes and isoprenoids of the shales from the Lodève Basin.

Sample	*n*-C_{10}	*n*-C_{11}	*n*-C_{12}	*n*-C_{13}	*n*-C_{14}	*n*-C_{15}	*n*-C_{16}	*n*-C_{17}	*n*-C_{18}	*n*-C_{19}	*n*-C_{20}	*n*-C_{21}	*n*-C_{22}	*n*-C_{23}	*n*-C_{24}	*n*-C_{25}	*n*-C_{26}	*n*-C_{27}	*n*-C_{28}	*n*-C_{29}	*n*-C_{30}	Pr	Ph
VF																							
BS-34			-31.87	-32.33	-31.48	-29.75	-30.63	-29.87	-29.57	-30.04	-29.78	-30.59	-30.85	-31.31	-31.76	-30.66	-31.78	-33.88	-35.43	-36.39		-28.92	-28.56
BS-33	-31.21	-30.86	-30.91	-31.38	-30.96	-30.80	-31.22	-30.99	-30.94	-30.64	-31.03	-31.32	-31.53	-32.02	-32.81	-32.74	-33.16	-32.36				-29.67	-29.55
BS-32			-29.96	-29.16	-30.59	-29.39	-29.86	-30.08	-30.38	-29.64	-30.30	-30.36	-30.70	-31.01	-31.55	-32.56	-34.08	-34.45	-36.71	-37.65		-30.91	-30.79
TLF																							
BS-30		-30.64	-30.39	-30.50	-30.68	-30.54	-30.89	-31.08	-31.14	-31.46	-31.51	-32.60	-34.33	-35.94	-34.01	-33.76	-32.92	-32.46				-30.01	-29.40
BS-29		-29.99	-30.44	-29.69	-30.37	-29.90	-30.61	-30.79	-30.88	-30.50	-31.25	-31.75	-31.92	-34.36	-32.51	-33.61	-33.79	-34.21	-35.67	-34.17		-30.25	-28.61
BS-26		-29.67	-29.22	-29.85	-29.89	-29.73	-30.21	-31.01	-30.99	-31.06	-31.39	-31.73	-32.14	-33.34	-33.88	-34.30	-34.27	-34.63	-34.29	-35.44	-38.77	-30.29	-29.56
BS-25	-30.67	-30.59	-31.02	-30.86	-31.12	-30.53	-31.22	-31.25	-31.59	-31.88	-32.82	-33.40	-33.21	-34.19	-34.48	-34.65	-34.46	-34.76	-35.34			-31.07	-29.09
BS-24		-29.11	-29.75	-29.38	-30.24	-29.71	-30.11	-30.02	-30.05	-30.47	-31.03	-31.25	-32.22	-32.24	-33.03	-32.72	-33.24	-33.95	-36.47			-30.06	-28.73
USPF																							
BS-21		-29.03	-29.16	-29.09	-28.61	-28.87	-29.12	-30.12	-29.52	-29.66	-30.05	-30.27	-29.61	-31.45	-31.66	-31.27	-32.00	-32.89	-34.02	-36.37	-35.27	-29.35	-28.62
BS-20		-29.39	-29.06	-28.67	-30.97	-31.27	-30.56	-30.64	-30.07	-30.57	-30.07	-31.06	-30.33	-31.66	-31.69	-31.44	-32.18	-34.53				-28.93	-27.18
BS-16	-31.09	-29.75	-30.28	-30.18	-30.15	-30.18	-30.61	-30.98	-30.37	-30.74	-30.62	-31.69	-31.34	-31.70	-31.38	-31.80	-32.09	-32.20	-32.32	-37.95		-32.25	-31.74
BS-15	-28.91	-29.15	-28.21	-30.28	-30.40	-29.94	-30.26	-29.94	-29.80	-30.23	-30.52	-30.50	-30.52	-31.68	-31.69	-31.80	-34.32	-32.36	-34.56	-37.95		-30.04	-29.35
BS-12	-28.32	-28.90	-27.90	-28.63	-30.79	-27.83	-29.17	-29.45	-29.42	-29.31	-30.62	-31.31	-30.55	-32.10	-32.73	-32.59	-33.37	-32.97	-33.60	-35.19	-39.37	-29.32	-27.76
BS-11		-30.06	-31.72	-30.92	-31.66	-31.28	-31.73	-32.28	-32.66	-32.51	-33.86	-34.29	-34.59	-34.92	-35.67	-35.14	-35.95	-35.63	-37.34	-38.93	-38.34	-29.69	-28.76
BS-9	-29.07	-29.58	-30.18	-30.09	-30.27	-30.06	-30.10	-30.20	-30.40	-29.99	-30.49	-31.65	-30.97	-31.52	-32.30	-32.60	-33.60	-32.34	-33.25			-29.64	-29.20
BS-5	-32.48	-31.85	-32.04	-33.43	-33.51	-32.54	-31.97	-31.71	-31.98	-31.77	-32.97	-32.90	-33.06	-33.25	-33.57	-33.83	-33.58	-34.74	-35.76	-39.55	-37.40	-31.50	-31.49
BS-2B	-31.15	-30.92	-31.34	-30.76	-31.10	-30.88	-30.98	-31.19	-31.18	-31.50	-31.58	-32.42	-31.68	-31.83	-32.65	-33.28	-33.05	-33.64	-35.55	-38.90		-30.81	-29.78
BS-2A	-29.54	-28.17	-30.64	-28.73	-31.28	-29.00	-32.28	-30.65	-30.54	-29.49	-30.72	-32.95	-31.98	-32.87	-32.34	-31.79	-32.67	-33.53	-34.47	-34.17	-34.67	-30.71	-27.19
BS-1B	-29.04	-29.54	-30.29	-30.18	-30.81	-30.63	-31.23	-31.61	-31.61	-31.15	-31.13	-33.79	-34.84	-33.62	-33.48	-34.28	-33.05	-33.08	-35.01	-35.42		-32.47	-30.04
BS-1A	-30.64	-30.10	-30.69	-30.89	-30.85	-30.77	-31.36	-31.29	-31.74	-31.49	-31.96	-33.38	-32.23	-34.25	-34.32	-33.56	-34.34	-35.26	-34.82	-35.64	-37.17	-30.28	-30.33

Table 4.7 Inorganic geochemical proxies of the shales from the Lodève Basin.

Sample	Cu/Al (10^{-2})	Ni/Al (10^{-2})	P/Al (10^{-2})	Rb/Sr	ln (Al_2O_3/ Na_2O)	CIA	CIA_{corr}	PIA	ICV	SiO_2 (10^{-2})	CaO (10^{-2})	Al_2O_3 (10^{-2})	TiO_2 (10^{-2})	Zr/K (10^{-2})	Zr/Rb	La/Th	Hf (10^{-6})	TiO_2/Zr (10^{-4})
VF																		
BS-34	0.01	0.07	0.73	0.06	1.44	50.91	52.77	51.12	2.69	35.87	13.12	10.72	0.38	0.32	0.71			79.16
BS-33	0.01	0.06	0.48	0.15	1.45	51.02	52.93	51.26	1.78	45.81	7.64	12.43	0.51	0.45	0.89	7.89	1.80	65.10
BS-32	0.01	0.08	0.52	0.42	1.51	50.94	54.35	51.23	1.65	37.28	7.85	14.66	0.58	0.31	0.72	5.13	2.35	71.24
TLF																		
BS-30	0.02	0.10	0.33	0.61	1.88	55.71	62.57	58.49	1.46	40.03	5.61	16.93	0.53	0.17	0.45			81.25
BS-29	0.06	0.07	0.38	0.26	1.83	54.85	61.50	57.17	1.77	43.79	8.67	12.70	0.45	0.19	0.35	3.86	2.10	81.74
BS-26	0.08	0.13	0.20	0.19	1.72	50.65	59.24	51.08	1.76	38.07	9.72	14.06	0.51	0.18	0.49	5.59	4.00	67.70
BS-24	0.05	0.23	0.52	0.12	1.97	52.49	64.35	54.68	2.54	32.37	14.09	11.92	0.41	0.08	0.25			120.73
USPF																		
BS-19	0.05	0.14	0.10	0.62	2.01	51.22	65.18	52.55	1.35	45.74	6.13	16.39	0.59	0.09	0.30	6.36	2.20	100.68
BS-15	0.15	0.25	0.94	0.18	1.48	48.14	53.81	47.27	2.35	34.56	11.42	11.77	0.43	0.20	0.66	2.67	3.85	73.37
BS-14	0.09	0.22	1.93	0.13	2.44	52.19	73.05	56.39	3.39	27.85	14.52	9.54	0.39	0.14	0.70	3.71	1.90	60.54
BS-12	0.11	0.17	0.33	0.41	3.87	61.75	87.96	86.79	1.60	46.77	7.10	13.00	0.47	0.14	0.46			63.64
BS-11	0.00	0.18	0.34	0.20	3.14	54.83	82.26	69.09	3.49	29.37	15.42	9.95	0.38	0.06	0.25			122.01
BS-9	0.02	0.15	0.22	0.99	2.03	54.36	65.54	57.80	1.16	45.63	4.02	16.13	0.98	0.41	1.28	4.21	4.35	47.10
BS-8	0.04	0.09	0.14	0.64	1.79	51.35	60.68	52.28	1.46	42.05	7.24	16.15	0.59	0.16	0.50	3.93	1.90	72.94
BS-4	0.13	0.15	0.62	0.12	2.78	57.75	78.08	69.87	3.25	30.88	14.90	9.57	0.34	0.14	0.45			64.05
BS-2A	0.13	0.12	0.43	0.20	3.43	65.21	84.95	84.35	1.87	37.08	8.39	12.21	0.44	0.17	0.46			64.11
BS-1B	0.01	0.10	0.51	1.11	3.80	57.16	89.37	85.43	0.85	55.87	0.31	19.15	0.72	0.08	0.31	5.62	1.80	83.74
BS-1A	0.01	0.10	0.47	0.30	3.27	59.28	83.54	77.81	1.78	42.50	10.10	15.24	0.44	0.09	0.35			74.20

4.5 Discussion

4.5.1 Thermal maturity

The T_{max} data, displaying an average temperature of 439 °C, indicates that the shales are situated within the oil window characterized by an early-peak stage, which aligns with the VR_r values of 0.75% on average (Tables 4.1, 4.2). This stage of maturity is corroborated by the CPI and OEP ratios, which exhibit values close to 1 (Peters et al., 2005), as presented in Table 4.3. Furthermore, in the cross-plot of C_{29} Ts/(C_{29} Ts + C_{29} hopane) versus Ts/(Ts + Tm), the samples closely align with those extensively investigated in the well studied Toarcian Posidonia Shale from the Dohnsen borehole, which have a VR_r of 0.73% (Fig. 4.8a). Additionally, the cross-plot of C_{29} ααα 20S/(20S + 20R) versus C_{29} ββ/(ββ + αα) sterane ratios reveals that samples are close to the equilibrium region, signifying a maturity characteristic of the oil window (Fig. 4.8b; Peters et al., 2005; Song et al., 2017). Indicators of maturity based on aromatic hydrocarbons, encompassing TNR-1, TNR-2, TMNr, MPI-1, DNR-1, and TA(I)/TA(I + II), along with the associated derived calculated vitrinite reflectance values (VR_{TNR-2}, VR_{MPI-1}, and VR_{DNR-1}), provide further insights into the maturity data collectively confirming a maturity stage at the (early) phase of oil generation (Fig. 4.8c, Table 4.5; Fang et al., 2019; Jiang and George, 2020; Qiao et al., 2021a; Zheng et al., 2022; Wu et al., 2023).

Following the equation proposed by Barker and Pawlewicz (1986) on vitrinite reflectance, a maximum burial temperature of 111−124 °C can be calculated for these Lower Permian black shales. Based on the work by Wygrala (1989) together with an approximate paleo lake water depth of 200 m (Pochat and Van Den Driessche, 2011), a sediment/water interface temperature of 22 °C can be assumed. In combination with an assumed thermal gradient of 50 °C/km during maximum burial, typical for such kind of rift basins (e.g. the Saar-Nahe Basin, which is of similar age and style; Hertle and Littke, 2020), this corresponds to a maximum burial depth of about 1800−2100 m.

4.5.2 Depositional environment

Any water column stratification and the preservation conditions of OM are closely linked to fluctuations in paleosalinity; these conditions have severe influence on type and quantity of aquatic biomass (Powell, 1986; Romero-Viana et al., 2012; Wu et al., 2023). Owing to the massive difference in aqueous sulfate content between ‘normal’ freshwater and marine water, Wei and Algeo (2020) introduced a TS/TOC ratio of 0.1 to differentiate between freshwater sediments and those of brackish or marine origin, with marine sediments being characterized by TS/TOC ratios surpassing 0.5. In this study, an analysis of six samples of the lower section of the USPF (BS-1A– BS-4) has revealed a notable elevation in the TS/TOC ratio, falling into the domain characterized as brackish-marine and marine (Fig. 4.9a). In contrast, the majority of samples originating from the upper strata of the USPF, the TLF, and the VF display low values, serving as a marker of a continuous freshwater-brackish water environment (Fig. 4.9a). Gammacerane, potentially generated by the reduction of tetrahymanol (ten Haven et al., 1989; Venkatesan, 1989), can be used as a reliable indicator of shifts in salinity levels

and water column stratification (Burnaz et al., 2022; Wu et al., 2023). The Gammacerane index values of the analyzed samples manifest a similar pattern as the TS/TOC ratios (Fig. 4.9b). The highest average values of 0.17 occur in the lower section of the USPF (BS-1A–BS-4, Table 4.4), suggesting dominantly seawater salinity conditions. These conclusions are also consistent with the highest average ETR value, which is commonly high in samples deposited under conditions marked by high salinity and reducing conditions (Hao et al., 2009, 2011); such high values were found in the lower section of the USPF (Table 4.4).

As detailed in Table 4.3, most samples examined in this study exhibit relatively high Pr/Ph ratios (>1.0) and low HHI values, indicating the prevalence of oxic-dysoxic conditions, which is further substantiated by the result represented in the Pr/*n*-C_{17} versus Ph/*n*-C_{18} diagram (Fig. 4.9c). Nevertheless, it is essential to note rather low Pr/Ph ratios identified in the lower section of the USPF (BS-1A–BS-4), suggesting the prevalence of more reducing conditions (Table 4.3). This conclusion is further substantiated by assessing the relative concentrations of TOC, TS, and Fe, which primarily indicate oxic-dysoxic bottom water conditions across the majority of the studied samples (Fig. 4.9d). However, it is noteworthy that several samples of the lower section of the USPF exhibit characteristics aligned with more oxygen deficient conditions (Fig. 4.9d).

Phosphorus stands as an indispensable element for all life forms on Earth, as it assumes a pivotal role in numerous metabolic processes and serves as a structural component in DNA and RNA, various enzymes, phospholipids, and other biomolecules (Tribovillard et al., 2006). Consequently, after mitigation of the dilution effect from detrital influx, the P/Al ratio is employed as a reliable indicator of productivity. Cu and Ni are primarily transported to sediments through their association with organometallic complexes, the high abundance of which can be employed as an indicator of relatively elevated OM flux and paleo-productivity (Tribovillard et al., 2006). As detailed in Table 4.7, these three proxies tend to exhibit similar values (avg. Cu/Al: 0.06; avg. Ni/Al: 0.13; P/Al: 0.51) among the analyzed samples, implying a relatively uniform paleoproductivity among the three formations.

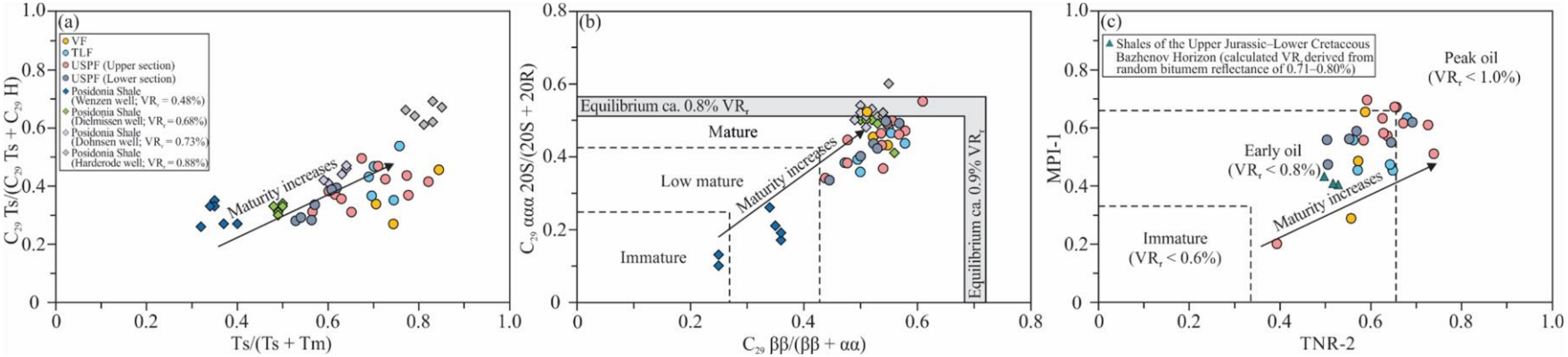

Figure 4.8 Molecular thermal maturity indicators of the shales from the Lodève Basin. (a) Cross-plot of C_{29} Ts/(C_{29} Ts + C_{29} H) versus Ts/(Ts + Tm). (b) C_{29} ααα 20S/(20S + 20R) versus C_{29} ββ/(ββ + αα). (c) MPI-1 versus TNR-2. Equilibrium is defined as the state at which equilibration levels are equivalent to vitrinite reflectance values (taken from Peters et al., 2005). For comparison, data of Posidonia Shale and shales of the Upper Jurassic–Lower Cretaceous Bazhenov Horizon at different maturities are taken from Fang et al. (2019) and Burnaz et al. (2022).

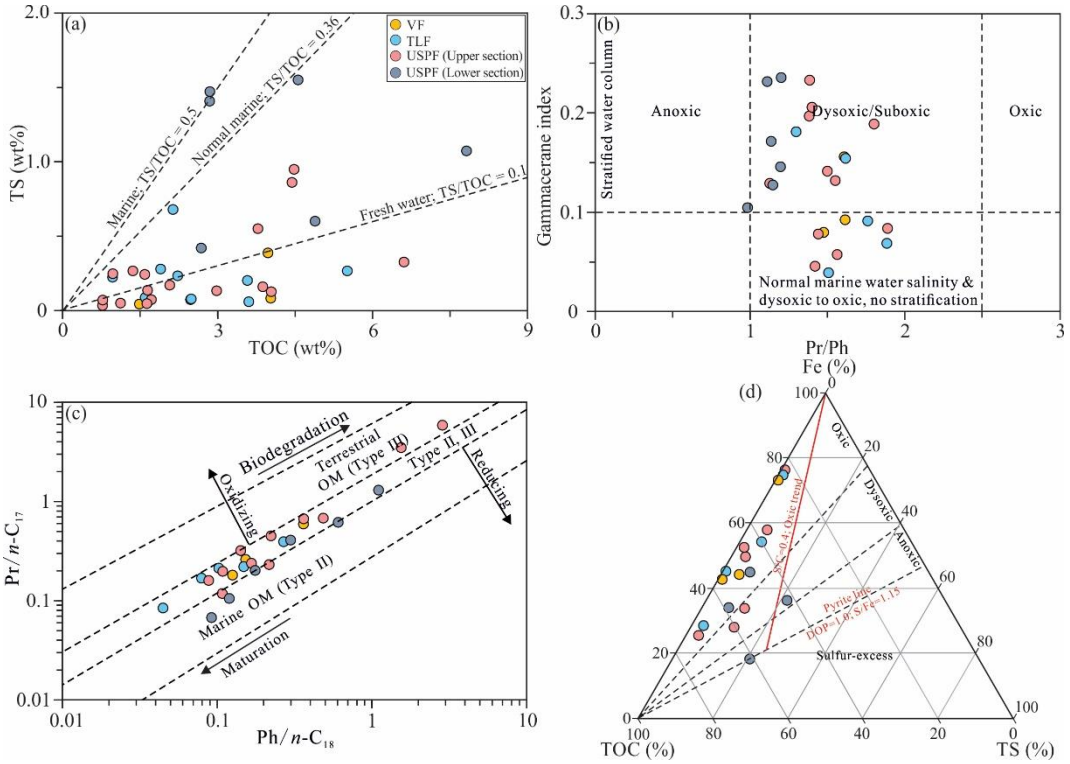

Figure 4.9 (a) Cross-plot of TS versus TOC. (b) Cross-plot of gammacerane versus pristane/phytane (Pr/Ph). (c) Cross-plot of Pr/n-C_{17} versus Ph/n-C_{18}. (d) Ternary diagram of relative concentrations of TOC, TS, and Fe. The normal-marine line is taken from Berner and Raiswell (1983).

4.5.3 Terrigenous influx, paleoclimate, weathering, and provenance

Aluminum originates predominantly from clay minerals, whereas Ti is primarily found in clay and heavy minerals (Rimmer, 2004; Calvert and Pedersen, 2007). The concentrations of Al and Ti are widely utilized as markers for clastic terrigeneous input (Burnaz et al., 2022; Wu et al., 2023). As shown in Fig. 4.10a, the three examined formations show values in a similar range (average Al_2O_3 and TiO_2 contents of 13.47 wt% and 0.51 wt%, respectively). Nevertheless, it is worth noting that the lower section of the USPF (samples No. BS-1A–BS-4) exhibits slightly higher levels of Al_2O_3 and TiO_2 contents, indicative of a rather high terrigenous detrital influx compared to the overlying layers, which might be attributed to a relatively intense fluvial activity at the beginning of the anoxic-deep lake system. Zr predominantly occurs within the coarse silt or very fine-grained sand components of siliciclastic sediments, primarily associated with zircon minerals (Bábek et al., 2016). In contrast, Rb and K exhibit a preferential enrichment within the fine-grained siliciclastic fractions, notably within clay minerals (Kalugin et al., 2007; Bábek et al., 2016; Xu et al., 2021). Consequently, the Zr/Rb and

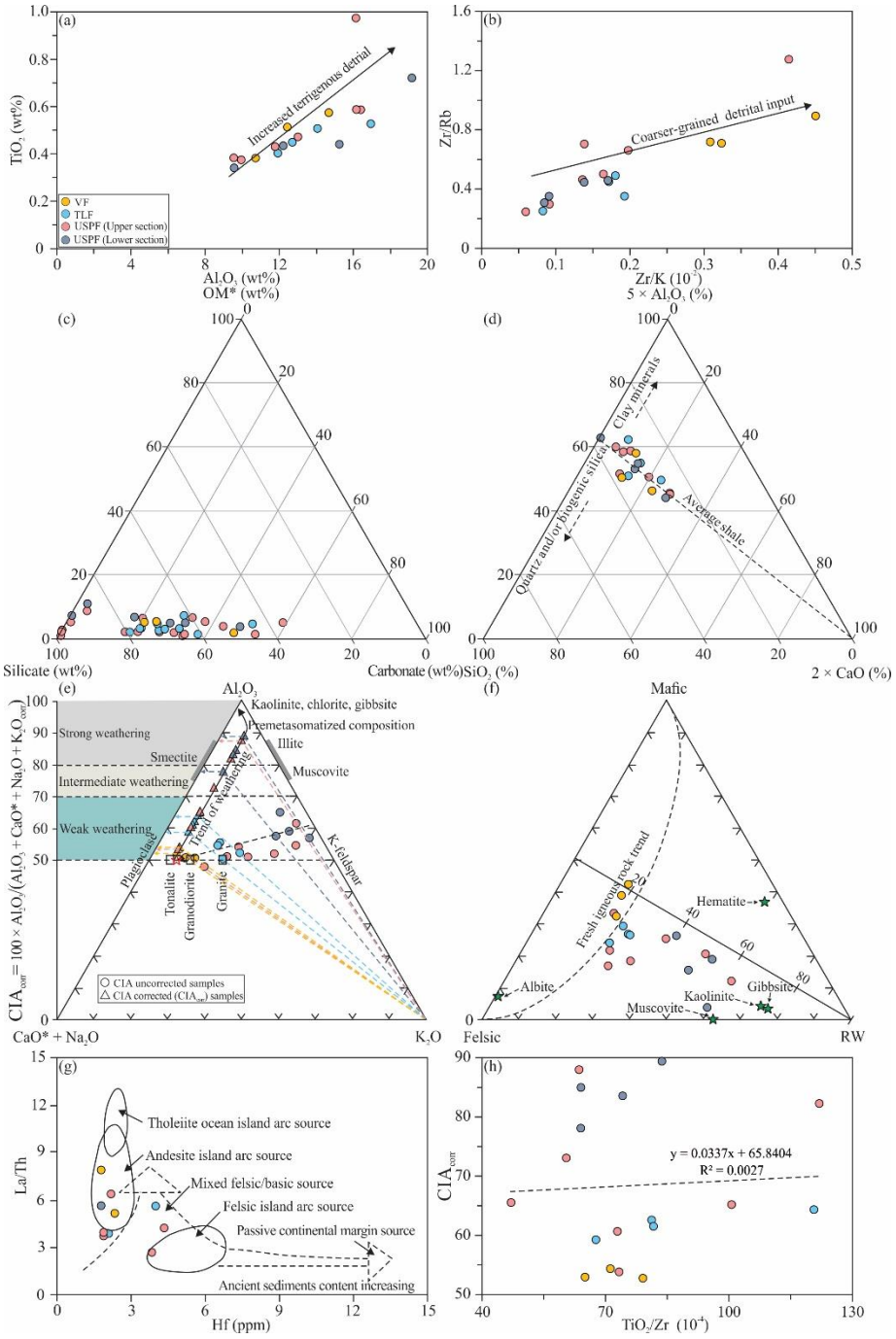

Figure 4.10 (a) Cross-plot of TiO_2 versus Al_2O_3. (b) Cross-plot of Zr/Rb versus Zr/K. (c) Ternary diagram of the three major sedimentary components (silicate, OM, and carbonate) (d) Ternary diagram of the relative concentrations of major elements SiO_2, Al_2O_3, and CaO, exhibiting generally slightly higher Al_2O_3 concentration than average shale (Wedepohl, 1971). (e) A–CN–K ternary diagram used for the K-metasomatism correction, revealing the corrected CIA value and the composition of the unweathered source rock (Fedo et al., 1995; Panahi et al., 2000; Yan et al., 2010). (f) Mafic–felsic–RW ternary plot (modified after Cho and Ohta, 2022). (g) Cross-plot of La/Th versus Hf (modified after Floyd and Leveridge, 1987). (h) Cross-plot of CIA_{corr} versus TiO_2/Zr.*

and Zr/K ratios are utilized as a metric for assessing grain size variations, offering also insights into sediment water depth (Sachsenhofer et al., 2017; Cao et al., 2020; Wu et al., 2022). It is observed that these two ratios exhibit an upward increasing trend, possibly indicative of a decline in water depth from the USPF to VF (Fig. 4.10b). Nonetheless, a sample from the upper part of the USPF (sample No. BS-9) shows also relatively high values, suggesting a fluctuation of the lake level or delivery of clastic terrigenous material to the lake owing to the periodic variations of fluvial intensity. The ternary plot of carbonate, silicate, and OM* contents suggests that silicate is the predominant constituent across almost all analyzed samples (Fig. 4.10c, Table 4.1) with carbonate contents ranging from 20 to 60% for most samples. A few samples of the USPF exhibit even higher silicate contents and lower carbonate, accounting for a proportion higher than 80 wt% silicate. The ternary diagram of the relative concentrations of major oxides SiO_2, Al_2O_3, and CaO indicates that most of the analyzed samples plot at or above the average shale line, suggesting a higher clay mineral content than what is typically found in standard shale (Fig. 4.10d; Wedepohl, 1971). This data suggests that biogenic silica is not a significant compound in any of the samples. In addition, the source of silica in the analyzed samples is linked to Al-bearing terrigeneous minerals; thus the silicates are predominately of clastic origin.

It is well-known that paleo-climate conditions exert a significant influence on various geological processes, including weathering intensity, terrigenous OM input, and evaporation, with further impact on the depositional environment, mineral composition, and OM sources (Wu et al., 2022). Multiple major and trace-element proxies, such as CIA, PIA, and Rb/Sr, have been extensively utilized to assess the weathering intensity and paleoclimate changes. CIA value is determined through the computation of the removal of labile cations in relation to stable residual constituents, with a low CIA value signifying a low degree of chemical alteration, potentially indicating cool and/or arid environmental conditions (Nesbitt and Young, 1982; Fedo et al., 1995). However, it is essential to note that the enrichment in K_2O can consequently result in a calculated CIA value lower than its pre-metasomatized counterpart (Fedo et al., 1995). To address this issue, researchers have utilized the A–CN–K (Al_2O_3 – CaO* + Na_2O – K_2O) ternary diagram to correct CIA values (Fedo et al., 1995; Qiao et al., 2022). Furthermore, the PIA is frequently employed as a robust tool for quantifying the extent of chemical weathering, a proxy that excludes the K component (Fedo et al., 1995). According to the fieldwork and description of paleosols, Michel et al. (2015) suggested that the study area experienced humid conditions during the Late Carboniferous. However, climatic conditions became drier during the deposition of the Early Permian strata. Specifically, the authors proposed that the paleoclimatic conditions transitioned from humid during the Ghzelian to a relatively dry state during the deposition of the TLF and VF in the earliest Sakmarian.

The CIA values of the analyzed samples exhibit an upward ascending trend yet consistently remain below the threshold of 70 (Table 4.7), indicating prevailing arid climatic conditions. However, the A–CN–K ternary diagram suggests that certain samples of the USPF, particularly those in the lower section (BS-1A–BS-4), are characterized by elevated CIA_{corr} values after correction procedure,

implying deposition under more humid and warm climatic conditions with stronger chemical weathering in nearby terrestrial areas (Fig. 4.10e, Table 4.7). Conversely, the reduced CIA_{corr} values observed in the remaining samples from the USPF suggest a weaker weathering under a more arid climate. The TLF and VF display low CIA_{corr} values, suggesting also rather weak weathering in arid conditions. Notably, the VF is characterized by the lowest CIA_{corr} value, indicative of a transition into a highly arid climate (Fig. 4.10e, Table 4.7). In summary, the CIA analysis indicates that during the Early Permian in the Lodève Basin, a climatic shift occurred, transitioning from a more humid environment to an arid one. This transformation has been comprehensively documented within the USPF analyzed in this study. It should be noted, however, that the CIA value of sediments may be subject to various influences, such as hydrodynamic sorting, grain size, and provenance, in addition to the intensity of chemical weathering (Rieu et al., 2007; Wang et al., 2020; Cho and Ohta, 2022). Typically, when transportation and hydrodynamic sorting result in an increase of the clay fraction characterized by a finer grain size, the CIA values of the sediment are also inclined to rise (Nesbitt et al., 1997; Bahlburg and Dobrzinski, 2011; Wang et al., 2020). Consequently, it is imperative to choose sediments with similar grain sizes prior to CIA value calculations. For instance, Rieu et al. (2007) exclusively utilized mudstone beds and mudstone matrices of diamictites to guarantee a thoroughly mixed provenance and minimize the impact of hydrodynamic sorting. In the present study, this requirement is fulfilled as all samples comprise shale lithologies with relatively small grain size variations. Moreover, previous studies suggested the importance of examining ICV before calculating CIA, as secondary sediment recycling can lead to an larger CIA compared to the actual value (Pan et al., 2020a; Huo et al., 2022). In this study, most of the analyzed samples are characterized by high ICV values (> 1), indicating that these samples are compositionally immature and possess minor recycled sedimentary sources (Table 4.7). Consequently, the calculated CIA values for these samples are suggested to be reliable proxies. The PIA values follow a trend similar to that observed in the K-corrected CIA pattern, indicating a transition from humid to arid conditions (Table 4.7). A transition from a humid to an arid climate during the Early Permian is further substantiated by variations in the Rb/Sr and $\ln(Al_2O_3/Na_2O)$ ratios (Table 4.7; Yang et al., 2006b; Cichon-Pupienis et al., 2021; Wu et al., 2022, 2023). Recently, in order to overcome the adverse effects arising from the presence of non-silicate contaminants in weathering intensity calculations, Cho and Ohta (2022) have introduced a RW index for reconstructing spatial-temporal paleoweathering conditions in terrestrial and marine sediments. The proposed RW index is indicative of variations in chemical weathering in response to rising temperature and humidity. For instance, aridisols developed in arid regions exhibit a low RW index. As shown in Fig. 4.10f, the plot of the studied samples is in accordance with the results indicated by the above-mentioned proxies, suggesting a transition from humid to arid conditions.

The A-CN-K ternary diagram also serves as a tool for constraining the initial compositions of parent rocks. A line extending through the data points intersects the feldspar join at a specific point, denoted by a red star, indicating the parent rock type (Fedo et al., 1995; Fig. 4.10e). In this study, the

intersection is located between the granodiorite and tonalite, implying an origin of the silicate in the analyzed samples from sources of felsic to intermediate rocks in composition (Fig. 4.10e). In addition, the bivariate diagram of La/Th versus Hf, a useful indicator for providing insights into the rock types prevalent in the sedimentary source area (Floyd and Leveridge, 1987), also suggests multiple potential origins, including felsic, mixed felsic/basic, and andesite compositions (Fig. 4.10g). Additionally, the TiO_2/Zr ratio observed in the analyzed samples span a range from 47.10 to 122.01, further signifying a source encompassing mixed felsic to intermediate igneous rock types (Hayashi et al., 1997; Table 4.7). The absence of a correlation between CIA_{corr} and the provenance proxy TiO_2/Zr in the examined shales indicates that the CIA value remains largely unaffected by variations in provenance (Fig. 4.10h). Magmatic rocks with a similar chemical composition might be present within the Precambrian or Lower Cambrian Mendic granites (Condomines et al., 2014) which were probably outcropping in the northwest of the Lodève Basin during Permian time (Fig. 4.1; Laurent et al., 2020). Therefore, paleo mountain ranges located northwest of the basin might be considered at least as one possible provenance for clastic sediment supply to the basin.

4.5.4 Origin of OM

For the lower USPF, Rock-Eval data mainly indicate type II or type I kerogen composition which fits to the expected marine influence in the lower USPF (Fig. 4.3). The other samples, however, show a wider range from type I to II-III. These results reflect not only the more anoxic conditions during deposition of lower USPF, but also the dominance of preserved algal biomass characterized by high H/C ratios. Lower degrees of preservation and relatively more terrigenous OM in the upper part of the sequence lead to diminished HI values; similar observations were published, e.g., for the lacustrine Green River Shale, western USA (Horsfield et al., 1994). These reasons might contribute to the variations of the Rock-Eval data of the analyzed samples in this study (Fig. 4.3). Thus, in this lacustrine depositional environment, samples plotting as a type II kerogen are either derived from degradation of initial, hydrogen-rich biomass or from a mix of aquatic algal-derived type I and higher land plant-derived type III (Fig. 4.3). This result aligns with the microscopy data (Fig. 4.4, Table 4.2). Microscopic observation reveals that liptinite predominates among the analyzed samples. The dominant algal and microorganism input is also indicated by the *n*-alkane patterns (Fig. 4.5a-c; Cranwell, 1977; Bechtel et al., 2012). On a molecular level, the majority of the examined samples exhibit *n*-alkane distributions that are characterized by the prevalence of shorter-chain alkanes (n-$C_{10–20}$), with n-C_{14} and n-C_{16} being particularly prominent. This is evident from the high ratios of n-C_{17}/n-C_{27} and n-C_{17}/(n-C_{23} + n-C_{25} + n-C_{27}) (Table 4.3). In contrast, the contribution of longer-chain *n*-alkanes (n-$C_{26–35}$) originating from the waxes of higher land plants is comparatively low (Eglinton and Hamilton, 1967; Killops and Killops, 2005). Kenig (2000) postulated that monomethylalkanes (MMAs) homologs in thermally mature sediments and crude oils are likely to originate from cyanobacterial assemblages. The 7- and 8-carbon substituted methylheptadecanes, the middle-chained

branched MMAs, are typically components produced by cyanobacteria and show high concentrations in pure-cultured cyanobacteria (Shiea et al., 1990). Conversely, the other MMA isomers, often regarded as potential biomarkers of cyanobacteria, have diverse potential sources (Kenig et al., 1995; Schwab and Spangenberg, 2007). The significantly higher concentrations of 7- and 8- monomethyl hepadecanes, in contrast to their homologs, serve as an indicator of cyanobacterial blooming (e.g., Ding et al., 2020). Therefore, the prevalence of 7- and 8- monomethyl hepadecanes in the samples studied (Fig. 4.5c) may serve as an indicator of the existence of cyanobacteria building microbial mats, particularly in samples BS-2A and BS-4 in the lower section of the USPF. These samples are characterized by the highest ratios of 10 × (7- + 8-methylhepadecane /*n*-C_{17} + *n*-C_{18}) of 0.71 and 1.06, respectively (Table 4.3). It can be speculated that the higher microbial input in the lower section of the USPF may be related to either more anoxic conditions in the bottom water or marine incursions leading to higher salinity (Fig. 4.5c). By examining biomarkers, Bechtel et al. (2012) proposed an increase in bacterial activity within the oil shale layer's water column at the lower section of the Qingshankou Formation, China, related to marine influx.

The elevated C_{19}/C_{23} Tri ratios and C_{24} Tet/C_{26} Tri ratios typically indicate substantial terrigenous OM input (Hanson et al., 2000; Hao et al., 2011). In addition, it is widely acknowledged that a high content of C_{27} steranes serves as a clear indicator of algal contributions, whereas a strong enrichment in C_{29} steranes is usually linked to prominent terrigenous OM (Huang and Meinschein, 1979; Volkman, 1986; Jiang and George, 2018; Wu et al., 2022, 2023). As shown in Fig. 4.11a, the majority of the samples are positioned within the mixed origin zone, a conclusion reinforced by the ternary plot of $C_{27\text{-}29}$ 20R steranes, which indicates an origin from mainly planktonic/algal or planktonic/bacterial biomass (Fig. 4.11b). Nonetheless, part of the samples of the USPF are in close proximity to, or within, the planktonic/land plants zone, implying a mixed origin and a pronounced contribution of terrigenous OM input (Fig. 4.11b). Similarly, most of the samples analyzed demonstrate consistently low values for C_{19}/C_{23} Tri and C_{24} Tet/C_{26} Tri ratios (Table 4.4). The steranes/hopanes ratio serves as an indicator of the relative contribution of eukaryotic (predominantly algae and higher plants) as opposed to prokaryotic (bacterial) organisms (Peters et al., 2005; Song et al., 2017). The majority of the examined samples demonstrate notably low steranes/hopanes values, suggesting considerable bacterial input (Table 4.4). The presence of C_{32} 2α-methylhopane biomarkers derived from cyanobacteria is evident in the majority of the samples (Fig. 4.5e; Summons et al., 1999; Brocks et al., 2003). Furthermore, the identification of 3β- methylhopane, even at a relatively low concentration, suggests a contribution of methanotrophs (Fig. 4.5e; Welander and Summons, 2012). Moreover, the relatively poor correlation between TOC content and the volumetric proportion of OM indicates the presence of substantial submicroscopic OM in most samples, likely originating predominantly from microbial biomass (Fig. 4.11c; Ghassal et al., 2016).

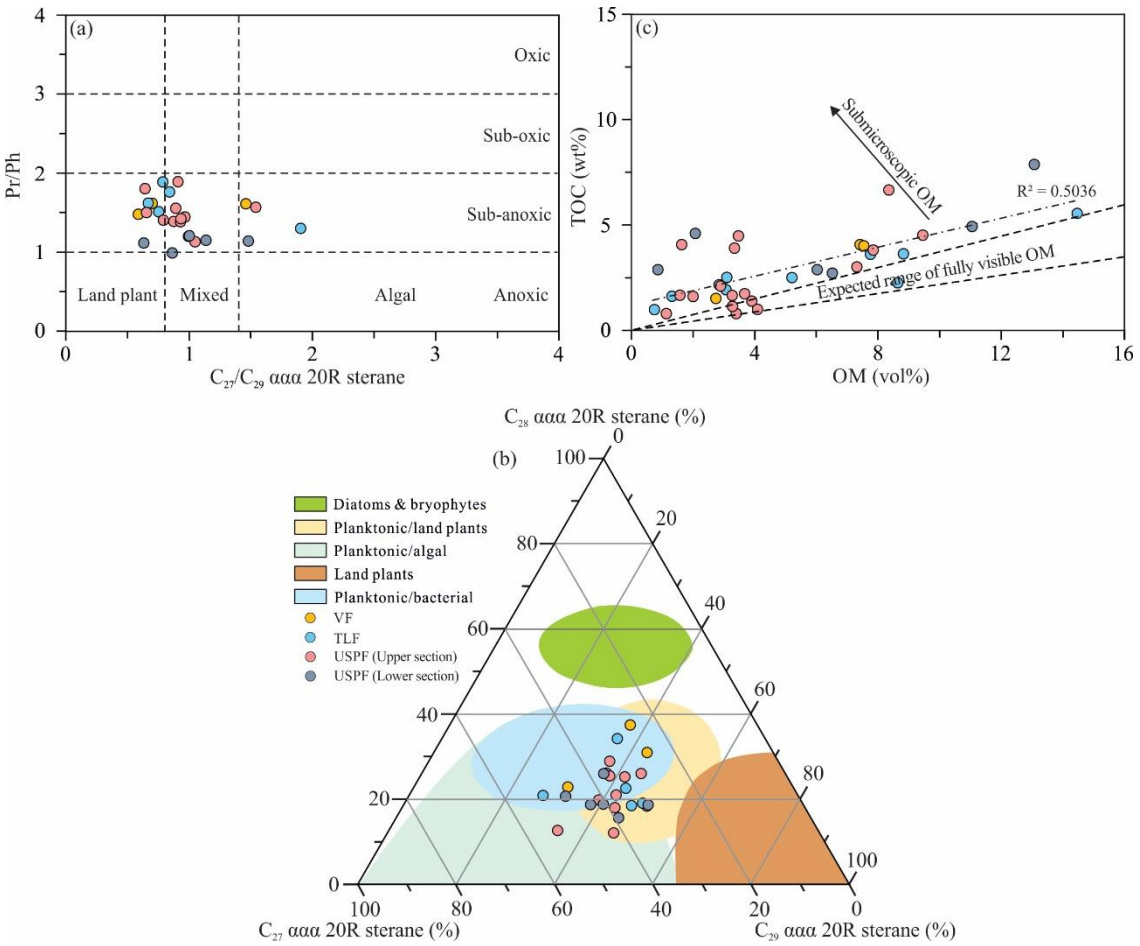

Figure 4.11 (a) Cross-plot of Pr/Ph versus C_{27}/C_{29} ααα 20R sterane (modified after Gorter, 2001). (b) Ternary plot of the distribution of C_{27}, C_{28}, and C_{29} ααα 20R steranes (modified after Huang and Meinschein, 1979). (c) Cross-plot of the TOC content (wt%) versus OM volume (vol%) (modified after Ghassal et al., 2016).

The aromatic hydrocarbon 1,2,5-TMN possibly originates from conifers, while 1,2,7-TMN is likely derived from angiosperms (Strachan et al., 1988). 1-MP and 1,7-DMP also have a possible origin from conifers, such as Araucariaceae-like resins, as indicated by the comparatively elevated levels observed in Jurassic samples (Alexander et al., 1988). In contrast, 9-MP is commonly enriched in type I-II kerogens (Budzinski et al., 1995). As shown in Table 4.5, the relatively low calculated log ratios of 1-MP/9-MP, (1,7- DMP/1,3- + 3,9- + 2,10- + 3,10-DMP), 1,2,5-TMN/1,3,6-TMN, and 1,2,7-TMN/1,3,7-TMN indicate a generally limited influx of terrigenous OM (Alexander et al., 1988; Strachan et al., 1988). The relative abundance of specific PAHs, generated through the incomplete combustion of OM, is employed as a tool for evaluating the relative contributions of combustion-derived versus petrogenic-derived OM (Cope, 1981; Grice et al., 2007; Xu et al., 2019a; Wu et al., 2022). Notably, the analyzed samples exhibit Fla/(Fla + Py) values <0.40, indicating a predominant petrogenic origin for the PAHs and, thus, suggesting that extensive wildfires were unlikely to have

taken place in the greater area of the Lodève Basin during the Early Permian shale deposition (Table 4.5). This result is consistent with the limited occurrence of inertinite particles with possible wildfire-derived charcoal formation (ICCP, 2001). Nevertheless, benzonaphthofuran was detected in all of the analyzed samples and exhibited relatively high concentrations, particularly in OM-lean samples in the upper section of the USPF, as exemplified by sample No. BS-16 (Fig. 4.6e). The occurrence of this biomarker in the analyzed samples may be associated with the incomplete combustion of OM (Wang et al., 2022).

Aryl isoprenoids, which are regarded as diagenetic degradation products stemming from isorenieratene and β-isorenieratene, a compound synthesized by anoxygenic photosynthetic green sulfur bacteria (chlorobiaceae), were identified within the lower section of the USPF (Fig. 4.6c; Liaaen-Jensen, 1978a, 1978b; Schwark and Frimmel, 2004). The presence of AIs derived from isorenieratene in sedimentary deposits serves as an indicative marker for the existence of photic zone euxinia (PZE) (Grice et al., 1996). During PZE, increased levels of toxic hydrogen sulfide, generated by anaerobic sulfate-reducing bacteria within the sediments or the overlying basal water column, spread into the photic zone. Anaerobic green sulfur bacteria flourish precisely at the chemocline, where they possess the capability to utilize hydrogen sulfide as an electron donor for their anoxygenic photosynthetic processes (Tulipani et al., 2015). Nonetheless, the AIs may alternatively have their source in β-isorenieratene, a compound resulting from the aromatization of β-carotene (Koopmans et al., 1996). This source of AIs introduces ambiguity when using them as evidence to ascertain the presence of PZE conditions and sulfur bacteria inputs (Schwark and Frimmel, 2004). In the samples investigated, β-carotene was not detected; thus it is plausible that the AIs serve as an indicator for the presence of PZE. However, as shown in Fig. 4.6c, the prevalence of the predominant low molecular weight constituents may indicate a relatively brief and episodic occurrence of PZE, because aerobic degradation results in an increase in low molecular weight AIs (Schwark and Frimmel, 2004; Xu et al., 2019c).

Murray et al. (1994) proposed that the main factor governing the configuration of the *n*-alkane isotope profile is the OM source and/or the depositional setting. Thus, the type of OM is the predominant determinant of the *n*-alkane isotope profile, particularly within the *n*-C_{12-34} range. In this study, the $\delta^{13}C$ values of the analyzed samples exhibit a progressive decline in $\delta^{13}C$ as the carbon number increases (Fig. 4.7). Such a negative correlation of $\delta^{13}C$ values and *n*-alkane chain length was also observed for terrestrial C_3 plants (−23‰ to −34‰; Smith and Epstein, 1971) and has been reported on terrestrial coals and marine and lacustrine shales with little terrigenous OM. However, the terrestrial OM is distinguished by a more pronounced negative correlation between $\delta^{13}C$ of *n*-alkanes and chain length, along with typically higher $\delta^{13}C$ values, when compared to the algal-derived OM (Schwarzbauer et al., 2013; Liu et al., 2017b; Körmös et al., 2020; Murillo et al., 2021). For example, as reported by Müller et al. (2006) in their investigation of the isotopic composition of bulk organic carbon in sediments from Permian Lake Odernheim in the Saar-Nahe Basin, Southwest Germany,

sediments with type III kerogen deposited in the fluvially dominated pre-lake environment exhibit higher $\delta^{13}C$ values of around −21.5‰ compared to those in the lake setting, ranging from −28‰ to −24‰. This phenomenon could be attributed to the higher $\delta^{13}C$ value in detrital vascular plant (approximately −21‰) compared to the lake-derived photosynthetic algal matter (around −27‰). In this context, it is important to highlight that the $\delta^{13}C$ values of the examined samples from the three formations follow a similar pattern as the carbon number increases (Fig. 4.7). For instance, sample No. BS-11, characterized by the lowest vitrinite and inertinite contents, exhibits the almost lowest $\delta^{13}C$ value, while sample No. BS-9, featuring the highest vitrinite and inertinite contents, displays a medium $\delta^{13}C$ value. It is crucial to note that this conclusion does not entirely align with the findings proposed by Müller et al. (2006) for lacustrine sediments of similar age. This discrepancy could be attributed to the limited input of terrigenous OM and the prevalence of alginite as the dominant maceral in all samples (Table 4.2). It is noteworthy that Ph is isotopically heavier compared to Pr (Fig. 4.12a). Peters et al. (2005) proposed that a common origin for Pr and Ph in crude oils is inferred by the similarity in $\delta^{13}C$ values, with differences typically within the range of ± 0.3‰. Therefore, the deviation observed in some data points may indicate an additional source of Ph and not only an origin from the phytol side chain of chlorophyll, the primary source of the Pr and Ph (Fig. 4.12a; Peters et al., 2005). However, another possible explanation could be linked to intramolecular isotopic differences within phytol. Diagenetic products derived from it by loss of a C atom, such as Pr, may naturally exhibit a depletion in ^{13}C by several per mil relative to Ph (Schouten et al., 2008). Similarly, Schwarzbauer et al. (2013) observed a ^{13}C-depletion in Ph relative to Pr in the majority of the coal samples (up to −3.5‰) and attributed these isotopic differences to distinct diagenetic pathways for both isoprenoids. As shown in Fig. 4.12b, the similar variation trends of Pr and Ph indicate the dominance of an algal origin and phytol as the main source for both isoprenoids.

Grice et al. (2005) introduced a method for discerning the origins of $C_{17\text{-}18}$ *n*-alkanes, spanning from primary producers to heterotrophs, involving comparing the $\delta^{13}C$ values of Pr and Ph relative to these *n*-alkanes. Pr and Ph typically exhibit isotopic values higher than $C_{17\text{-}18}$ *n*-alkanes of primary sources such as algae and cyanobacteria. However, the isotopic enrichment in ^{13}C of *n*-alkanes can arise from heterotrophic processing of primary photosynthate or predominant inputs of isotopically heavier bacterial biomass. In this study, the isoprenoids Pr and Ph tend to be more enriched in ^{13}C than *n*-C_{17} and *n*-C_{18} alkanes in the samples studied, suggesting an autotrophy origin (Fig. 4.12c).

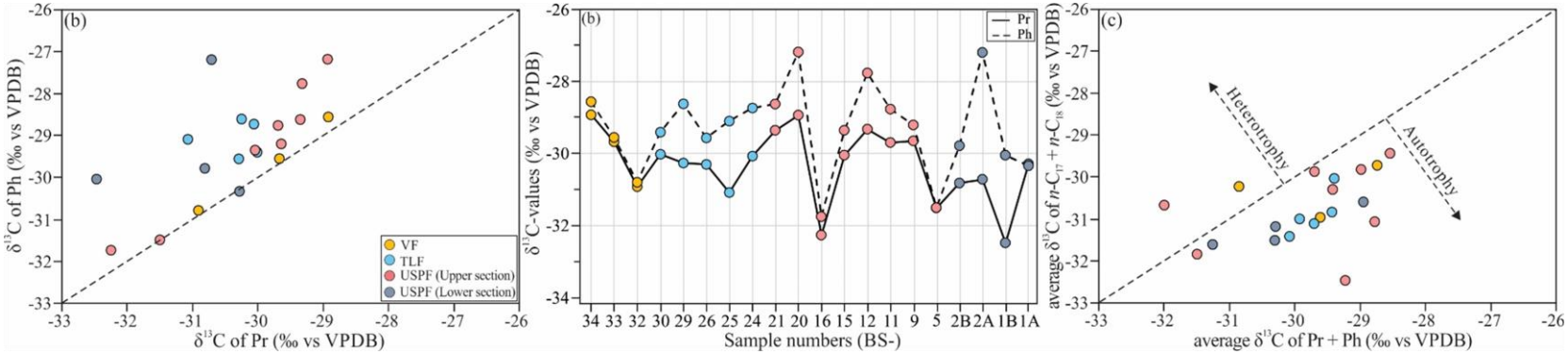

Figure 4.12 (a) Cross-plot of $\delta^{13}C$ of Ph versus $\delta^{13}C$ of Pr. (b) The $\delta^{13}C$ values of Pr and Ph for the selected shale samples. (c) Cross-plot of average $\delta^{13}C$ of n-C_{17} + n-C_{18} versus average $\delta^{13}C$ of Pr + Ph (modified after Grice et al., 2005).

4.5.5 Mechanism of OM enrichment and source rocks depositional model

During the Pennsylvanian, the terrestrial Lodève Basin, situated at a northern low-latitude position (0−10°N) on the Pangean landmass, was located north of the Tethys ocean and remained within the low-latitude belt throughout the entire Permian. However, sedimentation shifted from humid, as documented by Pennsylvanian coals, towards arid, as documented by red beds (Schneider et al., 2006; Michel et al., 2015). Previous research findings have indicated that OM accumulation in marine and lacustrine sediments is predominantly driven by primary productivity, benthic redox conditions, and sedimentation rates (Algeo et al., 2013; Cichon-Pupienis et al., 2021; Qiao et al., 2021a; Burnaz et al., 2022). Simultaneously, external factors, encompassing climatic and tectonic evolution, as well as marine incursions, may exert an influence by regulating these aforementioned factors (Wei et al., 2018; Cao et al., 2021). The intrusion of marine waters into the lake system could potentially enhance the enrichment of OM by augmenting nutrient influx, thereby influencing primary productivity, or by inducing more reducing conditions, typically linked to stratified water columns (Katz, 1995; Erbacher et al., 2001; Wei et al., 2018; Cao et al., 2021). Furthermore, inflowing seawater into the paleo-lake leads to a strong increase in dissolved sulfate. Sulfate-reducing bacteria play a crucial role in this context, as they produced H_2S through the reduction of aqueous sulfate (SO_4^{2-}) to sulfides, which is essential for sustaining anoxygenic photosynthesis by green sulfur bacteria in the PZE (Grice et al., 2005). Given the continuous marine influence indicated by the fossil evidence within the Central Massif region of France during the Upper Carboniferous to Lower Permian (Gottfried, 1987; Poplin et al., 2001; Schultze, 2009), it is possible that the Lodève Basin, situated in the southern Massif Central, may have experienced seawater incursions. Likewise, the notably elevated salinity proxy values observed in the lower section of the USPF may also act as an indicator of a marine incursion (Fig. 4.13a). The magnitude and spatial impact of marine incursions into various lake systems can vary. For instance, marine water incursions into the Songliao Basin predominantly affected the Southeastern Uplift but did not completely extend to the Central Depression (Zhang et al., 2022). During this period, the lake attained its maximum depth and coverage, encompassing an area of approximately ~87×10^3 km^2 (Feng et al., 2010). Given the comparatively modest dimensions of the Graissessac–Lodève lake, with a width of only 15 km and a length ranging from 60 to 70 km, as well as a water volume estimated between 10 and 30 km^3 during the Early Permian, it is conceivable that the entire paleo lake was susceptible to marine influence.

Pochat and Van Den Driessche (2011) proposed that the Late Paleozoic basin-fill sequence within the studied basin is characterized by a predominant lacustrine environment. The lake morphology displays an asymmetry, featuring a steep slope constrained by faults on one side and a gentler slope on the other (Fig. 4.13). The ancestral drainage networks, represented by Late Carboniferous conglomeratic units, transitioned into a prevalent deep lake setting from the Late Carboniferous to the Early Permian. Subsequently, thick shallow lake sediments accumulated. Finally, a new drainage

emerged in the Early Triassic. The depositional environment in the paleolake as documented by its sedimentary rocks was predominantly triggered by the expansion of the basin due to tectonic activity and the accumulation of sediments rather than being primarily driven by climatic variations. Michel et al. (2015), however, challenged this perspective, asserting that although tectonics might have influenced the depositional conditions in the Lodève Basin, the prevailing factor governing the evolution of the sedimentary fill in the Lodève Basin was the long-term, pan-tropical climate change. In this study, multiple molecular and elemental geochemical proxies are presented providing insight into the depositional environment within the Lodève Basin during the Early Permian (Fig. 4.13).

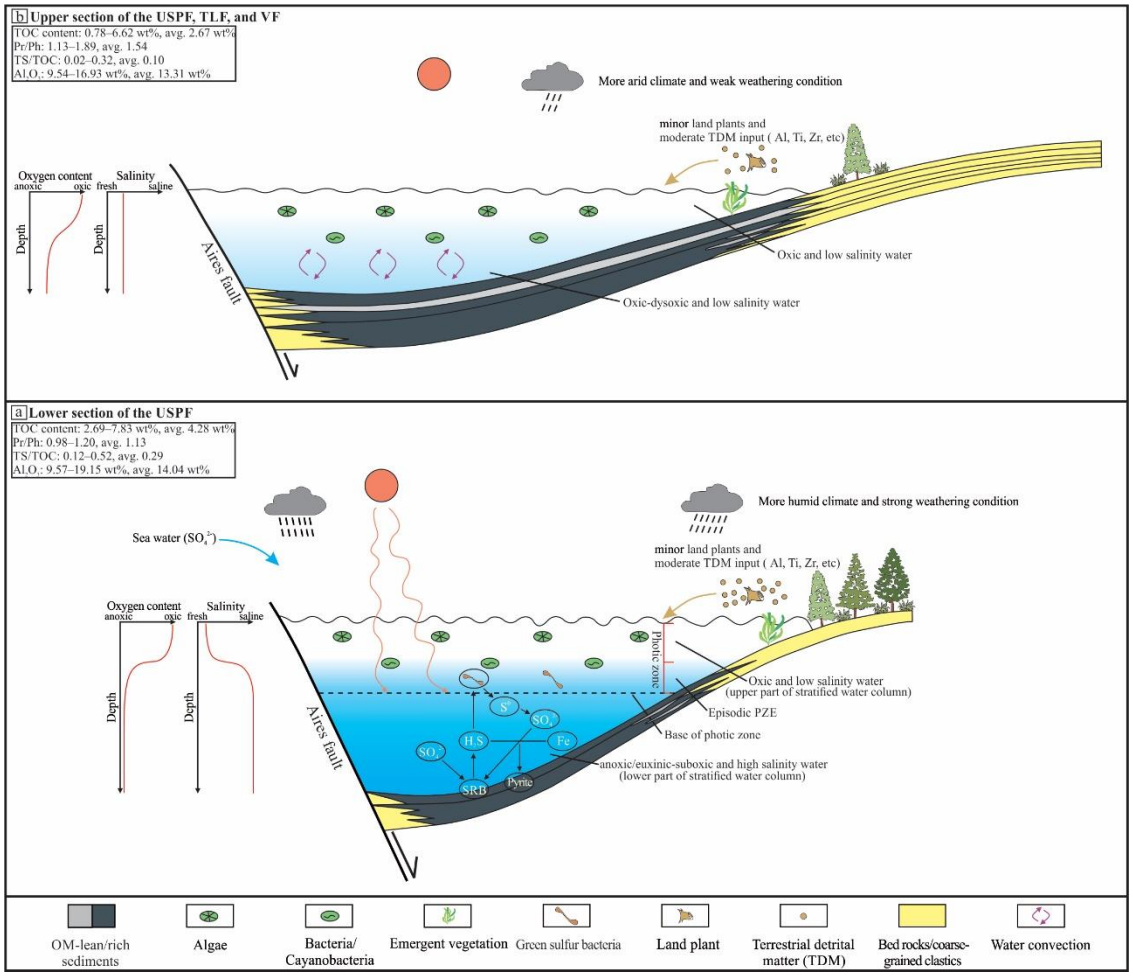

Figure 4.13 Depositional model of the Early Permian lacustrine shales from the Lodève Basin. SRB = sulfate-reducing bacteria.

The input of terrigenous debris (indicated by Al and Ti contents) remained rather constant within the lakes (Fig. 4.13), except for a slightly higher contribution during deposition of the lower USPF (Fig. 4.11b). Thus, the influence of a more humid climate may have led to an augmented weathering and detrital input during the deposition of the lower section of the USPF (Fig. 4.13a). Furthermore,

the steep slopes of the lake margins at that time could have induced a greater clastic sediment influx into the lake (Fig. 4.13a). Based on the data presented in Fig. 4.10e, it is evident that the overall weathering intensity was low, with a trend towards weaker weathering from the lower USPF to the youngest VF unit. This tendency towards greater aridification is generally in line with conclusion proposed by Michel et al. (2015). Interestingly, it seems that this climatic aridification appears to exert only a limited impact on the source of OM and detrital input. This is obvious from the limited variability in maceral composition as well as kerogen quality. As shown in Fig. 4.13a, it is postulated that there existed a deep-water lacustrine environment characterized by anoxic-suboxic conditions, as tectonic subsidence exceeded the rate of sedimentary accumulation during deposition of the lower USPF. This conclusion aligns with the findings of Lambiase (1990), who suggested that large lakes are contingent upon forming an accommodation zone and a topographic depression bounded by rift shoulders. This lacustrine setting can endure only for as long as the depression remains unfilled by sediment and it is limited to a specific phase within the tectonostratigraphic evolution of a basin. Consequently, the thickness of the deep-lake sediments is constrained. Increased salinity proxies for the lower USPF, including TS/TOC and the Gammacerane index, are linked to the intrusion of seawater, signifying the existence of a saline bottom water environment as well as a temporarily stratified water column with restricted circulation, basically a favorable condition for the preservation of OM. Such a more anoxic environment for the lower USPF is also deduced from low Pr/Ph ratios (see Figs. 4.9c and 4.11a). This saline and anoxic environment resulting from the marine incursion may have compensated for the adverse impact of the humid climatic conditions, such as more clastic material and freshwater input to the lake system. Nonetheless, it appears that anoxia was not the decisive factor behind the formation of the most OM-rich source rocks within this basin, given that samples exhibiting elevated TOC levels are also found in the TLF, which exhibits higher Pr/Ph ratios (Table 4.3). Harris et al. (2004) documented a similar phenomenon in their investigation of the Lower Cretaceous synrift section of the Congo Basin. They proposed that the development of anoxia during the active rift stage did not initiate the formation of the most OM-rich intervals.

In contrast, during the late rift phase, as the topography experienced degradation due to reduced faulting and increased soil thickness, there was a notable expansion in nutrient and carbon storage. This, in turn, led to a more efficient conversion of plant detritus into dissolved inorganic carbon and associated nutrients. Given that soil processes heavily influence the concentration of nitrate in lake system (Meyers, 1997), the heightened efficiency in the transformation of plant material in soils into dissolved compounds in both ground and surface water would likely result in an increased supply of nitrate and other nutrients to the rift lake and to an enhanced aquatic bioproductivity. A similar example can be found in the Early Cretaceous rift sequence within the Camamu Basin, eastern Brazil (Gonçalves, 2002). There, the obvious increase in TOC contents in the upper rift sequence likely resulted from enlarged primary bioproductivity, driven by an augmented influx and recycling of nutrients.

Influenced by the gradual expansion of the basin area, it is postulated that relatively shallow and oxic-dysoxic environments dominated during the sedimentation of the upper section of the USPF, TLF, and VF, supported by the various proxies (Fig. 4.13b). Furthermore, the diminished values of salinity markers indicate the presence of freshwater to brackish environment typified by a relatively weakly stratified water column. Such shallow lake settings are commonly marked by enhanced vertical water column mixing and elevated dissolved oxygen levels. These conditions are typically detrimental to the preservation of OM, as they promote oxidative decomposition. However, rather high bioproductivity and sufficiently high sedimentation rate contributed to the preservation of hydrogen-rich OM and sapropel deposition. Carroll and Bohacs (1999) suggested that the interplay between potential accommodation rates (mainly tectonic) and sediment + water supply rates (primarily climatic) governs the occurrence, distribution, nature, and architecture of lakes, allowing the classification of ancient lake basins into three types. They outlined characteristic lacustrine facies associations corresponding to each type, proposing that sediments in under-filled lake basins exhibit salinity-tolerant structure, hypersaline aquatic biomarkers, and low to high TOC contents, whereas those in balanced-fill lake basins are deposited in environments ranging from fresh to saline, with moderate to high TOC contents. Considering the alginite-dominated maceral type and the variation of the salinity proxies and terrestrial input proxies, the sedimentation of Early Permian sediments in the Lodève basin may imply a transition from an under-filled lake to a more balanced-filled system, although Pochat and Van Den Driessche (2011) suggested a constant volume of water in the lake with constant evaporation–precipitation rate during the Late Carboniferous to the Late Permian in the study area.

4.6 Conclusions

Through a comprehensive analysis, this study provides an extensive dataset for the assessment of Early Permian lacustrine shales within the Lodève Basin of southern France. The subsequent conclusions can be drawn:

1) The Early Permian lacustrine shales in the Lodève Basin encompass a large number of rather thin lacustrine source rocks with average VR_r values of 0.75%, indicating early oil window maturity. This thermal maturity is supported by Rock-Eval T_{max} values and specific biomarker ratios. These shales probably reached maximum temperatures of about 120°C and burial depths of about 2000 m.

2) In the lower section of the USPF, the oldest of the black shale units, there are notably higher TS concentrations of about 1.1 wt.%, with average TOC contents of 4.3 wt%. In contrast, a decline in TS content is observed in the overlying upper section of the USPF, TLF, and VF (avg. TOC 2.6, 2.7 and 3.2 wt%; avg. TS 0.3, 0.2, and 0.2 wt%, respectively). This fact might indicate that marine incursions were more common during deposition of the older black shales.

3) The lower section of the USPF was developed under more humid climatic conditions characterized by strong weathering intensity, as indicated by the A–CN–K ternary diagram and multiple elemental proxies. The climatic indicators in the upper section of the USPF suggest a shift

towards more arid conditions. The VF is distinguished by the lowest CIA value, signifying a transition towards an arid climate.

4) The lower section of the USPF, characterized by the lowest Pr/Ph ratio and the highest TS/TOC value, was deposited in oxygen-depleted and saline bottom water. In contrast, the upper section of the USPF, the TLF, and the VF were deposited under oxic-dysoxic and freshwater-brackish bottom water conditions. The analyzed shales contain little terrigenous OM. Thus, OM is mainly derived from planktonic/algal biomass, with some additional microbial contribution, including cyanobacteria.

5) The tectonically driven synrift configuration of the basin, postrift basin enlargement due to cooling of the lithosphere, as well as postulated marine incursion events played a pivotal role in shaping the deposition environments of the lacustrine black shales, consequently influencing the OM accumulation mechanisms. In contrast, the significant climatic aridification observed during the deposition of the USPF appears to have had only a relatively minor effect on the depositional environment and sedimentary facies, in particular with respect to OM quantity and quality.

5 General discussion

5.1 Characteristics of the typical lacustrine OM-rich sediments in different basins in China

5.1.1 Bulk geochemistry and organic petrography

Lacustrine OM-rich sediments, spanning from the Permian to the Neogene, are present in several characteristic basins, including Songliao, Bohai Bay, Ordos, Qaidam, and Junggar and play a pivotal role as primary source rocks for oil-producing reservoirs (Zou et al., 2019; Fig. 5.1). These organic-rich deposits in diverse sedimentary basins exhibit variations in TOC contents, kerogen types, depositional environments, and the mechanisms of accumulation.

The primary source rock in the Songliao Basin is the K_2qn^1, characterized by type II kerogen, with overall TOC and TS contents ranging from approximately 1 wt% to 3 wt% and 0.1 wt% to 1.5 wt%, respectively (Wu et al., 2023; Fig. 5.2). The VR_r value is generally below 1.0%. The lower part of the K_2qn^1 exhibits diminished levels of TOC and TS in comparison to the upper portion. Furthermore, samples influenced by seawater display elevated TOC and TS contents (Fig. 5.2b). Organic petrographic examination disclosed the presence of vitrinite in the form of small gray detrital particles scattered within the mineral matrix (Fig. 5.3a). This terrigenous maceral constitutes a generally low volumetric percentage. Liptinite, primarily represented by lamalginite and telalginite, emerges as the predominant maceral group in the majority of the examined samples.

The HI values in the oil shale and OM-rich mudstone of the J_2d^7 from the upper part collected from the Qaidam Basin are higher compared to those in OM-rich mudstone from the lower part (Wu et al., 2022; Fig. 5.2a). Specifically, the oil shale and OM-rich mudstone from the upper section exhibit a closer proximity to type I-II_1 kerogen, while the OM-rich mudstone from the lower section predominantly consists of type II_2-III kerogen. In addition, the TOC contents of OM-rich mudstone from the J_2d^7 exhibit considerable variability, spanning from 3.1 wt% to 15.2 wt%, with an average of 6.6 wt%. Notably, oil shale displays relatively elevated TOC contents, reaching 14.6 wt%. Conversely, the TS contents of the J_2d^7 are notably low. The T_{max} values indicate that the J_2d^7 is thermally immature to early mature. In OM-rich mudstone, the primary maceral group is liptinite (Wu et al., 2022; Fig. 5.3b). Lamalginite is observed in the form of stripe-like lamellae, exhibiting yellow fluorescence. Additionally, telalginite is predominantly present in structured *Botryococcus*, displaying a greenish-yellow fluorescence.

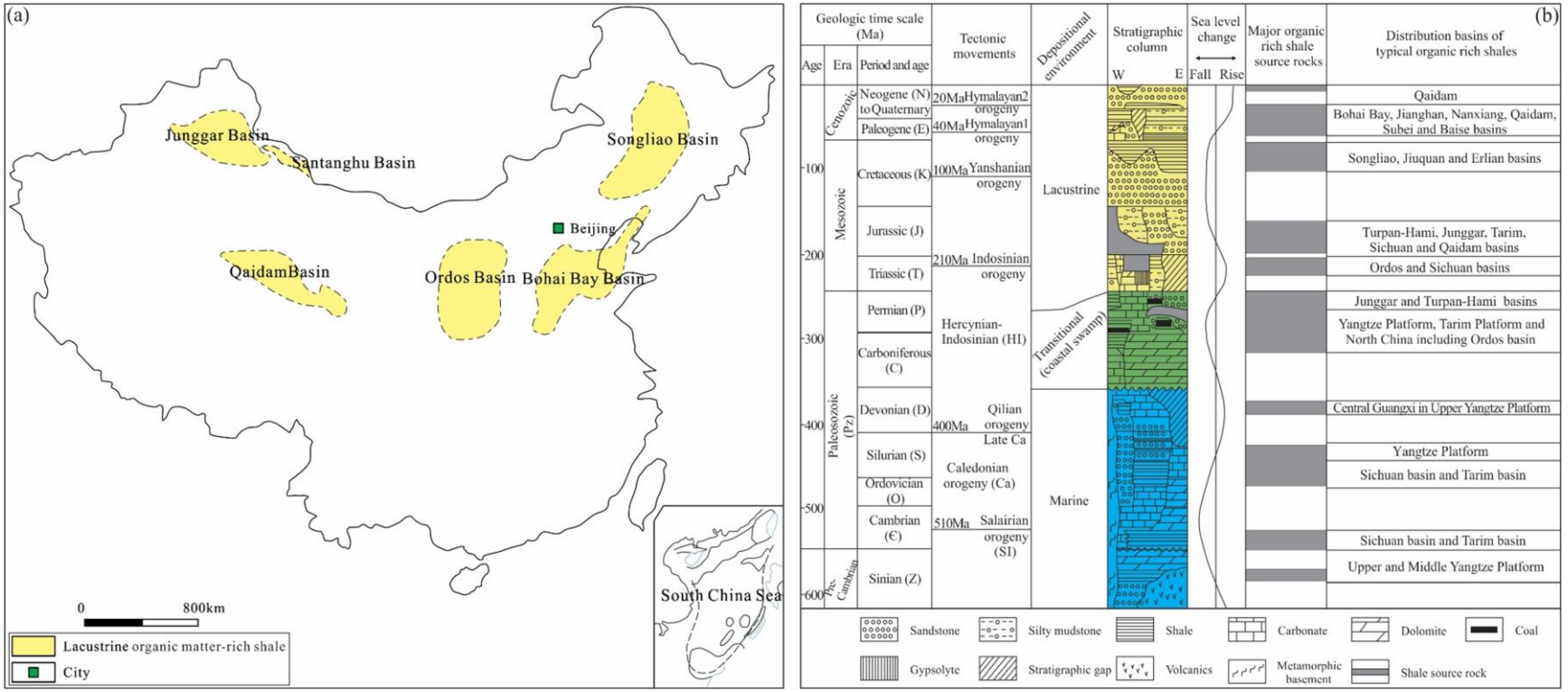

Figure 5.1 (a) Simplified map showing the regional distribution of the main lacustrine shales acting as petroleum source rocks in China (modified from Zou et al., 2019); (b) The depositional environmentand age distribution of major OM-rich shales in China (modified from Jiang et al., 2016).

HI values of the 3rd member of the Shahejie Formation in the Dongpu Depression, Bohai Bay Basin, range from 102 to 729 mg HC/g TOC, indicating the presence of typical type II kerogen (Zheng et al., 2022; Fig. 5.2a). The TOC contents of the Shahejie Formation vary between 0.33 wt% and 5.33 wt%. Notably, most samples exhibit elevated ratios of TS/TOC (Fig. 5.2b). The results of organic petrographical analyses indicate low concentrations of vitrinite and inertinite (Fig. 5.3c). Alginite is the predominant OM in all analyzed samples, predominantly in the form of lamalginite exhibiting distinct layering or as submicroscopic particles interspersed among mineral grains. Notably, alginite displays intense fluorescence when exposed to UV light.

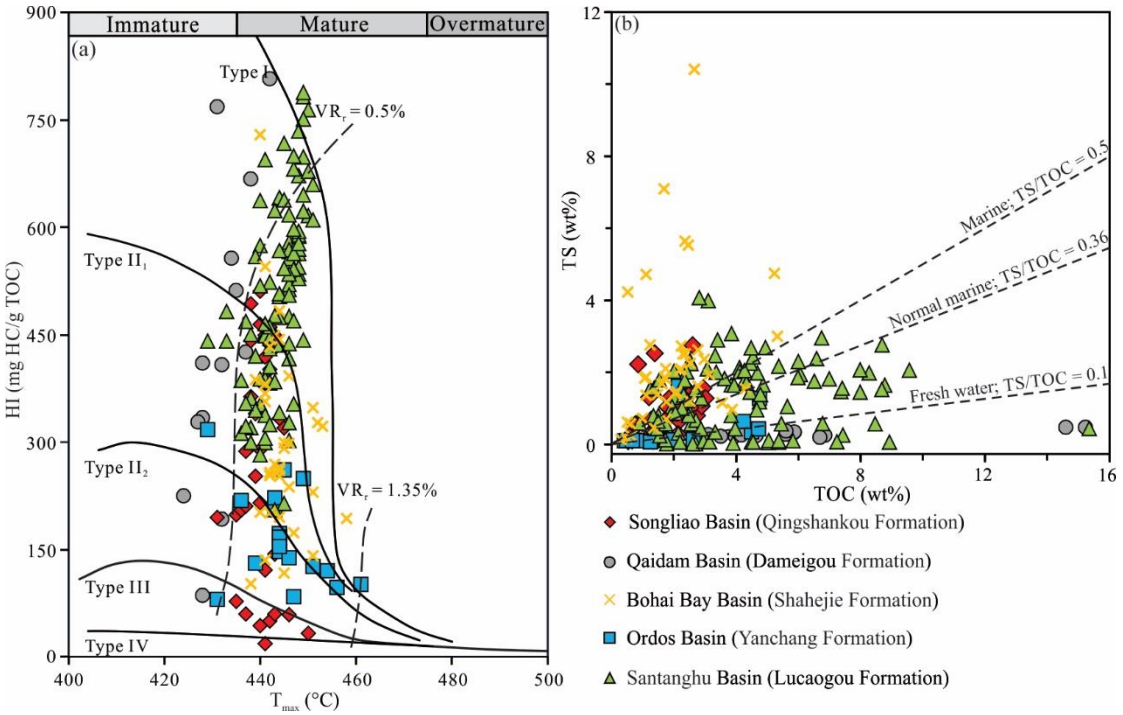

Figure 5.2 (a) Cross-plot of HI versus T_{max}; (b) Cross-plot of TS versus TOC. Data of the Songliao, Qaidam, Bohai Bay, Ordos, and Santanghu Basins are taken from Liu et al. (2017b); Qiao et al. (2021a); Zheng et al. (2022); Wu et al. (2022, 2023).

The plot of the HI vs. T_{max} suggests the prevalence of type II_2 kerogen in the Yanchang Formation (Fig. 5.2a). T_{max} values of the samples indicate thermal maturity within the oil window. The TOC contents of the samples from the Yanchang Formation predominantly vary between 0.24 wt% and 4.76 wt%. Additionally, most samples exhibit low values of TS/TOC. Vitrinite particles are abundant in all the samples analyzed (Fig. 5.3d). Vitrinite particles are prevalent in all examined samples (Fig. 5.3d). The influx of OM derived from terrestrial plants is further demonstrated by the existence of semifusinite. Yellow sporophyte and brightly yellow lamalginite are also observed under fluorescence (Fig. 5.3d).

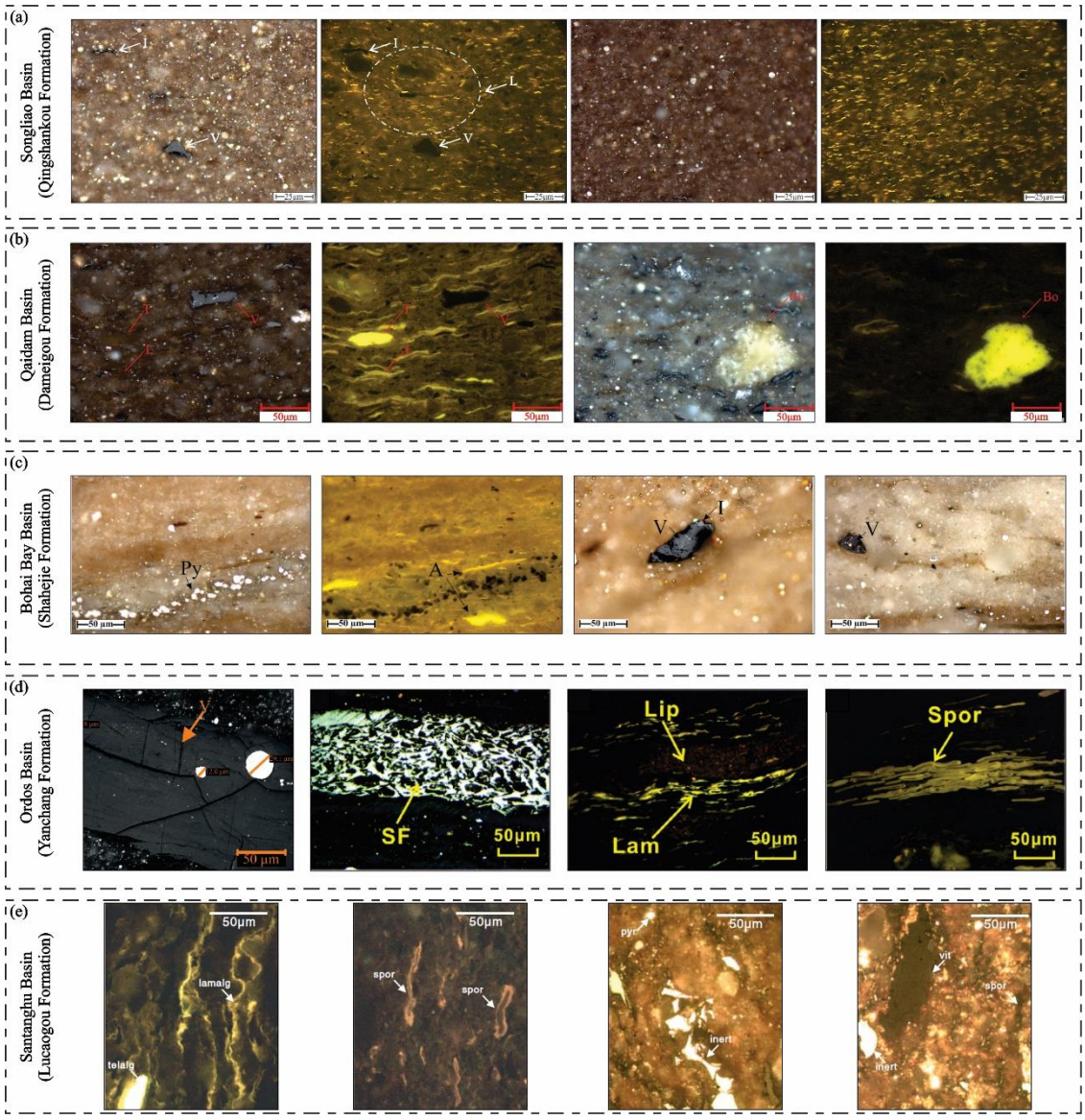

Figure 5.3 Photomicrographs of organic petrology characteristics. All photomicrographs were taken under oil immersion. (a) The Cretaceous Qingshankou Formation of the Songliao Basin (Wu et al., 2023); (b) The Jurassic Dameigou Formation of the Qaidam Basin (Wu et al., 2022); (c) The Eocene Shahejie Formation of the Bohai Bay Basin (Zheng et al., 2022); (d) The Triassic Yanchang Formation of the Ordos Basin (Qiao et al., 2021a; Zhang et al., 2021b); (e) The Permian Lucaogou Formation of the Santanghu Basin (Liu et al., 2017b). V-vitrinite, I-inertinite, L-lamalginite, T-telalginite, Bo-botryococcus, A-alginite, Py-pyrite, SF-semifusinite, Lip-liptodetrinite, Lam-lamalginite, Spor-sporophyte, lamalg-lamalginite, telalg-telaginite, spor-sporinite, vit-vitrinite, inert-inertinite, pyr-pyrite.

The HI values of the second member of the Lucaogou Formation in the Santanghu Basin range from 205 to 788 mg HC/g TOC (Fig. 5.2a). The samples fall within the region characteristic of types I and II kerogen in the HI versus T_{max} diagram. T_{max} data indicate that the source rocks are within the oil window. The samples exhibit TOC contents primarily ranging between approximately 1 wt% and 10 wt%. The TS/TOC ratios of the samples show considerable variation. The predominant maceral in the majority of hydrogen-rich shales is lamalginite (Fig. 5.3e). Sporinite, exhibiting elongated thread-like or spindle-shaped characteristics and displaying an orange-brown fluorescence, was identified. Terrigenous organic particles, identified as vitrinite and inertinite, are present in all analyzed samples.

5.1.2 Depositional environment and OM origin

The boundary proposed to distinguish freshwater sediments from brackish and marine sediments is a TS/TOC ratio of 0.1, based on an extensive analysis of numerous data points (Wei and Algeo, 2020). They also indicated that the TS/TOC range of 0.1–0.5 represents an overlapping area for brackish and marine samples, while nearly all marine samples exhibit TS/TOC ratios higher than 0.5. The TS/TOC ratios of the K_2qn^1 exhibit variability, spanning the range from freshwater to the brackish-marine and marine zones (Fig. 5.2b). Gammacerane (Gam), potentially formed through the reduction of tetrahymanol (gammaceran-3β-ol) (ten Haven et al., 1989; Venkatesan, 1989), is commonly utilized as an indicator of changes in salinity (Peters et al., 2005). The presence of abundant Gam (Gam index > 0.1) is considered indicative of a hypersaline environment and a stratified water column during the deposition of the source rocks (Sinninghe Damsté et al., 1995; Sepúlveda et al., 2009; Song et al., 2017). As shown in Fig. 5.4a, the fluctuations in the Gam index value align with the outcomes of the TS/TOC ratios. The K_2qn^1 exhibits Pr/Ph ratios predominantly exceeding 1.0, signifying the prevalence of relatively oxidizing conditions throughout the deposition (Fig. 5.4a). This conclusion is consistent with the result suggested by the Pr/*n*-C_{17} versus Ph/*n*-C_{18} plot (Fig. 5.4b). The ternary plot of $C_{27–29}$ ααα 20R steranes suggests a mixed source from planktonic/land plants, planktonic/algal, and planktonic/bacterial biomass (Fig. 5.5), which is consistent with conclusions from the Pr/*n*-C_{17} versus Ph/*n*-C_{18} plot (Fig. 5.4b).

The lower TS/TOC and Gam index values suggest that the Ordos Formation and the mudstones from the J_2d^7 were deposited in freshwater environments without salinity stratification (Figs. 5.2b, 5.4a). The presence of oxygenated bottom water deposition conditions is supported by the elevated Pr/Ph ratio and the Pr/*n*-C_{17} versus Ph/*n*-C_{18} plot (Fig. 5.4). The ternary distribution diagram of C_{27-29} ααα 20R steranes illustrates a mixed origin of OM from algae, higher land plants, and bacteria deposited in a terrestrial setting (Fig. 5.5). However, the presence of more terrestrial macerals (Fig. 5.3b, d) suggests a relatively substantial input of OM derived from higher land plants, a finding proved by the Pr/*n*-C_{17} versus Ph/*n*-C_{18} plot (Fig. 5.4b).

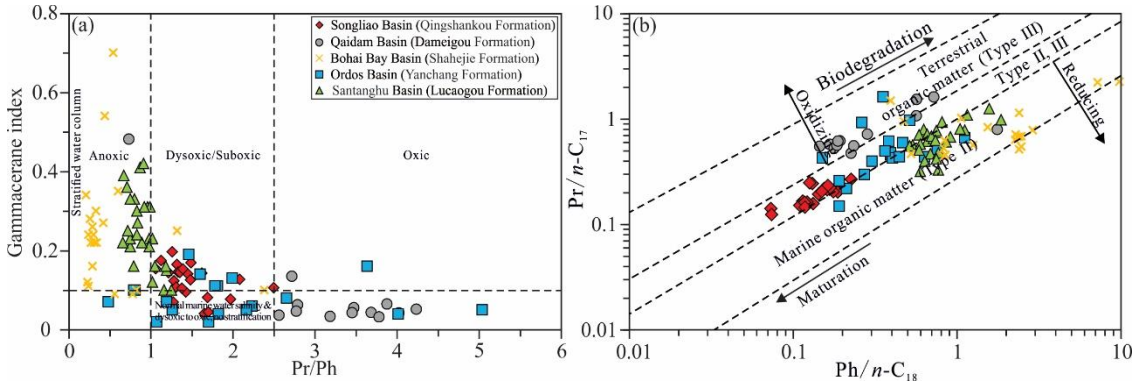

Figure 5.4 (a) Cross-plot of Gam index versus Pr/Ph; (b) Cross-plot of Pr/n-C_{17} versus Ph/n-C_{18}. Data of the Songliao, Qaidam, Bohai Bay, Ordos, and Santanghu Basins are taken from Liu et al. (2017b); Qiao et al. (2021a); Zheng et al. (2022); Wu et al. (2022, 2023). The Gam index for the Qaidam, Ordos, and Santanghu samples is calculated as Gam/C_{30} H, while others are calculated as Gam/(C_{30} H + Gam).

In contrast, the Shahejie Formation was primarily deposited in anoxic and saline bottom water conditions with the presence of a stratified water column (Figs. 5.2b, 5.4a). The paleoenvironment during the deposition of the examined Lucaogou Formation transitioned from an anoxic and highly saline to a dysoxic and freshwater lake system (Figs. 5.2b, 5.4a). The Pr/*n*-C_{17} versus Ph/*n*-C_{18} plot and the ternary distribution of steranes suggest a mixed origin of OM deposited in a generally reducing environment during the sedimentation of these two formations (Figs. 5.4b, 5.5).

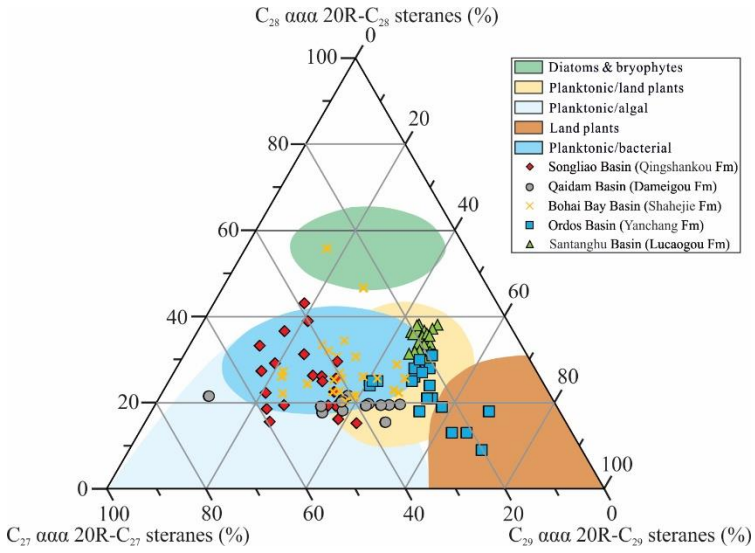

Figure 5.5 Ternary diagram showing the distribution of C_{27}, C_{28}, and C_{29} steranes (modified after Huang and Meinschein 1979). Data of the Songliao, Qaidam, Bohai Bay, Ordos, and Santanghu Basins are taken from Liu et al. (2017b); Qiao et al. (2021a); Zheng et al. (2022); Wu et al. (2022, 2023).

5.2 Characteristics of several lacustrine OM-rich sediments in Europe

5.2.1 Bulk geochemistry and organic petrography

Lacustrine OM-rich sedimentary rocks are widespread in Europe as well. For comparison with Permian Lodève samples, the Miocene Nördlinger Ries and Eocene Messel oil shale samples were considered. The Permian shales in the Lodève Basin exhibit significant variability in HI values and consist of kerogen types ranging from type III to type I kerogen (Wu et al., 2024; Fig. 5.6a). The T_{max} data, indicating an average temperature of 439 °C, suggest that these shales are within the oil window, characterized by an early-peak stage. Significant increases in the TS/TOC ratio are observed exclusively in samples from the lower portion of the USPF, as illustrated in Fig. 5.6b. Conversely, the majority of samples obtained from the upper layers of the USPF, the TLF, and the VF exhibit low values. Terrigenous macerals and solid bitumen are prevalent in nearly all samples, although they make up a relatively modest volumetric fraction within the samples under investigation (Fig. 5.7a). Liptinite, distinguished by the presence of lamalginite and liptodetrinite, displays strong orange fluorescence and serves as the primary maceral group.

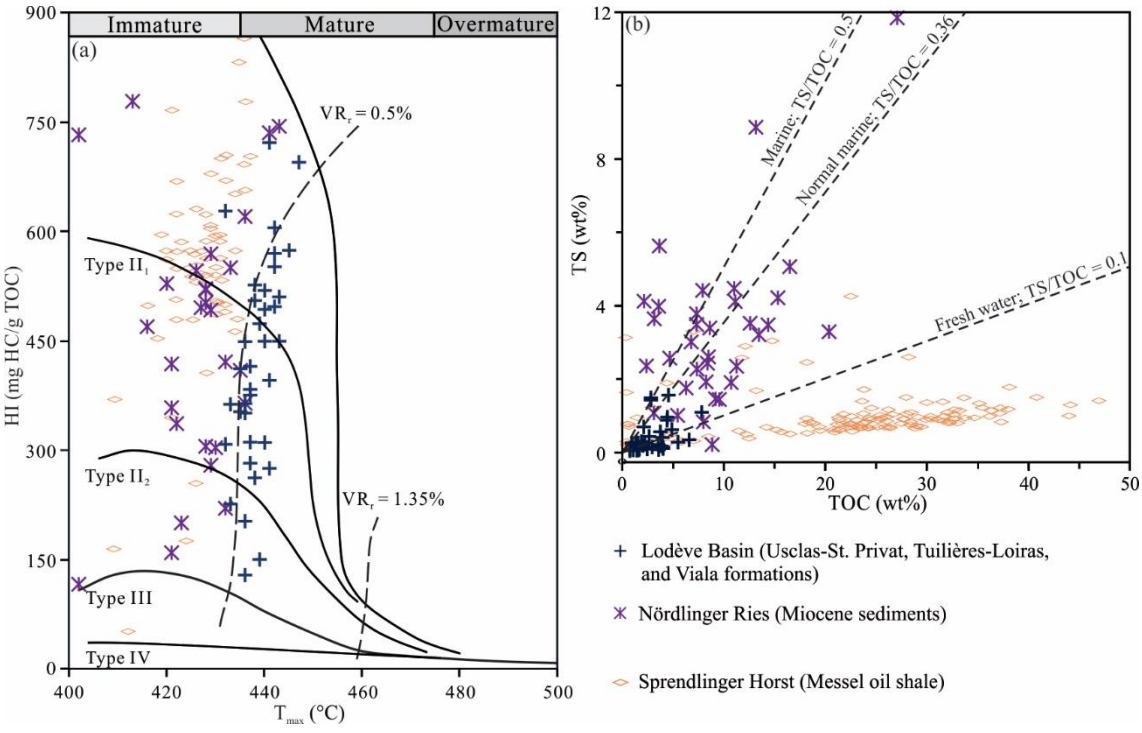

Figure 5.6 (a) Cross-plot of HI versus T_{max}; (b) Cross-plot of TS versus TOC. Data of the samples of the USPF, TL, VF, Messel oil shale, and Miocene sediment are taken from Bauersachs et al. (2014); Zhao et al. (2022a); Wu et al. (2024).

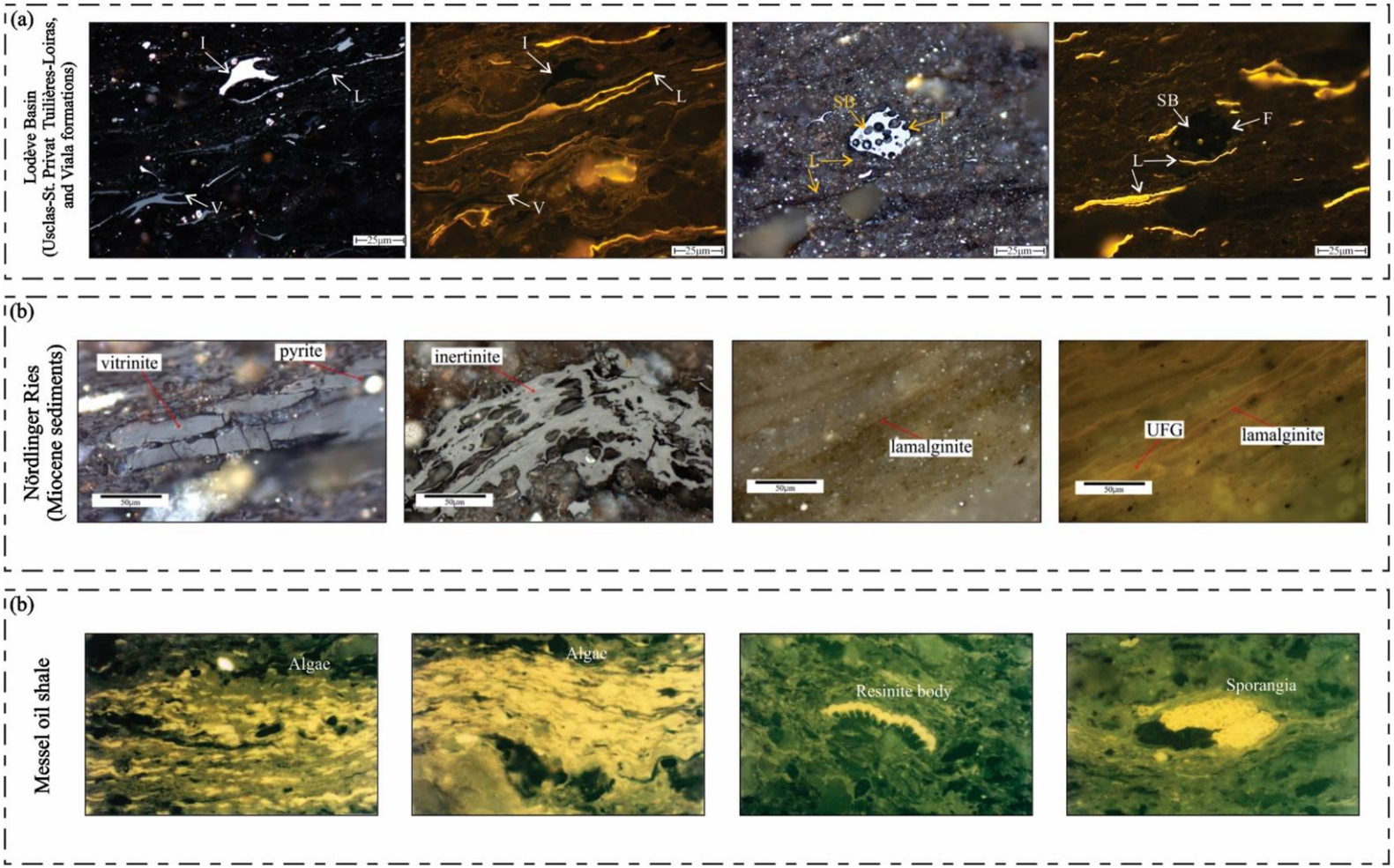

Figure 5.7 Photomicrographs of organic petrology characteristics. All photomicrographs were taken under oil immersion. (a) The USPF, TL, and VF of the Lodève Basin (Wu et al., 2024); (b) The Miocene sediments of the Nördlinger Ries (Zhao et al., 2022b); (c) The Eocene Messel oil shale (Jankowski, and Littke, 1986). V-vitrinite, I-inertinite, L-lamalginite, F-fusinite, SB-solid bitumen, UFG-unstructured fluorescent groundmass.

The Miocene lacustrine samples obtained from the Nördlinger Ries display HI values ranging from 12 to 880 mg HC/g TOC, showcasing variable kerogen types from type III to type I (Zhao et al., 2022a; Fig. 5.6a). The T_{max} data indicate that these samples are thermally immature to early mature, with a random vitrinite reflectance of 0.33% for the measured samples in the uppermost unit (Zhao et al., 2022b; Fig. 5.6a). The elevated TS values observed in the sediments suggest high salinities (Fig. 5.6b). Vitrinite and inertinite particles are prevalent in the uppermost unit (Zhao et al., 2022b; Fig. 5.7b). Alginite exhibits bright yellow fluorescence, and the majority of samples exhibit substantial amounts of amorphous OM with intense fluorescence.

In the Messel deposits, elevated HI values were consistently observed across the units containing oil shale. The predominant sedimentary OM in the Messel oil shale closely aligns with the type II pathway or falls between those associated with types I and II (Bauersachs et al., 2014; Fig. 5.6a). The T_{max} values of the oil shale generally remained low, ranging from 409 to 437 °C (average 427 °C), indicative of thermally immature kerogen. This suggests that the oil shale underwent minimal burial and alteration of the initially deposited OM. Most of the oil shale samples are characterized by low TS/TOC ratios (Bauersachs et al., 2014; Fig. 5.6b). Alginite, resinite bodies, and sporangia, exhibiting bright yellow fluorescence, were observed (Jankowski and Littke, 1986; Fig. 5.7c).

5.2.2 Depositional environment and OM origin

The lower section of the USPF exhibits a significant increase in the TS/TOC ratio, falling within the category characterized as brackish-marine and marine conditions (Fig. 5.6b). Conversely, the majority of samples from the upper strata of the USPF, the TLF, and the VF display low values, indicating a freshwater-brackish water environment. The Gam index values of the examined samples show a similar pattern to the TS/TOC ratios (Fig. 5.8a). The highest average values of 0.17 are

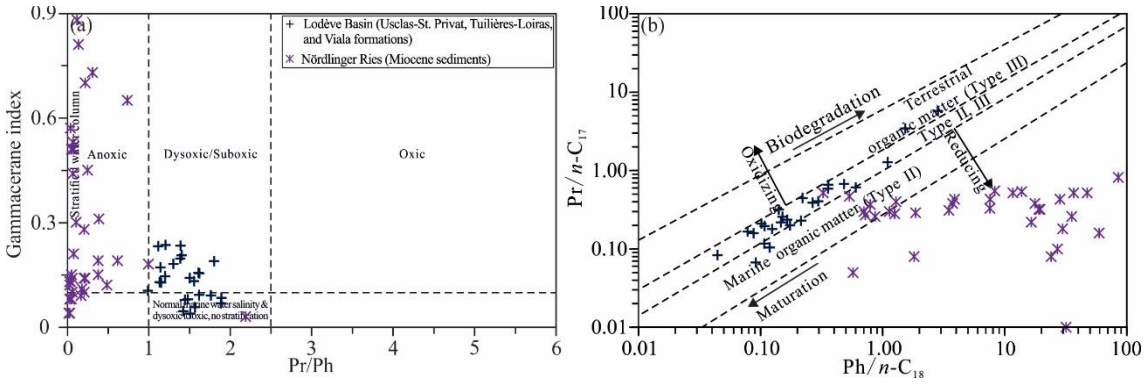

Figure 5.8 (a) Cross-plot of Gam index versus Pr/Ph; (b) Cross-plot of Pr/n-C_{17} versus Ph/n-C_{18}. Data of the samples of the USPF, TL, VF, and Miocene sediment are taken from Zhao et al. (2022b); Wu et al. (2024). The Gam index is calculated as Gam/(C_{30} H + Gam).

observed in the lower section of the USPF, suggesting predominantly marine conditions. The majority of samples investigated in this study display elevated Pr/Ph ratios (>1.0), indicative of prevailing oxic-dysoxic conditions (Fig. 5.8a). This observation is reinforced by the findings illustrated in the Pr/*n*-C_{17} versus Ph/*n*-C_{18} diagram (Fig. 5.8b). However, it is crucial to highlight the relatively diminished Pr/Ph ratios identified in the lower section of the USPF, signifying the prevalence of more reducing conditions.

The majority of the samples from the Lodève Basin lie within the mixed origin zone, a deduction supported by the ternary plot of $C_{27\text{-}29}$ 20R steranes, suggesting an origin primarily from planktonic/algal or planktonic/bacterial biomass (Fig. 5.9). However, it is noteworthy that a portion of the USPF samples is either in close proximity to or within the planktonic/land plants zone, indicating a mixed origin with a significant contribution from terrigenous OM.

The elevated TS values in the Nördlinger Ries sediments, along with the Gam index values, signify a prevailing high water salinity (Figs. 5.6b, 5.8a). The Pr/Ph ratio exhibits a range from 0.01 to 2.19, with the majority of samples falling below 0.5, indicating prevailing anoxic conditions. Except for the coaly shale sample deposited under oxic conditions based on high Pr/Ph and low Ph/*n*-C_{18} values, all other samples are suggested to have formed under anoxic bottom water conditions showing high concentrations of Ph (Fig. 5.8). Diatoms/bryophytes, halophilic red algae/plankton, and bacteria contributed to OM during the entire evolutionary stage of the paleo-lake (Fig. 5.9).

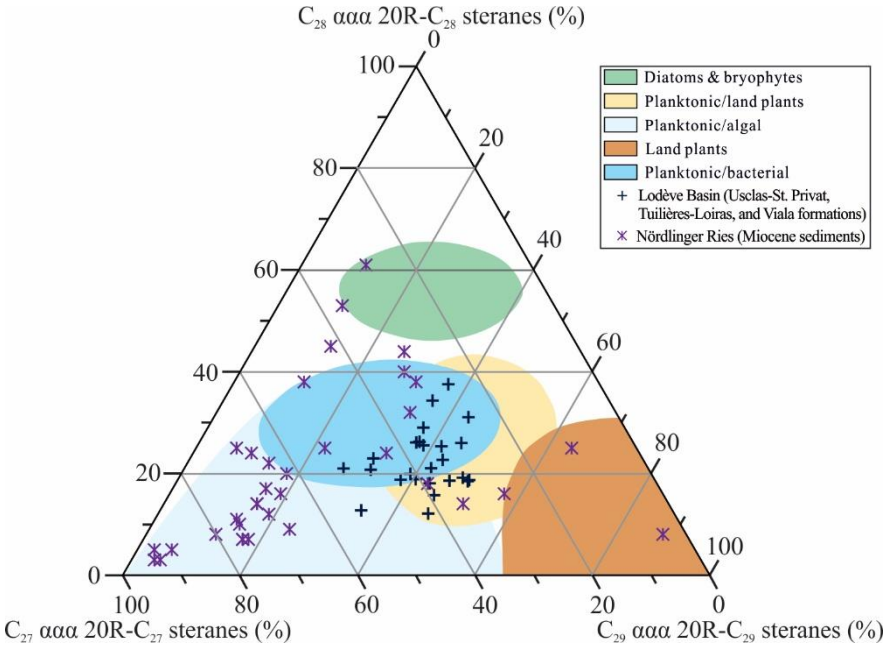

Figure 5.9 Ternary diagram showing the distribution of C_{27}, C_{28}, and C_{29} steranes (modified after Huang and Meinschein 1979). Data of the samples of the USPF, TL, VF, and Miocene sediment are taken from Zhao et al. (2022b); Wu et al. (2024).

5.3 Depositional models for lacustrine OM-rich source rocks

The paleontological, isotopic composition and geochemical evidence from the black shale sequences indicate that certain periodic bottom currents were intricately linked to occurrences of seawater incursions into the Songliao paleo-lake during the deposition of the Qingshankou Formation (Hou et al., 2000; Huang et al., 2013; Zou et al., 2019; Wu et al., 2023). Variations in geochemical indices align with regional sea-level fluctuations. These episodes of seawater intrusion into the Qijia–Gulong, Sanzhao, and Changling sags impacted approximately two-thirds of the total lake basin area. Influxes of marine waters into the lake system might have facilitated the enrichment of OM by elevating nutrient input, potentially impacting primary productivity, and/or inducing more reducing conditions typically linked to stratified water columns (Katz, 1995; Erbacher et al., 2001; Wei et al., 2018). Moreover, the marine influence led to an increase in sulfate concentrations, promoting the salinization of the Songliao paleo-lake (Huang et al., 2013). This salinization intensified lake stratification and contributed to anoxic bottom waters during the deposition of K_2qn^1 in the Songliao Basin (Cao et al., 2021). According to Cao et al. (2021), sulfate input from marine transgression events is the primary factor influencing the redox conditions of the paleo-lake. In addition, the heightened nutrient availability results in increased primary productivity, leading to accelerated oxygen consumption in the bottom water.

It is postulated that a water column was characterized by relatively shallow depths and oxic-dysoxic conditions during the deposition of the less TOC-rich sediments in the lower K_2qn^1 unit in the Songliao Basin. The diminished values of salinity indicators imply the presence of a freshwater-brackish environment with a water column that was weakly or not permanently stratified (Fig. 3.16a). The intrusion of marine waters into the paleo-lake likely increased salinity and induced water column stratification. The diminished oxygen levels in the bottom waters facilitated the preservation of OM, contributing to the elevated TOC content in the samples, indicative of the presumed marine transgressive events (Fig. 3.16b). Elevated primary productivity, driven by algae and microbial communities, likely resulted in the transfer of excess OM to the bottom water, intensifying oxygen deficiency in the water column. Furthermore, factors such as arid climatic conditions, weak weathering intensity, and increasing water depth collectively reduced the susceptibility of the source rocks to land plant detritus, terrigenous clastic materials, and fluvial freshwater influx. Consequently, the identified samples, representing the postulated marine transgressive events with high TOC contents, were deposited in dysoxic and saline environments with minimal terrigenous input (Fig. 3.16b). The upper unit was deposited in environments characterized by generally lower oxygen levels in bottom waters compared to the lower unit, potentially linked to an increase in lake level (Fig. 3.16c).

The OM-rich mudstone and the oil shale in the J_2d^7 from the Qaidam Basin were deposited in an environment that gradually became more arid. During periods of higher humidity, freshwater influx occurred continuously through precipitation and surface runoff, leading to well-mixed lake water conditions (Fig. 5.10). During this phase, water column productivity remained at a normal level,

resulting in moderate formation and preservation of OM. Simultaneously, there was a notable increase in the input of OM and detrital minerals from terrestrial sources, including detrital quartz, feldspar, and OM from higher plants (Wang et al., 2021).

As arid climatic conditions developed, the freshwater supply to the Yuqia Lake Basin experienced a rapid decline, resulting in the gradual salinization of the initial freshwater lake. Due to density differences, the lake water established a stable saline-stratified environment characterized by oxic, lower salinity surface waters (Wang et al., 2021). The bottom waters became highly saline, and dissolved oxygen was quickly depleted, creating an anoxic environment. The lake stratification remained stagnant, ensuring prolonged periods of anoxia and salinity in the bottom water, thereby providing favorable conditions for the preservation of OM. Additionally, the absence of oxygen in the bottom water facilitated the effective recycling of nutrients like phosphorus back into the water column, intensifying eutrophication. Hence, both heightened primary productivity and enhanced preservation potential played crucial roles in the OM enrichment observed in the oil shale (Fig. 5.10).

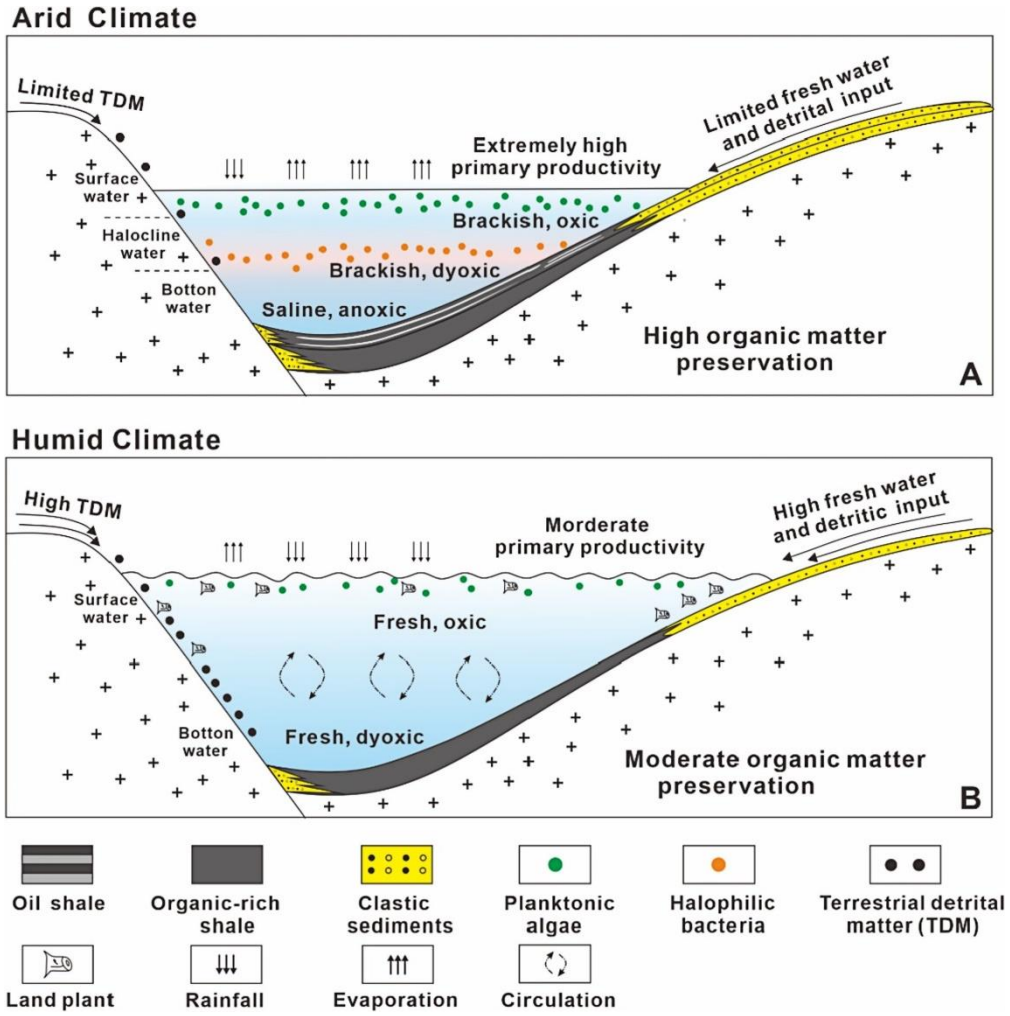

Figure 5.10 Depositional model of lacustrine source rocks of the J_2d^7 in the Qaidam Basin (Wang et al., 2021).

The lower segment of the third member of the Shahejie Formation was deposited in an enclosed lake (Tang et al., 2020). The climate was characterized by extreme dryness and strong evaporation, leading to high-salinity water conditions (Fig. 5.11a). Terrestrial higher plants did not thrive, resulting

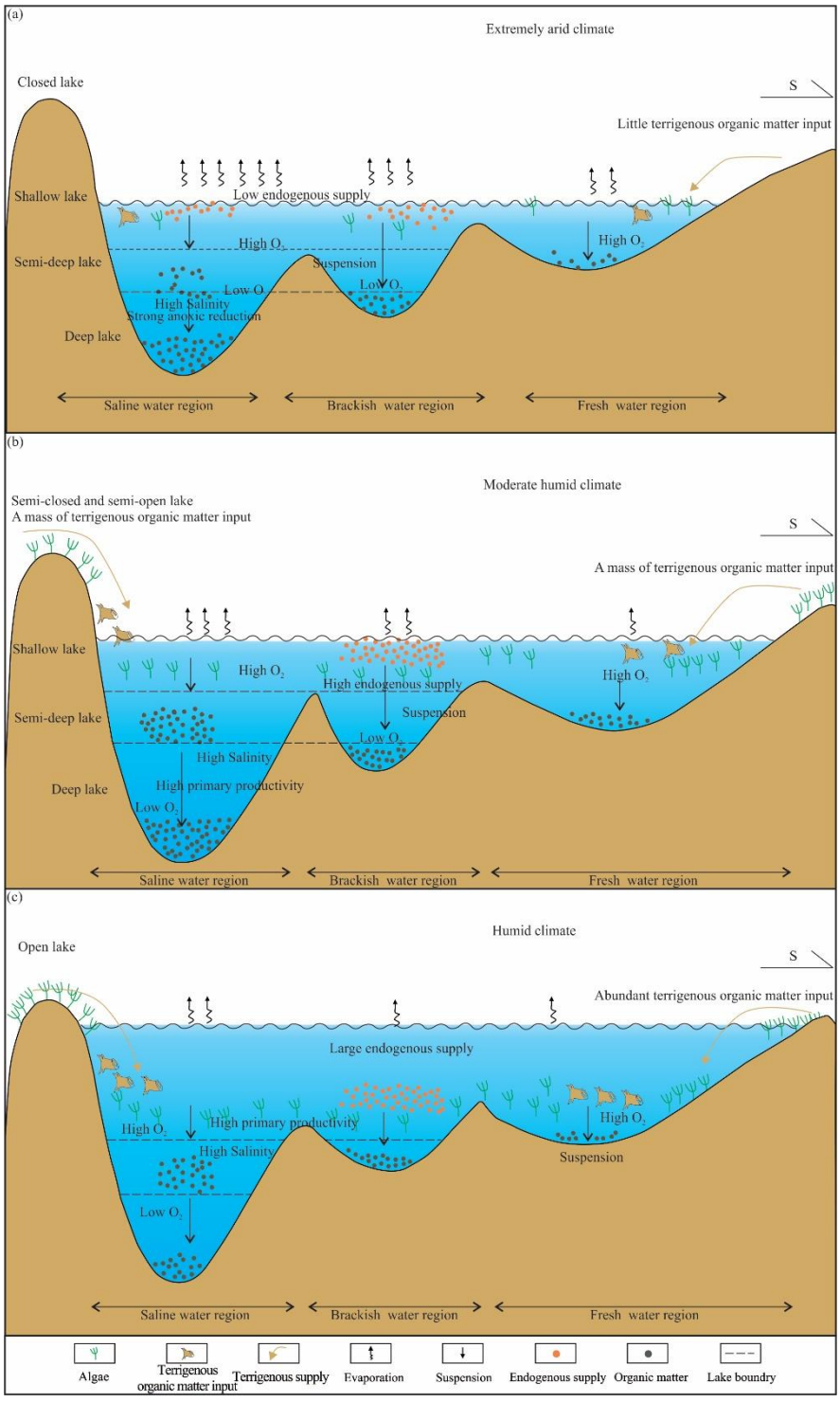

Figure 5.11 Depositional model of lacustrine source rocks of the third member of the Shahejie Formation in the Dongpu Depression, Bohai Bay Basin (modified after Tang et al., 2020).

in limited input of terrestrial OM into the saline lacustrine rift basin. Concurrently, aquatic plankton also faced challenges in development due to the elevated salinity of the water. Consequently, the saline lacustrine rift basin experienced a shortage of both exogenous OM input and endophytic OM supply. Despite the salinity stratification of the lake water, creating stagnant and anoxic bottom waters conducive to OM preservation, the enrichment of OM was hindered by the scarcity of OM supply.

During the sedimentation of the middle section, the lacustrine basin underwent strong rifting, and the entire basin experienced alternating semi-closed and semi-open depositional environments (Fig. 5.11b). The climate exhibited moderate humidity and dryness with relatively strong evaporation, resulting in slightly higher salinity. Under these climatic conditions, terrestrial higher plants thrived, leading to a substantial input of terrestrial OM into the lacustrine basin. Simultaneously, aquatic plankton flourished, ensuring a significant supply of both exogenous OM and endophytic OM to the saline lacustrine rift basin. The salinity stratification of the lake water caused the bottom water to become stagnant and anoxic, creating optimal conditions for OM accumulation and preservation and facilitating the easy enrichment of OM during the sedimentary period.

The upper section was deposited in an open lake environment (Fig. 5.11c). The climate was warm and humid, and the salinity was generally lower, although the northern region still exhibited higher salinity. The warm and humid climate fostered the flourishing of terrestrial higher plants, resulting in a substantial input of terrestrial OM into the saline lacustrine rift basin. Concurrently, aquatic plankton thrived in appropriately saline water, ensuring a significant supply of both exogenous and endophytic OM to the lacustrine basin. However, in the southern and central areas where the lake water had lower salinity and the bottom water was oxygen-rich, the preservation conditions for OM were poor, making the enrichment of OM challenging. In contrast, in the northern region, where preservation conditions for OM were favorable, OM was enriched.

The accumulation of OM in the second member of the Lucaogou Formation was mainly affected by volcanism (Pan et al., 2020b). During periods of intense volcanic activity, a significant influx of volcanic ash from the basin's periphery descended into the lake, providing essential nutrients for algal growth and inducing algal blooms (Fig. 5.12a). Coupled with the suboxic-euxinic environment and high salinity of the lake, these conditions favored the enhanced preservation of OM. Consequently, the synergistic effects of high primary productivity, a suboxic-euxinic setting, and elevated salinity collaborated to enrich the OM.

During periods of intermittent or weak volcanic activity, there was a decline in tuffaceous material, and dolomite deposition became predominant (Fig. 5.12b). With limited nutrient input from volcanic ash, algal growth was constrained, causing a reduction in primary productivity and, consequently, lower OM content in both dolomite and tuffaceous dolomite. The diminished presence of volcanic ash allowed sunlight to reach the ground with unabated intensity, contributing to drier paleoclimate accompanied by increased evaporation. Moreover, the combination of a tightly sealed lake and inadequate external water supply led to heightened salinity. The initial abundance of thriving

algae continued to respire and consume oxygen, fostering a more euxinic environment that further supported OM preservation.

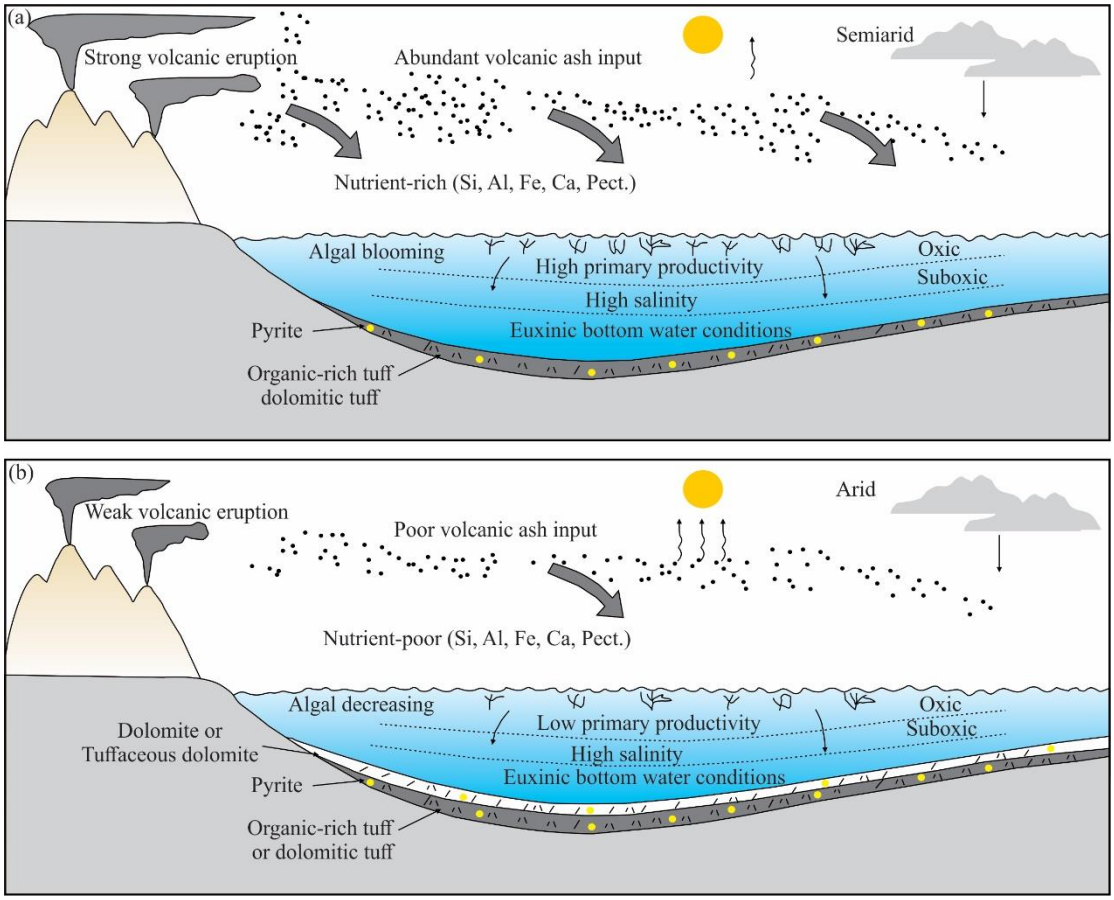

Figure 5.12 Depositional model of lacustrine source rocks of the second member of the Lucaogou Formation in the Santanghu Basin (modified after Pan et al., 2020b).

During the sedimentation of the lower part of the 7th member of the Yanchang Formation, the volcanic eruption resulted in a substantial influx of ash into the lake, providing abundant nutrients for the aquatic ecosystem (Zhang et al., 2021b). Concurrently, intense low-temperature hydrothermal activity occurred at the bottom of the lake, introducing a significant influx of nutrients and reinforcing the anoxic conditions. The prevailing warm and humid paleoclimate conditions led to higher rainfall. This climatic setting facilitated the formation of a maximum flooding surface in the lake, maintaining a relatively high and stable base level. Sediments along the southern margin of the basin primarily represented semi-deep to deep lake facies with a low sedimentation rate. Phytoplankton, bacteria, and other aquatic organisms constituted the primary source of OM. The bottom environment featured anoxic fresh to brackish water rich in OM, leading to the development of thick oil shale deposits (Fig. 5.13a). During the sedimentation of the upper part, volcanic and hydrothermal activities gradually diminished, leading to the deposition of a limited quantity of volcanic ash in the lake. The paleoclimate shifted to semi-humid conditions, accompanied by a reduction in rainfall and a decrease in the base

level. Deposition along the southern margin of the basin transitioned to shallow lake and delta front facies deposits. This area was characterized by an increased sedimentation rate and a reduction in the water body's depth. The primary source of OM became more diverse, with an increased input of higher plants from the land. The lake bottom exhibited suboxic freshwater conditions. Consequently, OM accumulation diminished, leading to the deposition of dark mudstone and thin oil shale (Fig. 5.13b).

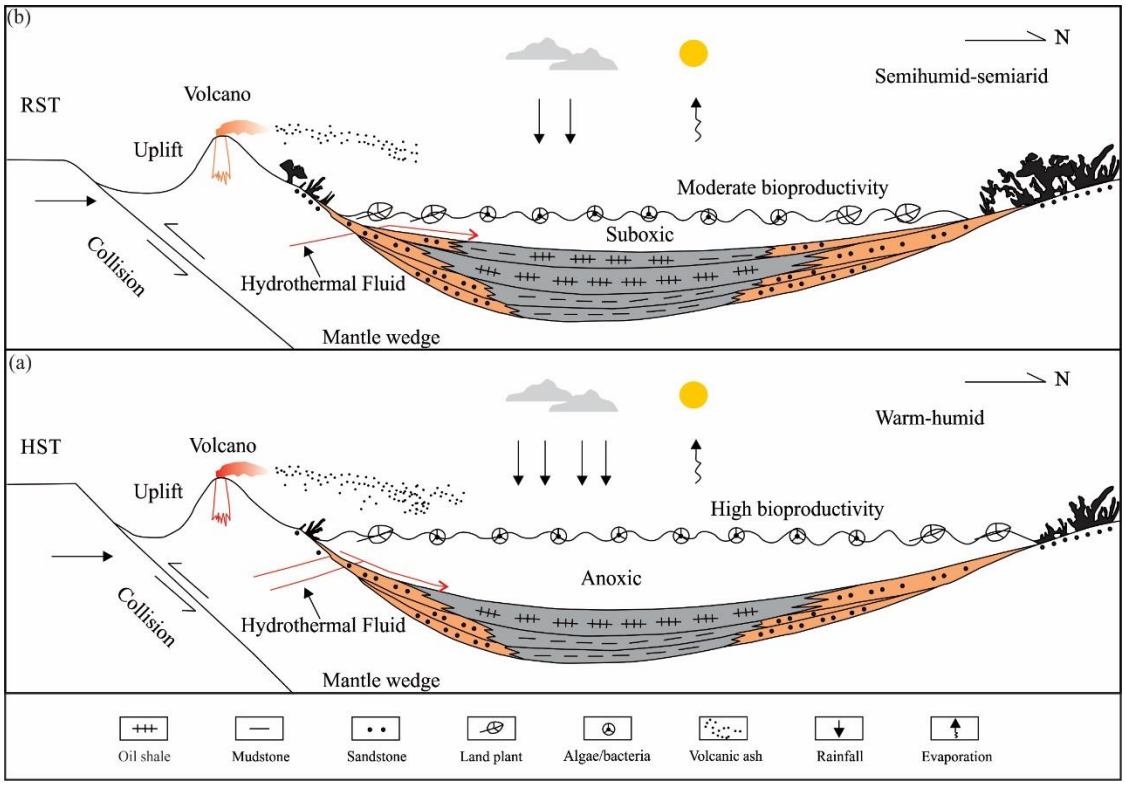

Figure 5.13 Depositional model of lacustrine source rocks of the 7th member of the Yanchang Formation in the Ordos Basin (modified after Zhang et al., 2021b).

During the sedimentation of Permian shales in the Lodève Basin, the lake's morphology displayed an asymmetry with a steep slope constrained by faults on one side and a gentler slope on the other (Wu et al., 2024; Fig. 4.13a). The transition from ancestral drainage networks, represented by Late Carboniferous conglomeratic units, to a prevailing deep lake setting occurred from the Late Carboniferous to the Early Permian, followed by the accumulation of thick shallow lake sediments. The depositional environment in the paleolake, as evidenced by its sedimentary rocks, was primarily influenced by basin expansion due to tectonic activity and sediment accumulation (Pochat and Van Den Driessche, 2011). It is hypothesized that a deep-water lacustrine environment with anoxic-suboxic conditions existed during the deposition of the lower USPF, as tectonic subsidence exceeded sedimentary accumulation (Fig. 4.13a). However, anoxia might not be the decisive factor in the formation of the most OM-rich source rocks within this basin. Considering the continuous marine influence indicated by fossil evidence in the Central Massif region of France during the Upper

Carboniferous to Lower Permian (Gottfried, 1987; Poplin et al., 2001; Schultze, 2009), it is plausible that the Lodève Basin, located in the southern Massif Central, experienced seawater incursions during the deposition of the Permian shales. Therefore, the significantly elevated salinity proxy values observed in the lower section of the USPF may also serve as an indicator of marine incursion (Fig. 4.13a). The influence of a more humid climate might have led to increased weathering and detrital input during the deposition of the lower section of the USPF. Additionally, the steep lake margins could have facilitated a greater influx of clastic sediments into the lake (Fig. 4.13a). Influenced by the gradual expansion of the basin area, it is hypothesized that the sedimentation of the upper section of the USPF, TLF, and VF was characterized by relatively shallow and oxic-dysoxic environments (Fig. 4.13b). Additionally, the reduced values of salinity markers suggest the presence of a freshwater to brackish environment characterized by a relatively weakly stratified water column. Such shallow lake settings typically involve increased vertical water column mixing and higher dissolved oxygen levels. Although these conditions are generally unfavorable for the preservation of OM as they promote oxidative decomposition, the combination of high bioproductivity and a sufficiently high sedimentation rate contributed to the preservation of hydrogen-rich OM and the deposition of sapropel.

According to Zhao et al., 2022b, the sedimentation of Miocene lacustrine fine-grained post-impact deposits of the Nördlinger Ries was characterized by a semi-arid climate and elevated paleotemperature. These environmental conditions restricted freshwater input into the lake, promoting enhanced evaporation. Consequently, water salinity increased from the early stage (Fig. 5.14a) to the mid-stage (Fig. 5.14b) of the lake. The elevated salinity of the water and the decomposition of OM inevitably led to intense stratification of the water column and anoxic conditions in the bottom water. Throughout the majority of the deposition period (Fig. 5.14a and b), the anoxic conditions in the bottom water of an alkaline lake with high salinities remained undisturbed, as evidenced by consistently low Pr/Ph ratios until the late lake stage. During this final stage, the formation of an outlet occurred, through which incoming freshwater pushed out saline water from the lake. This led to a shift in the overall environmental conditions towards oxic or suboxic conditions, as reflected by high Pr/Ph ratios (Fig. 5.14c). The prevalence of halophilic algal species over prokaryotes, as observed in the early-middle Nördlinger Ries lake, suggests high biological productivity with minimal contribution from aerobic bacteria, cyanobacteria, and methanotrophic bacteria to the OM (Fig. 5.14a and b). In the swampy stage, the bio-community was dominated by higher land plants (Fig. 5.14c).

In contrast to the previously discussed lacustrine deposits, there have been limited investigations of the origins of OM and the environmental conditions prevailing during the deposition of the lacustrine sequence in Messel oil shale. According to Bauersachs et al. (2014), the Messel oil shale accumulated at the bottom of a small maar lake characterized by a permanent water column stratification and persistent anoxia in the bottom water. These conditions facilitated the preservation of high concentrations of OM, which, based on comprehensive organic-geochemical and stable isotope fingerprinting, comprises a diverse mixture of autochthonous and allochthonous sources (e.g.,

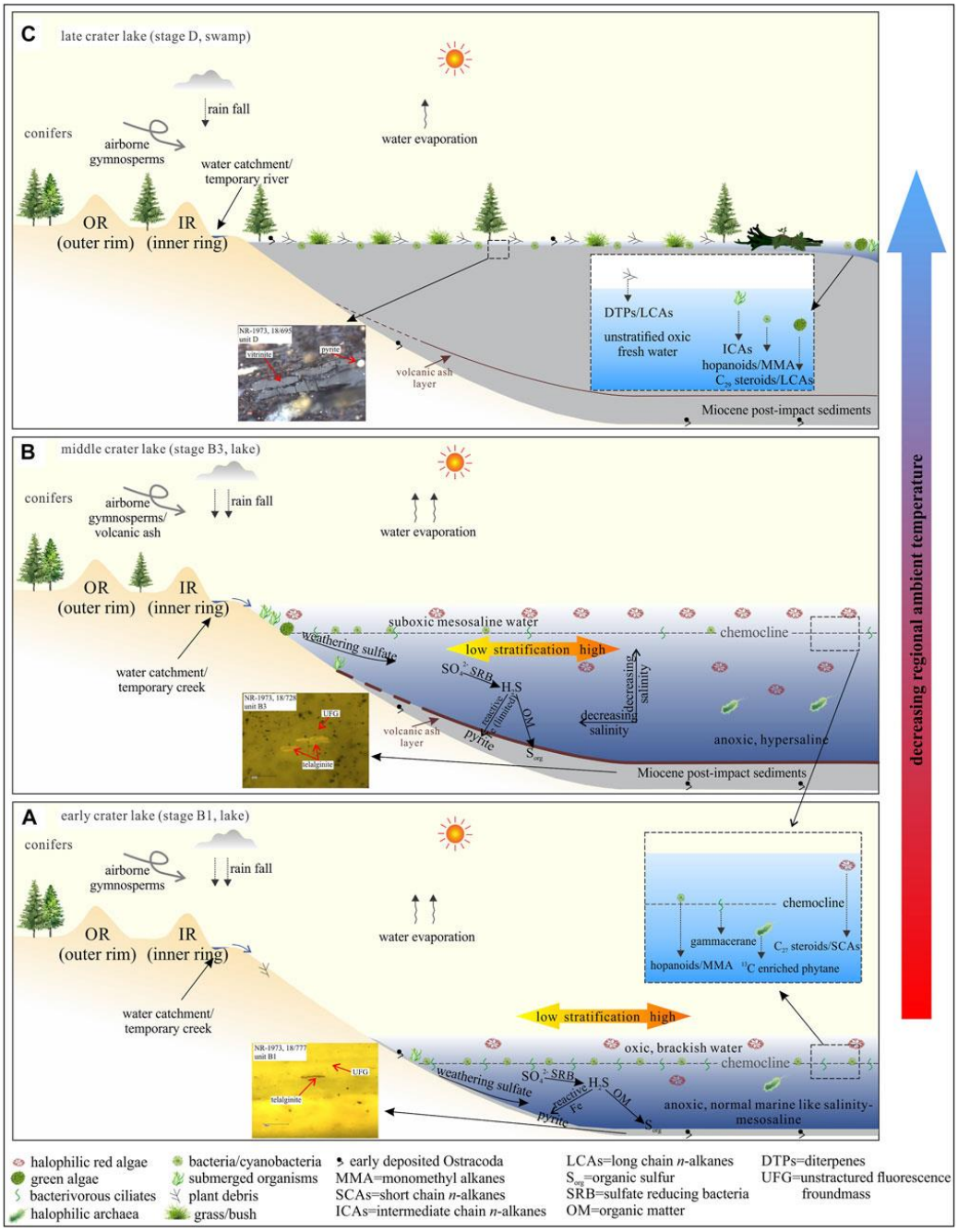

Figure 5.14 Depositional model of the lacustrine source rocks in the paleo Nördlinger Ries lake (modified after Zhao et al., 2022b).

terrestrial plants, aquatic macrophytes, algae, and a diverse microbial community). Notably, lipid-rich components from vascular plants, forming a dense paratropical rainforest in the proximity of the small maar lake, are possibly a significant contributor to the sedimentary OM. The occurrence of stable carbon isotope excursions toward heavier bulk carbon isotopic values, particularly evident in the Middle Messel-Formation, is interpreted as indicative of periods marked by increased algal productivity from various phytoplankton species and heightened input of autochthonous OM into the lake sediments. The overall decrease in bulk carbon isotopic values coupled with an elevation in bulk

nitrogen isotopic composition values across the Middle Messel oil shale is viewed as evidence of escalated rates of microbial reworking of the sedimentary OM.

In conclusion, it can be inferred that sedimentation in lakes can lead to the deposition of OM-rich sediments with excellent, very good, or good petroleum generation potential. Multiple external factors, including the seasonal or periodic paleoclimatic conditions, weathering of rocks surrounding the lakes, marine incursions, volcanic eruptions, hydrothermal activity, as well as the tectonically driven configuration of the basin, control the accumulation of OM in the lakes by significantly impacting redox conditions, water salinity, OM sources, and bioproductivities.

6 References

Alexander, R., Larcher, A.V., Kagi, R.I., Price, P.L., 1988. The use of plant derived biomarkers for correlation of oils with source rocks in the Cooper/Eromanga Basin System, Australia. APPEA J. 28, 310–324.

Alexander, R., Kagi, R.I., Roland, S.J., Sheppard, P.N., Chirila, T.V., 1985. The effects of thermal maturity on distributions of dimethylnaphthalenes and trimethylnaphthalenes in some ancient sediments and petroleum. Geochimica et Cosmochimica Acta 49, 385–395.

Algeo, T.J., Henderson, C.M., Tong, J.N., Feng, Q.L., Yin, H.F., Tyson, R.V., 2013. Plankton and productivity during the Permiane-Triassic boundary crisis: an analysis of organic carbon fluxes. Global and Planetary Change 105, 52–67.

Algeo, T.J., Tribovillard, N., 2009. Environmental analysis of paleoceanographic systems based on molybdenum–uranium covariation. Chemical Geology 268, 211–225.

Algeo, T.J., Liu, J.S., 2020. A re-assessment of elemental proxies for paleoredox analysis. Chemical Geology 540, 119549.

Aquino Neto, F.R., Trendel, J.M., Restle, A., Connan, J., Albrecht, P.A., 1983. Occurrence and formation of tricyclic and tetracyclic terpanes in sediments and petroleums. In: Bjorøy, M., et al. (Eds.), Advances in Organic Geochemistry 1981. John Wiley and Sons, pp. 659–667.

Bábek, O., Kumpan, T., Kalvoda, J., Grygar, T.M., 2016. Devonian/Carboniferous boundary glacioeustatic fluctuations in a platform-to-basin direction: A geochemical approach of sequence stratigraphy in pelagic settings. Sedimentary geology 337, 81–99.

Bahlburg, H., Dobrzinski, N., 2011. A review of the Chemical Index of Alteration (CIA) and its application to the study of Neoproterozoic glacial deposits and climate transitions. In: Arnaud, E., Halverson, G.P., Shield-Zhou, G. (Eds.), The Geological Record of Neoproterozoic Glaciations. 36. pp. 81–92 Geological Society, London, Memoirs.

Bao, J., Wang, Y., Song, C., Feng, Y., Hu, C., Zhong, S., Yang, J., 2017. Cenozoic sediment flux in the Qaidam Basin, northern Tibetan Plateau, and implications with regional tectonics and climate. Global and Planetary Change 155, 56–69.

Barker, C.E., Pawlewicz, M.J., 1986. The correlation of vitrinite reflectance with maximum temperature in humic organic matter. In: Buntebarth, G., Lefler, J. (Eds.), Paleogeothermics: Evaluation of Geothermal Conditions in the Geological Past, Vol. 5 of Lecture Notes in Earth Sciences. Springer, Berlin/Heidelberg, pp. 79–93.

Bauersachs, T., Kremer, B., Schouten, S., Sinninghe Damsté, J.S., 2009. A biomarker and δ^{15} N study of thermally altered Silurian cyanobacterial mats. Organic Geochemistry 40, 149–157.

Bauersachs, T., Schouten, S., Schwark, L., 2014. Characterization of the sedimentary organic matter preserved in Messel oil shale by bulk geochemistry and stable isotopes. Palaeogeography, Palaeoclimatology, Palaeoecology 410, 390–400.

Bechtel, A., Jia, J.L., Strobl, S.A., Sachsenhofer, R.F., Liu, Z.J., Gratzer, R., Püttmann, W., 2012. Palaeoenvironmental conditions during deposition of the Upper cretaceous oil shale sequences in the Songliao Basin (NE China), implications from geochemical analysis. Organic Geochemistry 46, 76–95.

Behar, F., Beaumont, V., Penteado, H.D.B., 2001. Rock-Eval 6 technology: performances and developments. Oil & Gas Science and Technology 56(2), 111–134.

Berner, R.A., Raiswell, R., 1983. Burial of organic carbon and pyrite sulfur in sediments over Phanerozoic time: a new theory. Geochimica et Cosmochimica Acta 47(5), 855–862.

Berner R. A., Raiswell R., 1984. C/S method for distinguishing freshwater from marine sedimentary rocks. Geology 12(6), 365–368.

Bohacs, K.M., Carroll, A.R., Neal, J.E., Mankiewicz, P.J., 2000. Lake-basin type, source potential, and hydrocarbon character: an integrated sequence-stratigraphicgeochemical framework. Lake basins through space and time: AAPG Stud. Geol. 46, 3–34.

Bom, M.H., Ceolin, D., Kochhann, K.G., Krahl, G., Fauth, G., Bergue, C.T., Savian, J.F., Junior, O.S., Simões, M.G., Assine, M.L., 2021. Paleoenvironmental evolution of the Aptian Romualdo Formation, Araripe Basin, Northeastern Brazil. Global and Planetary Change 103528.

Bordoloi, M., Shukla, V.S., Nath, S.C., Sharma, R.P., 1989. Naturally occurring cadinenes. Phytochemistry 28, 2007–2037.

Bourbonniere, R.A., Meyers, P.A., 1996. Anthropogenic influences on hydrocarbon contents of sediments deposited in eastern Lake Ontario since 1800. Environmental Geology 28(1), 22–28.

Bray, E.E., Evans, E.D., 1961. Distribution of n-paraffins as a clue to recognition of source beds. Geochimica et Cosmochimica Acta 22, 2–15.

Brocks, J.J., Buick, R., Logan, G.A., Summons, R.E., 2003. Composition and syngeneity of molecular fossils from the 2.78 to 2.45 billion-year-old Mount Bruce Supergroup, Pilbara Craton, Western Australia. Geochimica et Cosmochimica Acta 67, 4289–4319.

Bruguier, O., Becq-Giraudon, J.-F., Champenois, M., Deloule, E., Ludden, J., Mangin, D., 2003. Application of in situ zircon geochronology and accessory phase chemistry to constraining basin development during post-collisional extension: a case study from the French Massif Central. Chemical Geology 201, 319–336.

Budzinski, H., Garrigues, P., Connan, J., Devillers, J., Domine, D., Radke, M., Oudins, J. L., 1995. Alkylated phenanthrene distributions as maturity and origin indicators in crude oils and rock extracts. Geochimica et Cosmochimica Acta 59, 2043–2056.

Burnaz, L., Kalmykov, A., Grohmann, S., Kalmykov, G., Littke, R., 2022. Geochemistry and organic petrology of organic-rich shales of the Upper Jurassic–Lower Cretaceous Bazhenov Horizon

in the Frolov Region, West Siberian Basin: Implications for the reconstruction of the organic matter origin and paleoredox conditions. Marine and Petroleum Geology 143, 105809.

Calvert, S.E., Pedersen, T.F., 2007. Chapter fourteen elemental proxies for palaeoclimatic and palaeoceanographic variability in marine sediments: interpretation and application. In: Hillaire–Marcel, C., De Vernal, A. (Eds.), Developments in Marine Geology, vol. 1, pp. 567–644.

Cao, H., He, W., Chen, F., Shan, X., Kong, D., Hou, Q., Pu, X., 2021. Integrated chemostratigraphy (δ^{13} C-δ^{34} S-δ^{15} N) constrains Cretaceous lacustrine anoxic events triggered by marine sulfate input. Chemical Geology 559, 119912.

Cao, L., Zhang, Z., Li, H., Zhong, N., Xiao, L., Jin, X., Li, H., 2020. Mechanism for the enrichment of organic matter in the Liushagang Formation of the Weixinan Sag, Beibuwan Basin, China. Marine and Petroleum Geology 122, 104649.

Carroll, A. M., K. M. Bohacs., 1999. Stratigraphic classification of ancient lakes: Balancing tectonic and climatic controls. Geology. 27(2), 99–102.

Cassani, F., Gallango, O., Talukdar, S., Vallejos, C., Ehrmann, U., 1988. Methylphenanthrene maturity index of marine source rock extracts and crude oils from the Maracaibo Basin. Organic Geochemistry 13, 73–80.

Cesar, J., Grice, K., 2019. Molecular fingerprint from plant biomarkers in Triassic-Jurassic petroleum source rocks from the Dampier sub-Basin, Northwest Shelf of Australia. Marine and Petroleum Geology 110, 189–197.

Cesar, J., Grice, K., 2017. δ^{13} C of polycyclic aromatic hydrocarbons to establish the facies variations in a fluvial deltaic Triassic record (Dampier sub-Basin, Western Australia). Organic Geochemistry 107, 59–68.

Chang, M., Chow, C., 1978. On the fossil fishes in Mesozoic and Cenozoic oilbearing strata from in East China and their sedimentary environment. Vertebr. Palasiatica. 15, 194–197 (in Chinese with English abstract).

Chen, X.H., Gehrels, G., Yin, A., Li, L., Jiang, R.B., 2012. Paleozoic and Mesozoic Basement Magmatisms of Eastern Qaidam Basin, Northern Qinghai–Tibet Plateau: LA–ICP–MS Zircon U–Pb Geochronology and its Geological Significance. Acta Geologica Sinica (English Edition) 86(2), 350–369.

Cho, T., Ohta, T., 2022. A robust chemical weathering index for sediments containing authigenic and biogenic materials. Palaeogeography, Palaeoclimatology, Palaeoecology 608, 111288.

Cichon-Pupienis, A., Littke, R., Lazauskienė, J., Baniasad, A., Pupienis, D., Radzevičius, S., Šiliauskas, L., 2021. Geochemical and sedimentary facies study-Implication for driving mechanisms of organic matter enrichment in the lower Silurian fine-grained mudstones in the Baltic Basin (W Lithuania). International Journal of Coal Geology 103815.

Clift, P.D., Hodges, K., Heslop, D., Hannigan, R., Hoang, L.V., Calves, G., 2008. Correlation of Himalayan exhumation rates and Asian monsoon intensity. Nature geoscience 1, 875–880.

Conrad, G., Odin, B., 1984. LeBassinPermiende Lodeve (Herault), Livret-guidede l'excursion. Laboratoire de Sedimentologie. Universite d'Aix, Congrese European de Sedimentologie a Marseille. Universite d'Aix-Marseille.

Condomines, M., Lloret, E., Seidel, J. L., Lopez, M., 2014. ($^{228}Ra/^{226}Ra$) ratios in hydrothermal carbonates and the origin of radium in CO_2-rich waters of the Lodève Basin (South of France). Chem. Geol. 372, 46–53.

Cope, M.J., 1981. Products of Natural Burning as a Component of the Dispersed Organic Matter of Sedimentary Rocks. Organic Maturation Studies and Fossil Fuel Exploration. Academic Press, London, pp. 89–109.

Cox, R., Lowe, D.R., Cullers, R.L., 1995. The influence of sediment recycling andbasement composition on evolution of mudrock chemistry in the southwestern United States. Geochimica et Cosmochimica Acta 59(14), 2919–2940.

Cranwell, P.A., 1977. Organic geochemistry of Cam Loch (Sutherland) sediments. Chemical Geology 20, 205–221.

Dang, Y.Q., Zhao, W.Z., Su, A.G., Zhang, S.C., Li, M.W., Guan, Z.Q., Ma, D.D., Chen, X.L., Shuai, Y.H., Wang, H.T., Tan, Y.H., Xu, Z.Y., 2008. Biogenic gas systems in eastern Qaidam Basin. Marine and Petroleum Geology 25, 344–356.

Dang, Y.Q., Hu, Y., Yu, H.L., Song, Y., Yang, F.Z., 2003. Oil geology of the north margin of Qaidam Basin, Northwest China: Beijing, Geological Publishing House (in Chinese).

Dean, W.E., Gardner, J.V., Piper, D.Z., 1997. Inorganic geochemical indicators of glacialinterglacial changes in productivity and anoxia on the California continental margin. Geochimica et Cosmochimica Acta 61, 4507–4518.

Demaison, G. J., Moore, G. T., 1980. Anoxic environments and oil source bed genesis. Organic geochemistry 2(1), 9–31.

Deng, T., Li, Y., Wang, Z., Yu, Q., Dong, S., Yan, L., Hu, W., Chen, B., 2019. Geochemical characteristics and organic matter enrichment mechanism of black shale in the Upper Triassic Xujiahe Formation in the Sichuan basin: implications for paleoweathering, provenance and tectonic setting. Marine and Petroleum Geology 109, 698–716.

Derenne, S., Largeau, C., Casadevall, E., Connan, J., 1988. Comparison of torbanites of various origins and evolutionary stages. Bacterial contribution to their formation. Causes of the lack of botryococcane in bitumens. Organic Geochemistry 12(1), 43–59.

Ding, W., Hou, D., Jiang, L., Jiang, Y., Wu, P., 2020. High abundance of carotanes in the brackish-saline lacustrine sediments: A possible cyanobacteria source? International Journal of Coal Geology 219, 103373.

Doner, Z., Kumral, M., Demirel, I.H., Hu, Q., 2019. Geochemical characteristics of the silurian shales from the central taurides, southern Turkey: organic matter accumulation, preservation and depositional environment modeling. Marine and Petroleum Geology 102, 155–175.

Dupuy, C., Leyreloup, A., Vernieres, J., 1979. The lower continental crust of the Massif Central (Bournac, France)—with special references to REE, U and Th composition, evolution, heat-flow production. Physics and Chemistry of the Earth 11, 401–415.

Dypvik, H., Harris, N.B., 2001. Geochemical facies analysis of fine-grained siliciclastics using Th/U, Zr/Rb and (Zr+Rb)/Sr ratios. Chemical geology 181, 131–146.

Dypvik, H., 1984. Geochemical compositions and depositional conditions of upper Jurassic and lower Cretaceous Yorkshire clays, England. Geological Magazine 121(5), 489–504.

Echtler, H., Malavieille, J., 1990. Extensional tectonics, basement uplift and Stephano-Permian collapse basin in a late Variscan metamorphic core complex (Montagne Noire, Southern Massif Central). Tectonophysics 177 125–138.

Eglinton, G., Hamilton, R.J., 1967. Leaf epicuticular waxes. Science 156, 1322–1335.

Ellis, L., Singh, R.K., Alexander, R., Kagi, R.I., 1996. Formation of isohexyl alkylaromatic hydrocarbons from aromatization-rearrangement of terpenoids in the sedimentary environment: A new class of biomarker. Geochimica et Cosmochimica Acta 60, 4747–4763.

El-Shafeiy, M., El-Kammar, A., El-Barkooky, A., Meyers, P., 2016. Paleo-redox depositional conditions inferred from trace metal accumulation in two Cretaceous-Paleocene organic-rich sequences from Central Egypt. Marine and Petroleum Geology 73, 333–349.

Erbacher, J., Huber, B.T., Norris, R.D., Markey, M., 2001. Increased thermohaline stratification as a possible cause for an ocean anoxic event in the Cretaceous period. Nature 409(6818), 325–327.

Espitalié, J., Laporte, J.L., Madec, M., Marquis, F., Leplat, P., Paulet, J., Boutefeu, A., 1977. Méthode rapide de caractérisation des roches mètres, de leur potentiel pétrolier et de leur degré d'évolution. Rev. Inst. Fr. Pét. 32(1), 23–42.

Fang, R., Littke, R., Zieger, L., Baniasad, A., Li, M., Schwarzbauer, J., 2019. Changes of composition and content of tricyclic terpane, hopane, sterane, and aromatic biomarkers throughout the oil window: A detailed study on maturity parameters of Lower Toarcian Posidonia Shale of the Hils Syncline, NW Germany. Organic Geochemistry 138, 103928.

Fedo, C.M., Nesbitt, W.H., Young, G.M., 1995. Unraveling the effects of potassium metasomatism in sedimentary rocks and paleosols, with implications for paleoweathering conditions and provenance. Geology 23(10), 921–924.

Feng, Z.Q., Jia, C.Z., Xie, X.N., Zhang, S., Feng, Z.H., Cross, T.A., 2010. Tectonostratigraphic units and stratigraphic sequences of the nonmarine Songliao Basin, Northeast China. Basin Research 22(1), 79–95.

Floyd, P.A., Leveridge, B.E., 1987. Tectonic environment of the Devonian Gramscatho basin, South Cornwall: framework mode and geochemical evidence from turbiditic sandstones. Journal of the Geological Society 144, 531–542.

Fralick, P.W., Kronberg, B.I., 1997. Geochemical discrimination of clastic sedimentary rock sources. Sedimentary Geology 113, 111–124.

Gao, F., Song, Y., Li, Z., Xiong, F., Chen, L., Zhang, Y., Liang, Z., Zhang, X., Chen, Z., Joachim, M., 2018. Lithofacies and reservoir characteristics of the Lower Cretaceous continental Shahezi Shale in the Changling Fault Depression of Songliao Basin, NE China. Marine and Petroleum Geology 98, 401–421.

Gehrels, G., Kapp, P., DeCelles, P., Pullen, A., Blakey, R., Weislogel, A., Ding, L., Guynn, J., Martin, A., McQuarrie, N., Yin, A., 2011. Detrital zircon geochronology of pre-Tertiary strata in the Tibetan-Himalayan orogen. Tectonics 30, TC5016.

George, S.C., Lisk, M., Eadington, P.J., 2004. Fluid inclusion evidence for an early, marine-sourced oil charge prior to gas-condensate migration, Bayu-1, Timor Sea, Australia. Marine and Petroleum Geology 21, 1107–1128.

George, S.C., Ruble, T.E., Dutkiewicz, A., Eadington, P.J., 2001. Assessing the maturity of oil trapped in fluid inclusions using molecular geochemistry data and visually-determined fluorescence colours. Applied Geochemistry 16(4), 451–473.

Ghassal, B.I., Littke, R., Sachse, V., Sindern, S., Schwarzbauer, J., 2016. Depositional environment and source rock potential of upper Albian to Turonian sedimentary rocks of the Tarfaya Basin, Southwest Morocco. Geologica Acta 14, 419–441.

Gonçalves, F. T., 2002. Organic and isotope geochemistry of the Early Cretaceous rift sequence in the Camamu Basin, Brazil: paleolimnological inferences and source rock models. Organic Geochemistry 33(1), 67–80.

Gonneea, M.E., Paytan, A., 2006. Phase associations of barium in marine sediments. Marine Chemistry 100(1–2), 124–135.

Goldberg, K., Humayun, M., 2010. The applicability of the Chemical Index of Alteration as a paleoclimatic indicator: an example from the Permian of the Paraná Basin, Brazil. Palaeogeography, Palaeoclimatology, Palaeoecology 293, 175–183.

Gorter, J., 2001. A Marine Source Rock in the Gippsland Basin? In: Hill, K.H., Bernecker, T. (Eds.), Eastern Australiasian Basins Symposium, a Refocussed Engry Perspective for the Future. Petroleum Exploration Society of Australia, Perspective for the Future, Melbourne, Special Publication, pp. 385–390.

Gottfried, M. D., 1987. A Pennsylvanian aeduelliform (Osteichthyes, Actinopterygii) from North America with comments on aeduelliform interrelationships. Paläontologische Zeitschrift, 61(1–2), 141–148.

Grimalt, J.O., van Drooge, B.L., Ribes, A., Fernandez, P., Appleby, P., 2004. Polycyclic aromatic hydrocarbon composition in soils and sediments of high altitude lakes. Environmental Pollution 131, 13–24.

Grice, K., Nabbefeld, B., Maslen, E., 2007. Source and significance of selected polycyclic aromatic hydrocarbons in sediments (Hovea-3 well, Perth Basin, Western Australia) spanning the Permian–Triassic boundary. Organic Geochemistry 38, 1795–1803.

Grice, K., Schaeffer, P., Schwark, L., Maxwell, J.R., 1996. Molecular indicators of palaeoenvironmental conditions in an immature Permian shale (Kupferschiefer, Lower Rhine Basin, north-west Germany) from free and S-bound lipids. Organic Geochemistry 25, 131–147.

Grice, K., Cao, C., Love, G.D., Bottcher, M.E., Twitchett, R.J., Grosjean, E., Summons, R. E., Turgeon, S.C., Dunning, W., Jin, Y., 2005. Photic zone euxinia during the Permian-Triassic superanoxic event. Science 307, 707–709.

Guenther, F., Aichner, B., Siegwolf, R., Xu, B., Yao, T., Gleixner, G., 2013. A synthesis of hydrogen isotope variability and its hydrological significance at the Qinghai–Tibetan Plateau. Quaternary International 313–314, 3–6.

Guo, Z., Ma, Y., Liu, W., Wang, L., Tian, J., Zeng, X., Ma, F., 2017a. Main factors controlling the formation of basement hydrocarbon reservoirs in the Qaidam Basin, western China. Journal of Petroleum Science and Engineering 149, 244–255.

Guo, T., Zhou, Z., Ren, S., 2017b. Jurassic shale gas discovered at chaiye-1 well on the northern margin of Qaidam Basin. Geology in China 44(2), 401–402 (in Chinese).

Hackley, P.C., Cardott, B.J., 2016. Application of organic petrography in North American shale petroleum systems: A review. International Journal of Coal Geology 163, 8–51.

Hanson, A.D., Zhang, S.C., Moldowan, J.M., Liang, D.G., Zhang, B.M., 2000. Molecular organic geochemistry of the Tarim basin. Northwest China. AAPG Bulletin 84, 1109–1128.

Hanson, A.D., Ritts, B.D., Zinniker, D., Moldowan, J.M., Biffi, U., 2001. Upper Oligocene lacustrine source rocks and petroleum systems of the northern Qaidam basin, northwest China. AAPG Bulletin 85, 601–619.

Hao, F., Zhou, X., Zhu, Y., Yang, Y., 2011. Lacustrine source rock deposition in response to co-evolution of environments and organisms controlled by tectonic subsidence and climate, Bohai Bay Basin, China. Organic geochemistry 42(4), 323–339.

Hao, F., Zhou, X., Zhu, Y., Yang, Y., 2009. Mechanisms for oil depletion and enrichment on the shijiutuo uplift, Bohai Bay Basin, China. AAPG Bulletin 93, 1015–1037.

Harris, N.B., Freeman, K.H., Pancost, R.D., White, T.S., Mitchell, G.D., 2004. The character and origin of lacustrine source rocks in the Low Cretaceous synrift section, Congo Basin, west Africa. AAPG Bulletin 88(8), 1163–1184.

Harnois, L., 1988. The CIW index: a new chemical index of weathering. Sedimentary geology 55(3), 319–322.

Hautevelle, Y., Michels, R., Malartre, F., Trouiller, A., 2006. Vascular plant biomarkers as proxies for palaeoflora and palaeoclimatic changes at the Dogger/Malm transition of the Paris Basin (France). Organic Geochemistry 37, 610–625.

Hayashi, K.I., Fujisawa, H., Holland, H.D., Ohmoto, H., 1997. Geochemistry of ca. 1.9 Ga sedimentary rocks from northeastern Labrador, Canada. Geochimica et Cosmochimica Acta 61, 4115–4137.

Heppenheimer, H., Steffens, K., Püttmann, W., Kalkreuth, W., 1992. Comparison of resinite-related aromatic biomarker distributions in Cretaceous-Tertiary coals from Canada and Germany. Organic Geochemistry 18, 273–287.

Hertle, M., Littke, R., 2000. Coalification pattern and thermal modelling of the Permo-Carboniferous Saar Basin (SW-Germany). International Journal of Coal Geology 42(4), 273–296.

Horsfield, B., Curry, D.J., Bohacs, K., Littke, R., Rullkötter, J., Schenk, H.J., Radke, M., Schaefer, R.G., Carroll, A.R., Isaksen, G, Witte, E.G., 1994. Organic geochemistry of freshwater and alkaline lacustrine sediments in the Green River Formation of the Washakie Basin, Wyoming, USA. Organic Geochemistry 22(3–5), 415–440.

Hou, D., Li, M., Huang, Q., 2000. Marine transgressional events in the gigantic freshwater lake Songliao: paleontological and geochemical evidence. Organic geochemistry 31, 763–768.

Hu, J.F., Peng, P.A., Liu, M.Y., Xi, D.P., Song, J.Z., Wan, X.Q., Wang, C.S., 2015. Seawater incursion events in a Cretaceous Paleo-lake revealed by specific marine biological markers. Scientific Reports 5, 9508.

Huang, W.Y., Meinshein, W.G., 1979. Sterols as ecological indicators. Geochimica et Cosmochimica Acta 43, 739–745.

Huang, H., Zhang, S., Su, J., 2015. Pyrolytically derived polycyclic aromatic hydrocarbons in marine oils from the Tarim Basin, NW China. Energy & Fuels 29, 5578–5586.

Huang, Y.J., Yang, G.S., Gu, J., Wang, P.K., Huang, Q.H., Feng, Z.H., Feng, L.J., 2013. Marine incursion events in the Late Cretaceous Songliao Basin: constraints from sulfur geochemistry records. Palaeogeography, Palaeoclimatology, Palaeoecology 385, 152–161.

Hughes, W.B., Holba, A.G., Dzou, L.I.P., 1995. The ratios of dibenzothiophene to phenanthrene and pristane to phytane as indicators of depositional environment and lithology of petroleum source rocks. Geochimica et Cosmochimica Acta 59, 3581–3598.

Huo, F., Wen, H., Li, L., Luo, B., Zhou, G., Xu, W., Sun, H., Wang, X., Jiang, H., Chen, S., Huang, H., 2022. Influence of the depositional environment on the formation of organic-rich marine shale: A case study of the first discovery of Anisian shale in the Sichuan Basin. Journal of Petroleum Science and Engineering 214, 110577.

ICCP, 1998. The new vitrinite classification (ICCP System 1994). Fuel 77, 349–358.

ICCP, 2001. The new inertinite classification (ICCP System 1994). Fuel 80, 459–471.

Idler, D.R., Saito, A., Wiseman, P., 1968. Sterols in red algae (Rhodophyceae). Steroids 11, 465–473.

Ingram, L. L., Ellis, J., Crisp, P. T., Cook, A. C., 1983. Comparative study of oil shales and shale oils from the Mahogany zone, Green River formation (USA) and Kerosene Creek seam, Rundle formation (Australia). Chemical Geology 38(3–4), 185–212.

Jankowski, B., Littke, R., 1986. Das organische Material der Ölschiefer von Messel. Geowiss. Unserer Zeit 3, 73–80.

Jarvie, D.M., 2012. Shale resource systems for oil and gas: Part 2—Shale-oil resource systems. AAPG Memoir 97, 89–119.

Ji, L., He, C., Zhang, M., Wu, Y., Li, X., 2016. Bicyclic alkanes in source rocks of the Triassic Yanchang Formation in the Ordos Basin and their inconsistency in oil-source correlation. Marine and Petroleum Geology 72, 359–373.

Jia, J.L., Liu, Z.J., Bechtel, A., Strobl, S.A.I., Sun, P.C., 2013. Tectonic and climate control of oil shale deposition in the Upper Cretaceous Qingshankou Formation (Songliao Basin, NE China). International Journal of Earth Sciences 102, 1717–1734.

Jia, J,L., 2012. Research on the recognition and resource evaluation of the Upper Cretaceous oil shale based on geochemistry-geophysics technique in the Songliao Basin (NE, China). Ph.D. thesis. Jilin University, Changchun, Jilin (in Chinese with English abstract).

Jin, Z., Zhang, M., Tang, L., Li, J., 2004. Evolution of Meso–Cenozoic Qaidam basin and its control on oil and gas. Oil Gas Geol 25, 603–608 (in Chinese with English abstract).

Jian, X., Guan, P., Zhang, W., Feng, F., 2013. Geochemistry of Mesozoic and Cenozoic sediments in the northern Qaidam basin, northeastern Tibetan Plateau: implications for provenance and weathering. Chemical Geology 360, 74–88.

Jiang, L., George, S.C., 2019. Biomarker signatures of Upper cretaceous Latrobe Group petroleum source rocks, Gippsland Basin, Australia: distribution and geological significance of aromatic hydrocarbons. Organic Geochemistry 138, 103905.

Jiang, S., Xu, Z., Feng, Y., Zhang, J., Cai, D., Chen, L., Wu, Y., Zhou, D., Bao, S., Long, S., 2016. Geologic characteristics of hydrocarbon-bearing marine, transitional and lacustrine shales in China. Journal of Asian Earth Sciences 115, 404–418.

Jiang, L., George, S.C., 2018. Biomarker signatures of Upper Cretaceous Latrobe Group hydrocarbon source rocks, Gippsland Basin, Australia: distribution and palaeoenvironment significance of aliphatic hydrocarbons. International Journal of Coal Geology 196, 29–42.

Jiang, C., Alexander, R., Kagi, R.I., Murray, A.P., 1998. Polycyclic aromatic hydrocarbons in ancient sediments and their relationships to palaeoclimate. Organic Geochemistry 29, 1721–1735.

Jiang, L., George, S. C., 2020. Geochemical comparison of three oil families from the Gippsland Basin, SE Australia. Marine and Petroleum Geology 121, 104575.

Jones, B., Manning, D., 1994. Comparison of geochemical indices used for the interpretation of palaeoredox conditions in ancient mudstones. Chemical geology 111, 111–129.

Jones, M.M., Ibarra, D.E., Gao, Y., Sageman, B.B., Selby, D., Chamberlain, C.P., Graham, S.A., 2018. Evaluating Late Cretaceous OAEs and the influence of marine incursions on organic carbon burial in an expansive East Asian paleo-lake. Earth and Planetary Science Letters 484, 41–52.

Kalugin, I., Daryin, A., Smolyaninova, L., Andreev, A., Diekmann, B., Khlystov, O., 2007. 800-yr-long records of annual air temperature and precipitation over southern Siberia inferred from Teletskoye Lake sediments. Quaternary Research 67(3), 400–410.

Katz, B.J., 1990. Controls on distribution of lacustrine source rocks through time and space. In: Katz, B.J. (Ed.), Lacustrine Basin Exploration: Case Studies and Modern Analogs, vol. 50. AAPG Memoir pp. 61–76.

Katz, B.J., 1995. Factors controlling the development of lacustrine petroleum source rocks-an update. In: Katz, B.J. (Ed.), Paleogeography pp. 61–79.

Kelts, K., 1988. Environments of deposition of lacustrine petroleum source rocks: an introduction. Geological Society, London, Special Publications 40(1), 3–26.

Kenig, F., 2000. C_{16}–C_{29} homologous series of monomethylalkanes in the pyrolysis products of a Holocene microbial mat. Organic Geochemistry 31(2–3), 237–241.

Kenig, F., Damsté, J. S. S., Kock-van Dalen, A. C., Rijpstra, W. I. C., Huc, A. Y., de Leeuw, J. W., 1995. Occurrence and origin of mono-, di-, and trimethylalkanes in modern and Holocene cyanobacterial mats from Abu Dhabi, United Arab Emirates. Geochimica et Cosmochimica Acta 59(14), 2999–3015.

Killops, S., Killops, V., 2005. Introduction to Organic Geochemistry, second ed. Blackwell Publishing, Oxford.

Kimura, H., Watanabe, Y., 2001. Ocean anoxia at the Precambrian-Cambrian boundary. Geology 29, 995–998.

Kirkland, D. W., Evans, R., 1981. Source-rock potential of evaporitic environment. AAPG Bulletin 65(2), 181–190.

Klaver, J., Desbois, G., Urai, J.L., Littke, R., 2012. BIB-SEM study of the pore space morphology in early mature Posidonia Shale from the Hils area, Germany. International Journal of Coal Geology 103, 12–25.

Kodner, R.B., Pearson, A., Summons, R.E., Knoll, A.H., 2008. Sterols in red and green algae: quantification, phylogeny, and relevance for the interpretation of geologic steranes. Geobiology 6(4), 411–420.

Koopmans, M.P., Schouten, S., Kohnen, M.E., Damste, J.S.S., 1996. Restricted utility of aryl isoprenoids as indicators for photic zone anoxia. Geochimica et Cosmochimica Acta 60(23), 4873–4876.

Körmös, S., Bechtel, A., Sachsenhofer, R. F., Radovics, B. G., Milota, K., Schubert, F., 2020. Petrographic and organic geochemical study of the Eocene Kosd Formation (northern Pannonian Basin): Implications for paleoenvironment and hydrocarbon source potential. International Journal of Coal Geology 228, 103555.

Lambiase, J.J., 1990. A model for tectonic control of lacustrine stratigraphic sequences in continental rift basins. In: Katz, B.J. (Ed.), Lacustrine Basin Exploration: Case Studies and Modern Analogs. AAPG Memoir 50, pp. 265–276.

Laurent, D., Lopez, M., Combes, P. J., Guerrot, C., Spangenberg, J. E., Gaucher, E. C., 2020. Synsedimentary to early diagenetic rejuvenation of barite-sulfides ore deposits: Example of the

Triassic intrakarstic mineralization in the Lodève basin (France). Marine and Petroleum Geology 119, 104464.

Lei, B., Que, H.P., Hu, N., Niu, Z.J., Wang, H., 2002. Geochemistry and sedimentary environments of the Palaeozoic siliceous rocks in western Hubei. Sedimentary Geology and Tethyan Geology 22, 70–79 (in Chinese with English Abstract).

Leventhal, J.S., 1983. An interpretation of carbon and sulfur relationships in Black Sea sediments as indicators of environments of deposition. Geochimica et Cosmochimica Acta 47(1), 133–137.

Li, M., Shao, L.Y., Lu, J., Spiro, B., Wen, H.J., Li, Y.H., 2014. Sequence stratigraphy and paleogeography of the Middle Jurassic coal measures in the Yuqia coalfield, northern Qaidam Basin, northwestern China. AAPG Bulletin 98, 2531–2550.

Li, M., Shao, L.Y., Liu, L., Lu, J., Spiro, B., W, H.J., Li, Y.H., 2016. Lacustrine basin evolution and coal accumulation of the Middle Jurassic in the Saishiteng coalfield, northern Qaidam Basin, China. Journal of Palaeogeography 5(3), 205–220.

Li, Q., Wu, S., Xia, D., You, X., Zhang, H., Lu, H., 2020. Major and trace element geochemistry of the lacustrine organic-rich shales from the Upper Triassic Chang 7 Member in the southwestern Ordos Basin, China: implications for paleoenvironment and organic matter accumulation. Marine and Petroleum Geology 111, 852–867.

Li, J., Wang, S., 1990. Study of mudstone geochemistry in several bearing oil and gas closed basin, East, China. Journal of Lake Sciences 1, 30–36 (in Chinese with English abstract).

Li, Z.Q., Chen, J.L., Zou, H., Wang, C.S., Meng, Q.A., Liu, H.L., Wang, S.Z., 2021a. Mesozoic–Cenozoic tectonic evolution and dynamics of the Songliao Basin, NE Asia: Implications for the closure of the Paleo-Asian Ocean and Mongol-Okhotsk Ocean and subduction of the Paleo-Pacific Ocean. Earth-Science Reviews 103471.

Li, Y., Sun, P., Liu, Z., Xu, Y., Liu, R., Ma, L., 2021b. Factors controlling the distribution of oil shale layers in the Eocene Fushun Basin, NE China. Marine and Petroleum Geology 134, 105350.

Li, Y., 2019. The geochemical cycle analysis for the 3rd member of Quantou Formation (K_2q_3)-the 1st member of QingshankouFormation (K_2qn_1) deposited in the Late Cretaceous from the Songliao Basin. Master thesis. China University of Geosciences (Beijing), Beijing (in Chinese with English abstract).

Li, L., Liu, Z., Jiang, L., George, S. C., 2021c. Organic petrology and geochemistry of Lower Cretaceous lacustrine sediments in the Chaoyang Basin (Liaoning Province, northeast China): Influence of volcanic ash on algal productivity and oil shale formation. International Journal of Coal Geology 233, 103653.

Liao, Z.W., Hu, W.X., Cao, J., Wang, X.L., Hu, Z.Y., 2019. Petrologic and geochemical evidence for the formation of organic-rich siliceous rocks of the Late Permian Dalong Formation, Lower Yangtze region, southern China. Marine and Petroleum Geology 103, 41–54.

Liaaen-Jensen, S., 1978a. Chemistry of carotenoid pigments. In: Clayton, R.K., Sistrom, W.R. (Eds.), Photosynthetic Bacteria. Plenum Press, pp. 233–247.

Liaaen-Jensen, S., 1978b. Marine carotenoids. In: Faulkner, D.J., Fenical, W.H. (Eds.), Marine Natural Products. Academic Press, pp. 1–73.

Lima, A.L.C., Farrington, J.W., Reddy, C.M., 2005. Combustion-derived polycyclic aromatic hydrocarbons in the environment—a review. Environmental Forensics 6, 109–131.

Littke, R., 1993. Deposition of organic matter-rich sediments. In: Deposition, Diagenesis and Weathering of Organic Matter-Rich Sediments, pp. 12–45.

Liu, B., Wang, Y., Tian, S., Guo, Y., Wang, L., Yasin, Q., Yang, J., 2022a. Impact of thermal maturity on the diagenesis and porosity of lacustrine oil-prone shales: Insights from natural shale samples with thermal maturation in the oil generation window. International Journal of Coal Geology 261, 104079.

Liu, S., Liu, B., Tang, S., Zhao, C., Tan, F., Xi, Z., Du, F., 2022b. Palaeoenvironmental and tectonic controls on organic matter enrichment in the Middle Jurassic Dameigou Formation (Qaidam Basin, North China). Palaeogeography, Palaeoclimatology, Palaeoecology 585, 110747.

Liu, W., Liu, M., Yang, T., Liu, X., Them II, T. R., Wang, K., Bian, C., Meng, Q., Li, Y., Zeng, X., Zhao, W., 2022c. Organic matter accumulations in the Santonian-Campanian (Upper Cretaceous) lacustrine Nenjiang shale (K_2n) in the Songliao Basin, NE China: Terrestrial responses to OAE3?. International Journal of Coal Geology 260, 104069.

Liu, C., Wang, Z., Guo, Z., Hong, W., Dun, C., Zhang, X., Li, B., Wu, L., 2017a. Enrichment and distribution of shale oil in the Cretaceous Qingshankou Formation, Songliao Basin, northeast China. Marine and Petroleum Geology 86, 751–770.

Liu, B., Wang, H., Fu, X., Bai, Y., Bai, L., Jia, M., He, B., 2019. Lithofacies and depositional setting of a highly prospective lacustrine shale oil succession from the Upper Cretaceous Qingshankou Formation in the Gulong sag, northern Songliao Basin, northeast China. AAPG Bulletin 103(2), 405–432.

Liu, B., Bechtel, A., Sachsenhofer, R. F., Gross, D., Gratzer, R., Chen, X., 2017b. Depositional environment of oil shale within the second member of Permian Lucaogou Formation in the Santanghu Basin, Northwest China. International Journal of Coal Geology 175, 10–25.

Lopez, M., Gand, G., Garric, J., Körner, F., Schneider, J., 2008. The playa environments of the Lodève Permian basin (Languedoc-France). Journal of Iberian Geology 34, 29–56.

Luccisano, V., Cuny, G., Pradel, A., Fourel, F., Lécuyer, C., Pouillon, J. M., Lachat, k., Amiot, R., 2023. Palaeoenvironmental and palaeoecological reconstructions based on oxygen, carbon and sulfur isotopes of Early Permian shark spines from the French Massif central. Palaeogeography, Palaeoclimatology, Palaeoecology 628, 111760.

Luo, B., Wang, Y., Meng, Q., Yang, X., Li, X., Chen, N., 1991. Geochemistry of bicyclic alkanes in sediments, coal and crude oil. Science China B 34, 363–376

McLennan, S.M., 1993. Weathering and global denudation. The Journal of Geology 101, 295–303.

McLennan, S.M., Hemming, S., McDaniel, D.K., Hanson, G.N., 1993. Geochemical approaches to sedimentation, provenance and tectonics. In: Johnsson, M.J., Basu, A. (Eds.), Processes Controlling the Composition of Clastic Sediment: Geol, pp. 21–40 Soc. Am. Spec. Pap. 284.

Meyers, P. A., 1997. Organic geochemical proxies of paleoceanographic, paleolimnologic, and paleoclimatic processes. Organic Geochemistry 27(5–6), 213–250.

Michel, L. A., Tabor, N. J., Montañez, I. P., Schmitz, M. D., Davydov, V. I., 2015. Chronostratigraphy and paleoclimatology of the Lodève Basin, France: evidence for a pan-tropical aridification event across the Carboniferous–Permian boundary. Palaeogeography, Palaeoclimatology, Palaeoecology 430, 118–131.

Moldowan, J. M., Seifert, W. K., Gallegos, E. J., 1985. Relationship between petroleum composition and depositional environment of petroleum source rocks. AAPG Bulletin 69(8), 1255–1268.

Moldowan, J.M., 1984. C_{30}-steranes, novel markers for marine petroleums and sedimentary rocks. Geochimica et Cosmochimica Acta 48(12), 2767–2768.

Montero-Serrano, J.C., Föllmi, K.B., Adatte, T., Spangenberg, J.E., Tribovillard, N., Fantasia, A., Suan, G., 2015. Continental weathering and redox conditions during the early Toarcian Oceanic Anoxic Event in the northwestern Tethys: Insight from the Posidonia Shale section in the Swiss Jura Mountains. Palaeogeography, Palaeoclimatology, Palaeoecology 429, 83–99.

Moradi, A.V., Sari, A., Akkaya, P., 2016. Geochemistry of the Miocene oil shale (Hançili Formation) in the Çankiri-Çorum Basin, central Turkey: implications for Paleoclimate conditions, source-area weathering, provenance and tectonic setting. Sedimentary geology 341, 289–303.

Murillo, W. A., Horsfield, B., Garcin, Y., Vieth, A., Sachse, D., 2021. Compound-specific δ^2H and $\delta^{13}C$ values of *n*-alkanes as a tool to unravel complex petroleum mixtures in the South Viking Graben, Norway. Organic Geochemistry 152, 104167.

Mujal, E., Marchetti, L., 2020. Ichniotherium tracks from the Permian of France, and their implications for understanding the locomotion and palaeobiogeography of large diadectomorphs. Palaeogeography, Palaeoclimatology, Palaeoecology 547, 109698.

Murray, A.P., Summons, R.E., Boreham, C.J., Dowling, L.M., 1994. Biomarker and nalkane isotope profiles for Tertiary oils: relationship to source-rock depositional setting. Organic Geochemistry 22, 521–542.

Müller, A. B., Strauss, H., Hartkopf-Fröder, C., Littke, R., 2006. Reconstructing the evolution of the latest Pennsylvanian–earliest Permian Lake Odernheim based on stable isotope geochemistry and palynofacies: A case study from the Saar-Nahe Basin, Germany. Palaeogeography, Palaeoclimatology, Palaeoecology 240(1–2), 204–224.

Nesbitt, H.W., Young, G.M., 1982. Early Proterozoic climates and plate motions inferred from major element chemistry of lutites. Nature 299, 715–717.

Nesbitt, H.W., 2003. Petrogenesis of siliciclastic sediment and sedimentary rocks. In: Lentz, D.R. (Ed.), Geochemistry of Sediment and Sedimentary Rocks: Evolutionary Considerations to Mineral-Deposit-Forming Environments, pp. 39–51 Geol. Assoc. Can.

Nesbitt, H.W., Fedo, C.M., Young, G.M., 1997. Quartz and feldspar stability, steady and non-steady-state weathering, and petrogenesis of siliciclastic sands and muds. The Journal of Geology 105, 173–192.

Obreht, I., Zeeden, C., Schulte, P., Hambach, U., Eckmeier, E., Timar-Gabor, A., Lehmkuhl, F., 2015. Aeolian dynamics at the Orlovat loess–paleosol sequence, northern Serbia, based on detailed textural and geochemical evidence. Aeolian Research 18, 69–81.

Pan, X., Wang, Z., Li, Q., Gao, J., Zhu, L., Liu, W., 2020a. Sedimentary environments and mechanism of organic matter enrichment of dark shales with low TOC in the Mesoproterozoic Cuizhuang Formation of the Ordos Basin: Evidence from petrology, organic geochemistry, and major and trace elements. Marine and Petroleum Geology 122, 104695.

Pan, Y., Huang, Z., Li, T., Guo, X., Xu, X., Chen, X., 2020b. Environmental response to volcanic activity and its effect on organic matter enrichment in the Permian Lucaogou Formation of the Malang Sag, Santanghu Basin, Northwest China. Palaeogeography, Palaeoclimatology, Palaeoecology 560, 110024.

Panahi, A., Young, G.M., Rainbird, R.H., 2000. Behavior of major and trace elements (including REE) during Paleoproterozoic pedogenesis and diagenetic alteration of an Archean granite near Ville Marie, Québec, Canada. Geochimica et Cosmochimica Acta 64, 2199–2220.

Pang, X., Zhao, W., Su, A., Zhang, S., Li, M., Dang, Y., Xu, F., Zhou, R., Zhang, D., Xu, Z., Guan, Z., Chen, J., Li, S., 2005. Geochemistry and origin of the giant Quaternary shallow gas accumulations in the eastern Qaidam Basin, NW China. Organic geochemistry 36, 1636–1649.

Patterson, G.W., 1971. The distribution of sterols in algae. Lipids 6, 120–127.

Pawlowska, M.M., Butterfield, N.J., Brocks, J.J., 2013. Lipid taphonomy in the Proterozoic and the effect of microbial mats on biomarker preservation. Geology 41(2), 103–106.

Peters, K.E., Walters, C.C., Moldowan, J.M., 2005. The Biomarker Guide: Column 2, Biomarkers and Isotopes in Petroleum Systems and Earth History, 2nd ed. Cambridge University Press, Cambridge.

Peters, K.E., Moldowan, J.M., 1993. The Biomarker Guide: Interpreting Molecular Fossils in Petroleum and Ancient Sediments. Prentice Hall, Englewood Cliffs, NJ.

Peters, K.E., Moldowan, J.M., 1991. Effects of source, thermal maturity, and biodegradation on the distribution and isomerization of homohopanes in petroleum. Organic Geochemistry 17, 47–61.

Philp, R.P., Gilbert, T.D., 1986. Biomarker distributions in Australian oils predominantly derived from terrigenous source material. Organic Geochemistry 10, 73–84.

Pickel, W., Kus, J., Flores, D., Kalaitzidis, S., Christanis, K., Cardott, B.J., Misz- Kennan, M., Rodrigues, S., Hentschel, A., Hamor-Vido, M., Crosdale, P., Wagner, N., ICCP, 2017. Classification of liptinite–ICCP System 1994. International Journal of Coal Geology 169, 40–61.

Powell, T. G., 1986. Petroleum geochemistry and depositional setting of lacustrine source rocks. Marine and Petroleum Geology 3(3), 200–219.

Pochat, S., Van Den Driessche, J., 2011. Filling sequence in Late Paleozoic continental basins: a chimera of climate change? A new light shed given by the Graissessac–Lodéve Basin (SE France). Palaeogeography, Palaeoclimatology, Palaeoecology 302, 170–186.

Poplin, C., Sotty, D., Janvier, P., 2001. Un Myxinoïde (Craniata, Hyperotreti) dans le Konservat-Lagerstätte Carbonifère supérieur de Montceau-les-Mines (Allier, France). Comptes Rendus de l'Académie des Sciences-Series IIA-Earth and Planetary Science, 332(5), 345–350.

Qiao, J., Littke, R., Grohmann, S., Zhang, C., Jiang, Z., Strauss, H., Zieger, L., 2022. Climatic and environmental conditions during the Pleistocene in the Central Qaidam Basin, NE Tibetan Plateau: Evidence from GDGTs, stable isotopes and major and trace elements of the Qigequan Formation. International Journal of Coal Geology 254, 103958.

Qiao, J., Baniasad, A., Zieger, L., Zhang, C., Luo, Q., Littke, R., 2021a. Paleo-depositional environment, origin and characteristics of organic matter of the Triassic Chang 7 Member of the Yanchang Formation throughout the mid-western part of the Ordos Basin, China. International Journal of Coal Geology 237, 103636.

Qiao, J., Grohmann, S., Baniasad, A., Zhang, C., Jiang, Z., Littke, R., 2021b. High microbial gas potential of Pleistocene lacustrine deposits in the central Qaidam Basin, China: an organic geochemical and petrographic assessment. International Journal of Coal Geology 245, 103818.

Qin, J., Wang, S., Sanei, H., Jiang, C., Chen, Z., Ren, S., Xu, X., Yang, J., Zhong, N., 2018. Revelation of organic matter sources and sedimentary environment characteristics for shale gas formation by petrographic analysis of middle Jurassic Dameigou formation, northern Qaidam Basin, China. International Journal of Coal Geology 195, 373–385.

Quan, Y., Hao, F., Liu, J., Zhao, D., Tian, J. and Wang, Z., 2017. Source rock deposition controlled by tectonic subsidence and climate in the western Pearl River Mouth Basin, China: Evidence from organic and inorganic geochemistry. Marine and Petroleum Geology 79, 1–17.

Radke, M., Welte, D.H., Willsch, H., 1986. Maturity parameters based on aromatic hydrocarbons: Influence of the organic matter type. Organic Geochemistry 10(1–3), 51–63.

Radke, M., Rullkötter, J., Vriend, S.P., 1994. Distribution of naphthalenes in crude oils from the Java Sea: source and maturation effects. Geochimica et Cosmochimica Acta 58(17), 3675–3689.

Radke, M., Welte, D.H., 1983. The methylphenanthrene index (MPI): a maturity parameter based on aromatic hydrocarbons. In: Bjorøy, M., Albrecht, C., Cornford, C., et al. (Eds.), Adv. Org. Geochem., 10 New York, USA, John Wiley & Sons, pp. 504–512.

Radke, M., Willsch, H., Leythaeuser, D., Teichmüller, M., 1982. Aromatic components of coal: relation of distribution pattern to rank. Geochimica et Cosmochimica Acta 46, 1831–1848.

Ratcliffe, K. T., Wright, A. M., Hallsworth, C., Morton, A., Zaitlin, B. A., Potocki, D., Wray, D., 2004. An example of alternative correlation techniques in a low-accommodation setting, nonmarine hydrocarbon system: The (Lower Cretaceous) Mannville Basal Quartz succession of southern Alberta. AAPG Bulletin 88(10), 1419–1432.

Ratcliffe, K.T., Wright, A.M., Montgomery, P., Palfrey, A., Vonk, A., Vermeulen, J., Barrett, M., 2010. Application of chemostratigraphy to the Mungaroo Formation, the Gorgon field, offshore northwest Australia. The APPEA Journal 371–388.

Ren, Y., Chen, D., Kelsey, D.E., Gong, X., Liu, L., 2017. Petrology and Geochemistry of the lawsonite (pseudomorph)-bearing eclogite in Yuka terrane, North Qaidam UHPM belt: An eclogite facies metamorphosed oceanic slice. Gondwana Research 42, 220–242.

Rieu, R., Allen, P.A., Plötze, M., Pettke, T., 2007. Climatic cycles during a Neoproterozoic "snowball" glacial epoch. Geology 35, 299–302.

Rimmer, S.M., Thompson, J.A., Goodnight, S.A., Robl, T.L., 2004. Multiple controls on the preservation of organic matter in Devonian–Mississippian marine black shales: geochemical and petrographic evidence. Palaeogeography, Palaeoclimatology, Palaeoecology 215, 125–154.

Rimmer, S.M., 2004. Geochemical paleoredox indicators in devonian–Mississippian black shales, central appalachian basin (USA). Chemical Geology 206, 373–391.

Ritts, B.D., Biffi, U., 2001. Mesozoic northeast Qaidam basin: response to contractional reactivation of the Qilian Shan, and implications for the extent of Mesozoic intracontinental deformation in central Asia. Geological Society of America Memoirs 194, 293–316.

Romero-Viana, L., Kienel, U., Sachse, D., 2012. Lipid biomarker signatures in a hypersaline lake on Isabel Island (Eastern Pacifc) as a proxy for past rainfall anomaly (1942–2006 AD). Palaeogeography, Palaeoclimatology, Palaeoecology 350, 49–61.

Ross, D.J.K., Bustin, R.M., 2009. Investigating the use of sedimentary geochemical proxies for paleoenvironment interpretation of thermally mature organic-rich strata: examples from the Devonian-Mississippian shales, Western Canadian Sedimentary Basin. Chemical geology 260, 1–19.

Roy, D.K., Roser, B.P., 2013. Climatic control on the composition of Carboniferous–Permian Gondwana sediments, Khalaspir basin, Bangladesh. Gondwana Research 23(3), 1163–1171.

Röth, J., Baniasad, A., Froidl, F., Ostlender, J., Boreham, C., Hall, L., Littke, R., 2023. The Birkhead and Murta formations—organic geochemistry and organic petrography of Mesozoic fluvio-lacustrine source rocks in the Eromanga Basin, central Australia. International Journal of Earth Sciences 112(1), 265–295.

Sachsenhofer, R.F., Popov, S.V., Akhmetiev, M.A., Bechtel, A., Gratzer, R., Groß, D., Horsfield, B., Rachetti, A., Rupprecht, B., Schaffar, W.B.H., Zaporozhets, N.I., 2017. The type section of the

maikop group (Oligocene-lower miocene) at the belaya river (north Caucasus): depositional environment and hydrocarbon potential. AAPG Bulletin 101, 289–319.

Sageman, B.B., Murphy, A.E., Werne, J.P., Ver Straeten, C.A., Hollander, D.J., Lyons, T.W., 2003. A tale of shales: the relative roles of production, decomposition, and dilution in the accumulation of organic-rich strata, Middle–Upper Devonian, Appalachian basin. Chemical geology 195, 229–273.

Schultze, H.P., 2009. Interpretation of marine and freshwater paleoenvironments in Permo-Carboniferous deposits. Palaeogeography, Palaeoclimatology, Palaeoecology 281, 126–136.

Schneider, J. W., Körner, F., Roscher, M., Kroner, U., 2006. Permian climate development in the northern peri-Tethys area—the Lodève basin, French Massif Central, compared in a European and global context. Palaeogeography, Palaeoclimatology, Palaeoecology 240(1–2), 161–183.

Schwark, L., Frimmel, A., 2004. Chemostratigraphy of the Posidonia Black Shale, SW-Germany: II. Assessment of extent and persistence of photic-zone anoxia using aryl isoprenoid distributions. Chemical Geology 206(3–4), 231–248.

Schwarzbauer, J., Littke, R., Meier, R., Strauss, H., 2013. Stable carbon isotope ratios of aliphatic biomarkers in Late Palaeozoic coals. International Journal of Coal Geology 107, 127–140.

Schouten, S., Ozdirekcan, S., van der Meer, M.T.J., Blokker, P., Baas, M., Hayes, J.M., Sinninghe Damsté, J.S., 2008. Evidence for substantial intramolecular heterogeneity in the stable carbon isotopic composition of phytol in photoautotrophic organisms. Organic Geochemistry 39, 135–146.

Schwab, V. F., Spangenberg, J. E., 2007. Molecular and isotopic characterization of biomarkers in the Frick Swiss Jura sediments: A palaeoenvironmental reconstruction on the northern Tethys margin. Organic Geochemistry 38(3), 419–439.

Seifert, W.K., Moldowan, J.M., 1980. The effect of thermal stress on source-rock quality as measured by hopane stereochemistry. Physics and Chemistry of the Earth 12, 229–237.

Seifert, W. K., Moldowan, J. M., 1986. Use of biological markers in petroleum exploration. Methods in Geochemistry and Geophysics 24, 261–290.

Sepúlveda, J., Wendler, J., Leider, A., Kuss, H.J., Summons, R.E., Hinrichs, K.U., 2009. Molecular isotopic evidence of environmental and ecological changes across the Cenomanian–Turonian boundary in the Levant Platform of central Jordan. Organic Geochemistry 40, 553–568.

Shao, L.Y., Li, M., Li, Y., Zhang, Y., Lu, J., Zhang, W., Tian, Z., Wen, H., 2014. Geological characteristics and controlling factors of shale gas in the Jurassic of the northern Qaidam Basin. Earth Science Frontiers 21, 311–322 (in Chinese with English abstract).

Shang, X., Shao, L., Zhang, W., Lv, J., Wang, W., Li, Y., Wen, H., 2018. Sequence paleogeography and coal accumulation of the Early-Middle Jurassic in central Qilian Mountain belt (Muli Basin), Qinghai Province, northwestern China. AAPG Bulletin 102(9), 1739–1762.

Shang, F., Zhu, Y., Hu, Q., Wang, Y., Li, Y., Li, W., Liu, R., Gao, H., 2020. Factors controlling organic-matter accumulation in the Upper Ordovician-Lower Silurian organic-rich shale on the

northeast margin of the Upper Yangtze platform: Evidence from petrographic and geochemical proxies. Marine and Petroleum Geology 121, 104597.

Shiea, J., Brassell, S.C., Ward, D.M., 1990. Mid-chain branched mono- and dimethyl alkanes in hot spring cyanobacterial mats: a direct biogenic source for branched alkanes in ancient sediments? Organic Geochemistry 15, 223–231.

Simoneit, B.R.T., 1985. Cyclic terpenoids in the geosphere. In: Johns, R.B. (Ed.), Methods in Geochemistry and Geophysics, vol. 25. Elsevier, pp. 43–99.

Simoneit, B.R.T., 1977. Diterpenoid compounds and other lipids in deep-sea sediments and their geochemical significance. Geochimica et Cosmochimica Acta 41, 463–476.

Sim M. S., Bosak T., Ono S., 2011. Large sulfur isotope fractionation does not require disproportionation. Science 333(6038), 74–77.

Sinninghe Damsté, J.S., Kenig, F., Koopmans, M.P., Köster, J., Schouten, S., Hayes, J.M., de Leeuw, J.W., 1995. Evidence for gammacerane as an indicator of water column stratification. Geochimica et Cosmochimica Acta 59, 1895–1900.

Smith, B.N., Epstein, S., 1971. Two categories of $^{13}C/^{12}C$ ratios for higher plants. Plant physiology 47, 380–384.

Song, D., Chen, Y., Wang, T., Li, M., Li, P., 2021. Organic geochemical compositions of Mesoproterozoic source rocks in the Yanliao Rift, Northern China. Marine and Petroleum Geology 123, 104740.

Song, Y., Li, S., Hu, S., 2019. Warm-humid paleoclimate control of salinized lacustrine organic-rich shale deposition in the Oligocene Hetaoyuan Formation of the Biyang Depression, East China. International Journal of Coal Geology 202, 69–84.

Song, J., Littke, R., Weniger, P., 2017. Organic geochemistry of the lower Toarcian Posidonia Shale in NW Europe. Organic Geochemistry 106, 76–92.

Strachan, M.G., Alexander, R., Kagi, R.I., 1988. Trimethylnaphthalenes in crude oils and sediments: effects of source and maturity. Geochimica et Cosmochimica Acta 52, 1255–1264.

Summons, R.E., Jahnke, L.L., Hope, J.M., Logan, G.A., 1999. 2α-methylhopanoids as biomarkers for cyanobacterial oxygenic photosynthesis. Nature 400, 554–557.

Suttner, L.J., Dutta, P.K., 1986. Alluvial sandstone composition and paleoclimate; I, Framework mineralogy. Journal of Sedimentary Research 56(3), 329–345.

Talbot, M. R., 1988. The origins of lacustrine oil source rocks: evidence from the lakes of tropical Africa. Geological Society, London, Special Publications 40(1), 29–43.

Tang, L., Song, Y., Pang, X., Jiang, Z., Guo, Y., Zhang, H., Pan, Z., Jiang, H., 2020. Effects of paleo sedimentary environment in saline lacustrine basin on organic matter accumulation and preservation: a case study from the Dongpu Depression, Bohai Bay Basin, China. Journal of Petroleum Science and Engineering 185, 106669.

Tang, L., Jin, Z., Zhang, M., You, F., Zhang, B., Luo, J., 2000. Tectonic evolution and oil (gas) pool-forming stage in northern Qaidam basin. Petroleum Exploration and Development 27(2), 36–39 (in Chinese).

Tao, S., Xu, Y., Tang, D., Xu, H., Li, S., Chen, S., Liu, W., Cui, Y., Gou, M., 2017. Geochemistry of the Shitoumei oil shale in the Santanghu Basin, Northwest China: implications for paleoclimate conditions, weathering, provenance and tectonic setting. International Journal of Coal Geology 184, 42–56.

Tapponnier, P., Xu, Z., Roger, F.,Meyer, B., Arnaud, N.,Wittlinger, G., Yang, J., 2001. Oblique stepwise rise and growth of the Tibet Plateau. Science 294, 1671–1677.

Taylor, G.H., Teichmüller, M., Davis, A., Diessel, C.F.K., Littke, R., Robert, P., 1998. Organic Petrology. Gerbrüder Borntraeger, Berlin, Stuttgart.

Taylor, S.R., McLennan, S.M., 1985. The Continental Crust: its Composition and Evolution. Blackwell, Oxford, p. 312.

ten Haven, H.L., de Leeuw, J.W., Rulkotter, J., Sinninghe Damsté, J.S., 1987. Restricted utility of pristane/phytane ratio as a palaeoenvironmental indicator. Nature 330, 641–643.

ten Haven, H.L., Rohmer, M., Rullkötter, J., Bisseret, P., 1989. Tetrahymanol, the most likely precursor of gammacerane, occurs ubiquitously in marine sediments. Geochimica et Cosmochimica Acta 53, 3073–3079.

Tian, J., Hao, F., Zhou, X., Zou, H., Lan, L., 2014. Charging of the Penglai 9-1 oil field, Bohai Bay basin, China: Functions of the delta on accumulating petroleum. Marine and Petroleum Geology 57, 603–618.

Tribovillard, N., Algeo, T.J., Lyons, T., Riboulleau, A., 2006. Trace metals as paleoredox and paleoproductivity proxies: an update. Chemical geology 232, 12–32.

Tribovillard, N., Algeo, T.J., Baudin, F., Riboulleau, A., 2012. Analysis of marine environmental conditions based on molybdenum–uranium covariation—Applications to Mesozoic paleoceanography. Chemical Geology 324, 46–58.

Tulipani, S., Grice, K., Greenwood, P. F., Schwark, L., Böttcher, M. E., Summons, R. E., Foster, C. B., 2015. Molecular proxies as indicators of freshwater incursion-driven salinity stratification. Chemical Geology 409, 61–68.

Tyson, R.V., 2001. Sedimentation rate, dilution, preservation and total organic carbon: some results of a modelling study. Organic Geochemistry 32, 333–339.

Tyson, R.V., 2005. The “productivity versus preservation” controversy; cause, flaws, and resolution. In: In: Harris, N.B. (Ed.), Deposition of Organic-Carbon-Rich Sediments: Models, Mechanisms, and Consequences, vol. 82. Society for Sedimentary Geology (SEPMSSG) Special Publication, pp. 17–33.

van Aarssen, B.G.K., Alexander, R., Kagi, R.I., 2000. Higher plant biomarkers reflect palaeovegetation changes during Jurassic times. Geochimica et Cosmochimica Acta 64, 1417–1424.

van Aarssen, B.G., Bastow, T.P., Alexander, R., Kagi, R.I., 1999. Distributions of methylated naphthalenes in crude oils: indicators of maturity, biodegradation and mixing. Organic Geochemistry 30(10), 1213–1227.

Venkatesan, M.I., 1989. Tetrahymanol: its widespread occurrence and geochemical significance. Geochimica et Cosmochimica Acta 53, 3095–3101.

Volk, H., George, S.C., Middleton, H., Schofield, S., 2005. Geochemical comparison of fluid inclusion and present-day oil accumulations in the Papuan Foreland–evidence for previously unrecognised petroleum source rocks. Organic Geochemistry 36, 29–51.

Volkman, J.K., Maxwell, J.R., 1986. Acyclic isoprenoids as biological markers. In: Johns, R.B. (Ed.), Biological Markers in the Sedimentary Record. Elsevier, New York, pp. 1–42.

Volkman, J.K., 1986. A review of sterol markers for marine and terrigenous organic matter. Organic Geochemistry 9, 83–99.

Volkman, J.K., Barrett, S.M., Blackburn, S.I., Mansour, M.P., Sikes, E.L., Gelin, F., 1998. Microalgal biomarkers: a review of recent research developments. Organic Geochemistry 29, 1163–1179.

Wang, Y., Xu, S., Hao, F., Poulton, S.W., Zhang, Y., Guo, T., Lu, Y., Bai, N., 2021. Arid climate disturbance and the development of salinized lacustrine oil shale in the Middle Jurassic Dameigou Formation, Qaidam Basin, northwestern China. Palaeogeography, Palaeoclimatology, Palaeoecology 577, 110533.

Wang, J.C., Hu, Y., Liu, Y.T., 2006. Control of multigeneration rotary normal faults on sediment migration in rift basin: An example from the Early and Middle Jurassic Qaidam Basin. Acta Geologica Sinica 80, 1141–1148 (in Chinese).

Wang, C., Feng, Z., Zhang, L., Huang, Y., Cao, K., Wang, P., Zhao, B. 2013a. Cretaceous paleogeography and paleoclimate and the setting of SKI borehole sites in Songliao Basin, northeast China. Palaeogeography, Palaeoclimatology, Palaeoecology 385, 17–30.

Wang, C., Scott, R.W., Wan, X., Graham, S.A., Huang, Y., Wang, P., Wu, H., Dean, W.E., Zhang, L., 2013b. Late Cretaceous climate changes recorded in Eastern Asian lacustrine deposits and North American Epieric sea strata. Earth-Science Reviews 126, 275–299.

Wang, P., Huang, Y., Wang, C., Feng, Z., Huang, Q., 2013c. Pyrite morphology in the first member of the Late Cretaceous Qingshankou formation, Songliao Basin, northeast China. Palaeogeography, Palaeoclimatology, Palaeoecology 385, 125–136.

Wang, Y.D., Mosbrugger, V., Zhang, H., 2005. Early to Middle Jurassic vegetation and climatic events in the Qaidam Basin, Northwest China. Palaeogeography, Palaeoclimatology, Palaeoecology 224, 200–216.

Wang, T., Yang, S., Duan, S., Chen, H., Liu, H., Cao, J., 2015. Multi-stage primary and secondary hydrocarbon migration and accumulation in lacustrine Jurassic petroleum systems in the northern Qaidam Basin, NW China. Marine and Petroleum Geology 62, 90–101.

Wang, P., Du, Y., Yu, W., Algeo, T.J., Zhou, Q., Xu, Y., Qi, L., Yuan, L., Pan, W., 2020. The chemical index of alteration (CIA) as a proxy for climate change during glacial-interglacial transitions in Earth history. Earth-Science Reviews 201, 103032.

Wang, T.G., Simoneit, B.R.T., 1995. Tricyclic terpanes in Precambrian bituminous sandstone from the eastern Yanshan region, North China. Chemical geology 120, 155–170.

Wang, Z., Wang, J., Fu, X., Zhan, W.Z., Yu, F., Feng, X., Song, C., Che, W., Zeng, S., 2017. Organic material accumulation of Carnian mudstones in the North Qiangtang Depression, eastern Tethys: controlled by the paleoclimate, paleoenvironment, and provenance. Marine and Petroleum Geology 88, 440–457.

Wang, J., Sun, P., Bai, Y., Liu, Z., Cheng, R., Li, Y., 2022. Carbon isotopes of n-alkanes allow for estimation of the CO2 pressure in the Early Jurassic-A case study from lacustrine shale and cannel boghead in the Dachanggou Basin, Xinjiang, Northwest China. Palaeogeography, Palaeoclimatology, Palaeoecology 607, 111252.

Warren, J.K., 2016. Evaporites. Springer, Berlin.

Wedepohl, K.H., 1971. Environmental influences on the chemical composition of shales and clays. Physics and Chemistry of the Earth 8(71), 305–333.

Wei, W., Algeo, T.J., 2020. Elemental proxies for paleosalinity analysis of ancient shales and mudrocks. Geochimica et Cosmochimica Acta 287, 341–366.

Wei, W., Algeo, T.J., Lu, Y., Lu, Y., Liu, H., Zhang, S., Peng, L., Zhang, J., Chen, L., 2018. Identifying marine incursions into the Paleogene Bohai Bay Basin lake system in northeastern China. International Journal of Coal Geology 200, 1–17.

Welander, P.V., Summons, R.E., 2012. Discovery, taxonomic distribution, and phenotypic characterization of a gene required for 3-methylhopanoid production. Proceedings of the National Academy of Sciences 109(32), 12905–12910.

Wen, Z., Ruiyong, W., Radke, M., Qingyu, W., Guoying, S., Zhili, L., 2000. Retene in pyrolysates of algal and bacterial organic matter. Organic Geochemistry 31, 757–762.

Wilkin, R.T., Barnes, H.L., Brantley, S.L., 1996. The size distribution of framboidal pyrite in modern sediments: an indicator of redox conditions. Geochimica et Cosmochimica Acta Acta 60(20), 3897–3912.

Wignall, P.B., Twitchett, R.J., 1996. Oceanic anoxia and the end Permian mass extinction. Science 272, 1155–1158.

Wu, Z., Littke, R., Baniasad, A., Yang, Z., Tang, Z., Grohmann, S., 2023. Geochemistry and petrology of petroleum source rocks in the Upper Cretaceous Qingshankou Formation, Songliao Basin, NE China. International Journal of Coal Geology 270, 104222.

Wu, Z., Grohmann, S., Littke, R., Guo, T., He, S., Baniasad, A., 2022. Organic petrologic and geochemical characterization of petroleum source rocks in the Middle Jurassic Dameigou Formation,

Qaidam Basin, northwestern China: Insights into paleo-depositional environment and organic matter accumulation. International Journal of Coal Geology 259, 104038.

Wu, Z., Grohmann, S., Littke, R., 2024. Geochemistry and petrology of Early Permian lacustrine shales in the Lodève Basin, Southern France: Depositional history, organic matter accumulation and thermal maturity. International Journal of Coal Geology 284, 104469.

Wu, H., Zhang, S., Jiang, G., Huang, Q., 2009. The floating astronomical time scale for the terrestrial Late Cretaceous Qingshankou Formation from the Songliao Basin of Northeast China and its stratigraphic and paleoclimate implications. Earth and Planetary Science Letters 278, 308–323.

Wygrala, B.P., 1989. Integrated Study of an Oil Field in the Southern Po Basin, Northern Italy. PhD Thesis. University of Cologne, Germany.

Xi, D., Wan, X., Feng, Z., Li, S., Feng, Z., Jia, J., Jing, X., Si, W., 2011. Discovery of Late Cretaceous foraminifera in the Songliao Basin: Evidence from SK-1 and implications for identifying seawater incursions. Chinese Science Bulletin 56(3), 253-256.

Xie, X.N., Jiao, J.J., Tang, Z.H., Zheng, C.M., 2003. Evolution of abnormally low pressure and its implications for the hydrocarbon system in the Southeast Uplift zone of Songliao Basin, China. AAPG Bulletin 87, 99–119.

Xie, W., Tan, J., Wang, W., Schulz, H.M., Liu, Z., Kang, X., Shahzad, A., Jan, I. U., 2021. Middle Jurassic lacustrine source rocks controlled by an aridification event: A case study in the northern Qaidam Basin (NW China). International Journal of Coal Geology 242, 103779.

Xu, J.J., Liu, Z.J., Bechtel, A., Meng, Q.T., Sun, P.C., Jia, J.L., Cheng, L.J., Song, Y., 2015. Basin evolution and oil shale deposition during Upper Cretaceous in the Songliao Basin (NE China): implication from sequence stratigraphy and geochemistry. International Journal of Coal Geology 149, 9–23.

Xu, H., George, S.C., Hou, D., 2019a. Algal-derived polycyclic aromatic hydrocarbons in Paleogene lacustrine sediments from the Dongying Depression, Bohai Bay Basin, China. Marine and Petroleum Geology 102, 402–425.

Xu, C., Shan, X., He, W., Zhang, K., Rexiti, Y., Su, S., Liang, C., Zou, X., 2021. The influence of paleoclimate and a marine transgression event on organic matter accumulation in lacustrine black shales from the Late Cretaceous, southern Songliao Basin, Northeast China. International Journal of Coal Geology 246, 103842.

Xu, J., Liu, Z., Bechtel, A., Sachsenhofer, R. F., Jia, J., Meng, Q., Sun, P., 2019b. Organic matter accumulation in the Upper Cretaceous Qingshankou and Nenjiang Formations, Songliao Basin (NE China): Implications from high-resolution geochemical analysis. Marine and Petroleum Geology 102, 187–201.

Xu, H., George, S. C., Hou, D., 2019c. The occurrence of isorenieratane and 24-*n*-propylcholestanes in Paleogene lacustrine source rocks from the Dongying Depression, Bohai Bay

Basin: Implications for bacterial sulfate reduction, photic zone euxinia and seawater incursions. Organic Geochemistry 127, 59–80.

Xu, Z., Wang, Y., Jiang, S., Fang, C., Liu, L., Wu, K., Luo, Q., Li, X., Chen, Y., 2022. Impact of input, preservation and dilution on organic matter enrichment in lacustrine rift basin: A case study of lacustrine shale in Dehui Depression of Songliao Basin, NE China. Marine and Petroleum Geology 135, 105386.

Yan, D., Chen, D., Wang, Q., Wang, J., 2010. Large-scale climatic fluctuations in the latest Ordovician on the Yangtze block, south China. Geology 38(7), 599–602.

Yandoka, B.M.S., Abdullah, W.H., Abubakar, M., Hakimi, M.H., Adegoke, A.K., 2015. Geochemical characterisation of Lower Cretaceous lacustrine sediments of Bima Formation, Yola Sub-basin, Northern Benue Trough, NE Nigeria: Organic matter input, preservation, paleoenvironment and palaeoclimatic conditions. Marine and Petroleum Geology 61, 82–94.

Yang, P., Xie, Z., Yuan, X., Zhu, S., Yi, D., 2006a. Palaeoecological characteristics and its palaeogeographic significance of the Jurassic in northern margin of Qaidam Basin. Journal of palaeogeography 8(2), 165–173.

Yang, S.Y., Li, C., Cai, J., 2006b. Geochemical compositions of core sediments in eastern China: implication for Late Cenozoic palaeoenvironmental changes. Palaeogeography, Palaeoclimatology, Palaeoecology 229(4), 287–302.

Yang, P., Yang, Y., Ma, L., Dong, N., Yuan, X., 2007. Evolution of the Jurassic sedimentary environment in northern margin of Qaidam Basin and its significance in petroleum geology. Petroleum Exploration and Development 34, 160–164 (in Chinese with English abstract).

Yang, X., Guo, S., 2021. Reservoirs characteristics and environments evolution of lower permian transitional shale in the Southern North China Basin: Implications for shale gas exploration. Journal of Natural Gas Science and Engineering 96, 104282.

Yang, Y.T., 2013. An unrecognized major collision of the Okhotomorsk Block with East Asia during the Late Cretaceous, constraints on the plate reorganization of the Northwest Pacific. Earth and Planetary Science Letters 126, 96–115.

Yunker, M.B., Macdonald, R.W., Snowdon, L.R., Fowler, B.R., 2011. Alkane and PAH biomarkers as tracers of terrigenous organic carbon in Arctic Ocean sediments. Organic Geochemistry 42, 1109–1146.

Yunker, M.B., Macdonald, R.W., Ross, P.S., Johannessen, S.C., Dangerfield, N., 2015. Alkane and PAH provenance and potential bioavailability in coastal marine sediments subject to a gradient of anthropogenic sources in British Columbia, Canada. Organic Geochemistry 89–90, 80–116.

Zakir Hossain, H.M., Sampei, Y., Roser, B.P., 2013. Polycyclic aromatic hydrocarbons (PAHs) in late Eocene to early Pleistocene mudstones of the Sylhet succession, NE Bengal Basin, Bangladesh: implications for source and paleoclimate conditions during Himalayan uplift. Organic Geochemistry 56, 25–39.

Zakrzewski, A., Kosakowski, P., Waliczek, M., Kowalski, A., 2020. Polycyclic aromatic hydrocarbons in Middle Jurassic sediments of the Polish Basin provide evidence for high-temperature palaeo-wildfires. Organic Geochemistry 145, 104037.

Zhang, P., Misch, D., Meng, Q., Sachsenhofer, R.F., Liu, Z., Jia, J., Gao, F., Bechtel, A., Hu, F., 2022. Lateral changes of organic matter preservation in the lacustrine Qingshankou Formation (Cretaceous Songliao Basin, NE China): evidence for basin segmentation. International Journal of Coal Geology 254, 103984.

Zhang, Y., Li, Y., Guo, W., Li, Y., Dang, H., 2020. Differential evolution and the influencing factors of low-maturity terrestrial shale with different types of kerogen: a case study of a Jurassic shale from the northern margin of Qaidam Basin, China. International Journal of Coal Geology 230, 103591.

Zhang, Q., Littke, R., Zieger, L., Shabani, M., Tang, X., Zhang, J., 2019. Ediacaran, Cambrian, Ordovician, Silurian and Permian shales of the Upper Yangtze Platform, South China: deposition, thermal maturity and shale gas potential. International Journal of Coal Geology 216, 103281.

Zhang, C., 2020. Late Mesozoic tectonic–sedimentary evolution of the northern Qaidam Basin and its dynamic meaning. Ph.D. Thesis. Zhejiang University, Hangzhou, Zhejiang (in Chinese with English abstract).

Zhang, P., Misch, D., Hu, F., Kostoglou, N., Sachsenhofer, R. F., Liu, Z., Meng, Q., Bechtel, A., 2021a. Porosity evolution in organic matter-rich shales (Qingshankou Fm.; Songliao Basin, NE China): Implications for shale oil retention. Marine and Petroleum Geology 130, 105139.

Zhang, K., Liu, R., Liu, Z., 2021b. Sedimentary sequence evolution and organic matter accumulation characteristics of the Chang 8–Chang 7 members in the Upper Triassic Yanchang Formation, southwest Ordos Basin, central China. Journal of Petroleum Science and Engineering 196, 107751.

Zhao, Z., Littke, R., Zieger, L., Hou, D., Felix, F., 2020. Depositional environment, thermal maturity and shale oil potential of the cretaceous Qingshankou Formation in the eastern Changling Sag, Songliao Basin, China: an integrated organic and inorganic geochemistry approach. International Journal of Coal Geology 232, 103621.

Zhao, J., Wan, X.Q., Xi, D.P., Jing, X., Li, W., Huang, Q.H., Zhang, J.Y., 2014. Late Cretaceous palynology and paleoclimate change: evidence from the SK1 (South) core, Songliao Basin, NE China. Science China Earth Sciences 57, 2985–2997.

Zhao, Z., Zieger, L., Littke, R., Schwarzbauer, J., 2022a. Structural and chemical variability and provenance of lacustrine organic matter in the Miocene Nördlinger Ries post-impact sediments. International Journal of Coal Geology 262, 104112.

Zhao, Z.Y., Zhao, J.H., Wang, H.J., Liao, J.D., Liu, C.M., 2007. Distribution characteristics and applications of trace elements in Junggar Basin. Natural Gas Exploration and Development 30, 30–33 (in Chinese with English abstract).

Zhao, Z., Grohmann, S., Zieger, L., Dai, W., Littke, R., 2022b. Evolution of organic matter quantity and quality in a warm, hypersaline, alkaline lake: The example of the Miocene Nördlinger Ries impact crater, Germany. Frontiers in Earth Science 10, 989478.

Zheng, T., Zieger, L., Baniasad, A., Grohmann, S., Hu, T., Littke, R., 2022. The Shahejie Formation in the Dongpu Depression, Bohai Bay Basin, China: Geochemical investigation of the origin, deposition and preservation of organic matter in a saline lacustrine environment during the Middle Eocene. International Journal of Coal Geology 253, 103967.

Zhou, Y., Littke, R., 1999. Numerical simulation of the thermal maturation, oil generation and migration in the Songliao Basin, Northeastern China. Marine and Petroleum Geology 16(8), 771–792.

Zhu, X., Zeng, H., Li, S., Dong, Y., Zhu, S., Zhao, D., Huang, W., 2017. Sedimentary characteristics and seismic geomorphologic responses of a shallow-water delta in the Qingshankou Formation from the Songliao Basin, China. Marine and Petroleum Geology 79, 131–148.

Zieger, L., Littke, R., 2019. Bolsovian (Pennsylvanian) tropical peat depositional environments: the example of the Ruhr Basin, Germany. International Journal of Coal Geology 211, 103209.

Zou, C., Zhu, R., Chen, Z.Q., Ogg, J.G., Wu, S., Dong, D., Qiu, Z., Wang, Y.M., Wang, Lan., Lin, S.H., Cui, J.W., Su, L., Yang, Z., 2019. Organic-matter-rich shales of China. Earth-Science Reviews 189, 51–78.